# Synthesis of silica Janus nanoparticles

# with metal semishells

**Inaugural-Dissertation**
**to obtain the academic degree**
**Doctor rerum naturalium (Dr. rer. nat.)**

**submitted to the Department of Biology, Chemistry and Pharmacy**
**of Freie Universität Berlin**

**by**

**Scheghajegh Kord Daroun Kalai**

**From Babol, Iran**

**2018**

This work has been done at Atotech Deutschland GmbH, Berlin, in the period from May 01, 2013 to October 31, 2016 under the supervision of Prof. Dr. C. Graf from the institute of physical and theoretical Chemistry of the Freie Universität Berlin.

Date of defense: January 23rd, 2019

1st Reviewer: Prof. Dr. Christoph A. Schalley

2nd Reviewer: Prof. Dr. Christina Maria Graf

# Abstract

Dielectric colloids with asymmetric metal shells (Janus particles) have attracted much attention over the years. Their unique properties enable the application in versatile areas. One of the potential application fields is as an adhesion promoter between a dielectric surface and a metal; where one side of the colloid can chemically interact with a polymer substrate, while the other side contains a metal that can directly catalyze the electroless deposition process. In this work, challenges in the fabrication of asymmetric silica colloids with different metallic semishell coatings were investigated; and for the first time, a facile route was found towards the synthesis of large quantities of silica Janus particles with tunable metal shells and thicknesses.

First, monodisperse silica particles in sizes ranging from 60–1900 nm in diameter were synthesized as starting materials. Since they were stored as a dry powder, different ultrasonic devices and sonication times were used to deagglomerate the colloids into their initial particle sizes with low polydispersity in a stable solution.

Then, the influence of different reaction conditions was tested for binding a monolayer of 3-aminopropyltriethoxysilane (APTES) molecules on the silica colloids in ethanol. The surface functionalization can be enhanced by the presence of a catalyst or an increase in reaction time, or temperature because the reaction is in a thermodynamic equilibrium in protic solvents. An environmental and industrial friendly approach was introduced to synthesize silica particles with one monolayer of APTES. The number of amino groups on the surface was quantified by converting the accessible amino moieties into UV-Vis detectable species with a ninhydrin assay for all colloid sizes, and the C/H/N elemental analysis was used for smaller diameters.

Subsequently, silica Janus particles were successfully synthesized with high mass yields (50—70%) when the surfactants didodecyldimethylammonium bromide (DDAB) or cetyltrimethylammonium bromide (CTAB) were present during the preparation of the particle-wax colloidosomes. Even a small concentration of the surfactant was sufficient to improve the mass yield. The radius of gyration of the surfactants was used to calculate the area that the molecules occupy on the silica

surface. It was possible to manufacture single colloidosomes with closed-packed monolayers of silica particles on the wax surface. The silica colloids, embedded in wax, were grafted with a monolayer of APTES in the presence of triethylamine (TEA) after reacting for 1 h at 0 °C. Two characterization methods were successfully applied to compare the ratio of grafted and non-grafted area of the silica spheres, the so-called Janus balance. Metal layers were regio-selectively deposited onto the APTES spheres, and the corresponding shell coverage degrees were calculated from the corresponding SEM images. Additionally, the amine density at the surface was quantified with the ninhydrin assay. Both methods demonstrate for both surfactants that the Janus balance on a particle cannot be predicted by varying the amount or concentration of surfactant.

In the next step, a method was successfully introduced to coat the APTES-functionalized spheres with Pd seeds with a density of ~30 Pd atoms/nm$^2$, calculated from the ICP-OES results, that catalyzes the electroless deposition of metals onto the activated sphere. Janus particles yielded a surface density of ~20 Pd atoms/nm$^2$, which corresponds to a ~2/3 coverage of the silica colloid, even small amounts of Pd was used. The distribution of Pd clusters was heterogeneous throughout the different batches, which might be caused by the state of the amino groups at the surface of Janus particles or the chain length of the Pd(II) oligomers before the reduction step.

The same batch of Pd-seeded precursor particles was utilized for the fabrication of silica-core-metal-nanoshell composites for Ni, Cu, Au, Ag, and Pd using electrolytes reported in the literature, as well as commercially available ones. The layer morphology corresponds directly to the Pd seeds density and distribution on the silica surface, regardless of the deposited metal composition. The metal deposition results showed that in the presence of a complexing agent or a stabilizer, the formation of metal nuclei as side reaction was suppressed. The outcome from the preparation of metal fullshells was used to introduce a general procedure for growing metal semishells with tunable thicknesses for five different metals and electrolytic baths. Different characterization methods were used to prove the shell types and thicknesses, such as inductively coupled plasma optical emission spectroscopy (ICP-OES) measurements, diameter differences measured in SEM;

and for selected samples, a cross-section of the colloid using a focused ion beam (FIB).

# Kurzfassung

In den vergangenen Jahren rückten dielektrische Kolloide mit asymmetrischen Metallschalen (Janusspartikel) immer mehr in den Fokus, denn sie können durch ihre einzigartigen Eigenschaften in verschiedenen Bereichen angewandt werden, wie z.B. im elektronischen Papier, in photonischen Materialien und in Sensoren. Unter anderem können sie als Haftvermittler zwischen dielektrischen Oberflächen und Metallen verwendet werden, wobei die eine Seite des Partikels chemisch mit dem Polymersubstrat reagiert, während die andere Seite ein Metall enthält, das die stromlose Metallabscheidung aktivieren kann. Im Rahmen dieser Arbeit wurden die Herausforderungen bei der Synthese von asymmetrischen Silikapartikel mit verschiedenen Semischalen untersucht und neue Wege entwickelt um großen Mengen von Silika-Janusspartikel mit einstellbaren Schichtdicken herzustellen.

Zunächst wurden monodisperse Silikapartikel mit unterschiedlichen Durchmessern (60–1900 nm) als Ausgangsmaterial hergestellt. Weil die Silikapartikel als trockenes Pulver gelagert wurden, wurden die Kolloide durch verschiedene Ultraschallgeräte und Behandlungszeiten in ihre Ausgangspartikelgröße, einschließlich der dazugehörigen Polydispersion Indizes, zu stabilen Dispersionen desagglomeriert.

Anschließend wurde untersucht, welchen Einfluss verschiedene Reaktionsparameter auf die Beschichtung der Silikapartikel mit einer Monolage von 3-Aminopropyltriethoxysilan (APTES)-Molekülen in Ethanol ausüben. Die Oberflächenbeschichtung konnte durch eine höhere Reaktionstemperatur, längere Reaktionszeit oder mittels eines Katalysators beschleunigt werden, da ein thermodynamisches Gleichgewicht in protischen Lösungsmittel besteht. Eine umwelt- und industriefreundliche Methode wurde eingeführt um Kolloide mit einer Monolage von APTES zu synthetisieren. Die Aminogruppen auf der Silikaoberfläche wurde mittels Ninhydrin-Probe in eine Spezies umgewandelt, die im UV-Vis nachweisbar ist. Dadurch konnte die Anzahl der Aminogruppen auf der Kolloidoberfläche für sämtliche Partikelgrößen bestimmt werden. Für kleine Partikel mit einem Durchmesser von ~60 nm wurde zusätzlich die Anzahl der Funktionellengruppen über C/H/N-Elementaranalyse bestimmt.

Zudem wurden Silika-Januspartikel mit einer hohen Massenausbeute dargestellt (50—70%) indem die Tenside Didodecyldimethylammoniumbromid (DDAB) und Cetyltrimethylammoniumbromid (CTAB) während der Herstellung der Partikel-Wachs-Kolloidosomen verwendet wurden. Um die Fläche zu berechnen, die die Tenside auf der Silikaoberfläche besetzen, wurde der Trägheitsradius der Ternside ermittelt. Somit war es möglich, gezielt Partikel-Wachs-Kolloidosomen herzustellen, die eine dicht-gepackte Monolage von Silikapartikeln auf der Wachsoberfläche aufweisen. Anschließend wurden die Silikapartikeln, die im Wachs einbettet waren, mit einer Monolage von APTES in Gegenwart von Triethylamin (TEA) bei 0°C für 1 h beschichtet. Zwei Methoden wurden verwendet um das Verhältnis zwischen beschichteter und nicht-beschichteter Silikaoberflächen, die sogenannten Janus-Balance, zu bestimmen. Die APTES-funktionalisierte Kugelflächen wurden regioselektiv mit einem Metallfilm beschichtet und der daraus resultierende Bedeckungsgrad im Rasterelektronenmikroskop (REM) ausgewertet. Zusätzlich wurde die Anzahl an Aminogruppen auf der Silikaoberfläche mittels Ninhydrin-Probe quantifiziert. Beide Methoden für die jeweiligen Tenside haben gezeigt, dass es nicht möglich ist, die Janus-Balance gezielt einzustellen, in dem die Tensidekonzentration variiert wird.

Im nächsten Schritt wurde erfolgreich eine Methode eingeführt mit der es möglich ist, APTES-funktionalisierte Partikelflächen mit Palladium (Pd)-Keimen mit einer Pd-Dichte von ~30 Pd-Atomen/nm$^2$ zu beschichten, so dass sie die stromlose Metallabscheidung katalysieren können. Die Silika-Januspartikel wurden mit einer Pd-Dichte von ~20 Pd-Atomen/nm$^2$ umhüllt, was einem Bedeckungsgrad von ~2/3 entspricht. Die Verteilung der Pd-Keimgruppen auf der Oberfläche variierte je nach Charge. Gründe hierfür könnte der Zustand der Aminogruppen auf der Oberfläche der Januspartikel oder die Kettenlänge der Pd(II)-Oligomere vor dem Reduktions-Schritt sein.

Die gleiche Charge mit Pd-Keimen funktionalisierter Silikapartikel wurde für die Herstellung von Silika-Kern-Metall-Nanoschalen für Ni, Cu, Au, Ag und Pd verwendet. Hierfür wurden nach Literaturvorschriften hegestellte Elektrolyte, sowie kommerziell erhältliche Zusammensetzungen verwendet. Die Beschich-

tungsmorphologie entsprach der Verteilung der Pd-Keimdichte auf der Silikaoberfläche unabhängig von dem abgeschiedenen Metalltyp. Die gewünschte Schichtdicke konnte einfach eingestellt werden, in dem die Elektrolytmenge variiert wurde. Die Daten zeigen, dass im Beisein von Komplexierungsreagenzien oder Stabilisatoren, weniger Metallkeime als Nebenprodukte entstehen. Die Ergebnisse von den Vollschalenexperimenten wurden verwendet um Silika-Januspartikel mit unterschiedlichen Metallbeschichtungen und einstellbaren Schichtdicken herzustellen. Dabei wurden verschiedene Charakterisierungs-methoden verwendet, um die Schichtdicken zu überprüfen: ICP-OES-Messungen; die Differenz der Durchmesser in den REM-Bildern vor und nach dem Schalenwachstum sowie für ausgesuchte Proben mittels einer Ionenfeinstrahlanlage Focused Ion Beam, FIB) hergestellte Querschnitte der Partikel.

# TABLE OF CONTENTS

# 1. INTRODUCTION

Small structures on a nanometer scale ($10^{-9}$ m) are present in nature as biological systems such as lotus flowers[1] and insect wings[2], or as inorganic materials such as opals.[3] Implementing nature's nano-architecture on materials produces compounds with unique functions. However, much of electronic, optical, and catalytical properties of nanoparticles originate from their quantum-scale dimensions.[4] Nanoparticles can be tailored in the shape of spheres, rods, wires, semishells, or cubes, and they can consist of organic, metals, oxides, or semiconductors materials. Additionally, the particle sizes and the surface functional moieties can be adjusted. Consequently, nanoparticles are ideal candidates for nanoengineering functional surfaces, because they can be fabricated according to the application.

One of the potential application fields is as an adhesion promoter between a dielectric substrate and metals for industrial processes. In the electronics industry, the manufacturing of printed circuit boards (PCB) is driven by the requirements of producing devices with small features and faster data transmission at low cost. Consequently, for higher interconnect densities, the PCB's conductor line width and spacing (L/S) have to decrease, whereas the data transmission frequency has to increase.[5] Meanwhile, a sufficient substrate-to-conductor adhesion strength has to be ensured. A facile and common method to achieve good adhesion is the wet chemical etching of surfaces,[6],[7],[8] in which the substrate is roughened before the deposition processes. The strong adhesion is achieved by mechanical interlocking between the deposited conductor and the substrate. With decreasing L/S, the performance of the printed circuit is likely to degrade through excessive cross talk and increased noise.[5] When high transmission frequencies are applied, the so-called skin-effect occurs in electrical conductors. In such cases, the current flows mainly near the outer surface, the skin, of the conductor.[9] The higher the roughness of the substrate, i.e., the higher the surface area of the conducting line, the longer the path of the electrical signal that travels through the conductor. The combination of very fine lines and a high substrate roughness can thus lead to considerably weaker signals or a loss of signal. For high frequency interconnects, it

is therefore desirable to achieve strong substrate-to-conductor adhesion without introducing further roughness. During PCB manufacture, the conducting structures are commonly prepared by wet chemical deposition of copper on dielectric substrates.[10]

Thomas et al. successfully introduced an adhesion promoter for this process containing amino-functionalized silica nanoparticles.[11] The adhesion promoter is deposited onto the dielectric substrate surface before the palladium (Pd) adsorption step. The Pd-activated surface catalyzes the electroless (eless) copper deposition onto the substrate surface (see Figure 1-1).

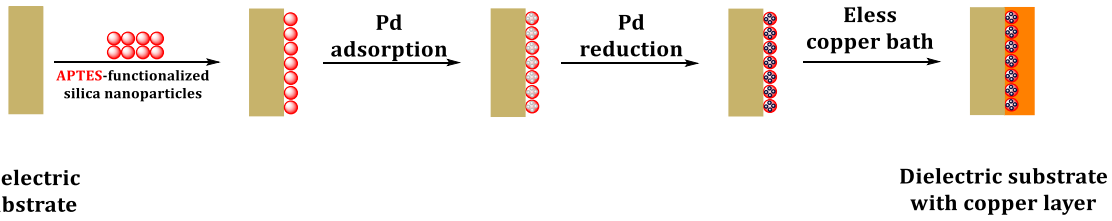


**FIGURE 1-1 SCHEMATIC ILLUSTRATION OF THE METALLIZATION PROCESS OF THE DIELECTRIC SUBSTRATE DESCRIBED BY THOMAS ET AL.[11] THIS PROCEDURE INVOLVES AMINE-FUNCTIONALIZED SILICA PARTICLES ON THE DIELECTRIC SURFACE, SUBSEQUENTLY ADSORBING AND REDUCING PD IONS ON THE SURFACE, AND FINALLY DEPOSITING COPPER ON THE SURFACE.**

Based on the outlined procedure, the current study was deduced. This work focuses on the synthesis of a new adhesion promoter consisting of two different moieties, the so-called Janus particles. One side of the spherical colloid can chemically interact with a polymer substrate, while the other side contains a metal that could directly activate the electroless deposition process. Once this new, asymmetric adhesion promoter is introduced in the PCB production, the process becomes time, ergo cost efficient, because the activation step with the Pd adsorption and the reduction can be omitted.

The objective of this present investigation was to synthesize and characterize new and versatile silica Janus particles. The main target was to find a facile route toward the synthesis of asymmetric silica colloidal particles with tunable metal semishell coatings. The starting point was the optimization of the synthesis of silica Janus particles in high mass yields and well-controlled ratios of the coated

and non-coated areas. The next step was to define optimum reaction conditions for the functionalization of the colloidal silica sphere with a monolayer of amino groups and to find suitable characterization methods. The crucial step was the partial activation of the silica Janus particles with a catalyst that was appropriate for different electroless metal deposition processes, and the ultimate synthesis of so-called semishells using different metal electrolytes.

# 2. THEORETICAL BACKGROUND

## 2.1. SILICA PARTICLES

Silica nanoparticles have unique chemical and physical properties and find application in many areas such as food, cosmetics, adhesives, and films.[12],[13] In recent years, labeled- and functionalized silica nanoparticles have even been applied for biological and medical purposes such as drug carriers.[14] These types of particles can be prepared using several methods. A common method of synthesis is the sol-gel procedure introduced by Stöber et al.,[15] which allows the preparation of size-controlled, spherical, monodisperse silica particles. With varying reagent concentrations, different colloid sizes can be obtained.[16] The underlying process consists of two main steps: hydrolysis and condensation. Brinker et al.[17] reported that in the base-catalyzed mechanism, the starting alkoxysilanes are hydrolyzed via a nucleophilic attack ($S_N2$) by the hydroxide ions on the silicon atoms. Penta-coordinate, negatively-charged intermediates are formed, and ethanol is displaced (hydrolysis) to form silanols (2-1). The negatively-charged intermediate becomes more stable and decreases the electron density at the silicon atom. As the stronger electron-withdrawing OH group replaces the ethoxygroup, the decrease in the electron density increases the hydrolysis rate for each subsequent hydrolysis step. For monomers, the hydrolysis of the first alkoxygroup is the rate determining step and can be accelerated by increasing the catalyst concentration.[17-18] Under basic conditions, the deprotonated silanolate ions attack Si atoms to form siloxane bonds (2-2), along with alcohol or water, in a condensation reaction.

**Hydrolysis**

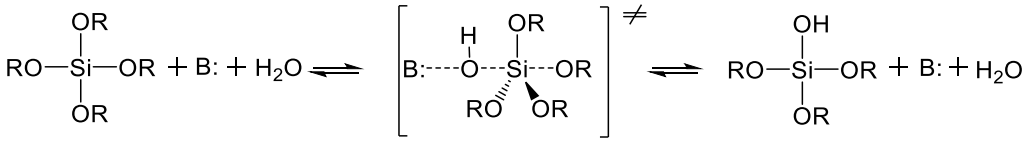


**(2-1)**

**Esterification through condensation**

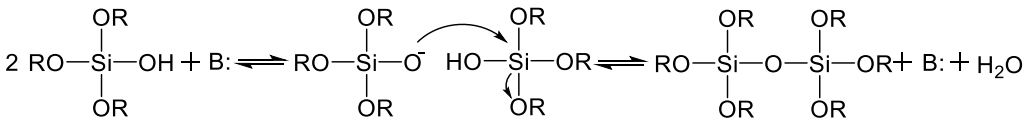


**(2-2)**

These repetitive hydrolysis and condensation reaction result in siloxane chains, which branch out into organized networks, clusters, or colloidal particles depending on the nature of the catalyst (see Figure 2-1). There are several models that describe the fractal structure growth as well as the classical nucleation and growth.[19],[20] In silicate systems, the predominant growth occurs by the condensation of monomers with clusters (monomer-cluster growth) or clusters with other clusters (cluster-cluster growth).

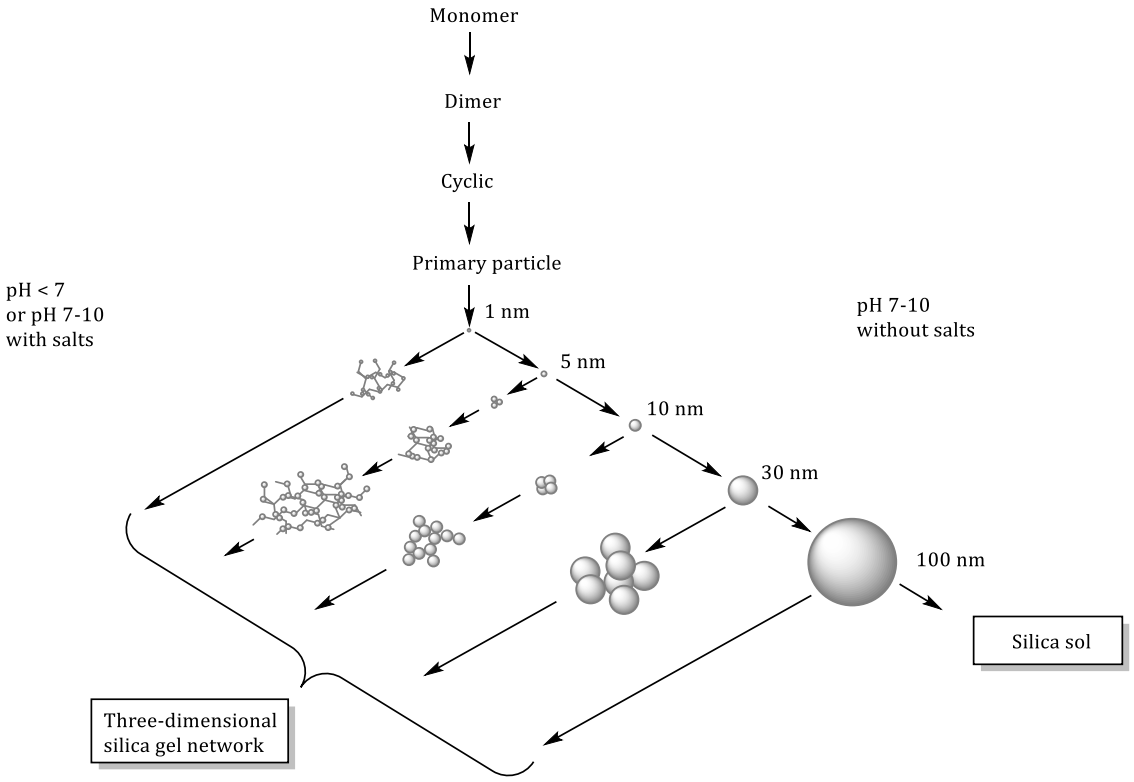


**FIGURE 2-1 SCHEMATIC ILLUSTRATION OF THE SILICA POLYMERIZATION BEHAVIOR IN AQUEOUS MEDIA, ADAPTED FROM ILER. [20] BELOW PH 7 OR IN THE PRESENCE OF FLOCCULATING SALTS, PARTICLES AGGREGATE INTO THREE-DIMENSIONAL NETWORKS AND FORM SILICA GELS. ABOVE PH 7 PARTICLES GROW IN SIZE WITH A DECREASED NUMBER.**

In the reaction-limited monomer-cluster aggregation (RLMCA) growth model proposed by LaMer et al., nuclei are formed at a critical degree of supersaturation.[21] Subsequently, these primary particles grow by the addition of monomers supplied by the supersaturated solution. With the decreasing degree of supersaturation, the oligomers dissolve and contribute to the growing nuclei in alkaline medium. The depolymerization of many small particles and the reorganization into fewer larger particles (Ostwald ripening) reduces the overall surface energy, which is the driving force for the reaction.[22] The depolymerization occurs at less stable sites, and the repeated dissolution/reprecipitation creates either monomers ($^0$Q) or stable configuration ($^4$Q) (see Figure 2-2), resulting in compact and smooth clusters. Once the particles reach a certain size, the electrostatic repulsion stabilizes the dispersion, and no gelation is observed. Since the Ostwald ripening alone cannot account for the rapid growth and controlled aggregation of primary particles, other researchers suggested that the particle nucleation proceeds through an aggregation process.[23],[24] Below a certain size, there is no mutual repulsion between primary particles, and they aggregate and cause a collective reduction of the surface area, leading to the reduction of the surface energy. Since the reaction proceeds under alkaline condition, monomers are supplied continuously.

Under acidic conditions, the depolymerization is minimized and no monomers are continuously supplied. Under such conditions, the cluster-cluster aggregation growth is expected to pertain. The hydrolysis of the monomers is completed at an early stage of the reaction. The hydrolyzed monomers move with Brownian trajectories and condense with other monomers or oligomers irreversibly.[25] The low-molecular-weight oligomeric species move at reduced velocity, and undergoe condensation reactions to form randomly branched open structures.

The different types of potential groups at the silica surface are displayed in Figure 2-2. There can be isolated surface silantriols ($-Si(OH)_3$, type $Q^1$); isolated germinal surface groups ($=Si(OH)_2$, silandiols, type $Q^2$); isolated surface silanols ($\equiv SiOH$, type $Q^3$); vicinal bridge silanols (i.e., single silanols, single germinal silanols, or combinations bound with one another by hydrogen bonds, or $\equiv Si-O-Si\equiv$,

siloxane bridges with the O atom at the surface, type $Q^4$); and internal silanols (located in the skeleton and/or in ultramicropores of $SiO_2$).

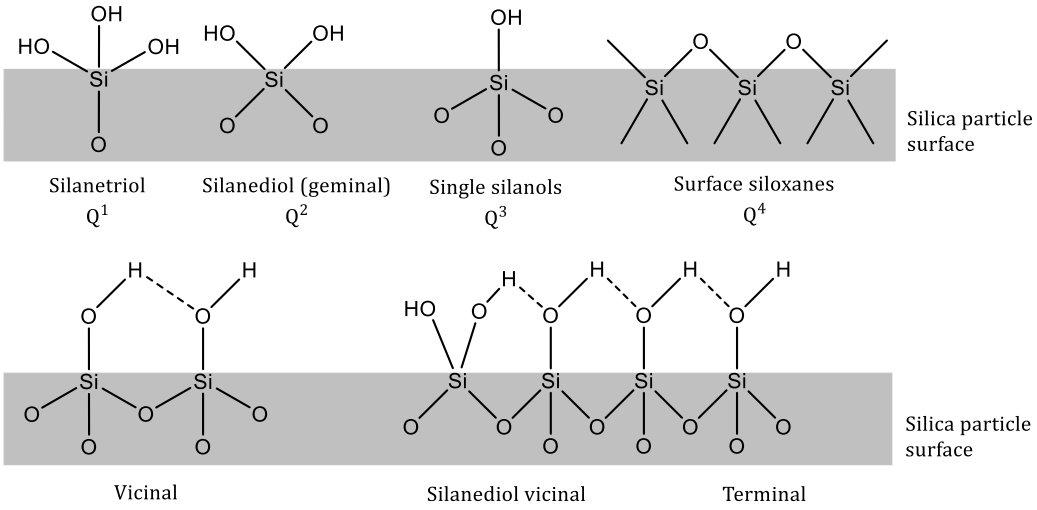


**FIGURE 2-2 SCHEMATIC ILLUSTRATION OF THE TERMINAL GROUPS ON SILICA PARTICLES, ADAPTED FROM ZHURAVLEV ET AL. [26]**

## 2.2. SILICA JANUS PARTICLES

Symmetric shapes are considered appealing, but many objects within our body consist mostly of asymmetric structures such as lipids, proteins, and tissues. In colloidal chemistry, asymmetric composites were introduced by Casagrande et al.,[27] who prepared spherical glass particles with a hydrophilic and a hydrophobic hemisphere. They were named "Janus bead" after the Roman god of beginning and ending (see Figure 2-3). After de Gennes addressed the potential of this class of colloids during his Nobel lecture,[28] Janus particles gained scientific attention over the years.[29] There is a wide range of possible applications for these particles, but the synthesis remains challenging.

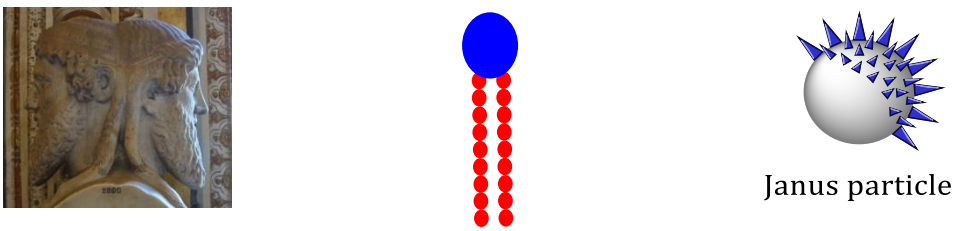


**FIGURE 2-3 PHOTO OF THE JANUS STATUE IN THE VATICAN MUSEUM[30] (LEFT), GRAPHIC ILLUSTRATIONS OF A LIPID STRUCTURE (MIDDLE) AND OF A JANUS PARTICLE (RIGHT).**

Several methods for the preparation of these particles have been reported, which allow the modification of one side of the nanospheres without altering the other side of the particle. Figure 2-4 illustrates a schematic overview of four methods described in the literature for toposelective surface modification of particles. Modification route (a) involves a temporary, partial protection of particles, which is one of the frequently applied methods. The masking is achieved either with a cellulose varnish film,[31] with the so-called "gel tapping technique,"[32] or with solidifying molten wax.[33] In the method (b), particles are partly modified with metals, using physical vapor deposition techniques. Here, the area of a monolayer of particles exposed to the metal vapor is modified, while leaving the opposite halves of the spheres pristine. This method is called "directional flux and fields." Examples of this type of modification are gold sputtering on latex microparticles,[34] and physical vapor deposition of gold, platinum, or palladium on submicrometer silica particles.[35] Method (c) is based on microcontact printing technique. A film of water-insoluble ionic surfactants is used on an elastomeric stamp, which is deposited onto monolayers of colloidal particles of opposite surface charge.[36],[37] In route (d), Janus particles are prepared by orientating colloidal particles along the interface of two media, where the reacting molecules are only present in one medium. Raspberry-like polymer microparticles[38] and patchy gold clusters on silica particles[39] were successfully generated at a liquid/solid and air/water interface.

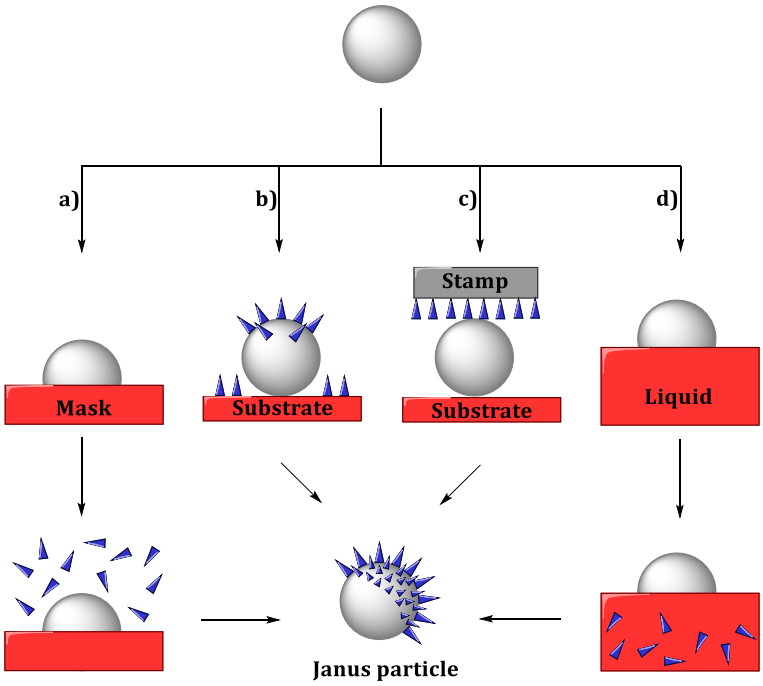


**FIGURE 2-4 SCHEMATIC OVERVIEW OF FOUR MODIFICATION METHODS FOR TOPOSELECTIVE FABRICATION OF JANUS PARTICLES: (A) MASKING, (B) DIRECTIONAL FLUX AND FIELDS, (C) MICROCONTACT PRINTING WITH A STAMP, AND (D) PARTIALLY CONTACTING WITH REACTIVE MEDIA, ADAPTED FROM PERRO ET AL.[40]**

An entirely different approach for the fabrication of Janus particles is based on bipolar electrochemistry.[41] In this case, electrically conductive particles dispersed in a metal salt solution are used as bipolar electrodes. When a sufficiently high voltage is applied, the potential difference in the conductive material will cause both oxidation as well as reduction reactions at each particle.[41] The synthesis of Janus particles using bipolar electrochemistry is a bulk technique with high yields but only applicable for large micrometer-sized and conducting particles such as carbon nanotubes[42] and glassy carbon.[43]

For the present study, the fabrication method of choice was the masking process (a) with generating so-called particle-wax colloidosomes, which is described in the next section.

### 2.2.1. Fabrication of particle-wax colloidosomes

Colloidosomes are named in analogy to liposomes, and were first introduced as hollow and elastic capsules, where the capsule surface consisted of a close-packed layer of colloids.[44] This work was the foundation for fabricating Janus particles by Hong et al.,[33] where bare silica particles were first dispersed in a molten paraffin wax/water emulsion at elevated temperature. Hydrophilic colloidal particles self-assemble at the interface of oil-in-water emulsion droplets,[45] generating so-called Pickering emulsions.[46] By lowering the temperature, the molten wax solidifies providing a removable coating on one side of the particle, while leaving the other side open for further modification (see Figure 2-5).

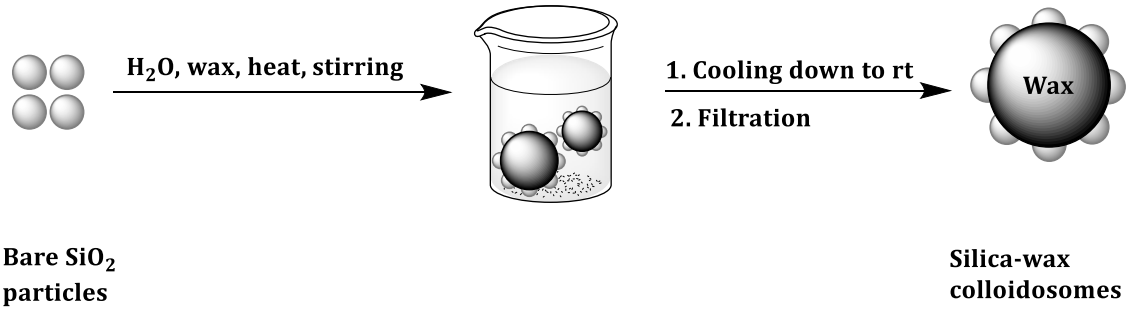


**Figure 2-5 Schematic illustration of the strategy to fabricate particle-wax colloidosomes after Hong et al.[33]**

The intrusion depth of silica particles into the molten wax can be increased by using surfactants. It was reported that didodecyldimethylammonium bromide (DDAB)[47] as well as cetyltrimethylammonium bromide (CTAB)[48] can partially hydrophobize the surface of the hydrophilic silica nanoparticles. The deprotonated silanol oxygen interacts with the positively charged surfactant head, forming alkyl chain terminated particles. According to both research groups, these hydrophobic nanocomposites can penetrate deeper into the molten wax in a controllable manner and the intrusion depth is tunable by varying the surfactant concentrations.

Consequently, one of the aims of the current project was to evaluate these claims by comparing the influence of DDAB and CTAB on the penetration depth and the mass yield, and to determine the optimum reaction conditions for the fabrication of particle-wax colloidosomes.

### 2.2.2. Synthesis of metal coated Janus particles

During the present study, the main target was to find a suitable route towards the synthesis of silica Janus particles with a broad range of metal semishell coatings. For the sake of convenience, the different shell types are specified in Figure 2-6 according to van Dorpe et al.[49] The term nanoshell refers to a dielectric core that is completely coated with a metal shell at a nanometer scale (fullshell). The term semishell corresponds to a dielectric core that is partially covered with an incomplete metal shell. Semishells can be classified as nanocaps, halfshells, or nanocups.

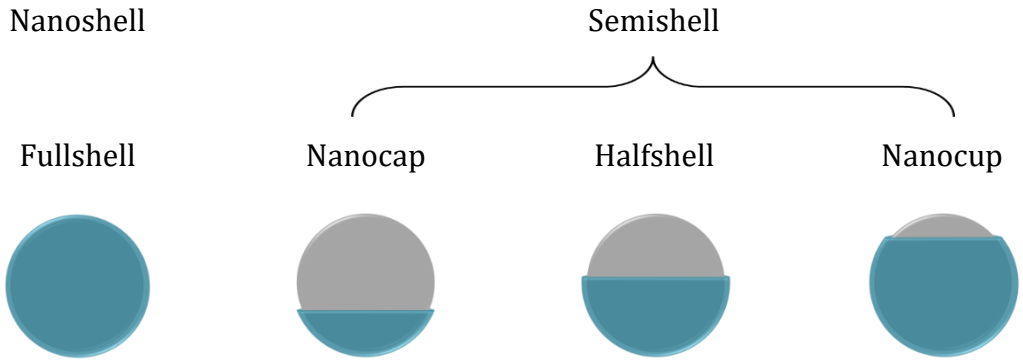


**Figure 2-6 Overview of different shell types: (left) entirely covered nanoshell with a dielectric core; (right) three types of semishells. Depending on the fractional metal coverage. They are classified as nanocap, halfshell, or nanocup, according to van Dorpe et al.[49]**

There are several reports focusing on the synthesis of spherical particles with metal semishells, especially with Au coating because of their unique optical properties.[39b, 49] Petit et al. illustrated different approaches for coating a monolayer of silica nano beads with Au nanoclusters.[39b] The colloids are spread at the air/Au colloid-containing medium interphase, or immobilized on a flat surface and exposed to Au vapor. The evaporation of a thin metal film upon a monolayer of particles on a flat surface is also used to prepare spherical colloids with palladium, platinum, or nickel halfshells.[35],[50] This procedure is expensive and not suitable for industrial applications since only little amounts of particles can be metalized in one step.

Another protocol to synthesize silica Janus particles with Au semishells comprises the preparation of amine-functionalized silica Janus particles according to Hong et al.,[33] and the selective adsorption of "small" Au nanoparticles as seeds for further modification.[51] Subsequently, these Au-activated spheres are added to an Au electrolyte containing a reducing agent. The Au seeds mediate the electron transfer from the reducing agent towards the Au ions, creating an Au layer.[52] This method is referred to as an electroless deposition process. During the present work, the deposition process was used to fabricate silica Janus particles with a wide range of different metal semishells. The corresponding electroless metal deposition mechanisms are described for each metal separately in the following sections.

## 2.3. ELECTROLESS METAL DEPOSITION

The electroless deposition process was introduced by Brenner and Riddell who deposited nickel and cobalt on a palladium-activated surface from a solution of metal ions as source and hypophosphite as reducing agent without the use of an external current.[53] In this process, the reducing agent inside the solution (Red) will donate electrons to the catalytic surface, which will then be utilized for the reduction of the metal ions ($M^{z+}$) while being converted to the corresponding oxidation product (Ox), (Equation (2-3)):[10b]

$$M^{z+}_{solution} + Red_{solution} \xrightarrow{\text{catalytic surface}} M_{lattice} + Ox_{solution} \qquad \textbf{(2-3)}$$

According to the so-called mixed-potential theory, the overall reaction (Equation (2-3)) can be separated into a cathodic reduction reaction (Equation (2-4)) and an anodic oxidation reaction (Equation (2-5)).[54] The letters z and m represent the number of electrons that are taken up by the metal ion or released back into the solution, respectively.

Reduction: $$M^{z+}_{solution} + z\,e^- \xrightarrow{\text{catalytic surface}} M_{lattice} \qquad \textbf{(2-4)}$$

Oxidation: $$Red_{solution} \xrightarrow{\text{catalytic surface}} Ox_{solution} + m\,e^- \qquad \textbf{(2-5)}$$

Both partial reactions occur at the same electrode (metal—solution interphase), and each of these reactions aims to establish its equilibrium potential $E_{eq}$, resulting in a compromised potential called steady-state mixed potential $E_{mp}$. For the electroless deposition to occur, the equilibrium potential of the reducing agent must be more negative than that of the metal electrode, causing the reducing agent to function as an electron donor and the metal electrode as an electron acceptor.[10b] Experimental data confirmed the accuracy of the mixed-potential theory for the electroless deposition of Cu, Ni, and Au.[10a]

The electroless deposition is an autocatalytic plating process, where the deposited metal layer catalyzes the deposition of more metal onto the layer. That means the layer can grow continuously, as long as the surface is in contact with the electrolyte containing all the necessary components. The Cu and Ni deposition are discussed in more details since the electrolytes applied during this present study contain more ingredients and are more complex (Chapter 2.3.1 and 2.3.2).

### 2.3.1. ELECTROLESS COPPER DEPOSITION

When applying the mixed-potential theory to investigate the electroless copper deposition in the presence of formaldehyde as a reducing agent (see Figure 2-7 a), the overall reaction can be described as two current-potential (i-E) curves, as illustrated using the Evans diagram in Figure 2-7 b.[55] The current-potential curve for the reduction of copper ions $i(Cu^{2+})=f(E)$ is recorded starting from the equilibrium potential $E_{eq}(Cu/Cu^{2+})$= -0.47 V versus the saturated calomel electrode (SCE). The current-potential curve for the oxidation of formaldehyde $i(CH_2O)=f(E)$ is recorded starting from the equilibrium potential $E_{eq}(CH_2O)$=-1.0 V versus SCE. The intersection coordinates of the two curves describe the mixed-potential ($y=E_m$=-0.65 V) and the current density ($x=i=1.0\cdot10^{-3}$ A/cm$^2$). The current density at the intersection is the deposition current density, which is the rate of the electroless deposition in terms of mA/cm$^2$.[56]

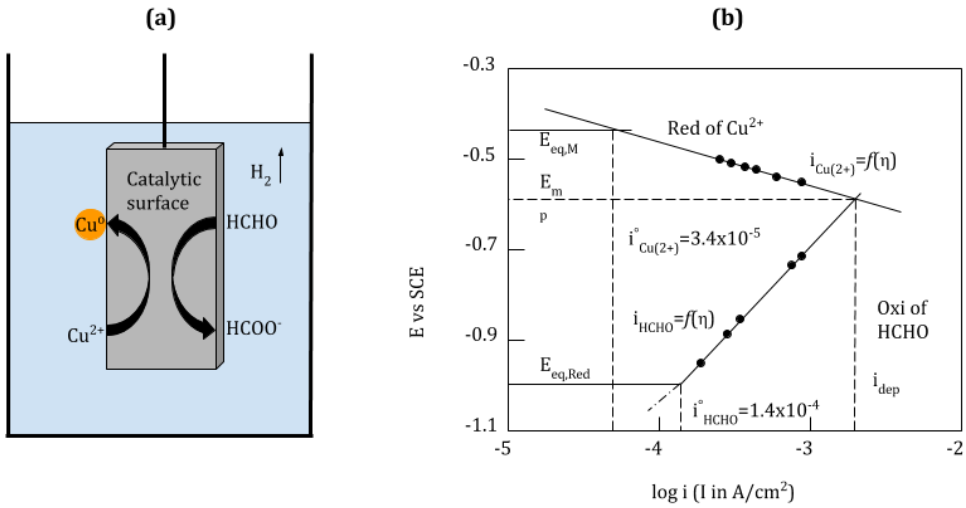


**FIGURE 2-7 SCHEMATIC ILLUSTRATION OF A) ELECTROLESS DEPOSITION OF CU ON A CATALYTIC ACTIVE SURFACE AND B) THE EVANS DIAGRAM ACCORDING TO THE MIXED-POTENTIAL THEORY FOR ELECTROLESS CU DEPOSITION WITH FORMALDEHYDE, ADAPTED FROM SCHLESINGER ET AL.[10B]**

#### 2.3.1.1. COPPER DEPOSITION MECHANISM

The following Equation (2-6) presents the stoichiometric cathodic reduction of copper (Cu) ions to elementary $Cu^0$ and the anodic oxidation of formaldehyde to formate anions in alkaline solution:

$$Cu^{2+} + 2\ HCHO + 4\ OH^- \rightarrow Cu^0 + 2\ HCOO^- + H_2 + H_2O \qquad \textbf{(2-6)}$$

Although the mixed-potential theory assumes two independently occurring reactions,[54],[55a] studies showed that interfering or side reactions influence the overall process.[56-57] Therefore, the partial reactions are examined in more detail.

**Anodic partial reaction**

The anodic partial reaction contains two main steps: 1) formation of an electroactive species and 2) the charge transfer from the electroactive species to the catalytic surface.[10b]

The generation of the electroactive species contains three steps. First, the hydrolysis of formaldehyde into methylene glycol occurs (Equation (2-7)):

$$H_2CO + H_2O \rightarrow H_2C(OH)_2 \qquad \textbf{(2-7)}$$

Followed by the dissociation of methylene glycol into its anionic intermediate (Equation (2-8)):

$$H_2C(OH)_2 + OH^- \rightarrow H_2C(OH)O^- + H_2O \quad \textbf{(2-8)}$$

The active species is formed when the anionic intermediate is dissociatively adsorbed onto the catalyst surface while breaking the C—H bond (Equation (2-9)):

$$H_2C(OH)O^- \rightarrow [HC(OH)O^-]_{ads} + H_{ads} \quad \textbf{(2-9)}$$

The adsorbed electroactive species transfers its charge to the catalyst while oxidizing to a formate anion ($HCOO^-$), which will be released back to the electrolyte (Equation (2-10)):

$$[HC(OH)O^-]_{ads} + OH^- \rightarrow HCOO^- + H_2O + e^- \quad \textbf{(2-10)}$$

The hydrogen $H_{ads}$ desorbs in two different manners, depending on the substrate. When the substrate is palladium or platinum, $H_{ads}$ is released back to the solution as a proton (Equation (2-11)), when the substrate is Cu, $H_{ads}$ is desorbed as hydrogen gas (Equation (2-12)):

$$H_{ads} \rightarrow H^+ + e^- \quad \textbf{(2-11)}$$

$$H_{ads} \rightarrow \tfrac{1}{2}\, H_2 \quad \textbf{(2-12)}$$

One of the side reactions is the Cannizzaro reaction, which describes the disproportionation of formaldehyde to formate (oxidation) and methanol (reduction, Equation (2-13)).

$$2\, HCOH + OH^- \rightarrow HCOO^- + CH_3OH \quad \textbf{(2-13)}$$

Important factors in the anodic partial reaction are the pH value and the additives inside the electrolyte.

**Cathodic partial reaction**

Experiments showed optimum electroless Cu plating results when the pH is above 11,[58] which imposes the usage of complexing agents to prevent Cu(II) hydroxide precipitation. The cathodic reaction can be divided into two kinetic steps. The first one describes the reduction of $Cu^{2+}$ into $Cu^{1+}$, which is the rate determining step (Equation (2-14)), followed by the reduction to $Cu^0$ (Equation (2-15)):

$$Cu^{2+} + e \rightarrow Cu^{1+} \quad \textbf{(2-14)}$$

$$Cu^{1+} + e \rightarrow Cu^{0} \quad \textbf{(2-15)}$$

The second reduction step comprises the formation of an electroactive species and the charge transfer from the catalytic surface towards it. Electroactive $Cu^{2+}$ species are formed by the dissociation of the complex $[CuL_x]^{2+xp}$ (Equation (2-16)), where p is the charge state of the ligand L and 2 + xp is the charge of the complexed Cu ion, followed by the electrochemical reaction (Equation (2-17)).

$$[CuL_x]^{2+xp} \rightarrow Cu^{2+} + xL^{p} \quad \textbf{(2-16)}$$

$$Cu^{2+} + 2e \rightarrow Cu_{lattice} \quad \textbf{(2-17)}$$

Important factors in the cathodic partial reaction are the concentration of Cu ions, the type of ligands, the pH value, and the additives inside the electrolyte. In Table 2-1, common components of the electroless Cu electrolytes are summarized.

**TABLE 2-1 OVERVIEW OF COMPONENTS OF THE ELECTROLESS CU ELECTROLYTES**

| Component | Example |
|---|---|
| Copper source | Copper sulfate |
| Reducing agent | Formaldehyde, dimethylamine borane (DMAB), sodium hypophosphite |
| Complexing agent | Potassium sodium tartrate (Rochelle salt), ethylenediamine-tetraacetic acid (EDTA), glycolic acid, triethanolamine |
| Stabilizer | 2,2'-bipyridine, N,N'-diethyl thiourea, oxygen, thiourea, 2-mercaptobenzothiazole, diethyldithiocarbamate |
| Accelerator | Cyanide, proprionitrile, o-phenanthroline |

### Growth mechanism

The copper growth mechanisms can be divided into two steps: (1) the thin-film stage (up to 3 µm) and (2) the bulk stage. The mechanism consists of three simultaneous crystal-building processes: nucleation, growth, and the coalescence of three-dimensional crystallites; followed by the formation of a linked network; and the formation of a continuous deposit. In general, the electroless deposition on

catalyzed nonconductors produce fine grain equiaxial growth initially with conversion to larger columnar grains as film thickness increases.[59]

### 2.3.2. Electroless nickel Deposition

The electroless Ni deposition process describes the chemical reduction of aqueous Ni ions on an activated substrate in the presence of a reducing agent. The following equation (2-18) presents the stoichiometric cathodic reduction of nickel ions to elementary Ni and the anodic oxidation of the hypophosphite to phosphonate anions, as mentioned in the literature.[59] Whereby, the equation (2-18) fails to include the presence of elemental phosphorous, which is also observed in the deposited Ni layer.

$$Ni^{2+} + 2\ H_2O + 2\ H_2PO_2^- \rightarrow Ni^0 + 2\ H_2PO_3^- + 2\ H^+ + H_2 \qquad \textbf{(2-18)}$$

Although the process is not entirely clarified, four mechanisms have been postulated over the years. Originally, Brenner and Riddell suggested that the actual Ni reductant is atomic hydrogen, which is generated when water molecules and hypophosphite anions adsorb with their hydrogen atoms on the catalytically active surface.[53] The oxidation of the hypophosphite occurs with the transfer of the hydroxyl group from an adsorbed water molecule, leading to the separation of a hydrogen atom while releasing an electron (Equation (2-19)). The hydrogen atom remains at the surface and can interact with an adjacent adsorbed hydrogen atom. Alternatively, the remaining proton from the water molecule can go back into the electrolyte after desorption, where it can be reduced to atomic hydrogen, after the uptake of an electron. The hydroxyl group transfer from the water molecule to the hypophosphite anion results in the formation of the phosphonate anion $H_2PO_3^-$ which is released back into the solution.[60]

$$H_2PO_2^-{}_{ads} + H_2O_{ads} \rightarrow H_2PO_3^- + H_{ads} + H^+ + e^- \qquad \textbf{(2-19)}$$

Subsequently, the adsorbed atomic hydrogen reduces a $Ni^{2+}$ ion at the catalytic surface (Equation (2-20)):

$$Ni^{2+} + 2\ H_{ad} \rightarrow (Ni^{2+} + 2\ H^+ + 2\ e) \rightarrow Ni^0 + 2\ H^+ \qquad \textbf{(2-20)}$$

The hydrogen gas evolution is a side reaction during the Ni reduction and results from the reaction between two atomic hydrogen atoms (Equation (2-21)):

$$H^0_{ads} + H^0_{ads} \rightarrow H_2 \quad \textbf{(2-21)}$$

Gutzeit complemented the postulated mechanism with the suggestion that the formation of atomic hydrogen results from the dehydrogenation of the hypophosphite ion during the formation of the metaphosphite ion (Equation (2-22)):[61]

$$H_2PO_2^- \xrightarrow{cat} PO_2^- + 2\,H \quad \textbf{(2-22)}$$

Subsequently, an orthophosphite molecule and a hydrogen ion are generated (Equation (2-23)):

$$PO_2^- + H_2O \rightarrow HPO_3^{2-} + H^+ \quad \textbf{(2-23)}$$

A secondary reaction between hypophosphite and atomic hydrogen results in the formation of elemental phosphorous (Equation (2-24)):

$$H_2PO_2^- + H \rightarrow P + OH^- + H_2O \quad \textbf{(2-24)}$$

The mechanism involving atomic hydrogen supports the observed results, but it fails to explain the simultaneous reduction of $Ni^0$ and $P^0$ or why the stoichiometric utilization of hypophosphite in less than 50 %. Consequently, Hersch introduced another mechanism called the hydride transfer.[62] Where it is assumed that hypophosphite acts as the donor of hydride ions ($H^-$) analogous to the reduction of Ni ions by borohydride ions, which constituted the groundwork for Lukes approach.[63] In acidic medium, the first step comprises the reaction between water and hypophosphite at the catalytic surface (Equation (2-25)):

$$2\,H_2PO_2^-{}_{ads} + 2\,H_2O_{ads} \xrightarrow{cat} 2\,H_2PO_3^- + 2\,H^+ + 2\,H^- \quad \textbf{(2-25)}$$

The released hydride ions reduce the Ni ions to elemental $Ni^0$ (Equation (2-26)):

$$Ni^{2+} + 2\,H^- \rightarrow Ni^0 + H_2 \quad \textbf{(2-26)}$$

In an acidic environment, the hydride ion can also react with a hydrogen ion (Equation (2 27)):

$$H^+ + H^- \rightarrow H_2 \quad \textbf{(2-27)}$$

Lukes suggested that the hydride ion was originally bonded to phosphorous in the hypophosphite. The codeposition of elemental phosphorous is provided in Equation (2-24). The hydride mechanism provides sufficient explanation for the reduction of Ni and P.

A third theory is the so-called electrochemical mechanism that was introduced by Brenner and Riddell.[53] In the anodic oxidation of hypophosphite with water, electrons are formed (Equation (2-28)):

$$H_2PO_2^- + H_2O \rightarrow H_2PO_3^- + 2\ H^+ + 2\ e^-,\ E^0 = 0.50\ V \quad \textbf{(2-28)}$$

The corresponding cathodic reaction uses the electrons formed in Equation (2-28) to produce elemental $Ni^0$ (Equation (2-29)) and elemental $P^0$ (Equation (2-31)). The hydrogen gas evolution occurs during the Ni deposition and is a result of a secondary reaction presented in Equation (2-30):

$$Ni^{2+} + 2\ e^- \rightarrow Ni^0,\ E^0 = -\ 0.25\ V \quad \textbf{(2-29)}$$

$$2\ H^+ + 2\ e^- \rightarrow H_2,\ E^0 = 0.00\ V \quad \textbf{(2-30)}$$

$$H_2PO_2^- + 2\ H^+ + e^- \rightarrow P^0 + 2\ H_2O,\ E^0 = 0.50\ V \quad \textbf{(2-31)}$$

The fourth mechanism comprises of the coordination of hydroxyl ions with hexaaqua nickel ion and the formation of a hydrolyzed Ni species.[64] The chemical reduction of Ni at a catalytic surface involves the ionization of water at a catalytic surface (Equation (2-32)) and the coordination of hydroxyl ions at solvated Ni ion to result in the hydrolyzed Ni species (Equation (2-33)):

$$H_2O \rightarrow H^+ + OH^- \quad \textbf{(2-32)}$$

$$Ni(H_2O)_6^{2+} + OH^- \rightarrow NiOH^+_{ads} + 6\ H_2O \quad \textbf{(2-33)}$$

Followed by the reaction of the hydrolyzed Ni species with hypophosphite (Equation (2-34)):

$$NiOH^+_{ads} + H_2PO_2^- \rightarrow Ni^0 + H_2PO_3^- + H^+ \quad \textbf{(2-34)}$$

The hydrogen atom generated in Equation (2-34) results from P-H bonds and can react with the hydrogen atom from Equation (2-32) to hydrogen gas (Equation (2-35)):

$$H + H \rightarrow H_2 \quad \textbf{(2-35)}$$

Salvago and Cavallotti suggested that the direct interaction between the catalytic Ni surface and hypophosphite leads to the codeposition of phosphorous (Equation (2-36)):

$$Ni_{cat} + H_2PO_2^- \rightarrow P^0 + NiOH^+_{ads} + OH^- \quad \textbf{(2-36)}$$

Moreover, the hydrolyzed species ($NiOH^+_{ads}$) can further react with water (Equation (2-37)):

$$NiOH^+_{ads} + H_2O \rightarrow [Ni(OH)_2]_{aq} + H^+ \quad \textbf{(2-37)}$$

Equation (2-34) and (2-37) describe two competitive reactions of the adsorbed $NiOH^+$ species, and Salvago and Cavallotti proposed that the adsorbed $NiOH^+$ species play an important role in the Ni layer morphology (Equations (2-38) and (2-39):

$$Ni(OH)^+_{ads} \xrightarrow{H_2PO_2^-} Ni^0 + H_2PO_3^- + H^+ \quad \textbf{(2-38)}$$

$$Ni(OH)^+_{ads} \xrightarrow{H_2O} [Ni(OH)_2]_{aq} + H^+ \quad \textbf{(2-39)}$$

Gutzeit postulated that as long as a constant supply of $NiOH^+$ species on the catalytic surface the reaction (2-34) is provided, the deposition of phosphorous (2-36) is suppressed.[61] The metallic $Ni_{cat}$ surface must be available for direct interaction with $H_2PO_2^-$ to deposit phosphors. However, if reaction (2-37) takes place, the metallic $Ni_{cat}$ surface that was previously covered by $NiOH^+$ species is free to interact with $H_2PO_2^-$. The periodic reaction between (2-34) and (2-37) leads to a lamellar morphology. For completness, the reaction between hypophosphite and water is provided in Equation (2-40):

$$H_2PO_2^- + H_2O \rightarrow H_2PO_3^- + H_2 \quad \textbf{(2-40)}$$

The overall reaction is given in Equation (2-41), according to literature:[64b]

$$Ni^{2+} + 4\ H_2PO_2^- + H_2O \rightarrow Ni^0 + 3\ H_2PO_3^- + H^+ + P^0 + 3/2\ H_2 \quad \textbf{(2-41)}$$

In the aforementioned example for the preparation of Ni/P layers nickel sulfate ($NiSO_4$) is used as Ni source and sodium hypophosphite is used as reducing agent as well as a P source. In the plating industry, components such as complexing agents, “stabilizers”, and “accelerators” are commonly employed inside electroless

Ni electrolytes (see Table 2-2). Other important process parameters of nickel plating baths are the pH value and the temperature which influence the deposition rate and properties of the deposit.[65]

**TABLE 2-2 OVERVIEW OF COMPONENTS OF THE ELECTROLESS NICKEL/PHOSPHOROUS ELECTROLYTE[66]**

| Component | Example |
|---|---|
| Nickel source | Nickel sulfate, -chloride, -carbonate |
| Reducing agent | Sodium hypophosphite |
| Complexing agent | Carboxylic acids, (malonic acid, succinic acid, malic acid, lactic acid), amine- and ammonium salts |
| Accelerators | Carboxylate species, fluoride, thiourea |
| Stabilizer | Lead, cadmium, antimony, bismuth, tin, or organic compounds |

### Growth mechanism

Similar to Cu deposition, the Ni layer growth is characterized by the seeded growth mechanism, where activator seeds serve as nucleation sites for the growth of Ni clusters, followed by the coalescence of three-dimensional crystallites, which is then linked to a network and continuous deposits are formed.[59]

### 2.3.3. Electroless gold Deposition

The electroless Au deposition is not only applied in the electronics industry,[10b, 67] but also finds application in the preparation of Au nanoshells on dielectric materials such as silica particles.[68] For the latter application, an Au electrolyte with only an Au source, a complexing agent, and a reducing agent are sufficient. Reducing agents such as sodium borohydride,[68a] formaldehyde,[68b, 68c] carbon monoxide,[68b] or hydroxylamine[68d] can be utilized. Whereby, only the reduction of the Au ions in the presence of hydroxylamine is described below. The Au complex has to be prepared in two steps.

First, potassium carbonate ($K_2CO_3$) hydrolyzes in water (Equation (2-43)):

$$CO_3^{2-} + 2\ H_2O \rightleftharpoons HCO_3^- + OH^- + H_2O \rightleftharpoons H_2CO_3 + 2\ OH^- \quad \textbf{(2-42)}$$

Then, the aqueous gold(III)-chloride reacts to tetrahydroxoaurate(III) in the basic solution[68d] (Equation (2-43)):

$$HAuCl_4 + 4\ OH^- \rightarrow [Au(OH)_4]^- + 4\ Cl^- + H^+ \quad \textbf{(2-43)}$$

Usually, the mixture is allowed to react for several days to ensure to full conversion to tetrahydroxoaurate(III).[68d] In the presence of the reducing agent hydroxylamine, elementary $Au^0$ is obtained. Equation (2-44) describes the overall stoichiometric reaction of the partial cathodic reduction of $Au^{3+}$ (Equation (2-44)) and the anodic oxidation of hydroxylamine (Equation (2-45)):

$$4\ [Au(OH)_4]^- + 6\ NH_2OH \rightarrow 4\ Au^0 + 3\ N_2O + 3\ H_2O + 16\ OH^- + 12\ H^+ \quad \textbf{(2-44)}$$

**Cathodic reaction**

$$[Au(OH)_4]^- + 3\ e^- \rightarrow Au^0 + 4\ OH^- \quad \textbf{(2-45)}$$

**Anodic reaction**

$$2\ NH_2OH \rightarrow N_2O + 4\ e^- + H_2O + 4\ H^+ \quad \textbf{(2-46)}$$

### 2.3.4. Electroless silver Deposition

The electroless Ag deposition finds application in the metallization of dielectric materials such as silica particles with Ag nanoshells,[69] apart from the plating industry.[10b] For laboratory use, the electrolytes can be freshly prepared and utilized within one day. These solutions contain an Ag source (silver nitrate), a complexing agent (ammonia), and a reducing agent (formaldehyde).[70] For industrial application, the Ag baths contain stabilizing agents to shield Ag nuclei formation to prevent the precipitation of the entire electrolyte.

In the presence of excess amount of ammonia, the $[Ag(NH_3)_2]^+$ complex is present. The deposition reaction comprises the cathodic reduction of $Ag^+$ to elementary $Ag^0$ and the anodic oxidation of formaldehyde to formate. As mentioned for the electroless Cu deposition (Chapter 2.3.1), the anodic reaction involves the formation of an electroactive species and the charge transfer from the electroactive species to the catalytic surface. The following equations (2-47) and (2-48) illustrate a possible stoichiometric reaction between formaldehyde and silver in a basic solution, adapted by Chou et al.[71]

$$2\ Ag^+ + HCHO + 3\ OH^- \rightarrow 2\ Ag^0 + HCOO^- + 2\ H_2O \quad \textbf{(2-47)}$$

$$2\ Ag^+ + HCHO + OH^- \rightarrow 2\ Ag^0 + HCOOH + ½\ H_2 \quad \textbf{(2-48)}$$

### 2.3.5. Surface activation

In the plating industry, investigations about surface activation demonstrated that only Pd clusters with >10 Pd atoms/nm$^2$ catalyze the electroless metal deposition.[72] This concentration of Pd atoms/nm$^2$ can be reached when polynuclear $Pd^{2+}$ complexes are used as activating species on the substrate surface before the reduction step.[73] These types of oligomers are prepared by hydrolyzing aqueous $Pd^{2+}$ solutions. As suitable candidates Pd(II) halogen complexes are used, because they hydrolyze above pH ~2 to hydroxo-and/or chloro-bridged $Pd^{2+}$ precipitates.[74] A proposed mechanism by Dressick et al.[73] is displayed below. The $Cl^-$ ligands are reversibly exchanged by water molecules to generate mixed chloro-aqua species (Equation (2-49) and (2-50)).

$$PdCl_4^{2-} + H_2O \leftrightarrow PdCl_3(H_2O)^- + Cl^- \quad \textbf{(2-49)}$$

$$PdCl_3(H_2O)^- + H_2O \leftrightarrow PdCl_2(H_2O)_2 + Cl^- \quad \textbf{(2-50)}$$

When the pH of the solution is increased to pH ~4, the coordinated water molecules deprotonate and form mixed chloro-aqua-hydroxo species (Equation (2-51)).

$$PdCl_2(H_2O)_2 \leftrightarrow PdCl_2(H_2O)(OH)^- + H^+ \quad \textbf{(2-51)}$$

With increasing pH, the complex condenses into μ-hydroxy and/or μ-chloro-bridged oligomers. The chain length of the oligomer depends on the pH value, chloride levels, and temperature.[75] The formation of a μ-hydroxy and μ-chloro-bridged Pd trimer is illustrated in Equation (2-52):

$3PdCl_2(H_2O)(OH)^- \rightarrow$ **(2-52)**

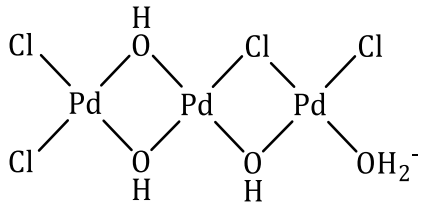


$+ 2Cl^- + 2H_2O$

Subsequently, these Pd oligomer complexes can be reduced using dimethylamine borane (DMAB). The reaction is described in Equation (2-53), and the proposed mechanism involves the cleavage of the B—N bond and the formation of a Pd⋯$BH_3$ radical complex.[76] Since borine is a strong Lewis acid, it hydrolyzes immediately generating boric acid and $H_2$.

$$H_2PdCl_4 + (CH_3)_2NHBH_3 + 4H_2O \quad \textbf{(2-53)}$$
$$\rightarrow Pd^0 + H_3BO_4 + 4HCl + 3H_2 + (CH_3)_2NH$$

Once the $Pd^{2+}$ is reduced, the colloidal Pd seeds self-assemble to stable islands because of the changes in binding energies between $Pd^{2+}$-ligand and $Pd^0$-ligand.[77]

## 2.4. FUNDAMENTALS OF APPLIED TECHNIQUES

### 2.4.1. DYNAMIC LIGHT SCATTERING/ZETA POTENTIAL

**Dynamic light scattering (DLS)**

Dynamic light scattering or photon correlation spectroscopy is a popular method to determine colloidal particle sizes ranging from 1—1000 nm in diameter. When a laser passes through a dispersion of colloidal particles in Brownian motion, the frequency of the outgoing light is shifted. This scattering can be directly correlated to the hydrodynamic radius (Stokes-Radius), which corresponds to the hydrodynamic diameter of a sphere, and the state of aggregation considering the polydispersity.[78]

In a light scattering experimental setup, a beam of laser light (electromagnetic wave) impinges on a sample, after passing through a polarizer, and accelerates the electrons in the molecule causing light scattering. The scattered light traverses an analyzer and is collected by a detector positioned at a defined angle according to the transmitted beam. The intersection of the incident beam and the scattered light is defined as the scattering volume. Since the colloids are in constant motion the distance between the scatters is fluctuating over time. The data analysis of this fluctuation intensity over time results in structural and dynamical information about the molecule, which can be used to deduce the diffusion coefficient. The Stoke-Einstein relation (Equation (2-54)) describes the correlation between the diffusion coefficient and the hydrodynamic diameter:

$$D = \frac{k_B \cdot T}{3\pi\eta d} \qquad \textbf{(2-54)}$$

D: diffusion coefficient, $k_B$: Boltzmann constant, T: temperature in Kelvin, η: viscosity of the solvent, d: hydrodynamic diameter.

The equation demonstrates that the diffusion coefficient decreases for particles with wider diameters and increases for smaller diameters since smaller particles move more rapidly. The fluctuation property of the scattered light can be analyzed using the second-order autocorrelation function (Equation (2-55)):

$$g^2(\tau) = \frac{< I(t) \cdot I(t+\tau) >}{< I(t) >^2} \quad \textbf{(2-55)}$$

$g^2(\tau)$ :normed autocorrelation function, $\tau$ : delay time, I(t) : intensity at time t, $<I(t)>^2$ : normalized factor.

In the case of monodisperse samples, the autocorrelation function can be described as an exponential decay function (2-56):

$$g^1(\tau) = \beta \exp(-\Gamma\tau) \quad \textbf{(2-56)}$$

$\beta$: intercept of the correlation function, $\Gamma$: decay constant.

The Siegert equation (2-57) relates the second-order autocorrelation functions with the first order autocorrelation functions:

$$g^2(\tau) = 1 + \beta[g^1(\tau)]^2 \quad \textbf{(2-57)}$$

Consequently, it can be calculated that the decay constant $\Gamma$ is proportional to the diffusion constant D and the scattering vector (2-58):

$$\Gamma = Dq^2; \quad q = \frac{4\pi n}{\lambda_0} = \sin\frac{\theta}{2} \quad \textbf{(2-58)}$$

$\lambda_0$: incident laser wavelength, n: refractive index, $\theta$: angle of the detector with respect to the cell.

In the case of polydisperse particles, the fluctuation of the scattered light depends on the diffusion coefficient D of particles with different sizes and hence, the autocorrelation function is a sum of exponential decay corresponding to the species. The cumulant methods analyze the polynomial fit of the logarithm of the autocorrelation function as the cumulant mean of Z-average (Equation (2-59)), which represent the diameter size referred to during this present study:

$$\ln(G1) = a + b\Gamma + c\Gamma^2 + d\Gamma^3 + e\Gamma^4 + \ldots.. \quad \textbf{(2-59)}$$

The polydispersion index (PDI) is a tool to evaluate the size distribution (see Table 2-3) and can be calculated by dividing the constant c by $2\Gamma^2$:

**TABLE 2-3 THE RATING SCALE OF THE DIFFERENT VALUES FOR THE PDI**

| PDI | | | | |
|---|---|---|---|---|
| < 0.05 | < 0.15 | < 0.25 | < 0.5 | > 0.5 |
| narrow distribution | narrow distribution | broad distribution | very broad distribution | Very, very broad distribution |

### Zeta potential (ζ-potential)

Zeta potential is an electro kinetic phenomena of the potential drop inside the mobile part of the double layer in a colloidal dispersion.[79] Figure 2-8 illustrates the different layers, charge distributions, and potentials of a negatively charged particle dispersed in a fluid. Negatively charged particles are electrostatically counterbalanced by firmly attached ions of the opposite charge, creating the Stern layer. The second layer, called diffuse layer, contains counter ions that are attracted to the surface via Coulomb force. These counter ions move loosely around due to electric attraction and the thermal motion of solvent molecules. The zeta potential is the electric potential inside the diffuse layer, located at the slipping plane and can be described as the potential difference between Stern layer and the bulk fluid interface.[80]

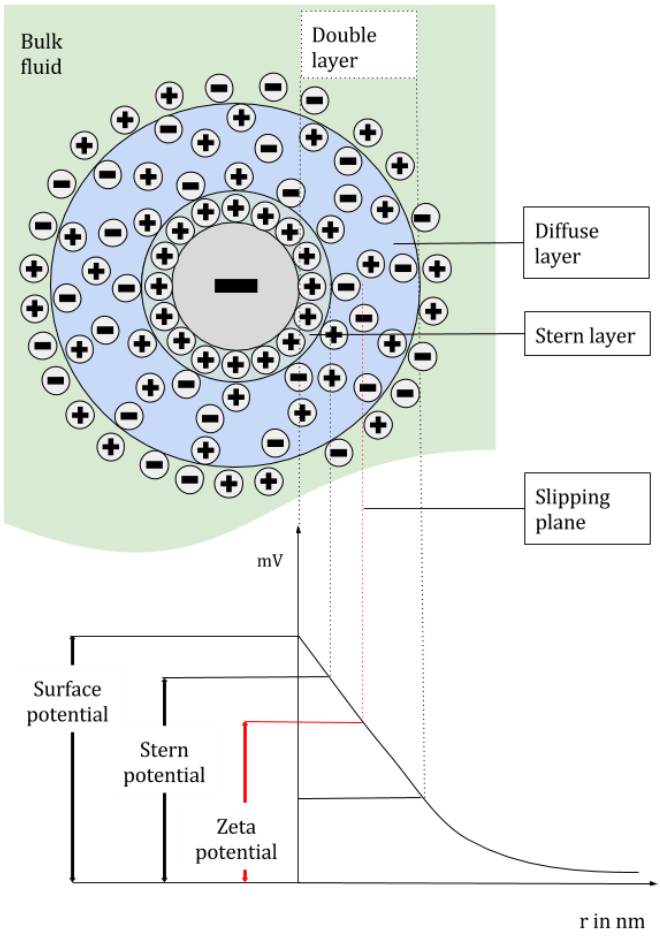


**FIGURE 2-8 SCHEMATIC ILLUSTRATION OF ALL THE POTENTIALS, LAYERS AND CHARGES OF A NEGATIVELY CHARGED PARTICLE INSIDE A FLUID, ADAPTED FROM LITERATURE.[80]**

Zeta potential values serve as an indicator for colloidal dispersion stability. For high absolute values, the electrostatic repulsion between particles is dominating, which results into stabile dispersion. In contrary, when the absolute potential values are low, the attractive forces increase, aggregates are formed, and the dispersion flocculates.[80] This method to measure the zeta potential is a result of experimental determined electrophoretic mobility and theoretical calculations. When an external electric field is applied, the charged particles will migrate toward the electrode of opposite charge. The velocity ν of the particle mobility U is proportional to the value of the zeta-potential and can be calculated by measuring the frequency change (Doppler effect) of the incident and scattered beam **(2-60)**:

$$\nu = \frac{Un}{\lambda}\sin\theta \qquad \textbf{(2-60)}$$

λ: wavelength of the primary beam, n: refractive index of the medium, θ: scattering angle.

In the next step, the magnitude of the zeta potential in can be calculated using the Henry equation **(2-61)**:

$$U = \frac{2\varepsilon\zeta \cdot}{3\eta} f(\mathrm{Ka}) \qquad \textbf{(2-61)}$$

ε: dielectric constant, *f*(Ka): Henry's function, η: viscosity.

Henry's function has a value of either 1.5 or 1. For aqueous solution the Smoluchowski approximation is used with the value 1.5.

### 2.4.2. UV-Vis spectroscopy

A method to characterize the organic moieties of silica particles is the derivatization of amino groups into a UV-Vis spectroscopic detectable species. Amino groups can be modified into the corresponding species by reacting with an organic compound with conjugated π systems. Amino groups react with salicylaldehyde into the yellow salicylimine derivative[81] or with ninhydrin into Ruhrmann's purple.[82] As it is illustrated in Figure 2-9, the colored product is attached to the silica surface when salicylaldehyde is used. However, when ninhydrin is introduced, the Ruhrmann's purple is detached from the particle surface.[82]

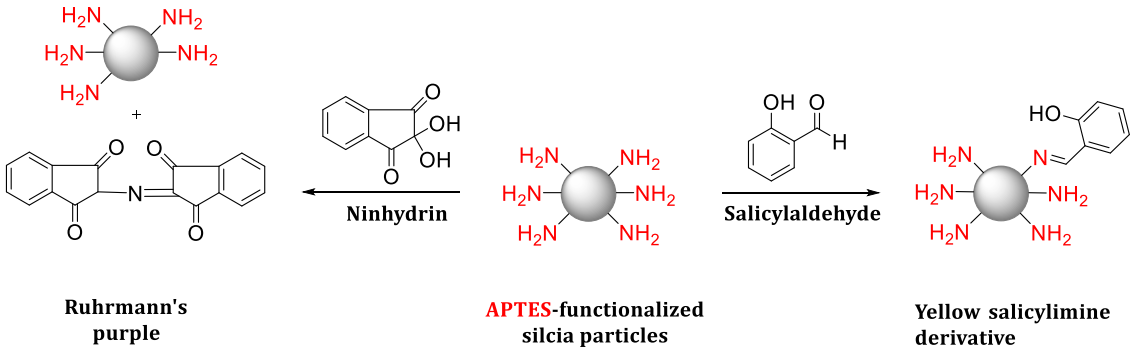


**Figure 2-9 Schematic illustration of the reactions between APTES-functionalized silica particles and salicylaldehyde yielding the yellow salicylimine derivative,[81] and with ninhydrin yielding Ruhrmann's purple.[83]**

In ultraviolet-visible (UV-Vis) spectroscopy, molecules are excited by the absorption of electromagnetic radiation of ultraviolet-visible light, causing an electronic transition from a lower energy to a higher energy molecular orbital (MO).[84] During the ground state, both electrons are paired in the lower energy bonding orbital, which is called highest occupied molecular orbital (HOMO). The antibonding orbital is called the lowest unoccupied molecular orbital (LUMO). When the light of a wavelength with energy equal to the HOMO-LUMO energy gap is applied, the energy is absorbed to lift the electron from HOMO to LUMO. Depending on the molecular structure, the HOMO-LUMO energy gap decreases for conjugated π-systems and hence the wavelength absorbed is longer. The Bouguer-Lambert-Beer law describes the basis of light absorption measurements in the UV-Vis and IR-region:

$$\varepsilon_{\tilde{\nu}} = \frac{A_{\tilde{\nu}}}{c \cdot d} \tag{2-62}$$

$\varepsilon_{\tilde{\nu}}$: the molar decadic extinction coefficient [L/(mol·cm)], $A_{\tilde{\nu}}$: the absorbance, c: the concentration [mol/L], d: the path length of the light which passes through the material [cm].

The extinction coefficient $\varepsilon_{\tilde{\nu}}$ is a quantity characteristic of the molecule and depends on the wavelength λ. The functional correlation between $\varepsilon_{\tilde{\nu}}$ and λ is the absorption spectrum of a substrate. Since the Bouguer-Lambert-Beer law is limited only for a diluted solution, dilutions have to be prepared where the absorbance value is < 1.

The colored product is attached to the silica surface and therefore results in a yellow dispersion with strong scattering when ethanol is used as a solvent. An alternative could be to utilize a solvent that has an equal refractive index to colloidal silica to obtain a clear solution. An appropriate solvent candidate would be chloroform with a refractive index of n=1.445 at 20°C (silica n = 1.45[18b]).

The advantage of this method is that the colored product is not attached to the particles surface but inside the solution.[82]

### 2.4.3. C/H/N/S ELEMENTAL ANALYSIS

C/H/N/S elemental analysis (EA) is a method to determine the mass fraction of carbon, hydrogen, nitrogen, and heteroatoms (halogen/sulfur/phosphor) in compounds using combustion analysis. During this study, this method was used to calculate the number of amino groups attached on the silica particles.

The exactly weight amount of the sample is catalytically burned (temperature >1000°C) in the presence of excess oxygen, causing the generation of oxidation products such as carbon dioxide ($CO_2$), water ($H_2O$), nitrogen oxide ($N_2$, $NO_x$), and sulfur oxide ($SO_x$). These combustion gases are carried by helium through a hot copper contact and reduced into the gases $CO_2$, $H_2O$, $SO_2$, and $N_2$. Subsequently, these gas mixtures are one after the other separated into their components by the purge & trap chromatography, and collected in the thermal conductivity detector (TCD).[85] The detected peak areas of the different gases and the exact amount of the sample are used to calculate the mass fraction of the elements in %.

### 2.4.4. ELECTRON MICROSCOPY AND ENERGY DISPERSIVE X-RAY SPECTROSCOPY

#### Scanning electron microscopy

Scanning electron microscopy (SEM) permits the visualization of particles down to nanometer scale and therefore, was the method of choice during this present study.[86] The method leads to precise information about the topography of the specimen and in combination with energy dispersive X-ray spectroscopy (EDX), the chemical composition is determined.[87] A scanning electron microscope consists of an electron column (see Figure 2-10) and a control console. The column has a vertical setup and is evacuated. As an electron source, the electron gun can be fitted with a tungsten filament cathode, that generates the beam and accelerates it with energy in a range between 0.1—30 keV. The thermionic emitter is relatively inexpensive and needs no special vacuum, but on the other hand, this emitter has low brightness, limited lifetime, and a large energy spread.[87] An alternative electron source for the beam is the cold cathode field emitter in the field emission scanning electron microscopy (FESEM). The cathode is usually a wire shaped into a

sharp tip (radius < 100 nm) and supported by tungsten hairpin. When a negative potential is applied to the cathode, the electric field is concentrated by the tip. After reaching a magnitude of about 10 V/nm, the potential barrier is lowered in height and width, which enables the electrons to "tunnel" through it and to leave the cathode.

The beam is focused by condenser lenses down to a spot size of < 10 nm in diameter, while traveling down the column. After passing through the electromagnetic deflection coils in the final objective lens, the beam is deflected point by point along the x and y-axes, causing a rectangular raster on the specimen.

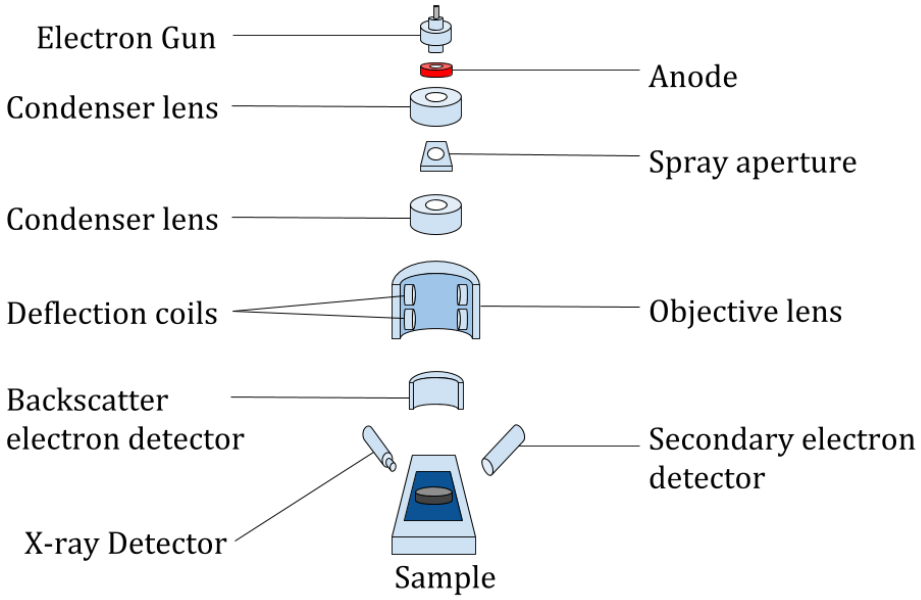


**FIGURE 2-10 SCHEMATIC SETUP OF THE ELECTRON COLUMN IN A SCANNING ELECTRON MICROSCOPE (SEM), ADAPTED FROM ELSEWHERE.[88]**

After the electron beam impinges the specimen surface, the energy is absorbed as a teardrop-shaped volume (interaction volume, see Figure 2-11), which penetrates approximately 0.1—5 µm into the surface, and a wide range of signals are generated (see Figure 2-11). The beam electron-specimen interaction results in a deflection of beam electrons along a new trajectory as elastic scattering (BSE) without energy loss, emission of secondary electrons (SE) of inelastic scattering and the emission of electromagnetic radiation. The resulting signals can be collected and measured using appropriate detectors.

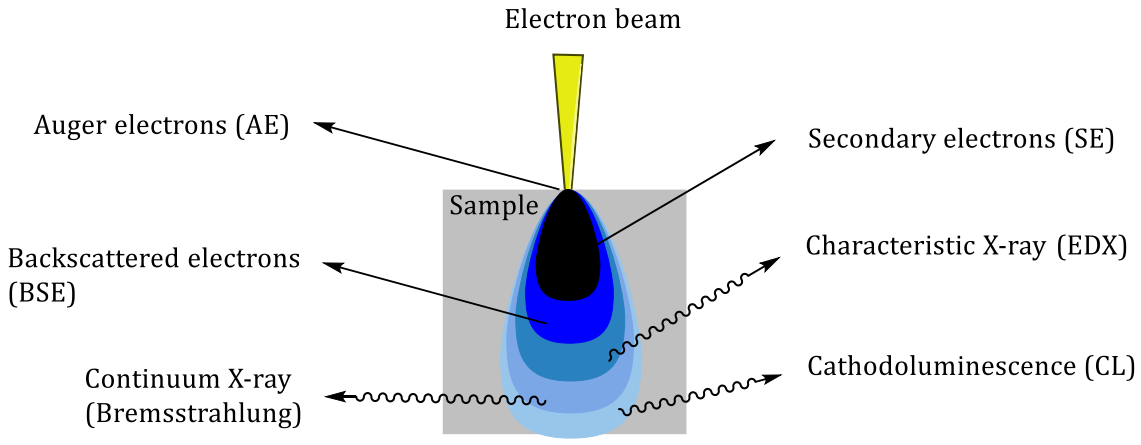


**FIGURE 2-11 SCHEMATIC OVERVIEW OF SIGNALS GENERATED AFTER THE ELECTRON BEAM IMPINGES THE SPECIMEN, ADAPTED FROM ELSEWHERE.[88]**

After the primary electron beam interacts with the specimen, a significant amount of the energy moves into electrons that will be reflected or back-scattered out of the specimen by elastic scattering. Elements with high atomic numbers, like metals, backscatter more strongly than light elements. The heavy elements appear brighter in the image, and therefore the BSE-detector is a suitable mode to detect areas of contrasting chemical compositions. In contrary, the secondary electron (SE) detector collects low energy electrons that are loosely located in the outer shell of the specimen atoms. After the inelastic scattering between the electron beam and the specimen, electrons are ejected from the atom. The generated characteristic X-rays are detected using energy dispersive X-ray (EDX) spectroscopy, which will be explained in the following subsection. Besides these three types of scattering, other signals are produced: Cathodoluminescence (CL), Auger electrons (AE), and continuum X-ray (Bremsstrahlung). CL describes the emission of photons after electrons return to their ground state. CL-detectors collect all the emitted wavelengths and create an emission spectrum or display CL distribution in visible colors. Auger electrons are generated after a core state electron left the atom, the vacant hole is filled by an electron from a higher shell, and the created transition energy is used to eject the Auger electron out of the atom. The Bremsstrahlung describes the phenomena when an electron is decelerated after interaction with another charged particle. This loss of kinetic energy is converted into a photon.

**Dual-beam system FIB/SEM**

The dual beam system incorporates a focused ion beam (FIB), as well as a scanning electron microscope (SEM) in a single system. The advantage is that an ion beam can be utilized for material removal and the SEM for imaging and analysis. Especially the investigation and monitoring of cross-section preparation is a wide-spread application area. FIB instruments have a similar setup like the SEM, but instead of an electron beam, an ion beam source is used. The setup consists of a vacuum system and chamber, a liquid metal ion source (LMIS), an ion column, a sample stage, and the detector gas delivery systems. A tungsten needle is attached to a reservoir containing the metal source material like gallium (Ga). When an electric field is applied to the end of the tip, Ga forms a point source (2-5 nm in diameter) in a shape of a cone. After force balance is achieved, the extraction voltage pulls down the Ga from the tip and ionizes it by field evaporation of the metal at the end of the cone. A continuous flow of Ga to the cone continuously replaces the evaporated ions. After the extraction of the $Ga^+$ ions, they are accelerated through a potential down the ion column.[89] Depending on the beam current intensity, the beam can be utilized for site-specific sputtering or milling when high currents are applied, or for imaging when a low current is used. When the primary $Ga^+$ ion beam impinges the specimen, the specimen surface is either left with secondary ions or neutral atoms. This sputtering process results in the ejection of the secondary electrons. The ion beam scans the surface, and signals from the sputtered surface and secondary electron are used for imaging. When high primary current is applied, once the beam strikes the surface, atoms and small clusters are removed by precise milling. The column setup resembles the SEM column. In a typical dual-beam system, the electron column has a vertical position, and the ion column is tilted. Both beams have a coincident point (see Figure 2-12), where both intersect with the sample, this enables the ion milling and the electron imaging of the same section.

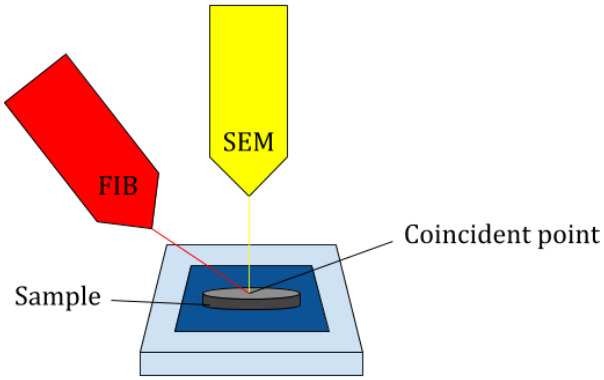


**FIGURE 2-12 SCHEMATIC ILLUSTRATION OF A TYPICAL DUAL-BEAM SYSTEM CONFIGURATION WITH A VERTICAL SEM COLUMN, A TILTED FIB COLUMN, AND THE COINCIDENT POINT ON THE SAMPLE.**

### Energy dispersive X-ray spectroscopy

Energy dispersive X-ray (EDX) spectroscopy is an analytical technique that provides information about the elemental composition of a specimen. As mentioned in the SEM section, characteristic X-rays are generated when the electron beam hits the specimen surface (see Figure 2-11). These X-ray photons have energies specific for the elements in the sample. A schematic illustration of the principle of EDX is displayed in Figure 2-13. The electron beam can interact with the inner shell electrons of a specimen atom and as a result, an electron will be ejected from the shell. The atom is left in an exited and unstable state, and subsequently, an L-shell electron fills the inner-shell vacancy. This energy difference between electron shells is well-defined for each element. The released energy from the electron transition can either eject an outer shell electron with a specific kinetic energy as Auger electrons or emit as a photon of electromagnetic radiation with characteristic energy. The emitted energy can be measured by an energy dispersive spectrometer.

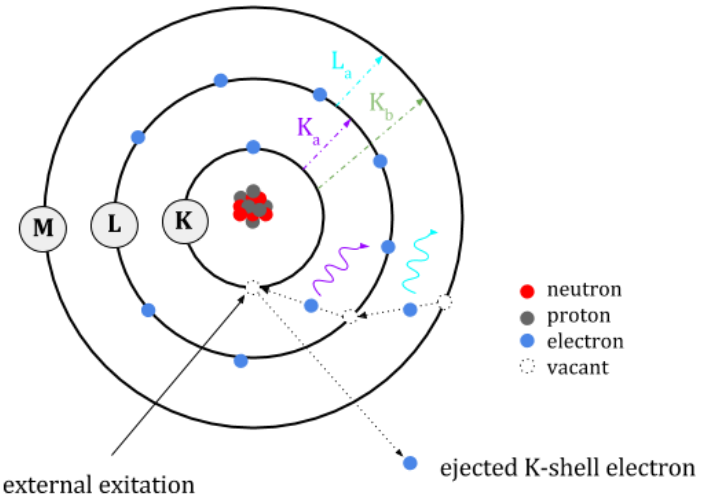


**FIGURE 2-13 SCHEMATIC OVERVIEW OF THE PRINCIPLE OF ENERGY DISPERSIVE X-RAY (EDX) SPECTROSCOPY, ADAPTED FROM LITERATURE.[90]**

### 2.4.5. INDUCTIVELY COUPLED PLASMA OPTICAL EMISSION SPECTROSCOPY (ICP-OES)

Inductively coupled plasma optical emission spectroscopy (ICP-OES) is utilized for the determination of trace metals. It is based on the excitation of atoms and ions by inductively coupled plasma and the emission of electromagnetic radiation at a specific wavelength for each element.[91],[92] The ICP-OES tool consists of two units: The ICP-torch with flowing argon gas and the optical spectrometer. The upper section of the torch is surrounded by a copper coil, which is connected to a radio frequency (RF) generator. After RF power is applied, the current oscillates inside the coil causing the same high-frequency oscillation of the electric and magnetic field inside the torch. The flowing argon is ignited with a Tesla coil creating "seed" electrons and ions inside the gas. They are accelerated by the magnetic field causing a collision with other argon atoms, generating more ionization until an intense, high-temperature plasma is formed. The liquid sample is transformed into an aerosol by the usage of a nebulizer and carried by argon to the center of the plasma, where it vaporizes or decomposes into gaseous state molecules and subsequently breaks down into atoms. In the final step, the excitation and ionization of the atom occurs, followed by the emission of radiation. The emission

data is collected, the light intensity is measured with a photomultiplier resulting into the determination of the elements qualitatively and quantitatively.

### 2.4.6. ULTRASOUND

Ultrasound (US) describes the sound generated in the frequency range between 20 kHz to GHz. Depending on the application field, different ultrasonic devices and energies can be utilized. Especially in the preparation of nano-sized colloidal dispersions and emulsions, sonication is a popular tool (20—40 kHz). Two procedures for ultrasonic applications are known: the direct and the indirect. In the direct sonication, an ultrasonic probe, with the transducer at the tip, is immersed in the dispersion. In the indirect sonication, the dispersion vessel is introduced into an ultrasonic bath with liquid, where the ultrasonic waves travel from the transducer, through the liquid, and through the vessel wall.[93]

The ultrasound waves that are transmitted through a solvent cause an alternating compression (high-pressure) and decompression (low-pressure/rarefaction) of the solvent molecular structure, which results in an oscillating change between the average distances of the solvent molecules. During the low-pressure cycle, the distance between the molecules can fall below the minimum distance required to keep the liquid undamaged, and the bonding between the liquid molecules is disrupted, and cavitation bubbles are formed.[94] During the process of compressing and decompressing, two different types of cavitation can occur: the stable or the transient. Stable cavitation bubbles are generated at low intensity and oscillate to an equilibrium size for many acoustic cycles. Whereas, transient cavitation bubbles double their initial size during several acoustic cycles and then collapse violently. The temperature within a collapsing bubble is supposed to be several thousand degrees, and the pressure exceeds 1000 atmosphere. The cavitation bubble can be regarded as a micro-reactor.[95] The collapsing bubble is considered to be one of the main sources of chemical and mechanical effects of ultrasound.

# 3. EXPERIMENTAL SECTION

## General procedure

The reaction vessels utilized in all reaction steps were cleaned before usage with aqua regia to dissolve all metal residues, followed by the treatment with a basic cleaner called Mucasol® to remove insoluble deposits from the glass surface.

## Chemical list

All the chemicals provided in Table 3-1 were used as received without further purification.

**TABLE 3-1 CHEMICAL LIST**

| **Chemical** | **Supplier** | **Quality** |
|---|---|---|
| Acetic acid | VWR | 99.8 % |
| Acetone | VWR | 99.8 % |
| 3-Aminopropyltriethoxysilane (APTES) | ABCR specialty chemicals | 98 % |
| 2,2'-Bipyridine | ALFA AESAR | 98 % |
| Ammonium hydroxide | AppliChem | 25 % |
| Cetyltrimethylammonium bromide (CTAB) | Sigma-Aldrich | ≥98 % |
| Chloroauric acid trihydrate ($HAuCl_4 \cdot 3H_2O$) | Sigma-Aldrich | ≥99.9 % |
| Chloroform | ALFA AESAR | 99.5 % |
| Copper sulfate pentahydrate ($CuSO_4 \cdot 5\ H2O$) | Alfa Aesar | 98 % |
| Dichloromethane | VWR International | 99.9 % |
| Didodecyldimethylammonium bromide (DDAB) | Sigma-Aldrich | 98 % |
| Dimethylamine borane (DMAB) | ALFA AESAR | 97 % |

| | | |
|---|---|---|
| Ethanol absolute | Merck | 99.9 % |
| Formalin solution | Avantor Performance Materials | 10 % |
| Hydrochloric acid (HCl, 37%) | VWR | 37% |
| Hydroxylamine hydrochloride | ALFA AESAR | 99 % |
| Lactic acid | ALFA AESAR | 90 % |
| Malic acid | VWR | 99 % |
| N,N'-Diethyl thiourea | Sigma-Aldrich | 98 % |
| Nickel sulfate hexahydrate<br>(NiSO4 · 6 H2O) | ALFA AESAR | 98.0% |
| Ninhydrin | ALFA AESAR | 99 % |
| Nitric acid | VWR Chemicals | 69 % |
| Palladium chloride solution($PdCl_4^{2-}$) | Heraeus | 10 % |
| Paraffin wax | VWR Chemicals | Melting point<br>55 - 58 °C |
| Polyvinylpyrrolidone (PVP) | VWR | 99 % |
| Potassium carbonate ($K_2CO_3$) | Honeywell Chemicals | ≥98 % |
| Potassium chloride (KCl) | VWR Chemicals | ≥99.5 % |
| Potassium sodium tatrate | MilliporeSigma | 99 % |
| Salicylaldehyde | ALFA AESAR | 99 % |
| Silver nitrate ($AgNO_3$) | ALFA AESAR | 99.9% |
| Sodium chloride (NaCl) | VWR International | 99 % |
| Sodium dodecylbenzenesulfonate (SDBS) | TCI America | 95 % |
| Sodium hydroxide (NaOH) | VWR Chemicals | ≥97 % |
| Sodium hypophosphite monohydrate | ALFA AESAR | 99 % |
| Succinic acid | VWR | 99 % |
| Sulphoric acid | VWR International | 95-98% |
| Tetraethoxysilane (TEOS) | Alfa Aesar | 99.9 % |

| | | |
|---|---|---|
| Triethylamine (TEA) | ALFA AESAR | 99 % |
| Ultrapure water | Millipore plant | Filter size: 0.22 µm, resistance: > 18.2 MΩ, 25 °C |
| **Atotech Deutschland GmbH Products** | | |
| Nichem 6200 | Nichem 6200 A (CH) | |
| | Nichem 6200 B (CH) | |
| Printoganth PV | Printoganth V Basis | |
| | Printoganth V Copper | |
| | Printoganth PV Starter | |
| | Printoganth PV Stabilizer | |
| | Reduction solution Cu (CH) | |
| | pH Correction solution (CH) | |
| PallaBond PD | EXPT 2 PallaBond PD Make-up | |
| | EXPT 3 PallaBond PD Reducer | |

## 3.1. EQUIPMENT AND PROCEDURES

### Field emission scanning electron microscopy (FESEM) and energy dispersive X-ray spectroscopy (EDX)

The surface topography and the material contrast were observed with FESEM using the Carl Zeiss Microscopy Supra® 55 VP. All images were collected in ultrahigh vacuum with an acceleration potential between 1 kV and 10 kV. Secondary electron and backscatter electron mode detectors were used to record the images with the processing program OLYMPUS® Stream. The chemical composition was investigated by the integrated energy dispersive x-ray (EDX) analysis (X-Max 80) with the EDX spectroscopy software AZtecEnergy®. To overcome the scattering of non-conductive materials, a thin layer of iridium (few nanometers) was deposited on the surface by sputtering to increase the conductivity. From the resulting images, the average diameters of the colloids, as well as the shell coverage degrees of the silica particles were determined using the image processing program ImageJ®. For the calculation of the shell coverage, the diameter of the ring opening was measured and converted into the surface area of the spherical cap (see Figure 3-1). The surface area of the cap was divided by the surface area of the silica colloid, which results in the shell coverage degree. A detailed calculation is provided in Appendix II Calculations.

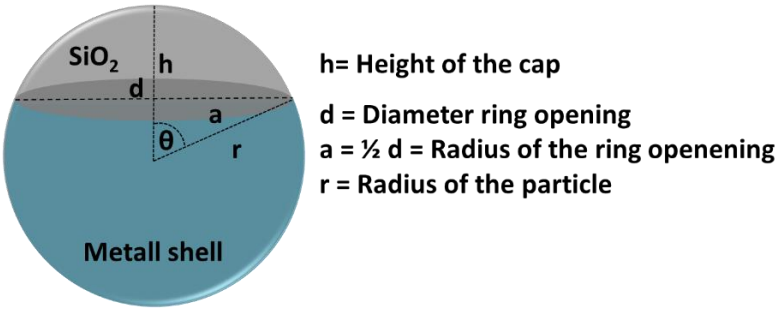


FIGURE 3-1 SCHEMATIC ILLUSTRATION OF THE SPECIAL CAP AND CORRESPONDING PARAMETERS USED TO CALCULATE THE METAL SHELL COVERAGE DEGREE.

**Dual-beam system focused ion beam (FIB) and scanning electron microscopy (SEM)**

The metal shell thickness and morphology were investigated using the cross-section images obtained from an integrated FIB and SEM (HELIO Nanolab660). After selecting an area in the SEM, a platinum protection layer is deposited in situ onto this area. Afterwards, an ion gun scans a focused beam of Ga ions over the area. When a Ga ion with high kinetic energy hits the sample, atoms or small clusters are removed from the surface. Within some minutes the FIB can cut a small trench of few microns wide and deep. From the resulting images, the metal shell thicknesses were determined using the integrated processing program (XT-userinterface Co.1.4).

**Inductively coupled plasma optical emission spectroscopy (ICP-OES)**

The amount of adsorbed metal ions on the silica surface was determined by using ICP-OES from the Varian 720-ES ICP Optical Emission Spectrometer. A precise amount of the coated silica particles was dissolved in different concentrated acid. Au-coated particles were dissolved in aqua regia (37 % HCl : 65 % HNO3 = 3 : 1) and for Pd-, Ni, and Cu-coated particles, 37 % HCl was used.

**Dynamic light scattering (DLS) and zeta potential**

The size distribution of particles and the zeta potential is obtained by dynamic light scattering (DLS) using the Malvern® Zetasizer nano zs with the software DTS v6.2. Silica nanoparticles were dispersed either in water or absolute ethanol and measured without further filtration in a disposable polystyrene cuvette. The average particle size (Z-average) is expressed as the intensity weighted harmonic mean size, derived from five measurements (each 10 runs) with a duration time of 120 s for each run. The temperature was 20 °C, and the samples were allowed to stand in the compartment for the sample temperature to be equilibrated before the measurement started. The zeta potential was measured with a potential measuring cell that was immersed into the cuvette with the dispersion inside. Concentrations were prepared in the range of 0.1 % to 0.0001 % for particles with diameters ranging from 1 nm to 1 µm, respectively. For the zeta potential measurements at

different pH values, the pH of the mixture was adjusted to pH 3 with 0.1 M HCl. After the measurement, the pH was adjusted to the desired value with 0.01—0.1 M NaOH.

### C/H/N/S Elemental analysis (EA)

C/H/N/S elemental analysis was used for the determination of the mass of carbon, hydrogen, and nitrogen in the samples. The measurements of the elements were performed with an elemental analyzer "Vario EL Cube" (Elementar®). Sulfanilic acid from Merck was used as the standard to check the performance of the device. The measurement uncertainty (MU) was calculated for each element on the basis of the sulfanilic acid measurements. Bare silica particles and amine-functionalized particles were dried and weighed in a tin foil (2-5 mg). Each sample was measured at least twice. The combustion was performed with oxygen at 1150 °C in a combustion tube for 90 s. For the evaluation of the data the EAS software from Elementar® was used. Using the measured diameter of the particles (SEM images), the density of silica ($\rho$ = 2.0 g/cm$^3$),[18b] and the detected amount of nitrogen from EA, the density of amino groups on the surface of silica in numbers of $NH_2$/nm$^2$ was determined.

### Ultraviolet-Visible Spectroscopy (UV-Vis)

UV-visible spectra were obtained from Analytikjena SPECORD® 210 with the software WinASPECT®. A calibration plot was obtained by measuring the absorbance area (475—750 nm) of 3-aminopropyltriethoxysilane (APTES) with 1 mL of 0.5 M ninhydrin solution and absolute ethanol in a 100 mL volumetric flask, after reacting for 2 hours at 70 °C, as a function of the APTES concentration (see Figure 3-2).

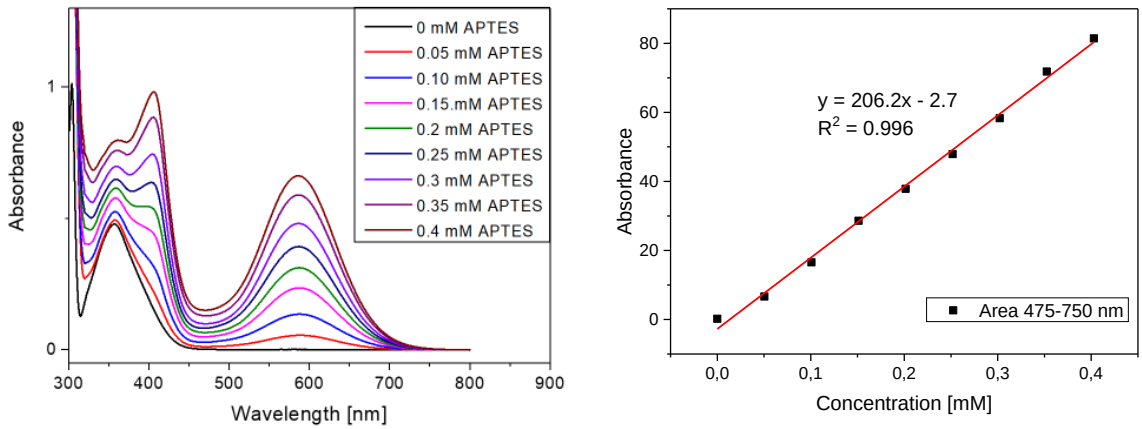


**FIGURE 3-2 GRAPHIC ILLUSTRATIONS OF THE ABSORBANCE SPECTRA OF APTES WITH 1 ML OF 0.5 M NINHYDRIN SOLUTION AFTER REACTING FOR 2 HOURS AT 70 °C (LEFT), AND THE CALIBRATION CURVE OF THE ABSORBED AREA (475—750 NM) AS A FUNCTION OF THE CONCENTRATION (RIGHT).**

A second calibration plot was generated by measuring the intensity (380—500 nm) of APTES with 1 mL of 0.5 M salicylaldehyde solution and chloroform in a 100 mL volumetric flask, after reacting for 30 min at rt, as a function of the APTES concentration (see Figure 3-3).

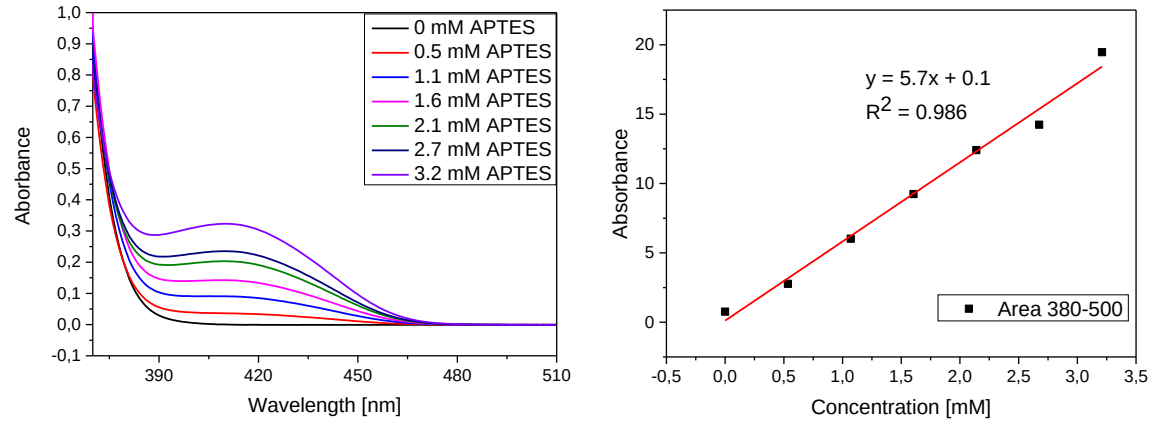


**FIGURE 3-3 GRAPHIC ILLUSTRATIONS OF THE ABSORBANCE SPECTRA OF APTES WITH 1 ML OF 0.5 M SALICYLALDEHYDE SOLUTION AFTER REACTING FOR 30 MIN AT RT IN CHLOROFORM (LEFT), AND THE CALIBRATION CURVE OF THE ABSORBED AREA (380—500 NM) AS A FUNCTION OF THE CONCENTRATION (RIGHT).**

Using the calibration curves, the amount of amine in mM can be calculated from the absorbance spectra of the corresponding samples. Subsequently, the value can be converted into the number of $NH_2$ groups/$nm^2$ on the silica surface with the

measured diameter of the particles (SEM images), the density of silica (ρ = 2.0 g/cm$^3$), [18b] the amount of the solvent, and the mass of the particles.

**Radius of gyration:** The radius of gyration was calculated for the surfactant molecules didodecyl-dimethylammonium bromide (DDAB) and cetyltrimethylammonium bromide (CTAB) with the program called Lammps® of an HPC cluster computer. The force-field (pcff) computation model was used to simulate molecular dynamics in a water molecule chamber with 30x30x30 Å$^3$ length.

**Centrifuge**: The samples were purified using a centrifuge device from Hettich Zentrifugen Universal 320® (1494 swing out rotor 4-times).

**Turrax stirrer**: For the preparation of molten-wax and water emulsion the stirrer IKA T25 digital ultra turrax was used.

**Calculation**: A silica density of 2 g/cm$^3$ was chosen for the calculation of all relevant values.[18b]

## 3.2. Synthesis of silica particles

### 3.2.1. Bare silica nanoparticles

#### Synthesis of silica particles with 60 nm and 500—600 nm diameter

Silica nanoparticles with 60 nm and 500—600 nm diameter and with low polydispersity were prepared according to the Stöber protocol.[15] To a mixture comprising of ammonium hydroxide ($NH_4OH$), absolute ethanol (EtOH), and water; tetraethoxysilane (TEOS) was added in one portion. After 2 h of stirring at room temperature (rt), the mixture was neutralized by adding diluted hydrochloric acid (HCl), followed by a purification step using ethanol (see Table 3-2). The solvent was evaporated, and the nanoparticles were stored as a white powder.

**Table 3-2 Overview of all the chemicals, equipment and purification steps used when preparing silica particles with 60 nm and 500—600 nm diameter**

| Particle size | | 60 nm | 500—600 nm |
|---|---|---|---|
| Chemicals | **EtOH** | 91.4 mL | 154 mL |
| | **$NH_4OH$ 25 %** | 3.7 mL, 0.5 M | 15 mL, 1.01 M |
| | **$H_2O$** | 1.1 mL, 0.61 mM | 17.6 mL, 4.89 mM |
| | **TEOS** | 3.8 mL, 0.17 M | 13.2 mL, 0.3 M |
| Equipment | **Magnetic stirrer** | 300 rpm | 300 rpm |
| Purification | **Centrifugation** | 3 x 2370 g | 3 x 210 g |

#### Synthesis of silica particles with 700 nm and > 1000 nm diameter

A modified method was used to obtain larger monodisperse silica colloids (700 nm and > 1000 nm in diameter).[96] Since the TEOS supply rate is crucial for the final silica particle size, the synthesis was carried out in a *Mettler Toledo* EasyMax workstation. Two solutions were prepared, with solution I containing potassium chloride (KCl), EtOH, $H_2O$, and $NH_4OH$; and solution II comprising a mixture of EtOH and TEOS. Solution II was added to the reaction vessel containing solution I with a defined supply rate. After the dosing had been finished, the mixture stirred for another 2 h, before being neutralized by adding diluted HCl, followed by a

purification step using EtOH (see Table 3-3). The solvent was evaporated, and the particles were stored as a white powder.

**TABLE 3-3 OVERVIEW OF ALL THE CHEMICALS, EQUIPMENT, AND PURIFICATION STEPS USED WHEN PREPARING SILICA PARTICLES WITH 700 NM AND > 1000 NM DIAMETER**

| Particle size | | 700 nm | > 1000 nm |
|---|---|---|---|
| **Solution I** | **EtOH** | 38 mL | 60 mL |
| | **$NH_4OH$ 25 %** | 3 mL, 0.37 M | 6 mL, 0.72 M |
| | **KCl** | 1.5 mg, 0.18 mM | 15 mg, 1.79 mM |
| | **$H_2O$** | 6 mL, 3.04 M | 7 mL, 3.46 M |
| **Solution II** | **TEOS** | 5.68 mL, 0.23 M | 4.23 mL, 0.17 M |
| | **EtOH** | 57 mL | 35 mL |
| **Temperature** | | rt | rt → 35°C |
| **Dosing rate** | | 0.2 mL/min | 0.12 mL/min |
| **Equipment** | **Mettler Toledo EasyMax** | 300 rpm | 300 rpm |
| **Purification** | **Centrifugation** | 3 x 95 g | 3 x 95 g |

### 3.2.2. DISPERSION TESTS

Dry silica particles (0.1 g) with different diameter sizes were redispersed in 100 mL ethanol using the ultrasonic devices that are provided in Table 3-4. After 5, 10, 15, 20, and 60 min dispersion time, the hydrodynamic diameters, as well as the polydispersity index (PDI) were measured by DLS.

**TABLE 3-4 OVERVIEW OF ALL ULTRASONIC DEVICES APPLIED FOR SILICA PARTICLES REDISPERSION**

| | Device name | Type | Model | Frequency [kHz] | Peak Power [W] |
|---|---|---|---|---|---|
| **Bath 1** | **Bandelin Sonorex** | Bath | RK514H | 35 | 860 |
| **Bath 2** | **Elmasonic** | Bath | TI-H-5 M3 | 35—130 | 400 |
| **Ultrasonic probe** | **Sonopuls** | Sonotrode | HD 2070 | 20 | 70 |

### 3.2.3. Synthesis of APTES-functionalized silica particles

Dry, bare silica particles were dispersed in EtOH (10 g/L) using the ultrasound bath (35 kHz) for 10 min. The dispersion was under argon atmosphere for 10 min before 3-aminopropyltriethoxysilane (APTES) was added. An amine group to hydroxyl group ratio of 5 was chosen assuming a sphere with a surface density of 4 OH groups/nm$^2$, according to literature.[97] 20 experiments were conducted where the silica colloids reacted solely with APTES as well as with two different equivalents of the basic catalyst triethylamine (TEA) or two different equivalents of the acidic catalyst glacial acetic acid. Table 3-5 lists exemplary amounts of APTES and different amounts of the catalyst for the surface grafting reaction of 0.3 g of silica particles with 550±49 nm diameter (estimated total number of OH groups = 1.1±0.5·10$^{-5}$ mol). For simplification reason, the standard deviation of the colloid size was not considered. Each of the mixtures reacted under the reaction conditions mentioned in Table 3-6. After the reaction was terminated, the dispersion was centrifuged (210 g) and the particles were washed 3 x 50 mL with EtOH. The APTES-functionalized colloids were either immediately used or stored as dispersion in EtOH (10 g/L) under argon atmosphere.

**Table 3-5 Amounts of chemicals used for the surface grafting of silica particles**

| | | APTES | TEA | | Acetic acid | |
|---|---|---|---|---|---|---|
| **Amount** | [mL] | 0.013 | 0.008 | 0.780 | 0.004 | 0.320 |
| | [mol] | $5.56 \cdot 10^{-5}$ | $5.77 \cdot 10^{-5}$ | $5.77 \cdot 10^{-3}$ | $6.99 \cdot 10^{-5}$ | $5.59 \cdot 10^{-3}$ |
| | [mM] | 1.11 | 1.15 | 112.5 | 1.40 | 111.8 |

**Table 3-6 Overview of different reaction conditions applied for the surface grafting of silica particles with APTES and catalysts**

| | 1 | 2 | 3 | 4 |
|---|---|---|---|---|
| **Reaction condition** | 1h, 0°C | 1h, RT°C | 1h, 75°C | 12h, 75°C |

Small particles (~60 nm in diameter) were dispersed in EtOH (1 g/L) and refluxed with APTES and TEA for 1 h under argon atmosphere. The corresponding amounts are provided in Table 3-7. The dispersion was purified with 3 x 50 mL EtOH and centrifuged (2370 g).

**TABLE 3-7 AMOUNTS OF CHEMICALS USED FOR THE SURFACE GRAFTING OF SILICA PARTICLES WITH ~60 NM IN DIAMETER**

| Sample | | | Silica particle dispersion | | APTES | | TEA | |
|---|---|---|---|---|---|---|---|---|
| Name | Diameter [nm] | [mg] | EtOH [mL] | $A_{Silica}$ $10^{19}$ [$nm^2$/L] | [µL] | [mM] | [µL] | [mM] |
| NP-1-I | 61±8 | 86 | 86 | 4.9±3.2 | 33 | 1.64 | 19 | 1.59 |
| NP-1-II | 62±9 | 100 | 100 | 4.8±3.5 | 38 | 1.62 | 22 | 1.59 |

#### 3.2.3.1. SAMPLE PREPARATION FOR QUANTIFICATION OF AMINO GROUPS USING UV-VIS SPECTROSCOPY

The APTES-functionalized silica particles with ~550 nm diameter (0.3 g) were dispersed in a 50 mL solution containing EtOH and 1 mL of 0.5 M ninhydrin solution using the ultrasonic bath (35 kHz) for 10 min. The mixtures reacted for 2 h at 70 °C, while stirring at 300 rpm. Subsequently, the mixture was allowed slowly to cool down to rt, the dispersion was centrifuged (210 g), and the corresponding supernatant was analyzed in a UV-Vis spectrometer. Bare, non-functionalized silica particles were measured as a reference.

### 3.2.4. Preparation of bare silica particles and Wax Colloidosomes

Dry, bare silica particles were dispersed in water using the ultrasonic bath (35 kHz) for 10 min. Different amounts of surfactant solution (didodecyldimethylammonium bromide (DDAB) (0.26 g/L) or cetyltrimethylammonium bromide (CTAB) (0.26 g/L) in water) were added to the mixture and agitated 5 min further. The reaction vessel was moved to a water bath at 75 °C. Paraffin wax was added to the dispersion in one portion, and the mixture was allowed to react for 30 min while stirring at 300 rpm. Subsequently, the reaction mixture was stirred with a turrax stirrer at 8000 rpm for 2 min, allowed to cool down to rt, and filtered through a funnel with a disposable, folded filter paper from VWR® with a particle retention of 25 µm, to remove unattached or weakly attached particles. The colloidosomes were carefully collected for further modification. Table 3-8 lists all reaction parameters for fabricating colloidosomes with 0.3 g silica particles (609±32 nm in diameter, estimated $9.8\pm2.6 \cdot 10^{-6}$ mol OH groups) and DDAB. Table 3-9 comprises of all parameters for the synthesis of colloidosomes using CTAB as the surfactant.

In the case of the 33 g/L, 20 g/L, and 10 g/L dispersion, the final solvent amount and the added wax were 9 mL solvent and 1.5 g wax; 15 mL solvent and 1.5 g wax; and 30 mL solvent and 3 g wax, respectively.

**TABLE 3-8 OVERVIEW OF ALL REACTION PARAMETERS FOR THE FABRICATION OF PARTICLE-WAX COLLOIDOSOMES USING DDAB AS SURFACTANT[47]**

| Sample | | DDAB solution (0.26 g/L) [mL] | DDAB Conc. [mM] | Ratio $Mol_{DDAB}/Mol_{OH}$ [%] |
|---|---|---|---|---|
| 33 g/L dispersion | 1 | 0 | 0 | 0 |
| | 2 | 0.5 | 0.031 | 2.9±0.8 |
| | 3 | 1 | 0.062 | 5.7±1.5 |
| | 4 | 1.5 | 0.094 | 8.6±2.3 |
| 20 g/L dispersion | 5 | 0 | 0 | 0 |
| | 6 | 0.1 | 0.0037 | 0.6±0.2 |
| | 7 | 0.2 | 0.0075 | 1.1±0.3 |
| | 8 | 0.25 | 0.0094 | 1.4±0.4 |
| | 9 | 0.5 | 0.019 | 2.9±0.8 |
| | 10 | 0.7 | 0.026 | 4.0±1.1 |
| | 11 | 1.0 | 0.037 | 5.7±1.5 |
| | 12 | 1.2 | 0.045 | 6.9±1.8 |
| | 13 | 1.5 | 0.056 | 8.6±2.3 |
| | 14 | 2 | 0.075 | 11.5±3 |
| 10 g/L dispersion | 15 | 0 | 0 | 0 |
| | 16 | 0.5 | 0.0094 | 2.9±0.8 |
| | 17 | 1 | 0.019 | 5.7±1.5 |
| | 18 | 1.5 | 0.028 | 8.6±2.3 |
| | 19 | 2 | 0.037 | 11.5±3 |

**TABLE 3-9 OVERVIEW OF ALL REACTION PARAMETERS FOR THE FABRICATION OF PARTICLE-WAX COLLOIDOSOMES USING CTAB AS SURFACTANT[48]**

| Sample | | CTAB solution (0.26 g/L) [mL] | CTAB conc. [mM] | Ratio $Mol_{CTAB}/Mol_{OH}$ [%] |
|---|---|---|---|---|
| 20 g/L dispersion | 1 | 0 | 0 | 0 |
| | 2 | 0.5 | 0.024 | 3,6±1.3 |
| | 3 | 1 | 0.048 | 7.3±2.5 |
| | 4 | 1.5 | 0.071 | 10.9±3.8 |
| | 5 | 2 | 0.095 | 14.5±5.0 |
| | 6 | 2.5 | 0.12 | 18.2±6.3 |
| 10 g/L dispersion | 7 | 0 | 0 | 0 |
| | 8 | 0.1 | 0.0024 | 0.7±0.3 |
| | 9 | 0.25 | 0.0059 | 1.8±0.6 |
| | 10 | 0.5 | 0.012 | 3.6±1.3 |
| | 11 | 0.75 | 0.018 | 5.5±1.9 |
| | 12 | 0.9 | 0.021 | 6.5±2.3 |
| | 13 | 1 | 0.024 | 7.3±2.5 |
| | 14 | 1.25 | 0.030 | 9.1±3.1 |
| | 15 | 1.4 | 0.033 | 10.2±3.5 |
| | 16 | 1.5 | 0.036 | 10.9±3.8 |
| | 17 | 2.0 | 0.048 | 14.5±5.0 |
| | 18 | 2.5 | 0.059 | 18.2±6.3 |

#### 3.2.4.1. REGIO-SELECTIVE GRAFTING OF SILICA PARTICLES

Silica particles embedded in wax were partially functionalized using a modified method based on the work of Jiang et al.[47] After collecting the particle-wax colloidosomes from the filter paper, the whole batch was added to 50 mL methanol at 0 °C and stirred at 300 rpm. APTES (13 µL, 1.11 mM) and TEA (8 µL, 1.15 mM) were introduced, and the mixture was stirred for 1 h at 0 °C under argon atmosphere. The colloidosomes were filtered with a disposable crepe fluted circles, folded filter paper with a particle retention of 25 µm, and washed 3 x with 50 mL methanol to remove the excess silane, TEA, and unattached particles. The wax was dissolved in chloroform for 30 min at rt. The particles were washed 3 x with 50 mL chloroform (centrifuge 210 g) to ensure the removal of the paraffin wax. The APTES-functionalized silica Janus colloids were either immediately processed or stored in ethanolic dispersion under argon.

## 3.3. Activation of the APTES-modified silica spheres

### 3.3.1. Preparation of the palladium (Pd) stock solution

The $PdCl_4^{2-}$ solution (10 % Pd content) used during this present work comprised of 120 g/L Pd (1.13 M Pd). To a solution of 40 mL water, 2 mL of the $PdCl_4^{2-}$ solution (48.6 mM Pd, 194.4 mM $Cl^-$) was added. After stirring for 5 min at 300 rpm, 4.4 mL of an aqueous solution of NaOH (1 N, 95 M) was added dropwise. The Pd stock solution (48.6 mM Pd) was used within several weeks. No sign of precipitation was observed during the usage time.

### 3.3.2. Palladium seeds

APTES-functionalized silica particles were dispersed in water (10 g/L) using ultrasonic agitation for 10 min. For entirely, as well as partially amine grafted particles a sphere was assumed with a surface density of 4 amino groups/$nm^2$.[97] Although Janus particles are only partially coated with amino groups, for simplifying the overall calculation, it was assumed that the entire sphere was coated with amino groups. Bare and non-functionalized silica particles were introduced as a blank sample. A variety of reaction conditions, as well as different Pd to amino groups ratios were chosen (see Table 3-10). After the addition of the Pd stock solution (48.6 mM Pd), the mixture was agitated in the ultrasonic bath for another 10 min. This was done to prepare well-dispersed colloids and to provide evenly distributed Pd ions on the silica surface, which enables a more complete encapsulation with metal shells during the subsequent plating step.[98] After the reaction was terminated, the dispersion was centrifuged (210 g), and the colloids were washed 3 x by redispersing and centrifuging the colloids to remove the weakly adsorbed Pd ions. *The surface coverage was determined using ICP-OES.*

**TABLE 3-10 OVERVIEW OF DIFFERENT AMOUNTS AND PARAMETERS FOR THE ACTIVATION OF SILICA PARTICLES WITH PD IONS**

| Sample | | Silica particle dispersion | | |
|---|---|---|---|---|
| Name | Diameter [nm] | Particles [mg] | Water [mL] | $A_{Silica}$ $10^{19}$ [$nm^2$/L] |
| Full-Pd-Act-1 | 547±36 | 0.30 | 30 | 5.5±1.8 |
| Full-Pd-Act-2 | 547±36 | 0.30 | 30 | 5.5±1.8 |
| Full-Pd-Act-3 | 547±36 | 0.30 | 30 | 5.5±1.8 |
| Full-Pd-Act-4 | 547±36 | 0.30 | 30 | 5.5±1.8 |
| Full-Pd-Act-5 | 568±36 | 0.29 | 29 | 5.3±1.7 |
| Full-Pd-Act-6 | 568±36 | 0.28 | 28 | 5.3±1.7 |
| Blank | 547±36 | 0.10 | 10 | 5.5±1.8 |
| JNP-Pd-Act-1 | 609±32 | 0.22 | 22 | 4.9±1.3 |
| JNP-Pd-Act-2 | 609±32 | 0.09 | 9 | 4.9±1.3 |
| JNP-Pd-Act-3 | 609±32 | 0.19 | 19 | 4.9±1.3 |
| JNP-Pd-Act-4 | 598±39 | 0.21 | 21 | 5.0±1.6 |

| Name | Pd solution (48.6 mM Pd) | | | Reaction conditions | Final volume [mL] |
|---|---|---|---|---|---|
| | [mL] | Pd content [mM] | Ratio $Mol_{Pd}/Mol_{NH2}$ [%] | | |
| Full-Pd-Act-1 | 4.8 | 6.70 | 21.3±7.0 | 1 h, rt | 34.80 |
| Full-Pd-Act-2 | 4.8 | 6.70 | 21.3±7.0 | 1 h, 70 °C | 34.80 |
| Full-Pd-Act-3 | 4.8 | 6.70 | 21.3±7.0 | 12 h, 70 °C | 34.80 |
| Full-Pd-Act-4 | 4.8 | 6.70 | 21.3±7.0 | 1 h, 70 °C, 24 h stirring at rt | 34.80 |
| Full-Pd-Act-5 | 5.02 | 7.17 | 24.0±7.6 | 1 h, 70 °C | 34.02 |
| Full-Pd-Act-6 | 4.9 | 7.24 | 24.2±7.7 | 1 h, 70 °C | 32.90 |
| Blank | 1.68 | 7.00 | 22.5±7.4 | 1 h, 70 °C | 11.68 |
| JNP-Pd-Act-1 | 0.65 | 1.39 | 4.4±1.1 | 1 h, 70 °C | 22.65 |
| JNP-Pd-Act-2 | 0.28 | 1.47 | 4.6±1.2 | 1 h, 70 °C | 9.28 |
| JNP-Pd-Act-3 | 0.56 | 1.38 | 4.4±1.1 | 1 h, 70 °C | 19.56 |
| JNP-Pd-Act-4 | 1.88 | 3.99 | 13.0±4.2 | 1 h, 70 °C | 22.88 |

An aqueous dimethylamine borane (DMAB) solution (0.01 M) was freshly prepared to reduce the Pd ions to metallic seeds. The particles were redispersed in water (5 g/L) by strong manual shaking, and an excess amount of DMAB solution was added dropwise to the dispersion stirring at 300 rpm (see Table 3-11). The color of the mixture changed immediately from orange/brown to dark gray/black. After reacting for 30 min, the dispersion was washed 3 x with water (centrifuge 210 g) to remove the excess DMAB, the generated byproducts, and possible Pd nuclei inside the solution. The silica colloids with Pd seeds were allowed to rest in aqueous solution for 3 d before the solvent was removed. The particles were stored as dry and gray/black powder before being further processed as described in the following subsection (Chapter 3.4). *The surface coverage was determined using SEM.*

**TABLE 3-11 OVERVIEW OF DIFFERENT AMOUNTS OF DMAB SOLUTION (0.01 M) FOR THE REDUCTION OF THE PD IONS**

| Sample | | | DMAB solution (0.01 M) | | Final volume [mL] |
|---|---|---|---|---|---|
| Name | Particle [mg] | Water [mL] | [mL] | [mM] | |
| Full-Pd-Act-1 | 0.30 | 60 | 46 | 4.34 | 106 |
| Full-Pd-Act-2 | 0.30 | 60 | 46 | 4.34 | 106 |
| Full-Pd-Act-3 | 0.30 | 60 | 46 | 4.34 | 106 |
| Full-Pd-Act-4 | 0.30 | 60 | 46 | 4.34 | 106 |
| Full-Pd-Act-5 | 0.29 | 58 | 48 | 5.38 | 106 |
| Full-Pd-Act-6 | 0.28 | 56 | 48 | 4.62 | 104 |
| Blank | 0.10 | 20 | 16 | 4.44 | 36 |
| JNP-Pd-Act-1 | 0.22 | 44 | 6 | 1.2 | 50 |
| JNP-Pd-Act-2 | 0.09 | 18 | 2 | 2 | 20 |
| JNP-Pd-Act-3 | 0.19 | 38 | 6 | 6 | 44 |
| JNP-Pd-Act-4 | 0.21 | 42 | 18 | 18 | 60 |

### 3.4. COATING THE ACTIVATED SILICA SPHERE WITH A METAL LAYER

**General procedure for metal shell coating**

A dispersion of silica particles coated with Pd seeds in water (0.5 g/L) was agitated for 10 min in an ultrasound bath (35 kHz) to ensure no aggregation of particles before the metallization step. Depending on the desired shell thickness different particles/metal ratios were used. Each metal electrolyte solution operated at different parameters (temperature, pH value), which are described in the following sections separately. The mixture was either stirred magnetically (300 rpm), or agitated in an ultrasonic bath (Elmasonic Bath TI-H-5 M3 at 35 kHz). It was assumed that the reaction ended when the dispersion bath color did not change further and when hydrogen evolution was completed. The dispersion was centrifuged (77 g) and the metal-coated silica particles were washed 3 x with water. *The shell growth and thickness was determined using SEM, FIB, and ICP-OES.*

#### 3.4.1. PREPARATION OF SILICA PARTICLES WITH NICKEL SHELL

Two freshly prepared electrolytes were used for the Ni shell deposition. The compositions of the first electrolyte (Ni-EL1) was adapted from Kanani et. al.,[99] and the second one was a commercially available solution called Nichem6200 from the company Atotech Deutschland GmbH. The dispersion with the precursor colloids reacted at ~60 °C with Ni-EL 1 or with Nichem6200 during ultrasonic agitation (bath 35 kHz) or stirring (300 rpm). The corresponding amounts for the different samples are provided in Table 3-12.

**Ni-EL 1**: A 100 mL aqueous solution was prepared comprising of nickel sulfate ($NiSO_4$ 6·$H_2O$, 2.63 g, 0.1 M, 5.87 g/L Ni), sodium hypophosphite ($NaH_2PO_2$·$H_2O$, 3.18 g, 0.3 M), malic acid (1.35 g, 0.1 M), lactic acid (0.9 g, 0.1 M) and succinic acid (0.65 g, 0.055 M). The freshly prepared solution had a pH ~4.8.

**Nichem 6200 (CH)**: The electrolyte was prepared according to the manufacture's instruction. The aqueous solution contained the ingredients Nichem 6200 A (CH) and Nichem 6200 B (CH). The solution was adjusted with ammonia to pH ~7.3. The Ni content after a fresh make-up was 5.0±0.5 g/L.

TABLE 3-12 OVERVIEW OF PARAMETERS FOR THE PREPARATION OF NI FULLSHELLS AND SEMISHELLS USING PD SEEDS COATED SILICA PRECURSOR PARTICLES AND NI-EL 1 AND NICHEM6200 ELECTROLYTE

| Sample | | Silica particle dispersion | | Ni-EL 1 | | Nichem6200 | |
|---|---|---|---|---|---|---|---|
| Name | Diameter [nm] | [g/L] | $A_{Silica}$ $10^{18}$ [$nm^2$/L] | [mL] | Ni [g/L] | [mL] | Ni [g/L] |
| Full-Ni-1 | 568±36 | 0.49 | 2.6±0.8 | 0.5 | 0.143 | – | – |
| Full-Ni-2 | 568±36 | 0.48 | 2.5±0.8 | 1 | 0.280 | – | – |
| Full-Ni-3 | 568±36 | 0.47 | 2.5±0.8 | 1.5 | 0.410 | – | – |
| Full-Ni-4 | 568±36 | 0.45 | 2.4±0.7 | 2 | 0.534 | – | – |
| Full-Ni-5 | 568±36 | 0.43 | 2.3±0.7 | 3 | 0.766 | – | – |
| JNP-Ni-1 | 609±32 | 0.45 | 2.2±0.6 | 2 | 0.534 | – | – |
| JNP-Ni-2 | 609±32 | 0.42 | 2.1±0.5 | 4 | 0.978 | – | – |
| JNP-Ni-3 | 609±32 | 0.40 | 2.0±0.5 | 5 | 1.174 | – | – |
| Full-Ni-6 | 547±36 | 0.40 | 2.2±0.7 | – | – | 5 | 1.0 |
| JNP-Ni-4 | 609±32 | 0.40 | 2.0±0.5 | – | – | 5 | 1.0 |

### 3.4.2. PREPARATION OF SILICA PARTICLES WITH COPPER SHELL

For the Cu shell deposition two freshly prepared electrolytes were used. The first electrolyte (Cu-EL 1) was a modified bath adapted from Schlesinger and Paunovic.[10b] The second one was a commercially available solution called Printoganth PV from Atotech Deutschland GmbH. The dispersion with the precursor colloids reacted in an ultrasonic bath (35 kHz) at ~35 °C with the Cu electrolyte or with Printoganth PV. Only the sample Full-Cu-5 reacted at a higher temperature (60 °C). The corresponding amounts for the different samples are provided in Table 3-13.

**Cu-EL 1**: A 100 mL aqueous solution was prepared comprising of copper sulfate ($CuSO_4$ $5{\cdot}H_2O$, 0.25 g, 0.01 M, 0.63 g/L Cu), formaldehyde (0.5 g, 0.17 M), potassium sodium tartrate (2.5 g, 0.12 M), 2,2'-bipyridine (0.5 mg, 0.03 mM), N,N'-diethyl thiourea (20 µg, 1.51 µM), and sodium hydroxide (1.0 g, 0.25 M).

**Printoganth PV**: The electrolyte was prepared according to the manufacture's instruction. The aqueous solution contained the ingredients Printoganth V Basis, Printoganth V Copper, Printoganth PV Starter, Printoganth PV Stabilizer, Reduction solution Cu (CH), pH Correction solution (CH). The Cu content after a fresh make-up was 2.2±0.2 g/L.

**TABLE 3-13 OVERVIEW OF PARAMETERS FOR THE PREPARATION OF CU FULLSHELLS AND SEMISHELLS USING PD SEEDS COATED SILICA PRECURSOR PARTICLES AND THE CU-EL 1 AND THE PRINTOGANTH PV CU ELECTROLYTE WITH**

| Sample | | Silica particle dispersion | | Cu-EL 1 | | Printoganth PV | |
|---|---|---|---|---|---|---|---|
| Name | Diameter [nm] | [g/L] | $A_{Silica}$ $10^{18}$ [$nm^2$/L] | [mL] | Cu [g/L] | [mL] | Cu [g/L] |
| Full-Cu-1 | 568±36 | 0.40 | 2.1±0.6 | 5 | 0.13 | – | – |
| Full-Cu-2 | 568±36 | 0.33 | 1.8±0.5 | 10 | 0.21 | – | – |
| Full-Cu-3 | 568±36 | 0.39 | 1.5±0.5 | 15 | 0.27 | – | – |
| Full-Cu-4 | 568±36 | 0.2 | 1.1±0.3 | 30 | 0.38 | – | – |
| Full-Cu-5 | 568±36 | 0.2 | 1.1±0.3 | 30* | 0.38 | – | – |
| JNP-Cu-1 | 609±32 | 0.36 | 1.8±0.4 | 8 | 0.18 | – | – |
| JNP-Cu-2 | 598±39 | 0.40 | 2.0±0.6 | – | – | 5 | 0.44 |
| JNP-Cu-3 | 598±39 | 0.40 | 2.0±0.6 | – | – | 5 | 0.44 |

### 3.4.3. Preparation of silica particles with gold shell

The gold (Au) fullshell fabrication was adapted from a procedure described by Graf et al.[68d] A 1 L electrolyte (Au-EL 1) was prepared by diluting an aliquot of a 25 mM chloroauric acid stock solution (17.4 mL, 0.44 mM, 86 mg/L Au) with 982.6 mL of water, followed by the addition of potassium carbonate (0.249 mg, 1.8 mM). The mixture was allowed to react at least 1 day in the dark. The color changed from light yellow to white because of the formation of Au hydroxide ($[Au(OH)_4]^-$).[100] The 1 L solution of the reducing agent hydroxylamine hydrochloride ($NH_2OH{\cdot}HCl$, 130 mg, 1.87 mM) in water was prepared separately. The dispersion with the precursor colloids was added to the Au hydroxide solution, and stirred for 10 min at 300 rpm at rt. Subsequently, the reducing agent was introduced dropwise to the mixture. The corresponding amounts for the different samples are summarized in Table 3-14.

**Table 3-14 Overview of parameters for the preparation of Au fullshells and semishells using Pd seeds coated silica precursor particles and the Au electrolyte (Au-EL 1)**

| Sample | | Silica particle dispersion | | Au hydroxide solution | | Reducing agent |
|---|---|---|---|---|---|---|
| Name | Diameter [nm] | [mg/L] | $A_{Silica}$ $10^{17}$ [$nm^2$/L] | [mL] | Au [mg/L] | $NH_2OH{\cdot}HCl$ solution (1.87 mM) [mL] |
| Full-Au-1 | 568±36 | 40.8 | 2.2±0.7 | 150 | 52.7 | 75 |
| Full-Au-2 | 568±36 | 37.3 | 2.0±0.6 | 165 | 53.0 | 83 |
| Full-Au-3 | 568±36 | 43.5 | 2.3±0.7 | 200 | 74.8 | 10 |
| Full-Au-4 | 568±36 | 25.3 | 1.3±0.4 | 250 | 54.4 | 125 |
| Full-Au-5 | 568±36 | 21.3 | 1.2±0.3 | 300 | 54.9 | 150 |
| Full-Au-6 | 568±36 | — | — | + 100 | +50.6 | 50 |
| JNP-Au-1 | 609±32 | 25.3 | 1.3±0.3 | 250 | 54.4 | 125 |

### 3.4.4. Preparation of silica particles with silver shel

A silver (Ag) bath described by Mayer et al.[101] was slightly modified and then utilized for the metal deposition. The Ag electrolyte comprised of four components: silver nitrate ($AgNO_3$) stock solution (5 mM, 0.54 g/L Ag); ammonia solution (3.7%, 2.14 M); aqueous formalin solution (12%, 11.4 M); and aqueous sodium dodecylbenzenesulfonate solution (SDBS, 5 mM). The sequencing had to be maintained to ensure Ag plating on the Pd-activated spheres. The Ag stock solution was introduced to the precursor dispersion followed by the addition of ammonia. The mixture was agitated in the ultrasonic bath throughout the process at rt. Subsequently, the reducing agent formalin and the stabilizing agent SDBS were added dropwise, simultaneously to the mixture. The corresponding amounts for the different samples are summarized in Table 3-15.

**Table 3-15 Overview of parameters for the preparation of Ag fullshells and semishells using Pd seeds coated silica precursor particles and the Ag electrolyte**

| Sample | | Silica particles dispersion | | $AgNO_3$ solution (5 mM) | |
|---|---|---|---|---|---|
| Name | Diameter [nm] | [mg/L] | $A_{Silica}$ $10^{18}$ [$nm^2$/L] | [mL] | Ag [mg/L] |
| Full-Ag-1 | 568±36 | 0.29 | 1.5±0.5 | 10 | 157.3 |
| Full-Ag-2 | 568±36 | 0.21 | 1.1±0.3 | 20 | 222.0 |
| Full-Ag-3 | 568±36 | 0.16 | 0.8±0.3 | 30 | 257.3 |
| Full-Ag-4 | 568±36 | 0.13 | 0.7±0.2 | 40 | 279.5 |
| Full-Ag-5 | 568±36 | 0.11 | 0.6±0.2 | 50 | 294.8 |
| JNP-Ag-1 | 563±35 | 0.16 | 1.3±0.3 | 15 | 195.3 |
| JNP-Ag-2 | 609±32 | 0.24 | 0.8±0.2 | 30 | 257.3 |

TABLE 3-16 OVERVIEW OF THE SECOND SET OF INGREDIENTS FOR THE PREPARATION OF AG FULLSHELLS AND SEMISHELLS USING PD SEEDS COATED SILICA PRECURSOR PARTICLES AND THE AG ELECTROLYTE

| Sample | Ammonia solution (3.7%) [mL] | Formalin solution (12%) [mL] | SDBS solution (5 mM) [mL] |
|---|---|---|---|
| Full-Ag-1 | 0.4 | 0.8 | 3.12 |
| Full-Ag-2 | 0.8 | 1.6 | 6.24 |
| Full-Ag-3 | 1.2 | 2.4 | 9.36 |
| Full-Ag-4 | 1.6 | 3.2 | 12.48 |
| Full-Ag-5 | 2 | 4 | 15.60 |
| JNP-Ag-1 | 0.6 | 1.2 | 4.68 |
| JNP-Ag-2 | 1.2 | 2.4 | 9.36 |

### 3.4.5. PREPARATION OF SILICA PARTICLES WITH PALLADIUM SHELL

For the palladium (Pd) shell deposition the commercial solution called PallaBond Pd from Atotech Deutschland GmbH was used and the solution was prepared according to the manufacture's instruction. The aqueous solution contained the ingredients EXPT 3 PallaBond PD Reducer and EXPT 2 PallaBond PD Make-up with pH ~5.5. The Pd content after a fresh make-up was 0.7±0.07 g/L. The dispersion with the precursor colloids reacted in the ultrasonic bath at ~45 °C with the Pd electrolyte. The corresponding amounts for the different samples are presented in Table 3-17.

TABLE 3-17 OVERVIEW OF PARAMETERS FOR THE PREPARATION OF PD FULLSHELLS AND SEMISHELLS USING PD SEEDS COATED SILICA PRECURSOR PARTICLES AND PALLABOND PD

| Sample | | Silica particle dispersion | | PallaBond Pd | |
|---|---|---|---|---|---|
| Name | Diameter [nm] | [g/L] | $A_{Silica}$ $10^{18}$ [nm²/L] | [mL] | Pd [g/L] |
| Full-Pd-1 | 451±40 | 0.17 | 1.1±0.5 | 40 | 0.47 |
| JNP-Pd-1 | 609±32 | 0.17 | 0.8±0.2 | 40 | 0.47 |

# 4. RESULTS AND DISCUSSION

Janus particles with metallic semishell coatings can be applied in versatile fields for example in electronic papers,[102] photonic materials,[103] sensors,[103] and also as adhesion promoters between dielectric substrates and metals in the electronics industry. Depending on the area of application, different metals are necessary such as Cu, Ni, Pd, Au, or Ag. Because of their plasmonic resonance, asymmetric or semishell nanostructures with noble metal (Au and Ag) coatings are widely applied, and many preparation methods have been developed over the years.[49, 52, 104] To our knowledge, other metal semishells are only fabricated by the evaporation of a metal film upon a monolayer of particles.[35, 50] The metal film evaporation is a simple technique, but since only small amounts of particles can be metalized in one step, this procedure is expensive and not suitable for applications on the industrial scale.

We present, for the first time, a facile route towards the synthesis of large amounts of silica Janus particles with tunable metal semishell coatings on defined areas. This approach consists of four steps starting from bare, non-functionalized silica particles (see Figure 4-1): 1) Fabrication of particle-wax colloidosomes; 2) grafting of the unprotected silica sphere with 3-aminoproyltriethoxysilane (APTES); 3) the activation of the APTES-functionalized area withPd seeds; and 4) the electroless deposition of metals onto the Pd-activated spheres.

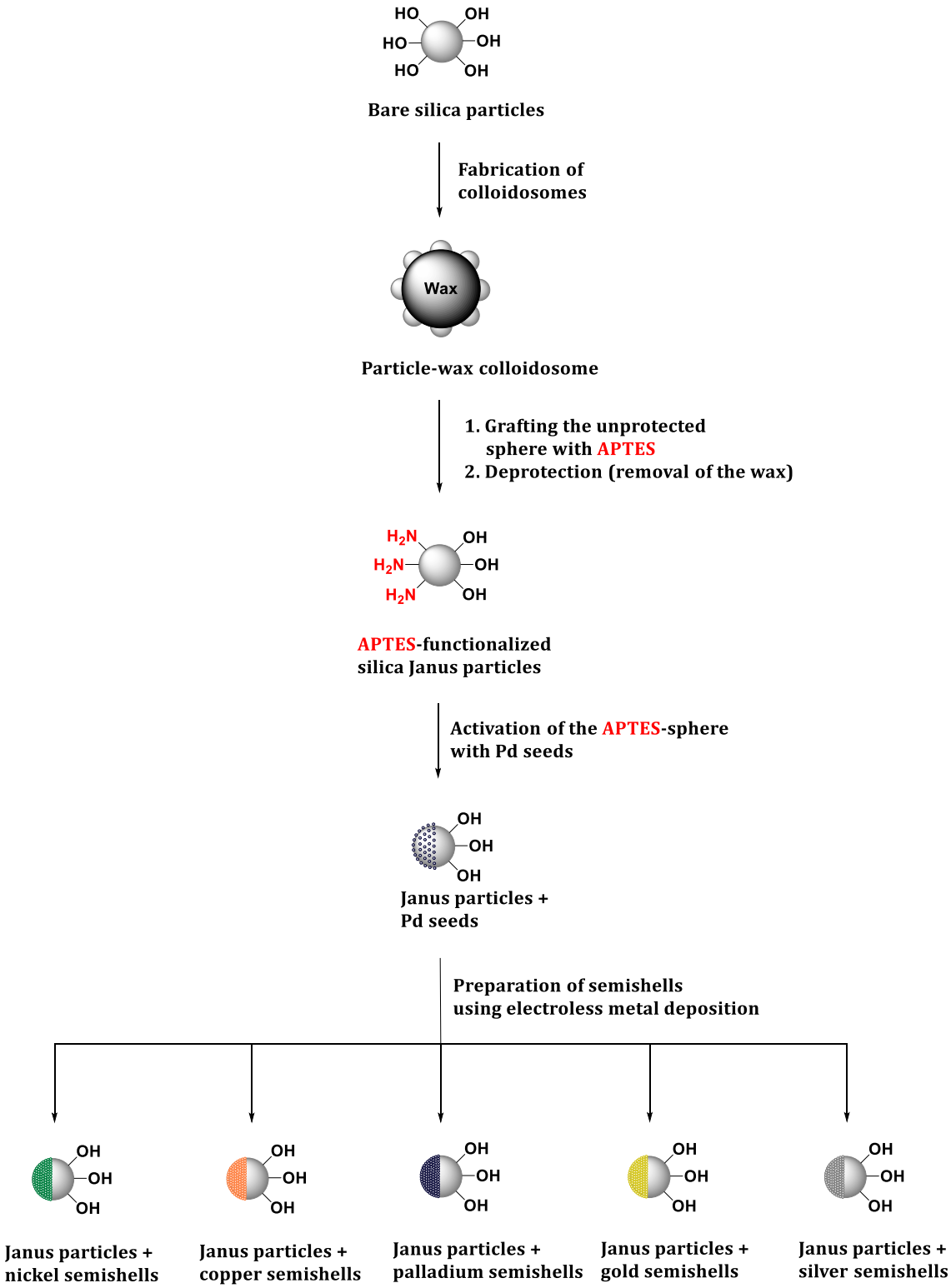


**FIGURE 4-1 SCHEMATIC OVERVIEW OF THE STRATEGY TO PREPARE SILICA JANUS PARTICLES WITH DIFFERENT METAL SEMISHELLS STARTING FROM BARE SILICA PARTICLES.**

First, the synthesis of different sizes of silica colloids and their redispersion using ultrasonic devices are presented (Chapter 4.1.1 and 4.1.2). Next, the influences of different reaction conditions are tested for binding a monolayer of APTES molecules on the silica surface. Additionally, reliable methods to quantify the number of amino groups on the silica surfaces are discussed (Chapter 4.1.3). Subsequently, colloidosomes of non-functionalized silica particles and wax are fabricated using two different surfactants. Their influence on the penetration depth of the particles into the wax is examined. Especially, the ability to control and to predict the ratio between masked and unprotected spheres of the silica particles is investigated by introducing reproducible and straightforward characterization methods. Additionally, their effect on the mass yield of silica Janus particles after the surface grafting with APTES is evaluated. For each surfactant molecule, the radius of gyration is calculated to estimate the silica surface area occupied by the corresponding amount of the surfactant. The theoretical degree of surface coverage is compared to the experimental results after evaluating the particle-wax colloidosomes (Chapter 4.2).

In the next step, APTES-Janus spheres and particles fully functionalized with APTES are coated with Pd seeds to catalyze the electroless metal deposition (Chapter 4.3.1). First, the optimal conditions for the Pd seed coating are defined, followed by the deposition of a variety of metal layers onto the Pd-activated silica surfaces using different metal salt electrolytes. As metal salt sources, electrolytes reported in the literature, as well as plating solutions from the company Atotech are used. By varying the amount of the electrolyte, various shell thicknesses are obtained, which are characterized by different methods (Chapter 4.3.2).

## 4.1. PREPARATION OF STARTING MATERIALS

### 4.1.1. BARE SILICA PARTICLES WITH ADJUSTABLE PARTICLES SIZE

Bare, non-functionalized silica particles were prepared using a variety of procedures depending on the desired particle size (60–1900 nm in diameter). Only silica particles of 500—600 nm in diameter were further modified as potential adhesion promoters. Particles of 700 and 1900 nm in diameter were employed as test substances to reproduce the synthetic protocol for the fabrication of particle-wax colloidosomes,[33, 47] before moving to smaller particles. Particles of 60 nm in diameter were used to investigate characterization methods, which are only applicable for particles < 100 nm in diameter (see Chapter 4.1.3), with a small coated monolayer to silica core ratio. The synthesis of the colloids can be catalyzed either by acid or base; the catalyst of choice in this study was ammonia. Because in the alkaline medium the formed silica particles are substantially ionized so that the particle growth can proceed without aggregation and gelation.[20] Table 4-1 provides an overview of the different batches of particles which were prepared as starting materials. Size characteristics were collected with DLS measurements (hydrodynamic particle diameter and polydispersity index) from the initial reaction mixture containing ethanol and ammonia and SEM images (mean particle size after evaluating at least 1000 particles). The corresponding SEM images are displayed in Figure 4-2.

**TABLE 4-1 DIAMETER OF OBTAINED SILICA PARTICLES**

| Name | Desired diameter size | DLS | | SEM |
|---|---|---|---|---|
| | | Hydrodynamic diameter [nm] | PDI | Diameter [nm] |
| NP-1 | 60 nm | 85±1 | 0.03±0.01 | 61±5 |
| NP-2 | 500—600 nm | 715±6 | 0.03±0.01 | 570±40 |
| NP-3 | 700 nm | 1030±40 | 0.04±0.02 | 680±30 |
| NP-4 | > 1000 nm | — | — | 1940±130 |

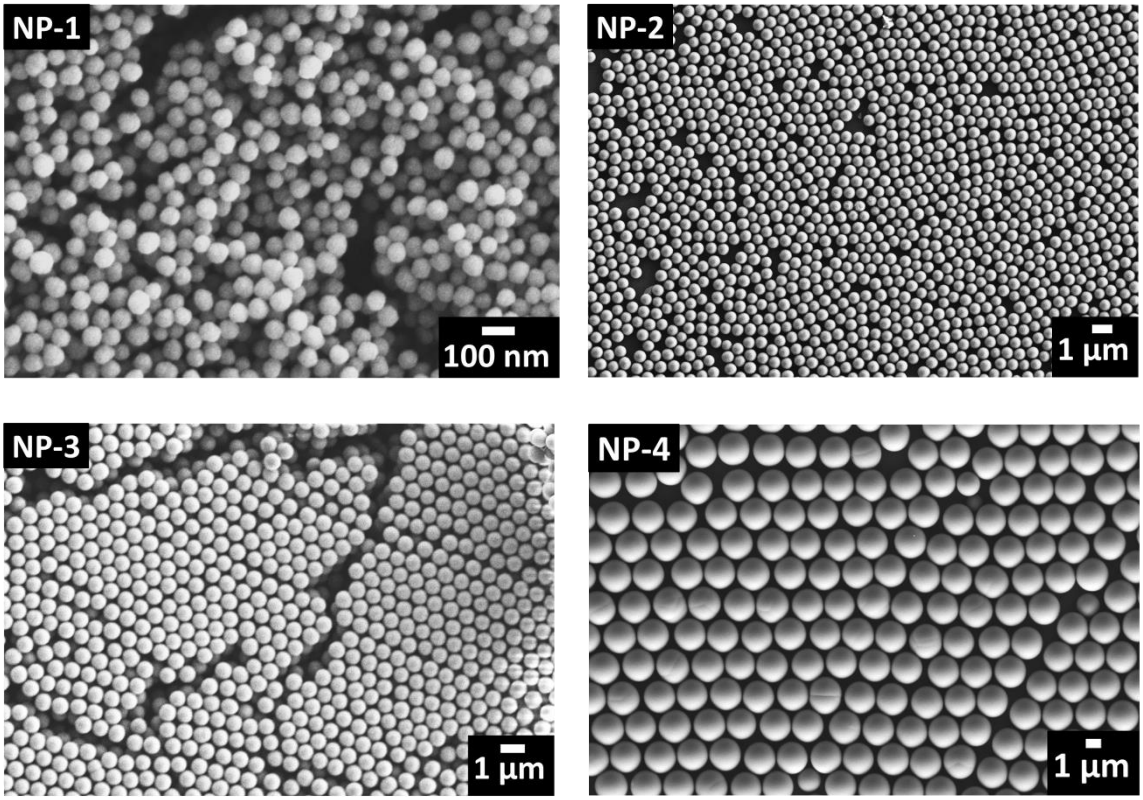


**FIGURE 4-2 SEM IMAGES OF NON-FUNCTIONALIZED SILICA PARTICLES WITH DIAMETERS OF NP-1) 61±5 NM, NP-2) 570±40 NM, NP-3) 680±30 NM, AND NP-4) 1940±130 NM.**

Highly monodisperse nanoparticles with 61±5 nm (NP-1) and 570±40 nm (NP-2) diameter are prepared using the well-known procedure by Stöber et al.[15, 105] The base-catalyzed hydrolysis and condensation reaction has been described in detail in Chapter 2.1. The results show that the hydrodynamic diameters measured with DLS for NP-1 and NP-2 (85±1 and 715±6 nm) are larger than the diameters determined by SEM. For the synthesis of sub-micrometer and micrometer-sized silica particles (NP-3 and NP-4) several protocols[106],[107],[108] were tried, but most of them led to particles with an uncontrollable polydispersity. The procedure published by Lei et al.[96] proves to be a viable route towards the desired larger particles (NP-3 and NP-4). In this semi-batch process, the dosing rate of solution II (containing ethanol and tetraethoxysilane (TEOS, 0.23 M (NP-3) and 0.17 M (NP-4)) into the solution I (containing ethanol, water, ammonia (0.37 M (NP-3) and 0.72 M (NP-4), and the electrolyte potassium chloride (0.18 M (NP-3) and 1.79 M (NP-4)) is controlled with a dosing unit of the workstation. The influence of different electrolytes and their concentration was investigated in previous studies of the nucleation and growth mechanism.[108],[109] The adsorption of cations with a

large ionic radius reduces the surface potential, which can promote coagulation at an early stage. These coagulated particles form the new nuclei, on which TEOS molecules hydrolyze and condense in the subsequent dosing step, causing the growth of larger colloids. Depending on the concentration of the electrolyte, particles with different sizes can be synthesized. A precise control of the electrolyte concentration and the dosing rate is of vital importance to reach monodisperse sub-micrometer and micrometer-sized particles.

The DLS method is not applicable for microparticles because the gravitational forces predominate the Brownian motion. The sedimentation accelerates the motion of the colloids, which result in a smaller hydrodynamic diameter (see Chapter 2.4.3).[78] Even the hydrodynamic diameter for sample NP-3 (1030±40 nm) is much higher than the measured diameter size from the SEM images (680±30 nm). Generally, the hydrodynamic diameter of a particle consists of the particle size plus the surrounding electric dipole solvent layer, which results in a few nanometer larger value than the diameter estimated by SEM.[78] Since the diameter discrepancy is much higher than a few nanometers, a possible explanation is the agglomeration of larger particles in the dispersion which can lead to significantly larger hydrodynamic diameters. Consequently, the DLS data for NP-2 and NP-3 must be interpreted with caution. It was reasoned that the evaluation of the SEM images results in a more comparable diameter for all sizes than the hydrodynamic diameter. For storage purposes in the industry, the dispersion was neutralized, the particles were washed, the solvent was removed, and the silica particles were stored as dry, white powders before being processed for different applications.

It can be summarized that during this current study, monodisperse silica particles in sizes ranging from 60–1900 nm in diameter were successfully synthesized using established protocols from literature.

### 4.1.2. DISPERSION TEST

Dry, bare silica particles needed to be dispersed in water to fabricate particle-wax colloidosomes or in ethanol for surface functionalization. Although the preparation of stable dispersion is an essential requirement for all applications, only few studies exist,[110] in which dry nanoparticles with different diameters are systematically redispersed in stable dispersions. Consequently, dispersion tests were made to find optimum parameters to prepare stable particle dispersions for the silica particles described in Chapter 4.1.1. Initially, the particles are agglomerated after being transferred into the dispersion medium. Two forces exist between two charged silica particles in a liquid according to the Derjaguin–Landau–Verwey–Overbeek (DLVO) theory,[111] (1) attracting forces (van der Waals) and (2) repulsive forces (electrical double layer forces). To overcome the attracting forces holding these agglomerates together and to break them down into single particles, mechanical stress from ultrasound can be applied.[112] The shear force imposed by the collapsing bubble (cavitation bubble), is capable to overcome the force holding them together.

The ultrasonic devices used during the present study are summarized in Table 3.3. Two bath type devices were utilized, whereby the frequency was only adjustable in bath 2. The third device was an ultrasonic probe (sonotrode), where the head of the probe has to be immersed in the dispersion before ultrasonication. In the preliminary test, the high-frequency mode (130 kHz) in the ultrasonic baths yielded poor dispersion results and was therefore discarded. An explanation can be that in high-frequency/low-intensity baths the production of cavitation bubbles is difficult. The cycles of compression and decompression become so short that the molecules in the liquid cannot be separated and hence, no voids (cavitation bubbles) are formed.[93b]

Subsequently, the focus in the dispersion study was on comparing the bath device (35 kHz) and the ultrasonic probe (20 kHz) and their ability to redisperse silica particles, so that they resume their initial hydrodynamic diameter with the corresponding polydispersity index (PDI). In Table 4-4 all obtained hydrodynamic diameters and PDI numbers are presented, when both ultrasonic apparatus were applied for different periods for a 1 g/L dispersion of silica particles in ethanol

(NP-5). The initial hydrodynamic diameters and PDI were measured by DLS from a non-purified dispersion containing all the starting materials, such as ethanol, water, TEOS, and ammonia.

**TABLE 4-2 OVERVIEW OF HYDRODYNAMIC DIAMETERS AND PDI OF NP-5 (SILICA DISPERSION WITH 1 G/L) AFTER APPLICATION OF DIFFERENT ULTRASONIC DEVICES WITH DIFFERENT DURATIONS**

| Device types | DLS | Sonication time [min] | | | | | |
|---|---|---|---|---|---|---|---|
| | | **Initial** | **5** | **10** | **15** | **20** | **60** |
| **Bath 1 and 2 (35 kHz)** | Diameter | 114±3 | Visible powder sediments | | | | 130±4 |
| | PDI | 0.09 ±0.06 | — | | | | 0.3 ±0.3 |
| **Sonotrode (20 kHz)** | Diameter | 114±3 | 170±4 | 140±5 | 129±3 | 111±3 | — |
| | PDI | 0.09 ±0.06 | 0.4 ±0.2 | 0.3 ±0.05 | 0.2 ±0.04 | 0.2 ±0.01 | — |

The ultrasonic bath (35 kHz) failed to disperse small particles (114±3 nm in diameter) into their original size with a PDI of ≤ 0.2 within 60 min. Whereas, the application of the ultrasonic probe with lower frequency (20 kHz) results in a regain of the initial hydrodynamic diameter and a PDI of ≤ 0.2 after 15 min, similar to the findings in literature.[110d-f] The lower the frequency, the higher the intensity, which can produce cavitation bubbles.[93b, 113] The attractive forces are higher between smaller particles and therefore, higher ultrasonic intensity or a more extended sonication period is needed. Another factor for the poor dispersion results, when using the bath apparatus, could be the indirect application of the ultrasound. In the bath setups, ultrasonic waves have to penetrate first the liquid in the bath, then the wall of the vessel to finally sonicate the dispersion. Whereas, the ultrasonic probe head is in direct contact with the dispersion medium. In an ultrasonic bath, the positioning of the reaction vessel is also crucial, because of the inhomogeneous distribution of ultrasonic intensity. A simple aluminum foil test can be used to localize the area with the highest intensity.[114] Further, when applying the ultrasonic probe, the higher intensity causes a stronger nucleation and collapse of solvent bubbles. The cavitation field (acoustic streaming) itself

agitates the solution with the particles. Subsequently, both devices were applied to sonicate a dispersion containing particles with larger hydrodynamic diameter NP-6 (526±11 nm) and NP-7 (727±10 nm). The corresponding hydrodynamic diameters and PDI from DLS measurements are summed up in Table 4-3.

**TABLE 4-3 OVERVIEW OF HYDRODYNAMIC DIAMETERS AND PDI OF SILICA DISPERSION (1 G/L) AFTER APPLICATION OF ULTRASONIC DEVICES WITH DIFFERENT DURATION**

| Device types | Sample | DLS | Sonication time [min] | | | | |
|---|---|---|---|---|---|---|---|
| | | | Initial | 5 min | 10 min | 15 min | 20 min |
| **Bath 1 and 2 (35 kHz)** | NP-6 | Diameter | 526 ±11 | 488 ±20 | 493 ±15 | 508 ±11 | 497 ±10 |
| | | PDI | 0.04 ±0.04 | 0.3 ±0.04 | 0.2 ±0.05 | 0.2 ±0.02 | 0.1 ±0.03 |
| **Sonotrode (20 kHz)** | NP-7 | Diameter | 727 ±10 | 682 ±10 | 665 ±9 | 668 ±10 | – |
| | | PDI | 0.05 ±0.04 | 0.03 ±0.03 | 0.03 ±0.04 | 0.02 ±0.03 | – |

The ultrasonic bath (35 kHz) redisperses the larger particles (> 500 nm in diameter) within 10 min so that the particles regain their initial hydrodynamic diameter (493±15 nm; 0.2±0.05) and a PDI of ≤ 0.2. When applying the ultrasonic probe (20 kHz) similar results are obtained after 5 min (682±10 nm; 0.03±0.03). Consequently, the sonication time and the devices applicable for particles with 500 nm diameter can also be utilized for submicron or micrometer-sized particles.

Although the ultrasonic probe is the most effective device, also confirmed by other researchers,[110d, 110e] it has several disadvantages. Since the probe needs to be immersed in the dispersion, cross-contamination from a previous dispersion or detaching of metals from the transducer can occur.[93a] Another drawback is the open vessel, where some reactants can be lost, or the solvent can quickly evaporate, due to the heat caused by the sonication itself. Thus, all particles with a diameter > 500 nm are deagglomerated using bath type devices (35 kHz) and depending on their sizes the sonication time is varied (see Table 4-4). The

produced colloidal suspensions were stable throughout the corresponding reaction step, but no long-term stability tests were made.

**TABLE 4-4 OVERVIEW OF ULTRASONIC DEVICES AND SONICATION TIME FOR OPTIMAL DISPERSION OF SILICA PARTICLES IN WATER**

| Particles diameter [nm] | Type | Model | Time [min] |
|---|---|---|---|
| **60** | Ultrasonic probe | HD 2070 | 15 |
| **500—600** | Bath | RK514H/TI-H-5 M3 | 10 |
| **> 800** | Bath | RK514H | 5 |

Optimal conditions were selected for the redispersion of silica particles with different sizes. Silica particles with ≤ 100 nm diameter can be deagglomerated using the ultrasonic probe and particles with a diameter ≥ 500 nm can be redispersed in ultrasonic baths (35 kHz). With varying the sonication time, the initial particle sizes with their corresponding low polydispersity are regained.

### 4.1.3. FUNCTIONALIZATION OF SILICA PARTICLES SURFACE

Silica particles functionalized with amino groups find application in broad areas and fundamental investigations. The quantification of the surface concentration of amino groups is crucial in many applications because most of the time there is a direct interaction between the accessible amino groups and the involved substrates or surfaces. Additionally, the number of amino groups provides information about the colloidal stability of the particles. A high number of amino groups at the surface results in an increased value of the zeta potential. The target particles, prepared during the present research, will be employed as potential adhesion promoter with a semishell coating. To prepare these semishells, the surface needs to be partially activated with Pd seeds as a catalyst. The proposed catalyst is covalently bonded to the nitrogen of the silica surface and is described in Chapter 4.3.1. To coat the surface homogeneously with Pd, the number of accessible amino groups and the state of the Pd complex itself are important factors.

#### 4.1.3.1. STATE OF THE ART

Much literature is published about the synthesis and application of these amine-functionalized silica colloids. The amino groups are mostly introduced by an organosilane coupling agent such as 3-aminopropyltrimethoxysilane (APTES). Two main procedures are reported to create amine-covered silica spheres:

grafting (post-modification)[18b, 115]

co-condensation method (in situ modification).[18b, 68d, 115a, 116]

In the grafting method, non-functionalized silica particles are utilized as precursors that are modified with an alkoxysilane with amino moieties via a hydrolysis and condensation reaction. The post-modification process does not increase the particle size because only a monolayer of APTES molecules is grafted ontp the surface. In the co-condensation method, TEOS and APTES are added simultaneously to the mixture. In this one-pot synthesis, hybrid organo-silica composites are prepared, where the organic groups are incorporated inside the silica core, as well as being attached to the surface. Since the focus during this

study was to prepare silica particles with a defined size and a monolayer of APTES molecules was sufficient; the post-synthesis modification method was chosen.

The functionalization of silica particles with APTES molecules proceeds in different solvents, with different reaction times, temperatures, and in the presence of nitrogen or air, according to the literature.[18b, 82, 117] Additionally, a basic or acidic catalyst can be involved in the process. Even when ethanol is used as a solvent, there is not a consistent reaction protocol. Van Blaaderen et al. grafted a monolayer of APTES on the silica surface using the original Stöber silica reaction mixture containing ethanol, ammonia, and water and stirring the mixture including the organosilane for 1 h at rt, followed by refluxing for 2 h.[18b] Choi et al. prepared Stöber silica particles and added acetic acid to change the pH to 4, once the desired colloid size was achieved. After stirring the acidic mixture for 1 h, APTES was added and the mixture was heated to reflux for 3 h.[117a] Other researchers reacted silica particles solely with APTES in ethanol for 12 h at rt,[82, 117b] or the mixture was heated for 10 min at 60°C, followed by the addition of glacial acetic acid to stop the reaction.[117c] Heating above 40 °C is not suitable for the further processing, because of the paraffin wax, where the silica particles are partially protected with, has a low melting point (Chapter 4.1.3). Jiang et al. successfully grafted silica particles embedded in wax with APTES at 0 °C for 1 h in the presence of trimethylamine (TEA) as basic catalyst.[47] This raised the question if the "harsh" protocols are necessary or what the advantages are.

It is especially challenging to find characterization methods that result in reproducible information about the number of accessible amino groups on the silica surface for all kinds of particles sizes. Most of the methods are applicable for particles smaller than ~100 nm in diameter such as C/H/N elemental analysis (EA) and potentiometric titration, since a small APTES monolayer to silica core ratio is required.[18b] When a monolayer is deposited onto particles with small diameters (< 50 nm), the increased hydrodynamic diameter might be detectable with DLS. With increasing colloid diameter, the detectability for a monolayer deposition with DLS is aggravated. In the case of multilayer deposition, the size difference can be observed in the SEM/TEM, when the images before and after the grafting are compared.[117c] It has also been reported that zeta potential measurements with

isoelectric point titration result in information about the surface coverage with amino groups.[115a] Most methods for characterizing the deposited layer of coupling agents are suitable on a flat surface such as ellipsometry, contact angle, atomic force microscopy (AFM), and X-ray photoelectron spectroscopy (XPS). Other procedures, such as Fourier-transform infrared spectroscopy (FTIR),[18a, 116a] $^{13}C$ and $^{29}Si$ nuclear magnetic resonance (NMR) spectroscopy,[116a] powder XRD measurements,[115a] mass spectrometry[24], and thermal gravimetric analysis (TGA), deliver qualitative information about the presence of amino groups although in some cases quantitative information is theoretically possible. An indirect method for the quantification of amino groups is to modify the functional groups into compounds which are detectable by UV-Vis or fluorescence spectroscopy.[82, 117a, 118] Depending on the reagent, the resulting UV/Vis-active product is either attached to the silica surface or inside the solution.

Within all the quantification methods, C/H/N EA is a reliable method that is applied in many studies. Van Blaaderen et al. calculated different numbers for two batches form the C/H/N EA data (6.5 $NH_2/nm^2$ and 5.6 $NH_2/nm^2$, respectively). When a third batch was investigated with a titration method developed elsewhere,[119] a surface coverage of 6.8 $NH_2/nm^2$ was calculated.[18b] According to these researchers the small difference in the values result from the state of the silanol groups on the colloids. Badley et al. obtained a surface coverage of ~9 $NH_2/nm^2$ when colloidal silica (58—59 nm in diameter) was prepared first, and then APTES was added to the original mixture upon sonication, and reacted for 20 h at rt in the presence of air. When the bare silica colloids were dispersed in DMF and reacted with APTES at 100 °C under a nitrogen atmosphere, the number of amino groups was ~7.5 $NH_2/nm^2$.[24] The reported numbers fluctuate even when similar synthesis protocols and characterization methods are used.[24] The EA method delivers only information about the content of nitrogen inside the composites but not about the accessibility of the nitrogen as a reaction partner.

Derivatization methods result in information about the accessible amino groups. Jung et al. reacted silica particles with 3-aminopropyltrimethoxysilane (APTMS) for 12 h at rt, and they obtained a surface coverage of 0.4 $NH_2/nm^2$ when the fluorescent labeling assay with rhodamine B isothiocyanate (RITC) was used.[117b]

When the same colloids were investigated with the acid-base back titration with phenolphthalein as indicator, the number of amino groups was 2.7 $NH_2$-groups/$nm^2$. The low number from the first method can result from the fact that once a RITC molecule interacts with an amine, it sterically hinders the interaction of other RITC molecules and amino groups in the near environment. An approach to obtain reproducible results from this method is using a reagent that cleaves the amino group from the silica core. Soto-Cantu et al. introduced the ninhydrin assay and detected a surface coverage of 4 $NH_2$-groups/$nm^2$,[82] which corresponds to a monolayer. Their obtained results were confirmed from the corresponding zeta potential measurements. [82]

When larger particles are prepared (500—600 nm in diameter), most of the methods mentioned above are not sensitive enough. The inconsistent grafting protocols and the incomparable characterization methods constituted the groundwork for this present research. Here, we present an overview of the influence of different reaction parameters such as temperature, time, and the presence of basic or acidic catalyst on the surface grafting. First, a reproducible quantification method is established for small APTES-functionalized silica particles (≤ 70 nm in diameter). UV-Vis detectable products are generated, and the results of the amine surface coverage are compared to the nitrogen amount detected with C/H/N EA. Once a facile procedure for quantification was established, the outcomes of different approaches for binding of APTES were compared.

#### 4.1.3.2. COMPARISON OF CHARACTERIZATION METHODS

Small, pure, and non-functionalized silica particles NP-1-I and NP-1-II (61±8 nm and 62±9 nm in diameter) were dispersed in ethanol (1 g/L) and reacted with APTES (1.4 mM) and TEA (1.4 mM) for 1 h at 75 °C under argon atmosphere. An amino group to hydroxyl group ratio of 5 was applied, assuming a sphere with a surface density of 4 OH groups/$nm^2$, according to the literature.[97] Also, hydroxyl surface densities of 5 OH groups/$nm^2$ have also been reported,[20, 120] but 4 OH groups/$nm^2$ was chosen as reference. The ratio of 5 APTES molecules could presumably yield multilayers of APTES on the silica particle surface.[121] The reactivity of the coupling agent is influenced by the hydrolysis rate of its three ethoxy groups,[122] the catalytic abilities of the amino group itself,[123] and/or the

addition of a catalyst. Therefore, the basic catalyst TEA was introduced in a ratio of 1:1 referred to APTES. After the reaction was finished, the particles were washed by centrifugation and redispersion, and the amount of nitrogen in the samples was determined by C/H/N EA. The accessible amino groups on the surface were modified into UV-Vis detectable species with ninhydrin[82, 124] and salicylaldehyde.[81, 117a] Primary amines react with ninhydrin to the colored Ruhmann's purple, which is detached from the colloids and can be detected inside the solution. Salicylaldehyde yields the yellow salicylimine derivative (Schiff's base), which is attached to the silica surface. To suppress the contribution of colloidal scattering during the UV-Vis measurements, chloroform was chosen as an appropriate solvent, because of its similar refractive index to Stöber silica particles ($n_{chloroform}$ = 1.445[125] and $n_{Stöber\_silcia}$ = 1.45 at 20°C[18b]). The obtained results from C/H/N EA and UV-Vis are summarized in Table 4-5. The theoretical amount of N in % was calculated for a potential monolayer deposition of APTES, assuming a surface density of 4 $NH_2/nm^2$, when each OH group reacts with 1 APTES molecule (NP-1-I: 0.46± 0.06 % and NP-1-II 0.45±0.07 %) as a reference to the detected number. The error margin for the calculation of the $NH_2/nm^2$ reflects the error margin of the measuring methods described in Table 4-5 and the error margin of the particle surface area according to the SEM results.

**TABLE 4-5 OVERVIEW OF RESULTS OBTAINED FROM C/H/N EA AND UV-VIS SPECTROSCOPY FOR THE SURFACE COVERAGE OF AMINO GROUPS ON SILICA PARTICLE SURFACE**

| | Elemental analysis | | | UV-Vis | |
|---|---|---|---|---|---|
| **Sample** | **Theoretical value for monolayer N [%]** | **Detected N [%]** | **Calculated [$NH_2/nm^2$]** | **Ninhydrin assay [$NH_2/nm^2$]** | **Salicyl-aldehyde assay [$NH_2/nm^2$]** |
| **NP-1-I 61±5 nm** | 0.46± 0.06 | 0.50±0.04 | 4.5±0.8 | 4.7±2.2 | 6.0±3.5 |
| **NP-1-II 62±6 nm** | 0.45±0.07 | 0.52±0.04 | 4.7±0.9 | 6.2±3.6 | 9.9±5.8 |

When the detected amount of nitrogen from EA was converted to an amine surface coverage, the numbers for NP-1-I and NP-1-II (4.5±0.8 and 4.7±0.9 $NH_2/nm^2$) are in good agreement with a monolayer deposition, assuming a surface density of 4-5 $OH/nm^2$, respectively. Similar C/H/N EA results are reported from van Blaaderen et al., when silica particles were coated with APTES in ethanol in the presence of ammonia (5.6—6.5 $NH_2/nm^2$).[18b] For sample NP-1-I, the data obtained from the ninhydrin assay with UV-Vis spectroscopy (4.7±2.2 $NH_2/nm^2$) confirm the results from C/H/N EA. The obtained surface density for NP-1-II is slightly higher (6.2±3.6 $NH_2/nm^2$) than the numbers from C/H/N EA, but still in the acceptable range, considering the high error margin.

When salicylaldehyde was used as a derivatization agent, the estimated amine group coverages are higher (NP-1-I: 6.0±3.5 $NH_2/nm^2$ and NP-1-II: 9.9±5.8 $NH_2/nm^2$) than the results from the ninhydrin assay and C/H/N EA, but the tendencies are similar to those with ninhydrin. A reason for the higher value is likely the sample preparation. After chloroform and salicylaldehyde were added to the mixture, the suspension was dispersed for 15 min with an ultrasonic probe. As described earlier (Chapter 4.1.2), one of the disadvantages of the application of the ultrasonic probe is the generated heat. Although the mixture was cooled, some of the chloroform might have evaporated during the dispersion procedure, so that the concentration of the dispersion was much higher than assumed in the calculations. The lack of colloidal stability in organic solvents can influence the absorption spectra and result in erroneous numbers of amino groups. Consequently, it was concluded that the derivatization method with salicylaldehyde and chloroform is not suitable for this present study.

A rapid and facile method to investigate the surface charge are zeta potential measurements. In Figure 4-3 the zeta potentials of bare and APTES-functionalized silica particles at different pH values in water are illustrated. The point where the surface carries no charge, the isoelectric point (IEP), is located around pH 6.6 for the APTES-functionalized particles. Below this pH the amino groups are protonated, hence the zeta potential is positive. With increasing pH value, negative zeta potential is measured, caused by the saturation of counterions ($OH^-$, $Cl^-$) inside the dispersion. The measured IEP is within the range found in the literature for

monolayer grafting of Stöber silica nanoparticles (pH 6.2 by Pálmai et al.[117c] and pH 6.7 by Synytska et al.[126]). The surface of bare silica particles contains deprotonated silanol groups in water and consequently has negative zeta potential values, even at pH~3. Although researchers reported a correlation between amine surface density and zeta potential while using IEP titration,[82, 115a] the experimental data obtained during this present study showed around the IEP a high standard deviation of the measurement. A reason can be that the electrostatic repulsion between particles decreases and the colloids can form agglomerates, which can affect the velocity of the particle mobility and can caus values afflicted with high errors. Another explanation is that around the zeta potential of zero, the frequency difference between irradiated and scattered light approximates zero. The small differences that are measured are sensitive even towards small fluctuations.

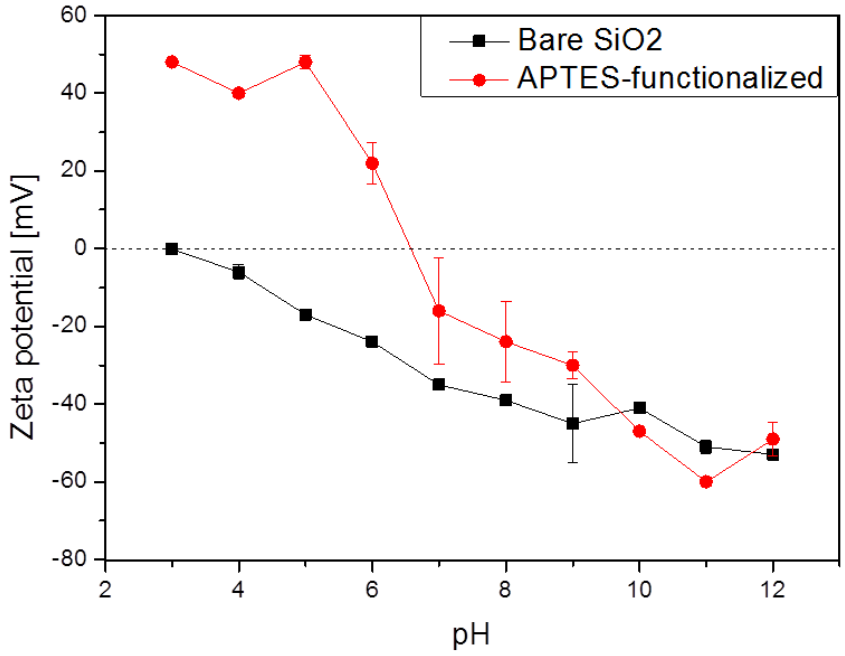


**FIGURE 4-3 GRAPHIC ILLUSTRATION OF ZETA POTENTIAL VALUES OF BARE SILICA PARTICLES AND AN APPROXIMATE MONOLAYER OF APTES-MOLECULES ON SILICA PARTICLES AS A FUNCTION OF DIFFERENT PH VALUES.**

It can be summarized that the ninhydrin assay is a suitable derivatization method to quantify amino groups on colloids of all sizes. The C/H/N EA confirms the obtained values from the absorption data. Because of unfeasible sample preparation and unstable colloidal dispersion with chloroform as a solvent,

salicylaldehyde can be ruled out as possible UV-Vis derivatization agent alternative. The zeta potential measurements are not suitable to quantify the number of amino groups on the particles surface. It is an indication for the surface charge.

#### 4.1.3.3. TESTING SEVERAL REACTION PARAMETERS FOR THE GRAFTING

Pure, non-functionalized silica particles (500—600 nm in diameter) were dispersed in ethanol (10 g/L) and coated with APTES as a coupling agent with an amino group to hydroxyl group ratio of 5. As mentioned in Chapter 4.1.3.1, for the functionalization of silica particles with APTES, different reaction conditions have been used.[18b, 82, 117] Therefore, the influence of different reaction parameters on the grafting of silica surface was investigated. First, different equivalents (equiv.) of basic catalyst (trimethylamine TEA) and acidic catalyst (glacial acetic acid) in comparison to APTES were chosen. Then, different reaction temperatures and reaction times were tested to compare the outcome of the surface functionalization. After the reaction was terminated, the dispersion was purified by multiple centrifugation/redispersion steps and both, the supernatant and the particles, were tested with a slightly modified ninhydrin assay to determine the amino groups on the particles surface and those still in solution. All the related calculations are provided in the Appendix II Calculations. The purpose of analyzing both quantities (supernatant and particles) was only to confirm the reliability of the results. The corresponding concentrations [mM] are converted into the number of amino groups per $nm^2$. It is vital for the conversion of amino groups into a UV-Vis spectroscopic detectable species with ninhydrin, to ensure the absence of ammonia from the previous step. Otherwise, the primary nitrogen of ammonia also reacts with ninhydrin, causing invalid results. Therefore, the initial mixture of the Stöber silica colloid dispersion was neutralized by the addition of diluted HCl, as described before by other researchers.[24]

Throughout the current study, two different APTES sources were utilized. One bottle was freshly opened and stored in the fridge under an argon atmosphere, which will be referred to in the following as “new”. The other one was around 3 years old and was stored at rt under argon, and will be referred to in the following as “old”. In Table 4-6, all reaction conditions for the silica particle surface grafting and the corresponding number of $NH_2$ groups/$nm^2$ are listed. The standard deviation of the particle size itself was not taken into consideration for the calculation of the amine surface density because the error would propagate throughout all the calculation steps. The error margins correspond to the standard

deviation of at least two experiments and reflect here the reproducibility of the quantification procedure itself. The pH values of each mixture were measured at rt, and listed below. Since the solvent was ethanol, the number fluctuated strongly. Consequently, the values represent a pH tendency.

**TABLE 4-6 OVERVIEW OF ALL REACTION CONDITIONS FOR SURFACE GRAFTING OF SILICA PARTICLES WITH APTES AND THEIR CORRESPONDING DETERMINED NUMBER OF AMINO GROUPS PER AREA**

| **Reaction condition** | **1h, 0 °C** | | | | |
|---|---|---|---|---|---|
| **Catalyst** | None | TEA 1 equiv. | TEA 100 equiv. | Acetic acid 1 equiv. | Acetic acid 100 equiv. |
| **$NH_2/nm^2$** (new) | 5.4±0.5 | 6.1±0.6 | 6.6±0.6 | 4.8±0.6 | – |
| **$NH_2/nm^2$** (old) | 3.4±0.3 | 2.7±0.2 | 2.6±0.2 | 2.2±0.2 | – |
| **Reaction condition** | **1h, RT** | | | | |
| **Catalyst** | None | TEA 1 equiv. | TEA 100 equiv. | Acetic acid 1 equiv. | Acetic acid 100 equiv. |
| **$NH_2/nm^2$** (new) | 3.0±1.4 | 4.2±1.4 | 2.2±1.6 | 2.7±1.1 | 4.1±0.3 |
| **$NH_2/nm^2$** (old) | 3.4±2.4 | 3.9±1.5 | 2.6±1.2 | 4.6±0.4 | 0.5±0.1* |
| **pH** | ~8 | ~8 | ~10 | ~8 | ~5 |
| **Reaction condition** | **1h, 75 °C** | | | | |
| **Catalyst** | None | TEA 1 equiv. | TEA 100 equiv. | Acetic acid 1 equiv. | Acetic acid 100 equiv. |
| **$NH_2/nm^2$** (new) | 5.4±0.5 | 5.5±0.6 | 4.1±1.0 | 6.2±0.6 | 1.9±1* |
| **$NH_2/nm^2$** (old) | 2.3±0.2 | 4.3±0.4 | 1.1±0.1* | – | – |
| **Reaction condition** | **12h, 75 °C** | | | | |
| **Catalyst** | None | TEA 1 equiv. | TEA 100 equiv. | Acetic acid 1 equiv. | Acetic acid 100 equiv. |
| **$NH_2/nm^2$** (new) | 5.1±0.6 | 5.8±0.4 | 4.8±1.0 | 4.2±0.5 | 2.6±0.5* |
| **$NH_2/nm^2$** (old) | 1.7±0.5 | 3.0±0.2 | 2.5±0.2 | 2.6±0.1 | – |

A significant difference in surface grafting was found between the "old" and the "new" APTES. In general, the estimated numbers of $NH_2/nm^2$ were higher when freshly opened APTES was utilized, throughout all different reaction conditions. Within the last 3 years, the APTES vessel could have been contaminated with either $CO_2$ and/or water due to the lack of inert gas atmosphere. In the presence of $H_2O$, the ethoxysilane groups can hydrolyze and condensate with other APTES molecules to longer chains,[127] hence it is recommended to distill the APTES regularly.[121] However, no evidence of oligomers was found in mass spectroscopy. On the other hand, the interaction between $CO_2$ and the amine-terminated silane can yield carbamic acid species.[128] The primary amine does no longer have a free electron pair, which enables a nucleophilic attack on ninhydrin. This could explain the overall lower numbers of $NH_2/nm^2$ when "old" APTES was used as coupling agent. According to this observation, the discrepancies between the reported numbers of functional groups in the literature might also result from the different APTES batches and their storage conditions.[18b, 24]

In the following subsection, the focus will be on the results obtained with the "new" APTES batch because in this case, a modification of the amino group can be excluded. After summarizing the results for each reaction condition, possible hydrolysis and condensation mechanism are postulated and schematically illustrated in Figure 4-4 for base-catalyzed reaction and in Figure 4-5 for acid-catalyzed reaction.

**Grafting reaction without any catalyst**

After an reaction time of 1 h 0 °C, the estimated amount of amine on the surface was 5.4±0.5 $NH_2/nm^2$, which corresponds to slightly more than one monolayer of APTES (assuming a sphere with a surface density of 4[97] or 5[20, 120] $OH/nm^2$). Similar results were obtained when the reaction temperature was increased to 75 °C. An increase in reaction time to 12 h at 75 °C did not alter the surface density. Only when the reaction mixture stirred for 1 h at rt, a lower surface coverage was observed (3.0±1.4 $NH_2/nm^2$), in comparison to the other values detected in the absence of a catalyst. In some batches, the particles have a surface coverage of 1—2 $NH_2/nm^2$, while in others samples, the particles were grafted with a monolayer. The low numbers indicate that the reaction was not completed at the time of the

measurement. According to Soto-Cantu et al., an increase in reaction time at rt to 12 h can result in a monolayer deposition.[82]

**Grafting reaction with 1 equiv. of TEA**

In the presence of 1 equiv. of TEA, the detected numbers of amine on the surface correspond to a monolayer of APTES. In general, more amino groups were detected on the surface in the presence of TEA than without any catalyst, although the pH did not change. However, similar to the data without a catalyst, when the reaction was stirred for 1 h at rt, the obtained numbers of amino groups on the surface varied a lot (4.2±1.4 $NH_2/nm^2$).

**Grafting reaction with 100 equiv. of TEA**

When the amount of TEA was increased to 100 equiv., the pH was around 10, and the outcome changed drastically. In the case of the reaction stirring for 1 h at 0 °C, the calculated number was 6.6±0.6 $NH_2/nm^2$, but when the temperature was raised to rt, the surface coverage decreased to 2.2±1.6 $NH_2/nm^2$. With heating the reaction mixture to 75 °C for 1 h, the coverage was 4.1±1.0 $NH_2/nm^2$, and when the reaction time was increased to 12 h, the amine density remained the same. The detected values fluctuate strongly, and in some cases, the dispersion precipitated when the reaction temperature was > rt. It is known that > pH 10 silica particles can be dissolved,[129] which alters the colloid surface charge and reduces the dispersion stability. For silica particles with a diameter of 550±40 nm, small changes in their diameter cannot be detected using electron microscopy, considering the high standard deviation of the colloid size itself. The dissolved components including amino-moieties float inside the solution and can be removed during the purification step. This might also explain the higher amine density when the reaction parameters were 1 h and 0 °C because the rate of possible dissolution process was decelerated by the cold environment.

**General consideration**

It is worth considering that uncontrollable parameters such as humidity and history of glassware may influence the reactivity between APTES and the surface.[121] As a consequence, the presence of moisture inside all of the mixtures and the subsequent hydrolysis and self-condensation of APTES-molecules has to be considered, since the reactions proceeded in ethanol as solvent. It has been reported that even small residues of water can accelerate the hydrolysis and self-condensation of APTES.[121] However, potential APTES oligomers can be easily removed during the centrifugation step and are not present during the quantification step with the ninhydrin assay anymore, owing to the different mass between colloidal silica and amino silane oligomers. Studies claim that in the presence of water an electrostatic interaction between positively charged amino groups and negatively charged silanol oxygen can exist.[121] In case of electrostatic interaction, a monolayer deposition of APTES is generated on the silica surface. However, during the purification step including treatment with ultrasound, non-covalently bonded APTES can be washed away.[121]

**Mechanism of the base-catalyzed hydrolysis and condensation reaction**

A proposed mechanism of base-catalyzed hydrolysis and condensation reaction is illustrated in Figure 4-4. When the reaction mixture contains only bare silica particles and APTES in ethanol; the amino group itself acts as a catalyst, owing to its basic character.[130] In the presence of traces of water, the base (TEA or APTES itself) generates a hydroxide anion that attacks the triethoxysilane derivative via an $S_N2$ reaction forming a pentacoordinate intermediate and displacing ethanol (hydrolysis). The electron density at the silicon decreases since the more electron-withdrawing hydroxy group replaces the ethoxy group. The decrease in electron density stabilizes the transition state, and it results in an increase in hydrolysis rate for each subsequent hydrolysis step. The steric hindering effects of the ethoxy group also impact this trend. Consequently, for monomers, the hydrolysis of the first alkoxy group is the rate-determining step. The subsequent base-catalyzed condensation resembles the hydrolysis reaction steps with the formation of a pentacoordinate intermediate. The nucleophile is the deprotonated silanol group on the colloid surface, and its acidity increases rapidly with the degree of

condensation of the silicon atom, because of the electron withdrawing effect of the siloxane bonds.[17-18]

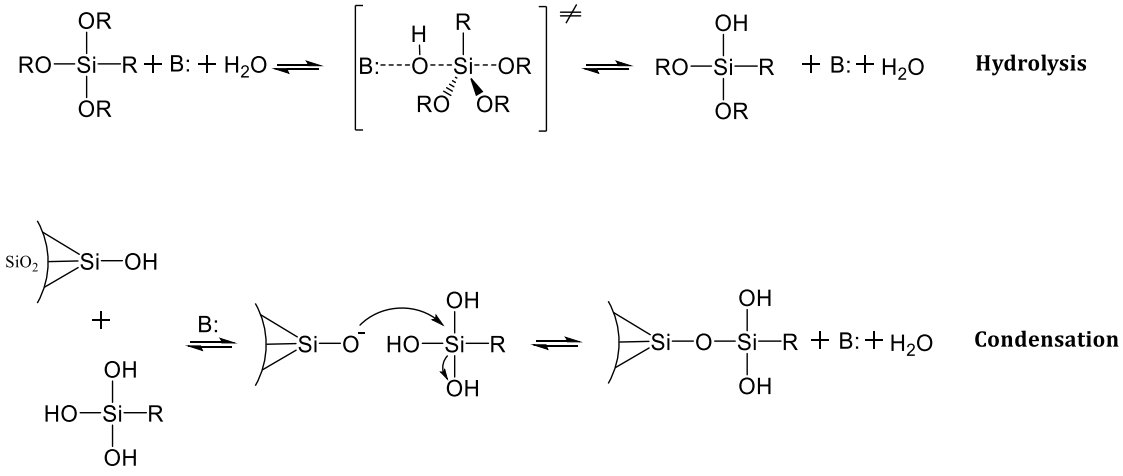


**FIGURE 4-4 SCHEMATIC ILLUSTRATION OF A PROPOSED BASE-CATALYZED HYDROLYSIS AND CONDENSATION MECHANISM OF A SILANE COUPLING AGENT.**

Since the accelerating factor is the creation of hydroxyl anions or the deprotonation of the silanol group, an increase in catalyst amount, increases the condensation process. This can explain the higher numbers of accessible amino groups in the presence of catalytic amounts of TEA, which correspond to literature findings of base-catalyzed silanization reactions in general.[131] Refluxing the mixtures with 1 equiv. of TEA and without a catalyst for 1 h resulted in equal numbers of amino groups. The heat accelerates the hydrolysis and condensation reaction. A further increase in refluxing time did not affect the amine surface density. These findings agree with the results from Howarter et al., who grafted the silicon oxide surface of a wafer with APTES in toluene at 75 °C, and reported that once the mixture was heated for 1h at 75 °C, an increase in reaction time had no further influence.[132] In general, the number of accessible amino groups (5—6 $NH_2/nm^2$) detected from the ninhydrin assay resulting from heating or stirring at 0°C is in agreement with reported numbers from van Blaaderen et al.[18b] They detected a surface density of 5.6—6.5 $NH_2/nm^2$ with C/H/N EA when the Stöber silica colloids reacted with APTES in the initial mixture with ammonia.[18b] The numbers of amine coverage obtained from stirring the mixtures for 1 h at 0 °C were unexpected, especially, when the reaction appeared to be incomplete at rt in comparison to 75 °C.

According to the findings of Grubb et al., the condensation reaction of the silanols to siloxanes in protic solvents approaches a thermodynamic equilibrium rather than completion.[133] In a detailed study, the condensation of trimethylsilanol in the solvents methanol was monitored. They proposed that the incomplete condensation is caused by the fast reaction described by Equation (4-1), which removes silanol from the system but the condensation equilibrium in Equation (4-2) is established slowly. It was also argued that the condensation rate of pathway (4-1) and (4-2) appeared to be faster than the direct condensation in Equation (4-3).

$$(CH_3)_3SiOH + CH_3OH \underset{k_{-1}}{\overset{k_1}{\rightleftharpoons}} (CH_3)_3SiOCH_3 + H_2O \quad \textbf{(4-1)}$$

$$(CH_3)_3SiOH + (CH_3)_3SiOCH_3 \underset{k_{-2}}{\overset{k_2}{\rightleftharpoons}} (CH_3)_3SiOSi(CH_3)_3 + CH_3OH \quad \textbf{(4-2)}$$

$$2\ (CH_3)_3SiOH \underset{k_{-3}}{\overset{k_3}{\rightleftharpoons}} (CH_3)_3SiOSi(CH_3)_3 + H_2O \quad \textbf{(4-3)}$$

The corresponding equilibrium constant in Equation (4-4) demonstrates that no trimethylsilanol is present at the equilibrium and has the same value when different concentrations of basic and acidic catalyst are used.[133]

$$K = \frac{[(CH_3)_3SiOCH_3]^2[H_2O]}{[(CH_3)_3SiOSi(CH_3)_3]} \quad \textbf{(4-4)}$$

For this present study, it can be postulated that the hydrolyzed amino silane coupling agent rapidly reacts with ethanol and then slowly condenses with the silica surface and forms siloxane bonds. This can explain the low amine density at rt in comparison to 75 °C because the condensation equilibrium was not reached at the time of the measurement. Once the temperature was elevated, the formation of the siloxane bonds was realized faster. To our knowledge, no investigation of this process was done at a reduced temperature up to now. It is possible that around 0 °C, the reaction between hydrolyzed amino silane and ethanol is suppressed, instead many free silanol groups are available, and the direct condensation is favored (similar to the pathway (4-3)).

**Grafting reaction with 1 equiv. of acetic acid**

When 1 equiv. of glacial acetic acid was introduced as a catalyst and the mixture was stirred for 1 h at 0 °C, the surface was covered with a monolayer. With increasing the temperature to rt, the number of amino groups decreased to 2.7±1.1 $NH_2/nm^2$. After refluxing the mixture for 1 h, the number of detected amino groups corresponds to slightly more than a monolayer. An increase in reaction time to 12 h yielded a surface coverage of 4.2±0.5 $NH_2/nm^2$.

**Grafting reaction with 100 equiv. of acetic acid**

An excess amount of acetic acid (100 equiv.) resulted in monolayer deposition of APTES when the reaction stirred for 1 h at rt. Occasional precipitation was observed when the reaction was heated up, with detected numbers of aineo groups per surface area that are lower than those expected for a monolayer of organosilane.

**Mechanism of the acid-catalyzed hydrolysis and condensation reaction**

The experimental data confirm that acid-catalyzed hydrolysis and condensation reaction between silanol and alkoxysilane results in the formation of siloxane bonds. Since glacial acetic acid is very hygroscopic and attracts $H_2O$ molecules from the surroundings, traces of water are likely involved. A proposed mechanism of the acid-catalyzed hydrolysis and condensation is illustrated in Figure 4-5. The ethoxy group is rapidly protonated which creates a more electropositive silicon that results in a slow nucleophilic attack of a non-protonated water molecule. In this $S_N2$-Si type process, a pentacoordinate intermediate is formed with ethanol as the leaving group. The subsequent condensation step comprises of similar steps, where the silanol group is protonated rapidly, followed by a slow nucleophilic attack by a non-protonated silanol group from the colloid surface with water as the leaving group in an $S_N2$ type reaction.[134] Since the $S_N2$ type attack is a slow process, additional accelerators like heat or more acid are needed.

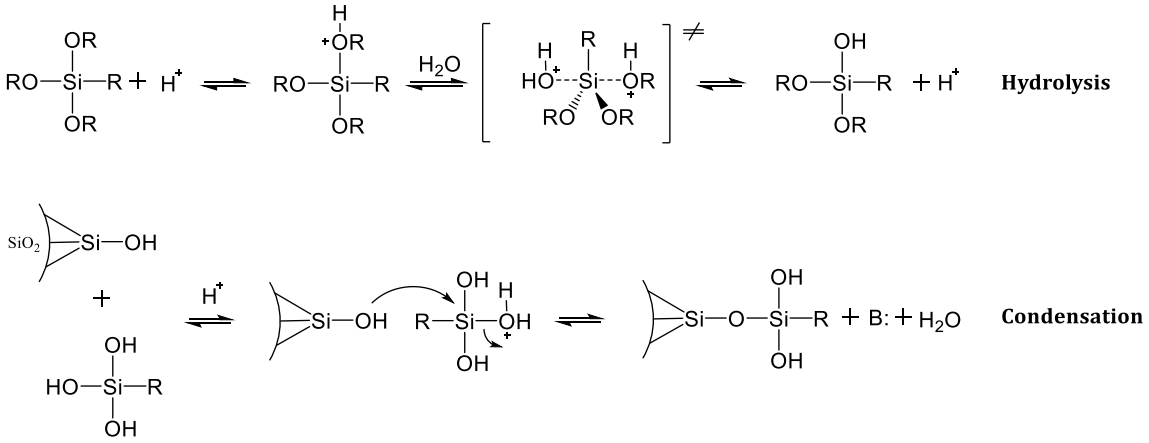


**FIGURE 4-5 SCHEMATIC ILLUSTRATION OF A PROPOSED ACID-CATALYZED HYDROLYSIS AND CONDENSATION MECHANISM OF A SILANE COUPLING AGENT.**

Therefore, higher numbers of amino groups per surface area are obtained when the mixture was refluxed instead of stirred at rt in the presence of 1 equiv. acetic acid, or when 100 equiv. of acetic acid were used at rt. When the mixtures with huge excess of acid were refluxed for 1 h or 12 hours, an increase in the hydrolysis and self-condensation of APTES-molecules might have occurred and resulted into an uncontrollable grafting of the surface. Presumably produced oligomeric chains inside in the solution can be removed during the purification step.

Similar to the results for the base-catalyzed synthesis, a monolayer was deposited onto the particle surface when the mixture was stirred for 1 h at 0 °C. The same explanation can be applied here that the hydrolysis of APTES is suppressed without influencing the formation of siloxane bonds.

**Summary**

Silica colloids can be grafted with APTES molecules in the presence of basic or acidic catalyst under different reaction conditions. For the surface grafting, an increase in reaction time, temperature, or the presence of catalyst enhances the surface functionalization. For further proceeding, it was concluded that the environmental and industrial friendly way to synthesize silica particles with one monolayer of APTES molecules, is the usage of slightly excess of APTES-molecules (5 equiv.), a $mol_{APTES}/mol_{TEA}$ ratio of 1, 75 °C reaction temperature, and 1 h reaction time. It could also be of interest to repeat these experiments with a temperature between rt and 75 °C and with shorter reaction periods to reduce

production costs. The results with the monolayer deposition at 0 °C and 1 h confirmed that the silica colloids embedded in wax can be successfully grafted with a monolayer of APTES.

## 4.2. FABRICATION OF PARTICLE-WAX COLLOIDOSOMES

The synthesis of silica Janus particles with metal semishells requires a step, in which the precursor particles are temporary partially masked. The strategy during this current investigation is to embed one silica hemisphere into wax, by creating so-called particle-wax colloidosomes. The accessible spheres are grafted with the coupling agent 3-aminopropyltriethoxysilane (APTES), and after dissolving the wax, the amine-functionalized area is coated with palladium (Pd) seeds, followed by a metal layer deposition onto the Pd-activated area (see Figure 4-6). The degree of the semishell coverage corresponds to the surface area that is unprotected during the masking step and is coated with APTES and Pd seeds. The fabrication protocol for colloidosomes of bare silica particles and wax was adapted from Hong et al.[33] and slightly modified. Hydrophilic particles were first dispersed in the aqueous phase, followed by the addition of wax. After the mixture was heated up, the wax melted, and the particles adsorbed at the liquid/liquid interface.[45] By lowering the temperature, the wax solidified providing a removable coating on one side of the particle, while leaving the other side open for modification with APTES (see Chapter 2.2.1).

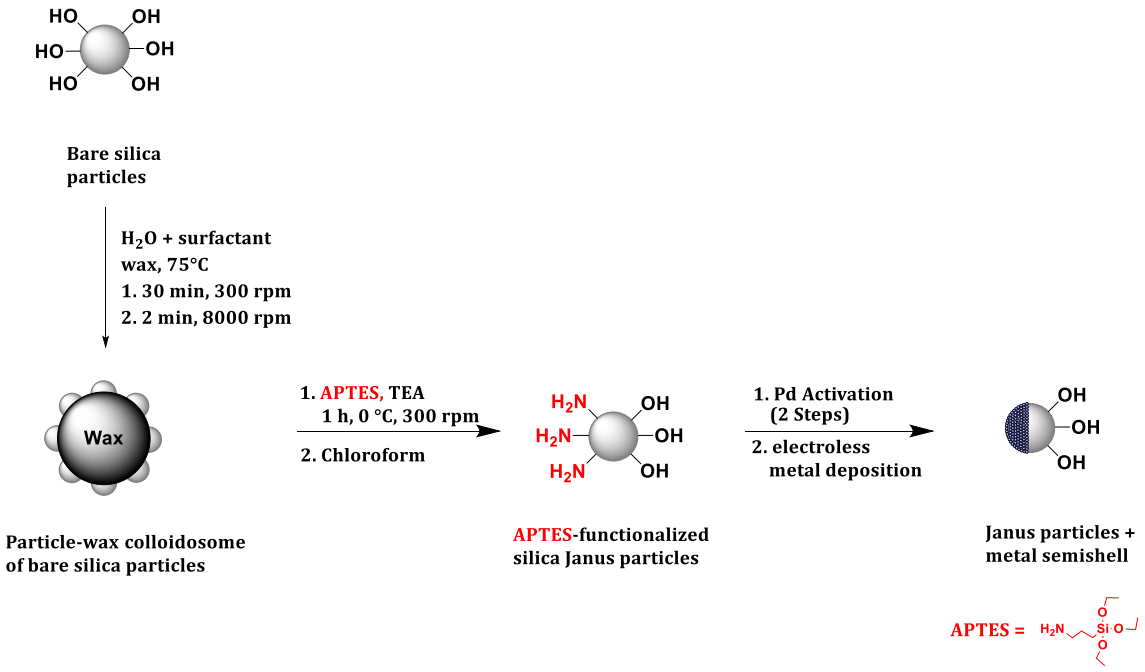


FIGURE 4-6 SCHEMATIC ILLUSTRATION OF THE STRATEGY FOR THE PREPARATION OF SILICA JANUS PARTICLES WITH A REGIO-SELECTIVE METAL COATING.

### 4.2.1. STATE OF THE ART

Based on the hydrophilic character of bare and non-functionalized silica particles, their penetration into the molten wax is limited. Hence, the number of particles being adsorbed at the wax surface is low. The small degree of penetration results in colloids where most of the silica surface area is accessible for surface modification. By increasing the penetration depth of the silica, the surface area for grafting can be decreased. The ratio of modified and non-modified areas on a colloid are referred to as the Janus balance.[135] An approach for increasing the penetration depth is the adsorption of a surfactant of opposite charge and with long alkyl chains on the colloid surface.[47-48] The deprotonated silanol groups at the silica surface adsorb onto the aqueous phase of the aqueous/oil interface. It has been reported that the penetration depth of particles into the molten wax can be controllably increased by the addition of different concentrations of didodecyldimethylammonium bromide (DDAB).[136] Hence, after the modification of the unprotected sphere, the surface area of the modified and the non-modified sphere respectively, can be predicted.[47] Perro et al. reported similar findings with a different surfactant, cetyltrimethylammonium bromide (CTAB).[48] Both research groups claimed that silica Janus particles down to 100-200 nm diameter could be produced in large quantities and with the well-controlled extension of the modification area of the silica surface.

Different characterization methods were applied to determine the Janus balance. Jiang et al. labeled several micrometer-sized particles with a fluorescent dye and observed them in fluorescence microscopy.[47] In the corresponding microscope image, asymmetric fluorescence emission profiles were detected according to which side of the colloid faced the light and the detector. Several complications such as the non-transparency of the particles; which side of the sphere is facing the laser; and the Brownian motion of the colloids resulted in a smeared optical image. Besides the challenges of the method itself, the colloids were analyzed in a conventional optical microscope, which is not suitable for submicron colloids. A different approach was the investigation of particle-wax colloidosomes in SEM. The size of the cavities, left by particles that have fallen off from the wax, were measured and so the so-called three-phase contact angle determined.[47] According

to the authors, the contact angle is a function of the DDAB concentration normalized by the critical micelle concentration (cmc). Experimental results showed that the investigation of the colloidosome surface in SEM is challenging because the electron beam can slowly alter the wax during the scanning process. However, when the colloidosomes are measured in a freeze-fracture, shadow-casting (FreSCa) cryo-scanning electron microscope, the wax surface is not compromised, and the contact angle can be obtained.[126] A different approach is to adsorb gold nanoparticles onto regio-selectively amine-functionalized spheres and observe the colloids in SEM.[48, 52] With this procedure, the ratio of grafted and non-grafted areas can be visualized. A statistical evaluation of surface coverage of several colloids can provide reliable information about the Janus balance, which was not provided in the study reported by Perro et al.[48]

Here, we present an extensive study of particle-wax colloidosomes synthesis while applying both surfactants (DDAB and CTAB). Their effects on wax coverage, penetration depth, and mass yields for Janus particles after the functionalization were investigated and compared. Several reaction conditions were tested, whereby the particles/solvent ratios and the surfactant concentrations were varied. We also introduced two characterization methods to determine the Janus balance (evaluation of SEM image and UV-Vis spectroscopy). In this context, the radius of gyration was calculated for each surfactant to determine the occupied surface area by the corresponding amount of the surfactant. The theoretical degree of occupancy is compared to the experimental findings to develop optimum reaction conditions for the fabrication of silica Janus particles.

### 4.2.2. USAGE OF DIDODECYLDIMETHYLAMMONIUM BROMIDE (DDAB)

Colloidosomes were fabricated using different particles/solvent ratios while varying the DDAB concentration. Subsequently, the unprotected silica spheres were grafted with APTES followed by dissolving the wax after filtration, and collecting the silica Janus particles as a powder. These collected particles were weighted and compared to the amount of the starting particles. The outcome of the silica Janus particles is referred to in the following as the mass yield. As mentioned above, only traces of particles were collected in the absence of surfactant because the majority of the colloids did not adsorb onto the wax surface and were removed during the purification step. The mass yields increased with the addition of DDAB until the mixture flocculated. Hence, it was concluded that the mass yield depends on the DDAB molecule density at the silica surface ($mol_{DDAB}/mol_{OH}$ in %) which is graphically illustrated in Figure 4-7.

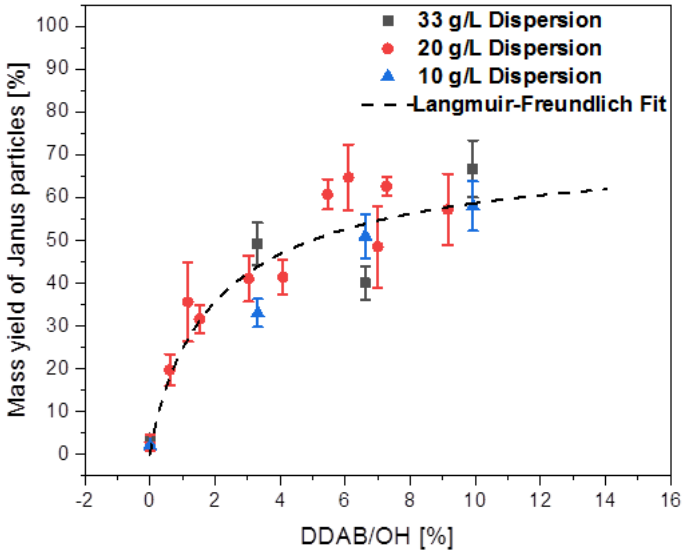


**FIGURE 4-7 MASS YIELD OF SILICA PARTICLES IN % DEPENDING ON THE $MOL_{DDAB}/MOL_{OH}$ RATIO FOR 33 G/L, 20 G/L, AND 10 G/L DISPERSION AND THE CORRESPONDING LANGMUIR-FREUNDLICH FIT.**

The highest yields (50—60 %) were obtained when the $mol_{DDAB}/mol_{OH}$ ratio was around 5—7 %, without any sign of flocculation of the molten wax and the particles. When the $mol_{DDAB}/mol_{OH}$ ratio was > 8 %, which also corresponds to the critical micelle concentration in this experimental setup (cmc = 0.05 mM),[137] the dispersion mixtures with particles concentration of 10 g/L and 20 g/L flocculated,

resulting in a clear supernatant. In the case of the concentrated dispersion (33 g/L), flocculation was already observed at a $mol_{DDAB}/mol_{OH}$ ratio of 3—4 %. In all three cases, the mass yield increased until saturation was reached. The increased number of DDAB molecules which are adsorbed onto the silica surface, influence the penetration depth into the wax, which results in an increase of the mass yield. The long alkyl chains of the surfactant are in continuous motion, and therefore, an increase in surfactant loading reduces the ability for further DDAB molecules to bind onto the surface. Instead, the additional molecules interact with one another and do not influence the mass yield. Since this phenomenon cannot be regarded as an ideal monolayer adsorption, the Langmuir isotherms[138] is not a suitable fit model. In the Langmuir model it is assumed that the adsorption occurs only at a fixed number of definite localized sites, that are identical and equivalent. It does not consider the lateral interaction and steric hindrance between adsorbed molecules.[139] However, the Freundlich model describes the non-ideal adsorption and is applicable for multilayer adsorption even on heterogeneous surfaces.[140] Consequently, the Langmuir-Freundlich isotherms fit was used to describe the adsorption (Equation (4-5)).

$$q = \frac{(Q_{sat} \cdot K \cdot c^n)}{(1 + K \cdot c^n)} = \frac{(73.2 \pm 46.8) \cdot (0.51 \pm 0.48) \cdot c^{(0.90 \pm 0.95)}}{(1 + (0.51 \pm 0.48) \cdot c^{(0.90 \pm 0.95)})}; R^2 = 0.872 \quad \textbf{(4-5)}$$

q = mass yield [%]; c = $mol_{DDAB}/mol_{OH}$ ratio, $Q_{sat}$ = saturation of mass yield (asymptote) [%]; K = coefficient; n = Freundlich exponent.

Although the adsorption does not reach a plateau according to the Langmuir-Freundlich model, the experimental data shows a saturation of the mass yield when the $mol_{DDAB}/mol_{OH}$ ratio is ~7 %. A further increase in the $mol_{DDAB}/mol_{OH}$ ratio did not increase the yield and but instead resulted in flocculation of the solution. The colloidosomes were collected and investigated in SEM. In this process four types of compositions were detected:

I. Single colloidosomes with a monolayer of closed-packed silica particles adsorbed at the wax surface;
II. Single colloidosomes and some colloidosome agglomerates, and some multilayers of silica particles adsorbed at the wax surface;

III. Large colloidosome agglomerates with multilayers of silica particles adsorbed at the wax surface;

IV. Wax coagulated into non-spherical structures with a multilayer of silica particles embedded at the surface.

Within the three different dispersions (10 g/L, 20 g/L, and 33 g/L), single colloidosomes with an adsorbed monolayer of closed-packed particles (composition I) were obtained when the $mol_{DDAB}/mol_{OH}$ ratio was < 4 % (see Figure 4-8).

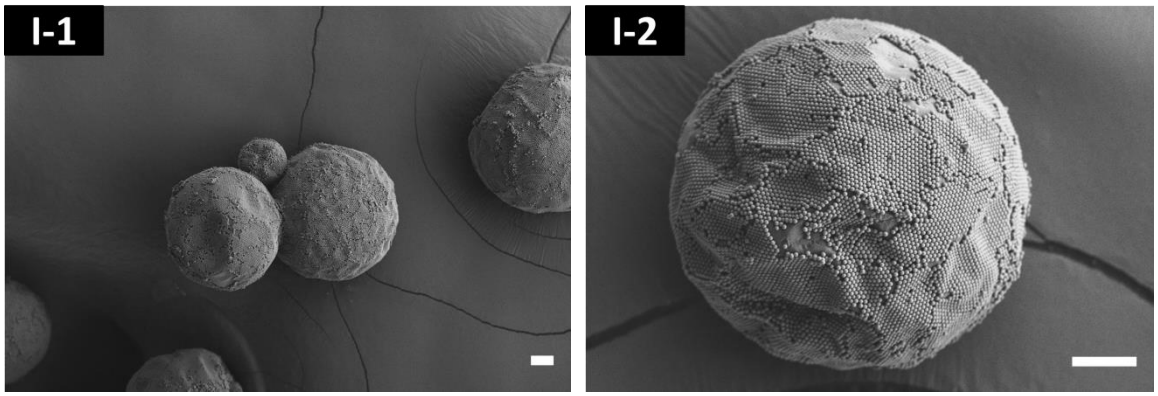


**FIGURE 4-8 SEM IMAGES OF SINGLE PARTICLE-WAX COLLOIDOSOMES WITH A MONOLAYER OF SILICA PARTICLES ADSORBED AT THE SURFACE, SCALE BAR = 10 µM.**

When the $mol_{DDAB}/mol_{OH}$ ratio was between 5—6 %, single colloidosomes and some colloidosome agglomerates were observed as well as occasional formation of the multilayer on top of the closed-packed layers of silica particles (composition II, Figure 4-9).

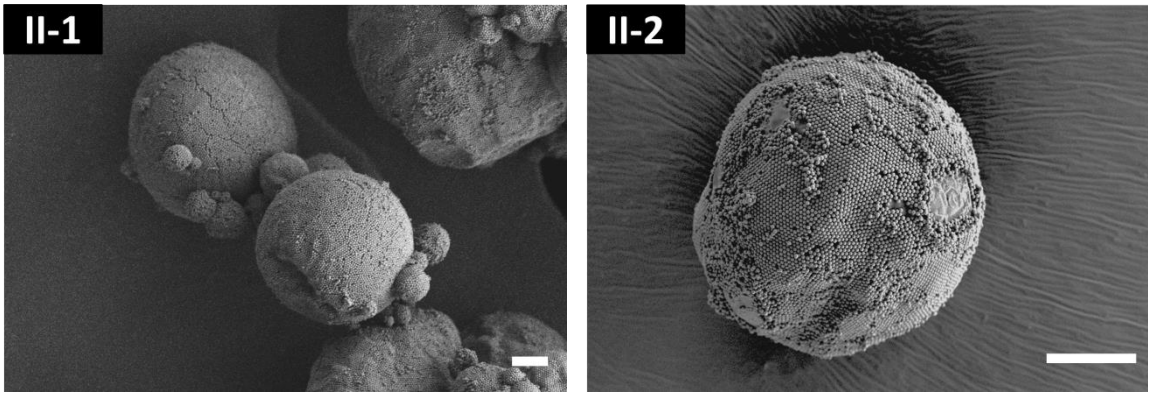


**FIGURE 4-9 SEM IMAGES OF COLLOIDOSOME AGGLOMERATES (II-1) AND MULTILAYER PF PARTICLES ADSORBED AT THE WAX SURFACE (II-2), SCALE BAR = 10 µM.**

When the $mol_{DDAB}/mol_{OH}$ ratio was > 6 %, large colloidosome agglomerates (Figure 4-10 III-1) with multilayers of silica particles (Figure 4-10 III-2) occurred for the dispersion of 10 g/L and 20 g/L (composition III). Non-spherical wax structures with embedded silica particles (Figure 4-10 IV-1 and IV-2) were generated in the concentrated dispersion (33 g/L, composition IV). The observed colloidosome compositions III and IV correspond to flocculated mixtures.

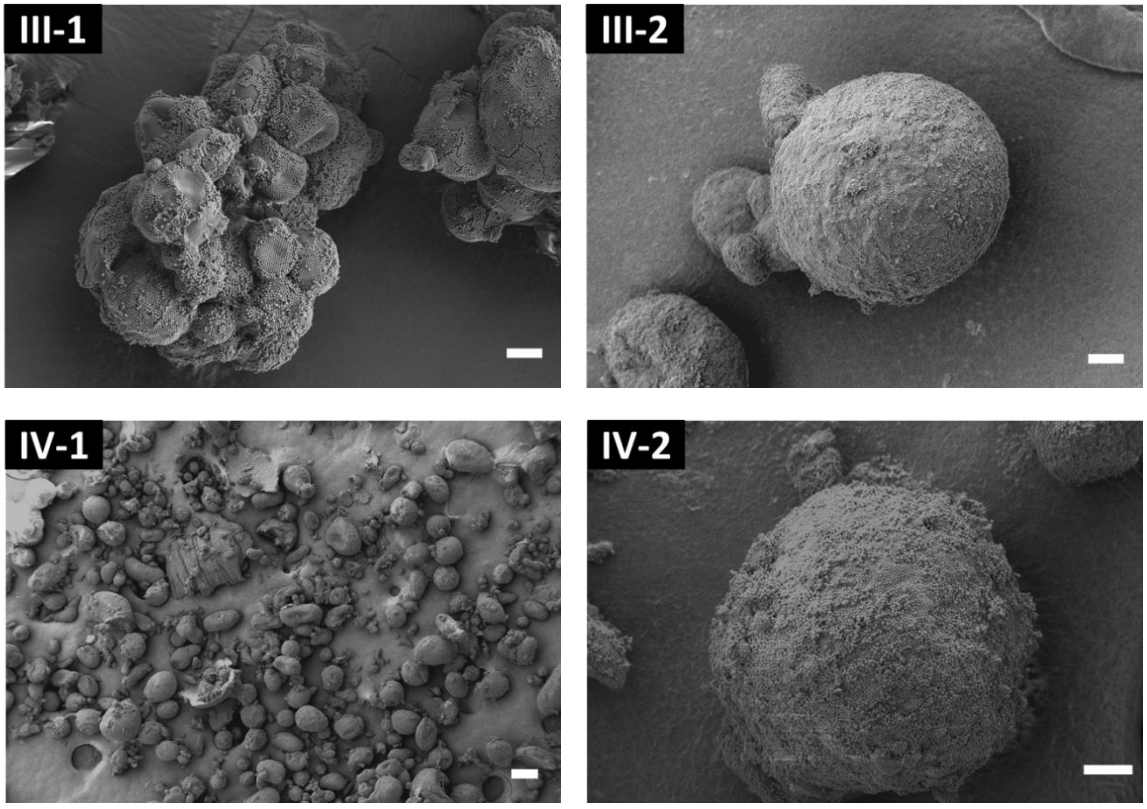


**FIGURE 4-10 SEM IMAGES OF LARGE COLLOIDOSOME AGGLOMERATES (III-1) WITH MULTILAYERS OF PARTICLES ADSORBED AT THE WAX SURFACE (III-2) AND NON-SPHERICAL PARTICLE-WAX STRUCTURES (IV-1) WITH MULTILAYERS OF PARTICLES (IV-2), SCALE BAR = 10 µM FOR III-1/-2 AND IV-2, SCALE BAR = 100 µM FOR IV-1.**

The experimental data demonstrate that the $mol_{DDAB}/mol_{OH}$ ratio has to be kept < 6 % to avoid colloidosome agglomerates and multilayers of silica particles. To better comprehend the impact of the DDAB amount on the penetration depth and the colloidosome stability, further investigations are necessary. In aqueous solution, the positively charged head of DDAB interacts electrostatically with the deprotonated silanol oxygen. The two long hydrocarbon chains are continuously in motion, and thus the distance between the terminal methyl groups can vary. The behavior of a single DDAB molecule was modeled in an aqueous medium, and the

distances between the terminal methyl moieties were monitored over time to calculate the area occupied by one DDAB molecule. Figure 4-11 DDAB-1 and DDAB-2 illustrate the maximum and minimum distance between the terminal methyl moieties.

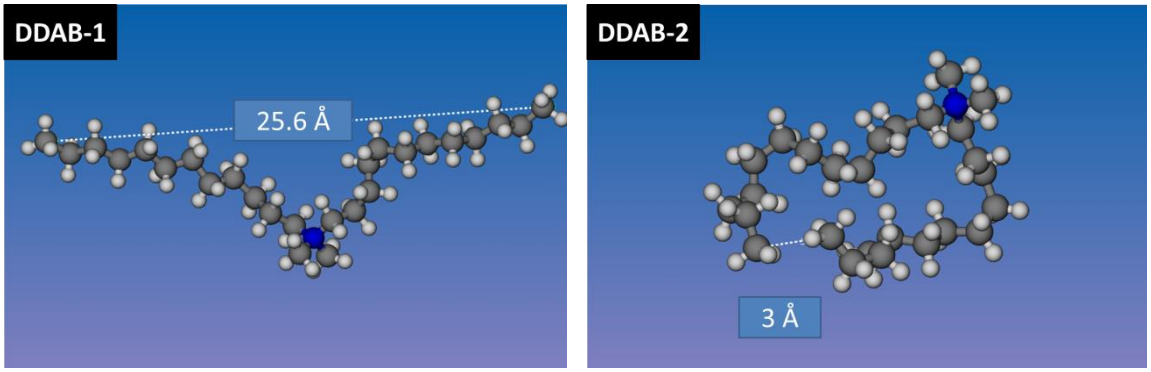


**FIGURE 4-11 ILLUSTRATION OF THEORETICAL MODELING OF A DDAB MOLECULE IN $H_2O$ WITH DDAB-1 THE MAXIMUM AND DDAB-2 THE MINIMUM DISTANCE BETWEEN THE TERMINAL METHYL MOIETIES.**

These calculations yield an average diameter distance between the two chains of 13.7±5.4 Å. Since the computed distance has a high standard deviation, another parameter was introduced to calculate the surface area occupied by one DDAB molecule. As an alternative, the radius of gyration was introduced that describes the distribution of the distances from the polymer chains to its center. Considering the mass momentum of inertia, it represents the perpendicular distance from the axis of rotation to a point mass that results in an equivalent inertia to the original object.[141] Although, it is usually applied to describe polymers moving freely in a solution and not for molecules that are electrostatically attached to a point (surface silanol group), it was used during this study to obtain an approximate value about the degree of occupancies by the surfactant molecule on the silica surface. Figure 4-12 illustrates the change of the radius of gyration with time.

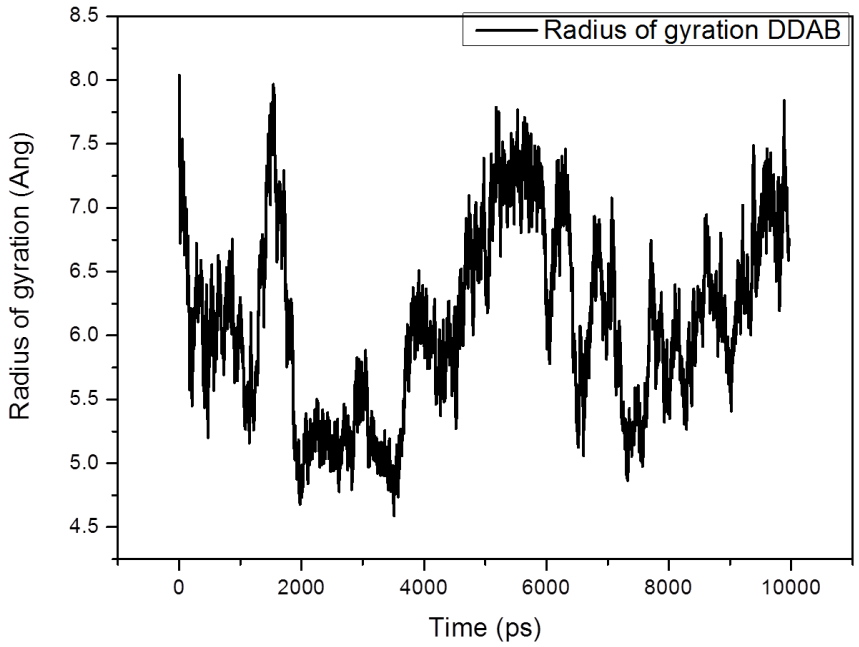


**FIGURE 4-12 THE RADIUS OF GYRATION OF A DDAB MOLECULE AS A FUNCTION OF TIME.**

The calculated radius of gyration is 6.1±0.7 Å, which is within the range of the calculated average distance between the terminal methyl groups and has a smaller standard deviation. Knowing the radius of gyration of DDAB, the potential area occupied by all DDAB molecules can be calculated which can be used to explain the effect of the surface concentration of the DDAB molecules on the surface silanol groups. Table 4-7 contains the sample data that were used for the calculations in Table 4-8. Here, the calculated surface areas occupied under different DDAB concentrations are summarized, when the final solvent amount was 15 mL. A detailed calculation is provided in Appendix II Calculations. The error margin of the surface coverage corresponds to the standard deviation of the radius of gyration and the error margin of the particle surface area.

**TABLE 4-7 SAMPLE DATA FOR THE CALCULATIONS PROVIDED IN TABLE 4-8**

| Sample information | Data |
|---|---|
| Mass of silica particles | 0.300±0.001g |
| Particle diameter | 549±31 nm |
| Particle total surface area | $1.6\pm0.5 \cdot 10^{17}$ nm$^2$ |
| Surface area occupied by 1 DDAB molecule | 4.7±1.1 nm$^2$ |

**TABLE 4-8 OVERVIEW OF THE RATIO OF THE SURFACE AREA OCCUPIED BY DDAB MOLECULES ($A_{All\ DDAB}$) DDAB TO THE SURFACE AREA OF ALL SILICA PARTICLES ($A_{All\ particle}$) ACCORDING TO DIFFERENT DDAB CONCENTRATIONS**

| DDAB conc. [mM] | Surface $A_{All\ DDAB}$ [$10^{18}$ nm$^2$] | Number $mol_{DDAB}$ / $mol_{OH}$ [%] | Surface ratio $A_{All\ DDAB}$ /$A_{All\ particle}$ [%] |
|---|---|---|---|
| 0 | 0 | 0 | 0 |
| 0.0037 | 0.2±0.0 | 0.5±0.1 | 10±5 |
| 0.0075 | 0.3±0.1 | 1.0±0.3 | 19±10 |
| 0.019 | 0.8±0.2 | 2.6±0.7 | 48±25 |
| 0.026 | 1.1±0.3 | 3.6±1.0 | 68±35 |
| 0.037 | 1.6±0.4 | 5.2±1.5 | 97±50 |
| 0.045 | 1.9±0.5 | 6.2±1.7 | 116±60 |
| 0.056 | 2.4±0.6 | 7.7±2.2 | 145±75 |

The calculated data confirm the experimental findings. The silica surface area coverage increases with elevated DDAB concentration up to a point when the surface is covered to around 97±50 %, when the $mol_{DDAB}/mol_{OH}$ ratio is 5.2±1.5 %. With an increasing amount of DDAB, the surface charge on the silica particles changes from negative to neutral or even positive.[142] This weakens the electrostatic repulsion between adjacent particles and results in a closed-packed silica monolayer at the wax surface, which is observed in SEM (see Figure 4-8) and therefore, causes higher mass yields of the silica Janus particles. Once the $mol_{DDAB}/mol_{OH}$ ratio exceeds > 6 %, the silica surface is over-saturated (116±60 %) and multilayers are starting to form, according to the calculations. The created hydrophobic colloids can attract each other in the aqueous phase through the hydrocarbon chains,[143] which can explain the detection of some particle agglomerates or multilayers at the surface (see Figure 4-9). At the $mol_{DDAB}/mol_{OH}$ ratio of 7.7±2.2 %, which is around the critical micelle concentration (cmc = 0.05 mM),[137] the silica surface is covered up to 145±75 % with molecules, according to the calculations. Generally, around the cmc, DDAB molecules self-assemble to bilayers, spherical, or cylindrical micelles through the interaction of the hydrophobic chains.[144] The terminal surfactant head contributes to a positively

charged colloid, which can interact with deprotonated silanol groups of other colloids, causing an agglomeration of the composites. These self-assembled molecules can also electrostatically interact with deprotonated silanol groups resulting in new hybrid nanostructures. These composites can have a decreased mobility and a decreased conductivity inside the solution, or can form colloidal aggregations. Besides exceeding the cmc, when the silica surface is oversaturated with DDAB molecules, the colloids can self-assemble to aggregated structures. In conclusion, single colloidosomes with monolayer deposition of closed-packed silica particles were successfully fabricated when the $mol_{DDAB}/mol_{OH}$ ratio was kept < 5 % (< 0.037 mM DDAB).

In the next section, the influence of DDAB on the penetration depth of the silica particles into the wax was investigated. During the sample preparation for SEM, a thin film of iridium was sputtered on the colloidosomes. Due to the possible development of heat inside the sputtering chamber, the wax surface could have been altered. Inside the microscope, the electron beam can also have an influence on the wax surface. Since a cryo-SEM was not available; the direct investigation of the penetration depth of particles into wax was not conclusive. Consequently, two indirect methods were utilized to investigate the Janus balance: 1) measuring the coverage degree of metal shell coatings from SEM images; and 2) calculating the amine density at the silica surface using UV-Vis spectroscopy.

**Measuring the metal shell coverage in SEM**

After the colloidosomes had been prepared, the unmasked sides of the spheres were grafted with APTES, the wax was dissolved, and the collected silica Janus particles were coated with palladium (Pd) seeds, which only interacted with the amine-functionalized parts of the spheres (see detailed description in Chapter 4.3.1). Then, a metal layer was electrolessly deposited onto the Pd-activated areas (see Chapter 4.3.2). The silica Janus particles with metal semishells were observed in SEM, and the results for all obtained coverage degrees are summarized in Table 4-9. For measuring the coverage, only metal-coated particles were considered where the non-coated area faced the electron beam. The diameter of the ring opening was measured and converted into the coverage degree of the colloid according to the calculation for a spherical cap (see Chapter 3.1). The error margin

relates to the different calculated shell coverages within one specimen and reflects here the reproducibility of the so-called Janus balance. The standard deviation of the particle diameter was not considered. The values for the degree of shell coverage and the error margin correspond to at least 100 measured particles.

**TABLE 4-9 OVERVIEW OF CALCULATED METAL SHELL COVERAGE OF JANUS PARTICLES IN % AT DIFFERENT DDAB CONCENTRATIONS.**

| Sample | DDAB conc. [mM] | Number $Mol_{DDAB}/mol_{OH}$ [%] | Surface ratio $A_{All\ DDAB}/A_{All\ particle}$ [%] | Shell coverage of particle [%] |
|---|---|---|---|---|
| DDAB-3 | 0 | 0 | 0 | 86±13 |
| DDAB-4 | 0.0094 | 1.4±0.4 | 26±1 | 64±16 |
| DDAB-5 | 0.037 | 5.2±1.5 | 97±5 | 69±16 |
| DDAB-6 | 0.056 | 7.7±2.2 | 145±7 | 60±13 |

In the absence of surfactant, silica Janus particles with a shell coverage of 86±13 % were observed (DDAB-3). Once DDAB was introduced, the shell coverages decreased to 64±16 %, 69±16 %, or 60±13 % without any correlation to the different $mol_{DDAB}/mol_{OH}$ ratios. Additionally, within one specimen, the number of the measured coverage degrees scatters strongly. The SEM image in Figure 4-13 DDAB-4 represents silica Janus particles with copper (Cu) shells that were fabricated when the $mol_{DDAB}/mol_{OH}$ ratio was 1.4±0.4 %. DDAB-6 represents silica Janus particles with gold shells where the corresponding colloidosomes were prepared with a $mol_{DDAB}/mol_{OH}$ ratio of 7.7±2.2 %. In both images, Janus halfshells (particles labeled as "1") as well as nanocups (2/3-shells, particles labeled as "2") were obtained. Particles with almost closed shells (particles labeled as "3") were also detected, and occasionally nanocaps (1/3-shells, particles labeled as "4) were found, which probably were fallen off the particles due to the high mass of the metal (see Figure 2-6 definition shell types). There was no difference between the specimens although different $mol_{DDAB}/mol_{OH}$ ratios were used and two different metals were deposited.

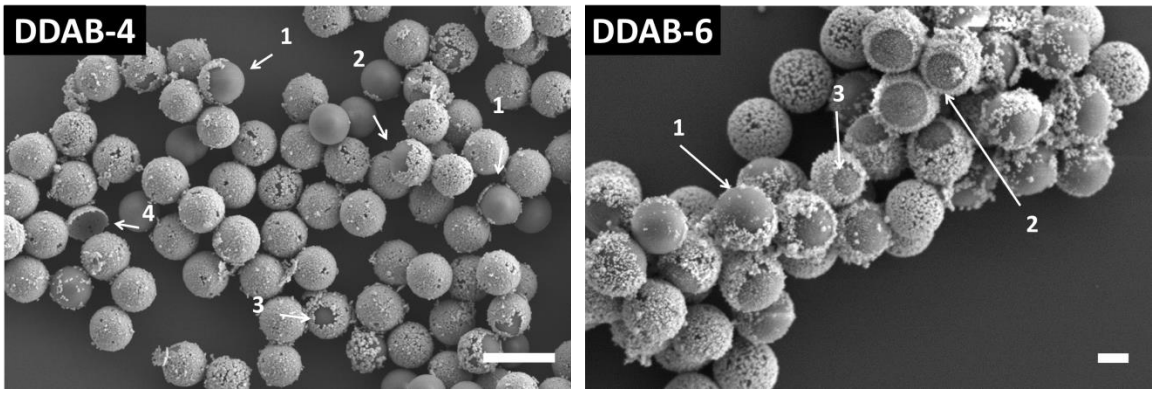


**FIGURE 4-13 SEM IMAGES OF SILICA JANUS PARTICLES WITH DDAB-4) COPPER SHELL IN THE PRESENCE OF 0.0094 MM DDAB, SCALE BAR = 1 µM AND DDAB-6) GOLD SHELL IN THE PRESENCE OF 0.056 MM DDAB, SCALE BAR = 300 NM.**

The results from SEM demonstrate that even a small $mol_{DDAB}/mol_{OH}$ ratio increases the penetration of the silica particles into the wax and consequently results in a reduction of the metal surface coverage degree from 86±13 % to around 64±15 %, but the Janus balance cannot be controlled with different $mol_{DDAB}/mol_{OH}$ ratios. Rodríguez-Fernández et al. observed a decrease in the degree of gold shell coverage in SEM with increasing DDAB concentration[52] whereby only few samples were shown.

### Determining the amine surface density in UV-Vis

In a second approach, the density of amino groups at the surface was determined using the earlier described ninhydrin assay (see Chapter 4.1.3.2).[82] Colloidosomes were fabricated using four different $mol_{DDAB}/mol_{OH}$ ratios, and for comparison, fully APTES-functionalized silica particles (Full-$NH_2$) were synthesized using the same reaction conditions as applied for the functionalization of the colloidosomes (reaction temperature: 0 °C, reaction time: 1 h). Since without DDAB, only traces of functionalized Janus particles were collected, the determination of the number of amino groups per surface area was not possible in this case. The results are presented in Table 4-10, and the error margin for the calculated amine density contains the error margin for the calculated number of amino groups from UV-Vis spectroscopy as well as the error margin for the silica particle surface area. The number of $NH_2/nm^2$ is converted into a degree of surface coverage, using the Full-$NH_2$ case as a reference.

**TABLE 4-10 OVERVIEW OF THE OBTAINED NUMBER OF AMINO GROUPS PER NM² ON SILICA JANUS PARTICLES, WHEN DDAB WAS USED AS SURFACTANT**

| Sample | DDAB conc. [mM] | Number $mol_{DDAB}/mol_{OH}$ [%] | Surface ratio $A_{All\ DDAB}/A_{All\ particle}$ [%] | Amine density [$NH_2/nm^2$] | Coverage of particle [%] |
|---|---|---|---|---|---|
| DDAB-7 | 0.0037 | 0.5±0.0 | 10±2 | 2.1±0.9 | 35±30 |
| DDAB-8 | 0.019 | 2.6±0.0 | 48±12 | 2.0±0.9 | 33±29 |
| DDAB-9 | 0.037 | 5.2±0.0 | 99±25 | 2.5±1.0 | 42±34 |
| DDAB-10 | 0.044 | 6.2±0.0 | 116±30 | 1.8±1.1 | 30±31 |
| Full-$NH_2$ | – | – | – | 6.0±2.5 | 100 |

When the colloidosomes were fabricated with a $mol_{DDAB}/mol_{OH}$ ratio of 0.5±0.0 % (DDAB-7), the resulting silica Janus particles had an amine density of 2.1±0.9 $NH_2/nm^2$ (corresponding to 35±30 % coverage). No significant changes were detected with increasing $mol_{DDAB}/mol_{OH}$ ratio. The overall number of amino groups is around 2.1±1 $NH_2/nm^2$, which corresponds to a 35±31 % surface coverage. The silica colloids in the Full-$NH_2$ sample carry 6.0±2.5 $NH_2/nm^2$ (100 %), which is more than one monolayer, assuming a sphere with a density of 4 or 5 $NH_2$ groups/$nm^2$. The surface of the reference contains around three times more amino groups than the Janus samples. The average coverage degree obtained from the ninhydrin assay is lower than the average metal shell coverage number (64±15 %). A reason could be the obtained high amine density for the reference itself. If one assumes a surface density of 4 $NH_2$ groups/$nm^2$ as reference, the coverage would be 53±25 %, which is closer to the average metal shell coverage number. It can be reasoned that the calculated coverage degree for the amine density is an indirect method and highly depends on the reference. Consequently, when the reference number is too high, the final result can be inaccurate.

In general, these results confirm the data from the shell coverage degree measurements, that the Janus balance cannot be predicted and controlled by using different DDAB concentrations, in contrary to literature claims.[47, 52] In the case of Jiang et al., bare silica particles were first dispersed in the molten wax, and then

added the aqueous surfactant, which created a water-in-oil emulsion,[47] rather than an oil-in-water emulsion. Additionally, the characterization methods they used are not applicable for these present studies colloids (three-phase contact angle, fluorescence microscopy), what complicates the comparison.

It can be summarized that in the presence of DDAB, colloidosomes are fabricated where the silica colloids penetrate deeper into the wax. Single colloidosomes with monolayer deposition of closed-packed particles were obtained when the $mol_{DDAB}/mol_{OH}$ ratio was ~5 % with high mass yields for silica Janus particles (~50 %). The radius of gyration of DDAB provided information about the area occupied by all DDAB molecules involved in the reaction, and the theoretical model confirmed experimental findings. Two methods were introduced to quantify the Janus balance of the particles, and both yield similar degrees of covered spheres when the reference for the amine density was adjusted (53±25 % amine density and 64±15 % metal shell coverage). However, neither the investigation of the coverage degree of the metal shells nor the amine group determination provided evidence of a synthesis providing a controllable or predictable Janus balance.

### 4.2.3. USAGE OF CETYLTRIMETHYLAMMONIUM BROMIDE (CTAB)

In the following section, the effects of CTAB on the fabrication of colloidosomes and the Janus balance are examined. Colloidosomes were prepared from silica particles dispersion batches (10 g/L and 20 g/L) with different $mol_{CTAB}/mol_{OH}$ ratios. Similar to the DDAB results, the mass yields increased with the increasing addition of CTAB until the mixture flocculated. The corresponding graph is shown in Figure 4-14.

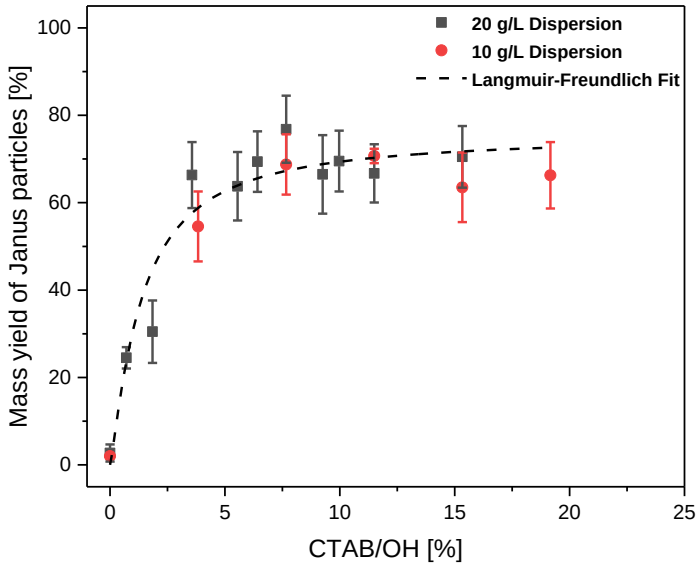


**FIGURE 4-14 MASS YIELD OF SILICA PARTICLES AS A FUNCTION OF THE $MOL_{CTAB}/MOL_{OH}$ RATIO FOR DISPERSION OF SILICA CONCENTRATIONS OF 20 G/L AND 10 G/L AND THE CORRESPONDING LANGMUIR-FREUNDLICH FIT.**

High mass yields (60—70 %) are obtained around the $mol_{CTAB}/mol_{OH}$ ratio of 5—8 %. When the CTAB number is > 9 %, both dispersion mixtures (10 g/L and 20 g/L) showed signs of flocculation of wax and particles. Similar to the DDAB curve (see Figure 4-7), the mass yields of the particles reache saturation when the $mol_{CTAB}/mol_{OH}$ ratio exceeds > 8 %. Although there should be no plateau in the adsorption model according to the Langmuir-Freundlich isotherm, the colloidal stability is compromised after a certain surfactant loading. The corresponding isotherm fit is proved in Equation (4-6)):

$$q = \frac{(Q_{sat} \cdot K \cdot c^n)}{(1 + K \cdot c^n)} = \frac{(75.5 \pm 15.4 \cdot (0.69 \pm 0.42) \cdot c^{(1.22 \pm 0.88)}}{(1 + (0.69 \pm 0.42) \cdot c^{1.22 \pm 0.88})} ; R^2 = 0.957 \quad \textbf{(4-6)}$$

q = mass yield [%]; c = $mol_{CTAB}/mol_{OH}$ ratio, $Q_{sat}$ = saturation of mass yield (asymptote) [%]; K = coefficient; n = Freundlich exponent.

The corresponding colloidosomes were investigated in SEM and four different samples are presented in Figure 4-15.

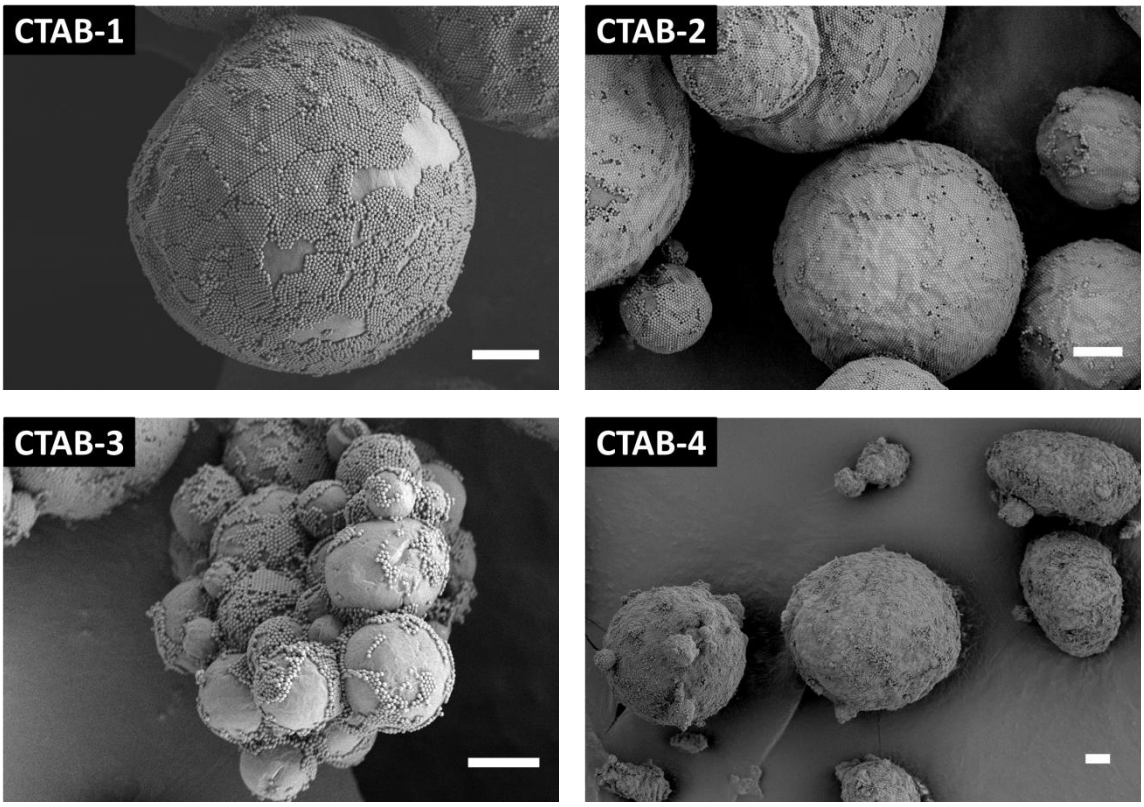


**FIGURE 4-15 SEM IMAGES OF CTAB-1) A SINGLE COLLOIDOSOME WITH A MONOLAYER OF SILICA AT THE SURFACE (CTAB RATIO < 4 %); CTAB-2) SINGLE COLLOIDOSOMES WITH CLOSED-PACKED MONOLAYER OF SILICA AT THE SURFACE (CTAB RATIO 5—8 %); CTAB-3) IRREGULAR COLLOIDOSOME CLUSTERS WITH FEW MULTILAYERS OF SILICA AT THE SURFACE (CTAB RATIO ~10 %); AND CTAB-4) COLLOIDOSOMES AGGLOMERATES WITH CLOSED-PACKED MULTILAYERS OF SILICA AT THE SURFACE (CTAB RATIO > 15 %), SCALE BAR = 10 µM.**

The addition of small amounts of CTAB ($mol_{CTAB}/mol_{OH}$ ratio < 4 %) resulted in single colloidosomes with a monolayer of silica particles at the wax surface (Figure 4-15 CTAB-1). When the CTAB amount was increased to a $mol_{CTAB}/mol_{OH}$ ratio of 5—7 %, the monolayer of silica particles appeared like a closed-packed film, while the colloidosomes show no sign of agglomeration (Figure 4-15 CTAB-2). The same explanation for the closed-packed silica monolayer as for DDAB can be applied

when dealing with CTAB as a surfactant. With an increased number of CTAB molecules interacting with silica, the surface becomes neutral, hence the repulsion between neighboring particles is weakened.[47] When the $mol_{CTAB}/mol_{OH}$ ratio is in the order of 10 %, colloidosome agglomerates were detected with occasional multilayers at the surface (Figure 4-15 CTAB-3). In the case of CTAB ratio > 15 %, the multilayers are closed-packed, and some colloidosomes are deformed (Figure 4-15 CTAB-4).

The behavior of one CTAB molecule was modeled in an aqueous medium, and the distances between the terminal methyl group and the silicon atom were monitored over time. The images of their maximum and minimum distance between the terminal moieties are illustrated in Figure 4-16.

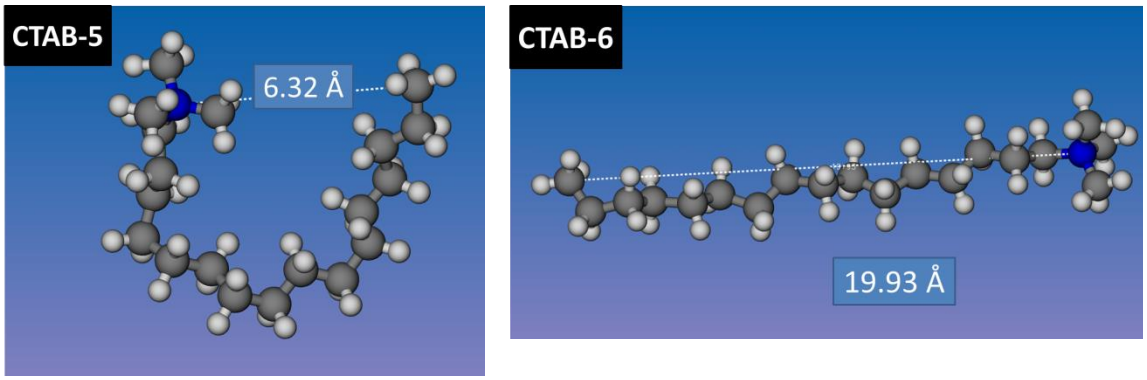


**FIGURE 4-16 ILLUSTRATION OF THEORETICAL MODELING OF A CTAB MOLECULE IN $H_2O$ WITH CTAB-5) THE MINIMUM AND CTAB-6) THE MAXIMUM DISTANCE BETWEEN THE TERMINAL METHYL GROUP AND SILICON.**

As described in the section dealing with DDAB (see Chapter 4.2.2), the radius of gyration for CTAB was determined as a function of time in ps (see Figure 4-17).

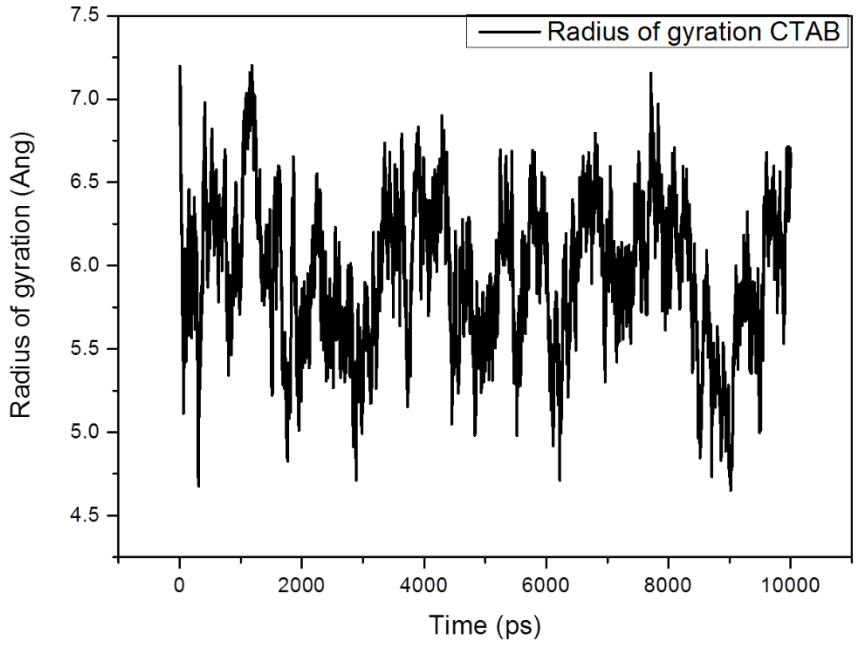


**FIGURE 4-17 RADIUS OF GYRATION OF A CTAB MOLECULE AS A FUNCTION OF TIME.**

The calculated radius of gyration of CTAB is 5.9±0.4 Å, and hence the area occupied by one molecule can be determined. Table 4-11 provides all the data needed for the calculations of the estimated surface areas occupied under different CTAB concentrations, with a final amount of solvent of 30 mL, which is summarized in Table 4-12.

**TABLE 4-11 SAMPLE DATA FOR THE CALCULATIONS PROVIDED IN TABLE 4-12**

| Sample information | Data |
|---|---|
| Mass of silica particles | 0.300±0.001g |
| Particle diameter | 586±39 nm |
| Particle total surface area | $1.5\pm0.5 \cdot 10^{17}$ nm$^2$ |
| Surface area occupied by 1 CTAB molecule | 4.4±0.6 nm$^2$ |

**TABLE 4-12 OVERVIEW OF THE RATIO OF THE SURFACE AREA OCCUPIED BY CTAB MOLECULES ($A_{All\ CTAB}$) CTAB TO THE SURFACE AREA OF ALL SILICA PARTICLES ($A_{All\ particle}$) ACCORDING TO DIFFERENT CTAB CONCENTRATIONS**

| CTAB conc. [µM] | Surface $A_{All\ CTAB}$ [$10^{18}$ nm$^2$] | Number $Mol_{CTAB}/mol_{OH}$ [%] | Surface ratio $A_{All\ CTAB}/A_{All\ particle}$ [%] |
|---|---|---|---|
| 0 | 0 | 0 | 0 |
| 2.38 | 0.2±0.3 | 0.7±0.2 | 12±6 |
| 5.95 | 0.5±0.7 | 1.8±0.6 | 31±15 |
| 11.89 | 1.0±1.3 | 3.6±1.2 | 62±29 |
| 17.84 | 1.4±0.2 | 5.2±1.7 | 93±44 |
| 21.40 | 1.7±0.2 | 6.3±2.1 | 112±52 |
| 23.78 | 1.9±0.3 | 7.0±2.3 | 124±58 |
| 29.73 | 2.4±0.3 | 8.7±2.9 | 155±73 |
| 33.29 | 2.7±0.4 | 9.8±3.1 | 174±82 |
| 35.67 | 2.9±0.4 | 10.5±3.5 | 186±87 |
| 47.56 | 3.8±0.5 | 14.0±4.6 | 248±117 |

The experimental findings and the theoretical calculation are in good agreement. When the $mol_{CTAB}/mol_{OH}$ ratio is 3.6±1.2 %, the surface is covered 62±29 % with CTAB, according to the calculations, which result in single colloidosomes with a monolayer of silica particles at the surface (see Figure 4-15 CTAB-1). Between the $mol_{CTAB}/mol_{OH}$ ratios of 5—7 %, the surface is entirely covered by CTAB molecules (93—124 %, respectively), assuming that multilayers are formed once the surface is occupied with a monolayer of molecules. Consequently, the negatively charged silica surface is neutralized, the repulsion between adjacent particles is weakened, and additionally hydrophobic particle-surfactant composites attract each other in aqueous phase caused by the hydrophobic effect of the hydrocarbon chains,[143] which result in single colloidosomes with a closed-packed silica layer at the surface (Figure 4-15 CTAB-2).

When the ratio is > 8 %, the silica surface is over-saturated with CTAB, according to the calculations. The additional molecules can either interacting with the silica

surface and form bilayers, or they can interact with other CTAB molecules in the aqueous phase. Above the ratio of 10 %, the CTAB molecules can theoretically cover twice the area of the silica surface (186±87 %), which can lead to bilayer formation as illustrated in Figure 4-18. The negatively charged silica surface electrostatically interacts with the hydrophilic head; the two hydrophobic tails attract one another in aqueous solution; leaving a hydrophilic head at the outer layer.[137] Similar to DDAB, these self-assembled nanocomposites affect the mobility and the conductivity inside the solution, and can form agglomeration clusters, which were observed in SEM (see Figure 4-15 CTA-3 and CTAB-4). Bilayer formations usually occur above the cmc = 0.09 mM[137] therefore, it is recommended to keep the surfactant concentration is below cmc/5, when preparing a stable molten wax-in-water emulsion.[145]

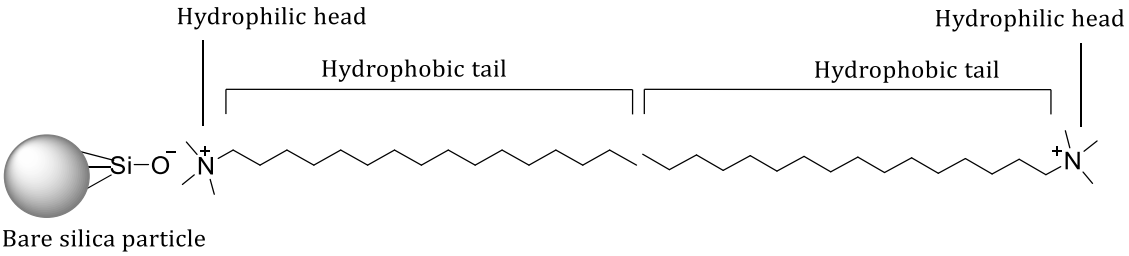


**FIGURE 4-18 SCHEMATIC ILLUSTRATION OF A BILAYER FORMATION OF CTAB MOLECULES ON BARE SILICA PARTICLE SURFACE IN AQUEOUS SOLUTION.**

During the studies of Giermanska-Kahn et al., silica-particles colloidosomes were prepared in the presence of CTAB. The surfactant concentration was calculated so that one CTAB molecule requires 13 $nm^2$ of the surface of the silica particle, assuming that all the surfactants from the bulk were employed to cover the silica surface.[50a] Relating this occupancy to experiments in this present study, it corresponds to a $mol_{CTAB}/mol_{OH}$ ratio of 1.9±0.6 %. According to the Equation (4-6), this would lead to a mass yield of 44 %, which is too low for this present study. Since they aimed to prepare kinetically stable emulsion droplets and not to increase the mass yield of the Janus particles, a 13 $nm^2$ occupancy area for one CTAB molecule is reasonable.

### Measuring the metal shell coverage in SEM

In the next step, the influence on the penetration depth into the wax with different CTAB amounts was investigated using the same methods as for DDAB. The silica Janus particles with metal shells were observed in SEM, and the results for all obtained coverages are shown in Table 4-13. Regardless of the deposited metal (gold or copper) and of the $mol_{CTAB}/mol_{OH}$ ratio, the silica Janus particles were covered to between 69±15 % and 66±16 % with the deposited metal layer for the sample CTAB-8 to CTAB-11, respectively. These samples show 16—20 % less metal coverage in comparison to sample CTAB-7, where no surfactant was involved (86±13 %). The average degree of shell coverage of the Janus samples is 68±17 %, which is similar to the results with different DDAB ratios (64±15 %).

**TABLE 4-13 OVERVIEW OF THE CALCULATED METAL SHELL COVERAGE OF JANUS PARTICLES IN % FROM SEM IN THE PRESENCE OF DIFFERENT CTAB CONCENTRATIONS.**

| Sample | CTAB conc. [µmol] | Number $mol_{CTAB}/mol_{OH}$ [%] | Surface ratio $A_{All\ CTAB}/A_{All\ particle}$ [%] | Shell coverage of particle [%] |
|---|---|---|---|---|
| **CTAB-7** | 0 | 0 | 0 | 86±13 |
| **CTAB-8** | 0.036 | 4±0 | 63±9 | 69±15 |
| **CTAB-9** | 0.071 | 7±0 | 126±19 | 70±16 |
| **CTAB-10** | 1.07 | 11±0 | 190±28 | 65±19 |
| **CTAB-11** | 1.43 | 14±0 | 253±37 | 66±16 |

Exemplary SEM images are shown in Figure 4-19 (CTAB-11 a and b), where metal layers consisting of a) gold and b) copper were deposited onto silica Janus spheres decorated with Pd seeds. Halfshells (particles labeled as “1”), nanocups (2/3-shells, particles labeled as “2”), and ¾-shells (particles labeled as “3") can be observed. When Perro et al. reported the preparation of partciles with a controllable Janus balance,[48] they only presented single particles coated with gold nanoparticles. However, in the present study, the statistical data demonstrated a broad distribution of degrees of shell coverages.

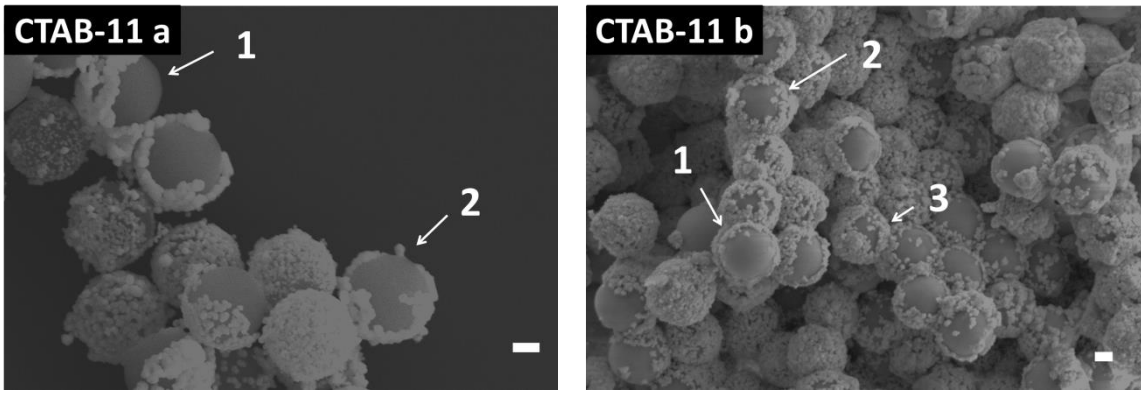


FIGURE 4-19 SEM IMAGES OF SILICA JANUS PARTICLES WITH (CTAB-11 A) GOLD SHELLS IN THE PRESENCE OF 1.43 µM CTAB AND WITH (CTAB-11 B) COPPER SHELL IN THE PRESENCE OF 1.43 µM CTAB, SCALE BAR = 200 NM.

### Determining the amine surface density in UV-Vis

Colloidosomes were fabricated using three different concentrations of CTAB. After the colloids were functionalized with APTES, the amino groups on the surface were quantified using the previously mentioned ninhydrin assay.[82] As a reference, fully APTES-functionalized silica particles were synthesized, using the same reaction conditions. The case where no CTAB is present could not be quantitatively analyzed, since only traces of functionalized Janus particles were collected. The results are presented in Table 4-14. The number of $NH_2/nm^2$ is converted into a degree of surface coverage using the obtained numbers for fully APTES-functionalized particles (Full-$NH_2$) as reference.

TABLE 4-14 OVERVIEW OF THE OBTAINED NUMBERS OF AMINO GROUPS PER $NM^2$ ON SILICA JANUS PARTICLES, WHEN CTAB WAS USED AS SURFACTANT

| | CTAB conc. [µM] | Number $mol_{CTAB}$ / $mol_{OH}$ [%] | Surface ratio $A_{All\ CTAB}$ / $A_{All\ particle}$ [%] | Amine density [$NH_2/nm^2$] | Coverage of particle [%] |
|---|---|---|---|---|---|
| **CTAB-12** | 0.07 | 0.7±0.2 | 12±2 | 3.1±1.5 | 52±47 |
| **CTAB-13** | 0.36 | 3.2±1.2 | 62±9 | 3.7±1.7 | 62±54 |
| **CTAB-14** | 0.64 | 5.8±2.1 | 112±16 | 3.5±1.6 | 58±51 |
| **Full-$NH_2$** | – | – | – | 6.0±2.5 | 100 |

Silica Janus particles with an amine density of 3.1±1.5 $NH_2/nm^2$ (52±47 %) were synthesized when the $mol_{CTAB}/mol_{OH}$ ratio during the colloidosome fabrication was 0.7±0.2 %. A further increase of the $mol_{CTAB}/mol_{OH}$ ratio did not affect the number of amino groups on the surface. The overall amine density was ~3.4±1.6 $NH_2/nm^2$, which corresponds to a coverage degree of 57±50 %. This number is slightly lower than the coverage degree for the metal shells (68±17 %) and similar to the results obtained for DDAB, a reason for this observation can be the reference itself. If instead of choosing a surface density of 6 $NH_2/nm^2$, an amine coverage of 5 $NH_2$ groups/$nm^2$ is used a reference, the overall density is 67±32 %. Another reason for the differences can be that the metal layers grow slightly beyond the Pd-seeds coated areas.[59] The experimental results support the previous finding that the Janus balance cannot be controlled with different CTAB concentrations.

Similar to the DDAB results, it can be summarized that in the presence of CTAB, the penetration depth of silica colloids into the molten wax can be increased. Single colloidosomes with monolayer deposition of closed-packed particles and high mass yields (~60 %) were obtained when the $mol_{CTAB}/mol_{OH}$ ratio was 4—6 %. The calculation of the degree of occupancies from the radius of gyration supports the experimental findings and allows the estimation of the concentration when the surface is over-saturated with CTAB molecules, and hence, results in the formation of large clusters of colloidosomes. Neither the investigation of the degree of shell coverage on the Janus particles nor the determination of the amine group surface density provided evidence that the Janus balance of the particles can be controllably or predictably tuned.

**Conclusion**

Silica Janus particles consisting of partially amine-functionalized spheres were successfully synthesized with high mass yields when the surfactants DDAB or CTAB were present during the preparation of the colloidosomes. For the first time, calculations were made using the radius of gyration as a parameter to calculate the area of occupancy of surfactant molecules on the particle surface. Using the radius of gyration, it will be possible to manufacture single colloidosomes with closed-packed monolayers of silica particles on the surface and with the Langmuir-Freundlich fit, the mass yield of these particles can be tailored. Two

characterization methods were successfully applied to compare the Janus balance. The observation of the semishells using SEM and the calculation of the shell coverage degree of around 100 particles served as statistical investigation method. In combination with the application of the ninhydrin assay as a second method, the Janus balance was detected by quantifying the amine density at the surface. Both processes for each surfactant demonstrate that the Janus balance on a particle cannot be controlled or predicted by varying the amount or concentration of surfactant, in contrary to the literature. In general, it can only be concluded that the surfactant does increase the percentage of silicar particles penetrating into the wax, but not their penetration depth.

## 4.3. SILICA PARTICLES WITH METAL FULLSHELLS AND SEMISHELLS

Metal fullshells with a dielectric core have unique properties and can be applied in areas such as labeling[146] and optical devices.[147] Especially silica-noble metal core-shell nanostructures attracted much attention over the years.[68d, 98, 104a, 148] A common preparation method is to coat the silica particles with gold (Au) or silver (Ag) seeds and then to deposit a metal layer onto the seeded areas from an electrolyte containing metal salt and a reducing agent (see Chapter 2.3). Metal layers such as Au,[52, 68, 148b, 149] Ag,[69] and Pd[68c, 149] were successfully deposited onto Au activated silica spheres. Not only fullshells but also silica Janus colloids with Au semishell can be prepared after depositing a metal layer[52] onto a regio-selectively Au-seeds-coated sphere,[48] using this method. Au colloids prepared according to Duff et al.,[100, 150] bind selectively to hydrophilic functional groups such as $NH_2$ and SH but not to hydrophobic groups,[51] when both group types are present on a sphere. In the plating industry, this type of selectively binding activators on a dielectric material is well-known.[59, 151] Whereby, Pd-activated surfaces are used instead of Au-activated ones. Not only do Pd ions interact with a wide range of functional groups,[152] they are also cheaper (1 g Au ~38 €, 1 g Pd ~23 €, 04/19/2017),[153] which makes them a more suitable candidate for industrial approaches.

Palladium-tin (Pd-Sn) catalysts used to be a suitable activation source for dielectric substrates in the electronics industry,[154] but the disadvantage of being an environmentally hazardous composition and non-selectively adsorbing on the substrate, enforced the search for alternatives. A promising approach was the usage of a covalently bound Pd catalyst, which resulted in an increased substrate-deposited metal adhesion and a selective surface activation.[73, 155] Functional groups, such as chelating or good π-acceptor ligands, were first created on the substrate surface to interact with the Pd ion. After the reduction of the Pd ion, a metal layer was electrolessly deposited on the surface.

These procedures constituted the groundwork to develop a novel approach to metalize silica Janus particle spheres since Pd-activated starting materials have

proven to enable the usage of a wide range of metals for the layer deposition on non-conductive substrates.[151, 156]

### 4.3.1. Activation of the functionalized sphere with Pd seeds

The preparation of the silica Janus particles with metal nanoshells and semishells can be described as a two-step coating process (see Figure 4-20). First, APTES-functionalized spheres are coated with small Pd seeds, which is referred to as the activation step in the following. Subsequently, these seeds serve as catalysts and start the reduction of metal ions on the activated spheres in an electroless metal deposition process. Using this two-step process, silica Janus particles with a variety of metal layers such as gold, silver, palladium, copper, and nickel can be successfully prepared. Before preparing the semishells, silica particles with the corresponding full metal nanoshells were fabricated to develop a synthetic protocol and to investigate the shell growth.

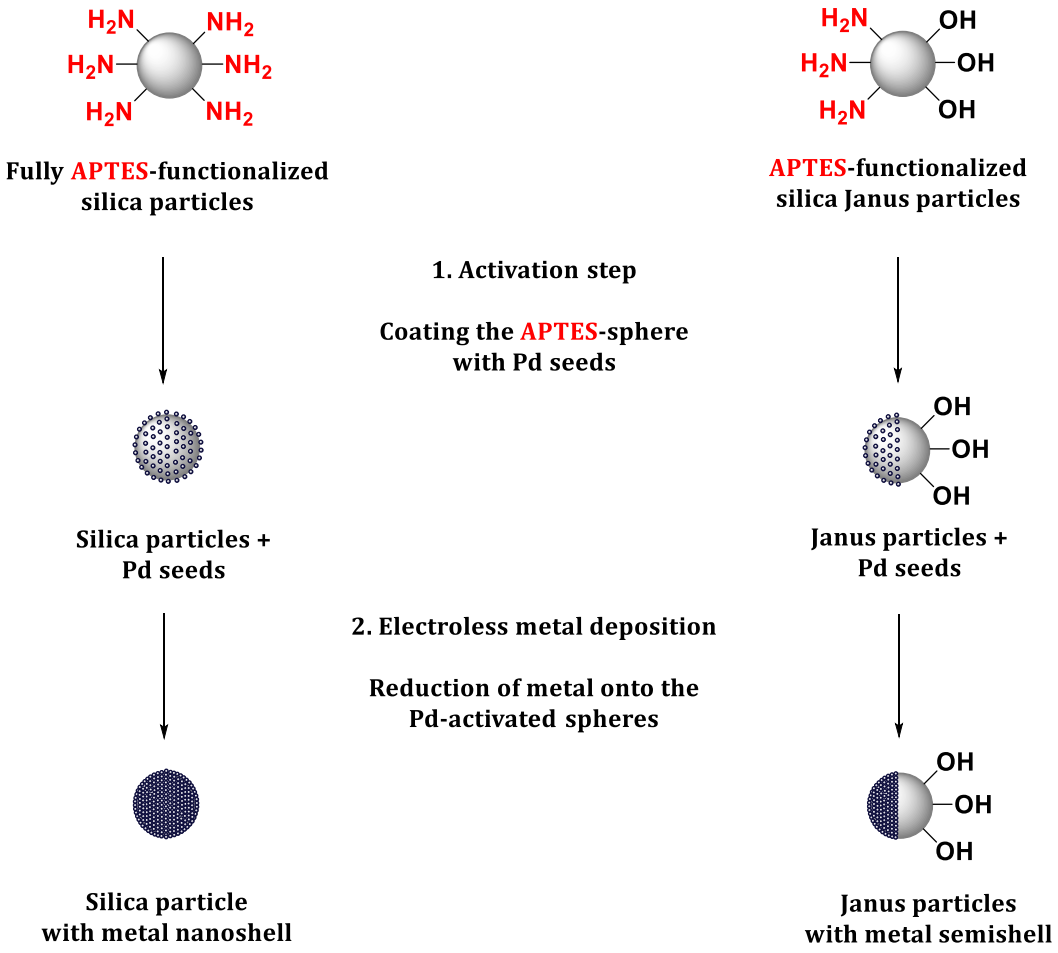


**FIGURE 4-20 SCHEMATIC OVERVIEW OF THE STRATEGY TO PREPARE SILICA PARTICLES WITH METAL FULLSHELLS AND SILICA JANUS PARTICLES WITH METAL SEMISHELLS.**

Preliminary test were made with fully APTES-functionalized silica particles. The colloids were dispersed in an aqueous solution and reacted with two different ($PdCl_4^{2-}$) stock solutions, where the pH values were set to pH ~1 or pH ~4. The Pd solution with pH ~1 was discarded as a suitable activator because no plating occurred in the following metallization step. The mixture containing the Pd(II) stock solutions (pH ~1) and the silica colloids had a pH value of 2—3. The environment supports the formation of the Pd oligomers, which is essential for the preparation of Pd islands with a density of 10 Pd atoms/nm² (see Chapter 2.3.5.).[72-73] However, zeta potential measurements demonstrated that the APTES-functionalized surface is protonated below pH < 5 (see Chapter 4.1.3.) and hence, aggravated the coordination towards the Pd(II) complex. In addition to the importance of the Pd(II) oligomer size, the protonation state of the nitrogen is also crucial for the coordination abilities towards palladium.

The reaction mixture comprising the Pd(II) solution (pH ~4) had a pH value of ~6, which supports the formation of Pd(II) oligomers as well as the existence of the free ion pair on nitrogen as a coordination side for Pd. The formation of polynuclear chains consisting of 3-9 Pd-(II) was assumed because the prepared palladium stock solution (0.049 M Pd, 0.194 M $Cl^-$, 0.095 M NaOH) was kept slightly below the precipitation point, and according to Boily et al., the size of the oligomer is around 3-9 Pd-(II) before precipitation.[157] The Pd cluster sizes on the silica surface were investigated in SEM after the reduction step.

To establish an activation protocol, different reaction conditions were tested to coat amine-functionalized colloids with Pd seeds. First, fully APTES-functionalized silica particles were reacted with the Pd(II) ions under different conditions to investigate the influence on the Pd adsorption, with a $mol_{Pd}/mol_{NH2}$ ratio of 21.3±7.0 (Full-Pd-Act-1,2,3, and4). The $mol_{Pd}/mol_{NH2}$ ratio corresponds to a sphere with a surface density of 4 $NH_2$ groups/$nm^2$. It is assumed that all the surface OH groups are fully converted, so that 1 OH group corresponds to 1 $NH_2$ group).[97] Table 4-15 lists the theoretical numbers of Pd atoms/$nm^2$ in case of the adsorption of all Pd ions inside the mixture and the calculated numbers of Pd atoms/$nm^2$ obtained from the ICP-OES results for the Pd content. The total surface area of all silica particles ($A_{Silica}$) was calculated considering the diameter and the number of particles that were reacted with concentrated HCl to dissolve the Pd atoms for the ICP-OES measurement. The error margins for the Pd densities contain the error margin for the determined Pd content as well as the error margin for the total surface area of silica particles.

**TABLE 4-15 OVERVIEW OF THE DIFFERENT NUMBERS OF PD ATOMS/NM² MEASURED USING ICP-OES AND THE THEORETICAL NUMBER FOR DIFFERENT REACTION CONDITIONS**

| Sample | | Amounts used for ICP-OES | | Number of Pd atoms/nm² calculated from | |
|---|---|---|---|---|---|
| Name | Reaction condition | $A_{Silica}$ [$10^{19}$ · nm²/L] | Pd content [mg/L] | Theoretical | ICP-OES |
| Full-Pd-Act-1 | 1 h, rt | 2.0±0.7 | 78.5±3.9 | 85±28 | 22±6 |
| Full-Pd-Act-2 | 1 h, 70 °C | 1.7±0.6 | 109.5±5.5 | 85±28 | 30±10 |
| Full-Pd-Act-3 | 12 h, 70 °C | 2.2±0.7 | 114.0±5.7 | 85±28 | 29±8 |
| Full-Pd-Act-4 | 1 h, 70 °C, then 24 h, rt | 1.9±0.6 | 122.5±6.1 | 85±28 | 37±10 |
| Full-Pd-Act-5 | 1 h, 70 °C | 0.3±0.1 | 17.6±0.9 | 96±30 | 30±6 |
| Full-Pd-Act-6 | 1 h, 70 °C | 0.5±0.15 | 25.7±1.3 | 97±31 | 27±6 |

When the reaction temperature was increased from rt to 70 °C, the detected numbers increase from 22±6 Pd atoms/nm² to 30±10 Pd atoms/nm². A reason can be the acceleration of the hydrolysis and condensation into the oligomeric complexes at elevated temperature, which interacted with the silica surface. An additional increase in reaction time from 1 h to 12 h at 70 °C did not influence the adsorption of more Pd ions (29±8 atoms/nm²). In the case of Full-Pd-Act-4, the additional stirring at rt for 24 h resulted in an increased number of adsorbed Pd atoms to 37±10 atoms/nm². Likely, the surface-bound Pd(II) oligomers undergo further reactions with Pd(II) complexes inside the solution. Hence, the adsorption of Pd is increased[73] or the higher value results from Pd(II) complexes that precipitated within the 24 h since no buffer was added to the solution. All the approaches yielded a higher Pd coverage density than the reported minimum of ~10 Pd atoms/nm² which are required for initiating electroless metal deposition.[73] Considering the error margins, stirring the mixture for 1 h at 70 °C

resulted in a reproducible Pd density of ~30 Pd atoms/nm$^2$. Similar results are obtained when the samples Full-Pd-Act-5 and Full-Pd-Act-6 reacted for 1 h at 70 °C with an increased $mol_{Pd}/mol_{NH2}$ ratio (~24). It can be noted that only a fraction of the theoretical value of Pd ions actually adsorbed at the surface of the Full-Pd-Act samples under these conditions.

In general, amino groups are suitable ligands for transition metal ions such as Pd. The lone electron pair of nitrogen has strong electron donor capability, and the empty lower energy orbitals of Pd(II) (electron configuration $4d^8 5s^0 5p^0$) are strong electron acceptors.[152b] Since $Pd^{2+}$—N bonds are stronger than those between $Pd^{2+}$—O or $Pd^{2+}$—Cl, the chlorine, and the oxygen will be replaced, forming complexes with high stability constants.[158] Different binding mechanisms can theoretically apply here; physisorption, electrostatic interaction,[159] or covalent bonding.[75c] Whereby, Dressick et al. excluded physisorption or electrostatic interaction during their studies and proposed covalent bonding/coordination between Pd(II) oligomers and nitrogen-containing ligands.[73, 75c]

After the Pd(II) deposition, the dispersion was washed, redispersed in water, and the Pd(II) ions were reduced using an excess amount of dimethylamine borane (DMAB). The dispersion color changed immediately to black because of the resulting elementary $Pd^0$. A possible stoichiometric reaction between Pd ions and the reducing agent DMAB is proposed in Chapter 2.3.1. Once the $Pd^{2+}$ ions are reduced to $Pd^0$, the seeds diffuse over the surface and self-assemble to stable Pd clusters. A theoretical explanation describes the cluster formation in general. The calculated $Pd^{2+}$—N binding energy of ~1.5 eV[160] is higher than the reduced $Pd^0$—N binding energy, according to electron configuration following ligand-field theory.[155b] Thus, the Pd seeds diffuse over the surface and grow with other Pd seeds ($Pd^0$—$Pd^0$ binding energy of 3-3.9 eV[155b]) to favorable stable islands (self-assembly). Although the silica colloids with Pd seeds can be immediately used for further processing, a more homogeneous distribution of Pd seeds was observed when precursor colloids rested for several days. The Pd-seeded colloids were investigated using SEM (see Figure 4-21). Since the distribution of the Pd seeds appears similar for the samples Full-Pd-2, Full-Pd-3 and Full-Pd-4, exemplary images of Full-Pd-1 and Full-Pd-2 are demonstrated.

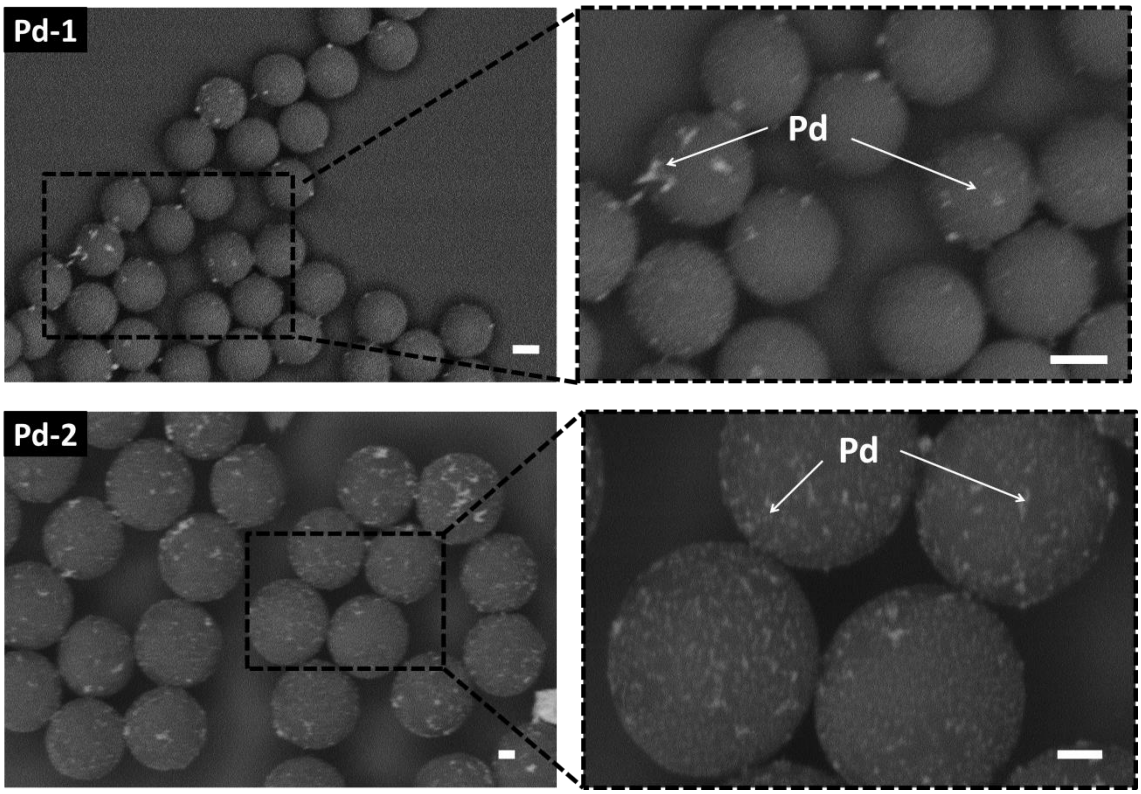


**FIGURE 4-21 SEM IMAGES OF TWO DIFFERENT BATCHES OF FULLY APTES-FUNCTIONALIZED SILICA PARTICLES WITH PD SEEDS COATING AFTER REACTING PD-1) FOR 1 H AT RT (FULL-PD-1) AND PD-2) FOR 1 H AT 70 °C WITH A PALLADIUM STOCK SOLUTION (48.6 MM), SCALE BAR = 200 NM (PD-1) AND SCALE BAR = 100 NM (PD-2).**

It can be noticed that the Pd clusters exist in different sizes, which can be split into small (4-9 nm diameter), medium (10-20 nm diameter), and large (20-40 nm diameter). Within one specimen these different seed diameters can be detected on each particle. Calvert and co-workers have investigated various Pd(II)-based catalysts for electroless metal deposition, which were also generated from $PdCl_2$. Their slightly different preparation method created colloidal catalysts with a particle size range of ~4—53 nm,[75b] which is in agreement with this study's findings after the reduction step. The distribution of the Pd seeds on Full-Pd-1 appears less dense and more heterogeneous, in comparison to the silica surfaces of Full-Pd-2 (see Figure 4-21), which supports the results for the coverage with Pd seeds per surface obtained from the ICP-OES measurements. Since it is well-known that the morphology of a deposited electroless metal corresponds to the seed distribution,[59] an Au layer was electrolessly deposited onto the Pd-activated surface of all the colloid samples, and the obtained Au layers were investigated using SEM (Figure 4-22).

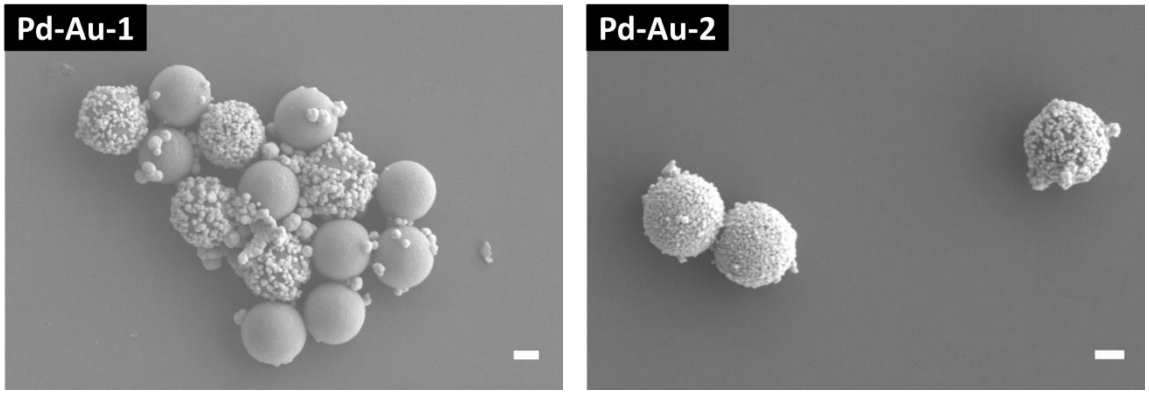


**FIGURE 4-22 SEM IMAGES OF AU LAYER DEPOSITION ONTO (PD-AU-1) PD SEEDS ACTIVATED SILICA PARTICLES PREPARED WITHIN 1H AT RT (FULL-PD-1-AU), AND (PD-AU-2) PD SEEDS ACTIVATED SILICA PARTICLES PREPARED WITHIN 1H AT 70 °C (FULL-PD-2-AU), SCALE BAR = 200 NM.**

The detailed mechanism of the gold deposition process is provided in Chapter 2.3. The image Pd-Au-1, corresponding to the Au plated sample Full-Pd-1, contains silica particles entirely covered with "small" gold colloids (15—40 nm in diameter) and particles with only a few "large" colloids (60—130 nm). The heterogeneous distribution of the Pd seeds at the silica surface (see Figure 4-21 Pd-1) can explain the uneven distribution of Au on the surface. Like the Pd-seeded colloids, the Au fullshells prepared from Full-Pd-2, Full-Pd-3 and Full-Pd-4 precursors resemble each other, and therefore, only one exemplary image for sample Full-Pd-2-Au is shown. The diameter of the observed Au clusters are ~15—40 nm and seeds with different sizes are homogeneously distributed on the surface, which is expected considering the obtained homogeneous distribution of Pd seeds in the activation step (see Figure 4-21 Pd-2).

It was concluded that the heating in the activation step increased the adsorption of Pd(II) ions onto APTES-functionalized silica spheres. Consequently, it can be concluded that all the silica Janus particles reacted with the Pd stock solution (pH ~4) for 1 h at 70 °C. Since only a fraction of the Pd ions was adsorbed at the surface of the fully APTES-functionalized particles, for efficiency reasons, a lower $mol_{Pd}/mol_{NH2}$ ratio was chosen for the surface coating of Janus particles. Table 4-16 provides an overview of the theoretical numbers of all adsorbed Pd atoms/nm$^2$ and the actual number of Pd atoms/nm$^2$ calculated from the ICP-OES results. These numbers are converted into a potential surface coverage degree,

taking a fully APTES-functionalized colloid, which is covered with ~30 Pd atoms/nm$^2$ as reference.

**TABLE 4-16 OVERVIEW OF THE THEORETICAL AND CALCULATED NUMBER OF PD ATOMS/NM$^2$ FROM THE ICP-OES RESULTS AND THE COVERAGE DEGREE FOR PD-ACTIVATED SILICA JANUS PARTICLES**

| | Amounts used for ICP-OES | | Number Pd atoms/ nm$^2$ calculated from | | Coverage degree with Pd [%] |
|---|---|---|---|---|---|
| Sample | $A_{Silica}$ $10^{18}$ [nm$^2$/L] | Pd [mg/L] | Theoretical | ICP-OES | |
| JNP-Pd-Act-1 (DDAB) | 5.4±1.4 | 16.1±0.8 | 17±5 | 17±4 | 57±13 |
| JNP-Pd-Act-2 (DDAB) | 0.3±0.1* | 2.2±0.1* | 19±5* | 23±3* | 77±10* |
| JNP-Pd-Act-3 (DDAB) | 0.8±0.2 | 4.9±0.2 | 17±5 | 17±3 | 57±10 |
| JNP-Pd-Act-4 (CTAB) | 4.9±1.6 | 19.9±1.0 | 53±17 | 23±6 | 77±20 |
| Full-Pd-Average | | | | 30 | 100 |

When the $mol_{Pd}/mol_{NH2}$ ratio was ~4.5 (JNP-Pd-Act-1 and 3), the measured numbers for Pd atoms are in good agreement with the theoretical numbers, which means that all the Pd ions were adsorbed. The higher number for sample JNP-Pd-Act-2 (23±3 Pd atoms/nm$^2$) can result from the low concentration of the measured sample itself because the detected Pd content is slightly above the detection limit of the ICP-OES (limit = 2.0 mg/L). These three Janus samples were prepared from different concentrations of DDAB during the colloidosome step. The average coverage of ~63±11 % agrees with the obtained experimental data in Chapter 4.2.2 for the metal shell coverage for the DDAB samples (64±15 %). An increase in $mol_{Pd}/mol_{NH2}$ ratio to 13, resulted in 23±6 Pd atoms/nm$^2$, which corresponds to a surface coverage of 77±20 %. This number is slightly higher than the results obtained in Chapter 4.2.3, where the average metal shell coverage is 68±17 % for Janus colloids prepared in the presence of CTAB. Likely, the increase in

$mol_{Pd}/mol_{NH2}$ ratio generated Pd islands that were slightly broader and higher, which could not be detected in the SEM images.

The obtained results confirm that even low $mol_{Pd}/mol_{NH2}$ ratios (~4.5) yielded silica Janus precursors suitable to catalyze the electroless metal deposition process.[73] Subsequently, the Pd-activated Janus particles were plated with copper (Cu), and the activated surfaces, as well as the semishells were investigated using SEM (see Figure 4-23).

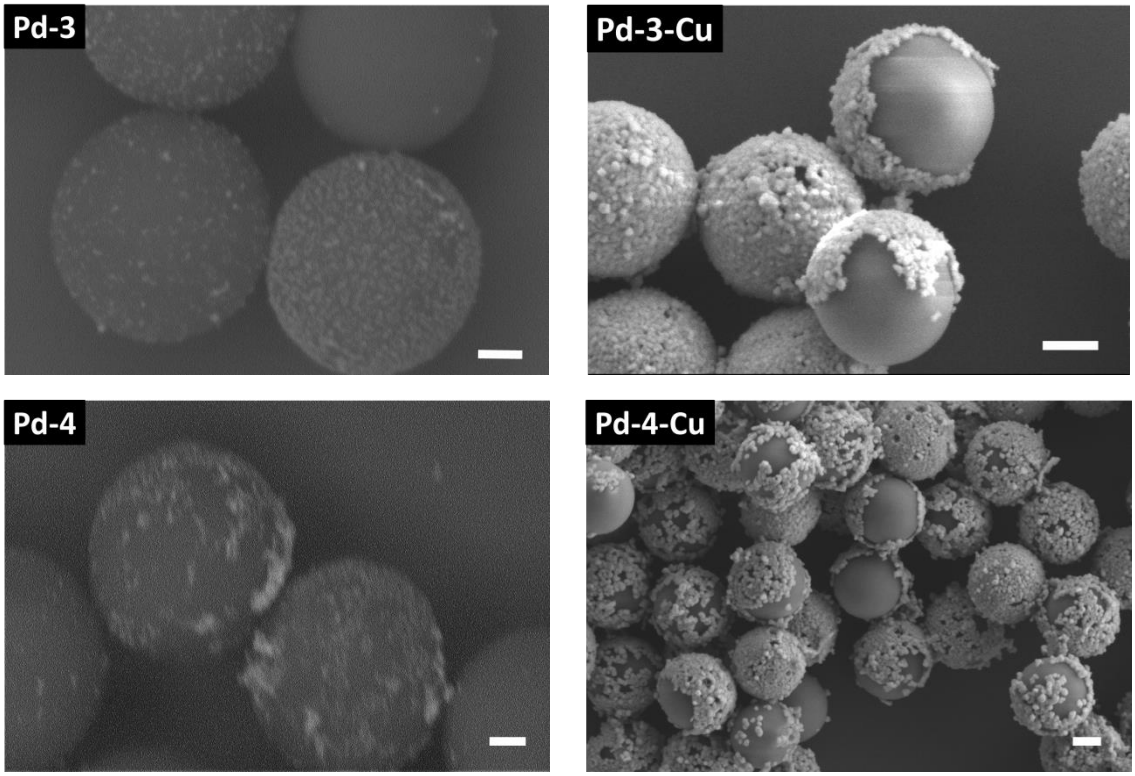


**FIGURE 4-23 SEM IMAGES OF SILICA JANUS PARTICLES COATED WITH PD SEEDS: (PD-3) SAMPLE JNP-PD-2 AND (PD-4) SAMPLE JNP-PD-4), SCALE BAR = 100 NM, AND CORRESPONDING IMAGES OF CU SEMISHELLS ON SILICA COLLOIDS PD-3-CU AND PD-4-CU, SCALE BAR = 200 NM.**

Two types of Pd-activated surfaces are found: Janus particles with homogeneously distributed "small" Pd seeds (10±3 nm size; Pd-3); and Janus particles with heterogeneously distributed "small" Pd seeds and "large" Pd clusters (9 to > 40 nm; Pd-4), although the same reaction conditions were applied with the same $mol_{Pd}/mol_{NH2}$ ratio. As expected, the Pd-coated sample JNP-Pd-2 (Figure 4-23 Pd-3) resulted in homogenously covered semishells with merged Cu layers (Figure 4-23 Pd-3-Cu) and JNP-Pd-3 (Figure 4-23 Pd-4) yielded semishells with Cu seeds with 30±7 nm in diameter (Pd-4-Cu). A detailed investigation of the growth

process of the Cu shells is presented in Chapter 4.3.4. Although the same reaction conditions were applied, the Pd seeds distribution varied throughout the batches. As mentioned before, a reason can be the state of the amino groups itself that reacted with the Pd ions. During the several fabrication steps of silica Janus particles, the amine group could have interacted with $CO_2$ and yielded carbamic acid species.[128] The primary amine would no longer have a free electron pair to interact with the Pd(II) ions. Notably, during the filtration step through a funnel, after the in-wax-embedded colloids were grafted with APTES, the amino groups were not under argon and could have reacted with $CO_2$ from the atmosphere. Another explanation can be that during the hydrolysis of the Pd-complex, different-sized Pd oligomers are generated which result in polydisperse Pd islands. To prepare a more uniformly coated surface, several approaches have been proposed. The surface can be grafted with bidentate nitrogen ligands instead of monodentate ligands to support Pd(II) complexes.[77] The coordination between Pd(II) and the bidentate ligand is stronger than with the monodentate one. Therefore, after the reduction step, the diffusion of the Pd seeds is hindered, which resulted in smaller Pd islands. Another method to create a homogeneous Pd size distribution and an improved surface coverage is to prepare monodisperse Pd colloids as catalysts.[75b] Since the morphology of the electroless metal deposition is directly related to the Pd cluster sizes and distribution on the surface,[75c] depending on the desired application the Pd islands can be easily modified.

It can be summarized that a method was successfully introduced to coat the APTES-functionalized sphere with Pd seeds as catalyst that support the electroless deposition of metals. When the reaction mixture stirred for 1 h at 70 °C, a surface density of ~30 Pd atoms/nm$^2$ was obtained. Janus particles coated with low $mol_{Pd}/mol_{NH2}$ ratios (~4.5) yielded a surface density of ~20 Pd atoms/nm$^2$, which corresponds to a ~2/3 coverage of the silica colloid. The distribution of clusters varied within different batches, which might be caused by the state of the amino groups at the surface of Janus particles or the chain length of the Pd(II) oligomers.

### 4.3.2. ELECTROLESS METAL DEPOSITION

Once the Pd seeds-coated precursors were prepared for fully APTES-functionalized particles and for Janus particles, the corresponding areas of the particles were plated with the desired metal using the electroless metal deposition process (see Chapter 2.3). The procedure is similar for all deposited metal types. The precursor dispersion (0.5 g/L) was added to the corresponding metal electrolyte. Since it is an autocatalytic process, the deposited metal mediates the electron transfer from the reducing agent towards the metal ions inside the solution to deposit more metal.[59] This process continued until all metal ions inside the solution was converted into the metal layer. Knowing the amount of the metal inside the electrolyte and the total surface area ($A_{Total}$) of all silica particles inside the mixture, a theoretical value for the shell thickness was calculated, assuming a full conversion for each metal example. A detailed calculation is provided in Appendix II Calculations. Since the same method was applied for the different metals, a detailed discussion is only given for nickel (Ni), the main steps of this process are the following:

1. The same batch of fully APTES-functionalized silica particles coated with Pd seeds was used to plate different amounts of metal electrolyte and to investigate the growth of full nanoshells in SEM.
2. Once a synthetic protocol was established for the growth of a full nanoshell, Janus particles, regio-selectively coated with Pd seeds, were plated with different amounts of the metal electrolyte and also investigated in SEM.
3. A theoretical shell thickness was calculated for each sample and compared to: (1) the thickness calculated from the metal concentration determined by ICP-OES and the known content of silica particles inside the dispersion; (2) the measured shell thickness from the colloid diameter before and after the plating in SEM, assuming that the microporous silica particles retain their initial size in SEM, and (3) in some cases, a cross-section of the colloids was obtained with a FIB allowing the direct measurement of the shell thickness. These three methods were chosen to confirm the reliability of each characterization method.

4. In some cases, a commercially available electrolyte from Atotech was used for the metal deposition. Since all the ingredients are confidential, this electrolyte was solely utilized to test the transferability of the approach to other electrolytes once a plating protocol was established.

### 4.3.3. JANUS PARTICLES COATED WITH NICKEL SEMISHELLS

To our knowledge, the only strategy to prepare silica Janus particles with nickel (Ni) semishells is achieved by evaporation or sputtering a thin film of Ni onto a monolayer of immobilized silica particles,[50] which yields only small amounts of Janus particles with semishells. Here, we present a simple process to prepare silica Janus particles region-selectively coated with Ni layers, which can easily be scaled up for industrial application. Silica colloids partially coated with Pd seeds catalyze the electroless Ni deposition. Two different Ni electrolytes were used as nickel source: a modified electrolyte described in the literature (Ni-EL 1);[99] and a commercially available solution called Nichem6200 for testing the reproducibility of the colloid plating with different electrolytes (see Figure 4-24).

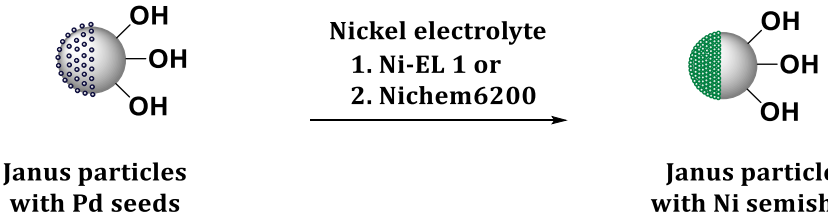


**FIGURE 4-24 SCHEMATIC ILLUSTRATION OF THE STRATEGY TO SYNTHESIZE SILICA PARTICLES WITH NI SEMISHELLS.**

The electroless Ni deposition mechanism is presented in detail in Chapter 2.3. The electrolyte Ni-EL 1 contained nickel sulfate ($NiSO_4$, 0.1 M, 5.87 g/L Ni content) as a metal ion source. The reduction of $Ni^{2+} \rightarrow Ni^0$ is achieved with a reducing agent that has more negative redox potential than $Ni^{2+}/Ni^0$ (-0.26 V (NHE)).[161] Sodium hypophosphite ($NaH_2PO_2$, 0.3 M) was chosen as a suitable candidate in acid medium considering its redox potential of -1.07 V (NHE) at pH 7 and -0.88 V (NHE) at pH 4.5.[99] Since the reducing agent delivers the electrons for the Ni ion reduction as well as for the formation of elementary phosphorous ($P^0$), it is supplied in three times excess. In aqueous solution, $NiSO_4 \cdot 6H_2O$ forms the

hexaaqua complex $[Ni(H_2O)_6]^{2+}$ in an octahedral coordination. Malic acid (0.055 M), lactic acid (0.1 M), and succinic acid (0.1 M) were used as complexing agents with the purpose to reduce the concentration of free $Ni^{2+}$ with generating nickel complexes, to hinder the precipitation of insoluble Ni compounds such as nickel hydroxide and nickel phosphite, and to buffer the pH value during the process. Two aspects are important when choosing the complexing agent: the redox-potential of the resulting complex and the stability constant. When the stability constants is too high, the complexing agent removes too many free Ni ions from the electrolyte and hence, the deposition rate is reduced. However, when the constant is too low, the nickel deposition cannot be controlled anymore.[59] Malic acid, lactic acid, and succinic acid meet these criteria. Since the electrolyte was used shortly after preparation, an additional bath stabilizer was not necessary (see Chapter 2.3.2). In the case of the commercial bath Nichem6200 the only provided information is that it is a low phosphorous electrolyte and that the Ni content is 5±0.5 g/L.

In the plating industry, the metal layer thickness is controlled by the immersion time of an activated sample inside an electrolyte, since the deposition rate is known for each bath. For preparing silica particles (500—600 nm in diameter) with 6—70 nm thick nanoshells, the appropriate amount of electrolyte was added, which would result in the desired layer thickness in the case of full conversion. After the addition of the dispersion mixture to the electrolyte, the evolution of hydrogen gas started (see Equation 2-18), and the dispersion color changed immediately to dark gray because of the formation of metallic Ni. The process continued until the Ni content in the bath was exhausted. The hydrogen evolution and the change of the solution color were used as indicators of the reaction progress. The nickel depositions resulted in similar layer deposition when applying ultrasonic agitation (bath 35 kHz) or stirring at 300 rpm.

In the following section, the shell deposition is investigated by observing the Ni shell thickness as a function of the amount of the Ni electrolytes (Ni-EL1) added to Pd-activated fully APTES-functionalized silica colloids (568±36 nm in diameter, Chapter 4.3.1.). The shell thickness was calculated for each sample in case of full conversion of all the metal source. This will be referred to in the following as the

theoretical value. Table 4-17 summarizes the theoretical shell thickness for each sample, and the corresponding experimental results for the step-by-step layer growth. Three methods were chosen to determine the layer thickness: 1) the Ni content obtained from ICP-OES measurements and the corresponding Si content are used to calculate the layer thickness; 2) the average diameter of at least 100 silica particles with nickel fullshells were measured and subtracted from the diameter of the non-plated colloids in SEM; and 3) for a selected sample, the layer thickness was directly measured from the prepared cross-section of the colloid using FIB.

**TABLE 4-17 OVERVIEW ALL SHELL THICKNESS DATA OBTAINED FROM DIFFERENT CHARACTERIZATION METHODS FOR SILICA PARTICLES WITH DIFFERENT NI FULLSHELL THICKNESSES USING NICKEL ELECTROLYTE NI-EL 1**

| | Amounts used for ICP-OES | | Shell thickness [nm] calculated from | | | |
|---|---|---|---|---|---|---|
| Sample | $A_{Silica}$ $10^{18}$ [nm²/L] | Ni content [mg/L] | Theoretical | ICP-OES | SEM | FIB |
| Full-Ni-1 | 3.6±1.1 | 89.8±4.5 | 6±2 | 3±2 | — | — |
| Full-Ni-2 | 3.2±1.0 | 262.5±13.1 | 12±2 | 9±3 | 10±35 | — |
| Full-Ni-3 | 4.5±1.4 | 545.5±27.3 | 16±1 | 13±2 | 24±33 | — |
| Full-Ni-4 | 4.4±1.3 | 888.0±44.4 | 23±1 | 21±2 | 33±32 | — |
| Full-Ni-5 | — | — | 33±1 | — | 39±34 | 40±5 |

The calculated layer thicknesses from the ICP-OES measurements are in good agreement with the theoretical values for the samples Full-Ni-1—Full-Ni-4, respectively. It can be reasoned that all Ni inside the electrolyte is deposited onto the silica surface, which is expected for an autocatalytic process. The average diameter of the silica particles coated with Ni (Full-Ni-1) is approximately the same as that of the non-plated particles. When the amount of Ni-EL 1 was increased to 0.28 g/L Ni content (Full-Ni-2), the shell thickness obtained from SEM is 10±35 nm, which is in good agreement with the theoretical thickness (12±2 nm).

In the case of Full-Ni-3 (0.41 g/L Ni content), the shell measured by SEM has a thickness of 24±33 nm, which is higher than the theoretical value (16±1 nm). Similar higher results are measured in SEM for the samples Full-Ni-4 (33±32 nm) and Full-Ni-5 (39±34 nm). A reason for the discrepancy can be that the initial silica colloids experience a decrease in diameter size caused by the heat of the electron beam itself,[162] whereby the metal shells are not affected. The activated precursor particles comprised of Pd seeds with 9±6 nm in diameter, measured from the SEM image (see Figure 4-25 Full-Pd-5). After the Ni deposition, these precursors are covered with Ni clusters with a narrow size distribution of 18±4 nm in diameter, measured from the SEM image in Figure 4-25 Ni-1. The Ni clusters grow laterally and coalescence with adjacent clusters, but since the surface is not fully covered, the overall particle diameter does not change significantly. The lateral growing Ni clusters expand further and some merge with neighboring clusters, while leaving small areas untouched (see Figure 4-25 Ni-2).

In general, the Ni layer deposition results in homogeneously grown shells. During the purification step using centrifugation, a clear supernatant was obtained, which indicates the absence of small Ni nuclei as side products. The investigation of the specimen in SEM confirms the absence of any Ni nuclei.

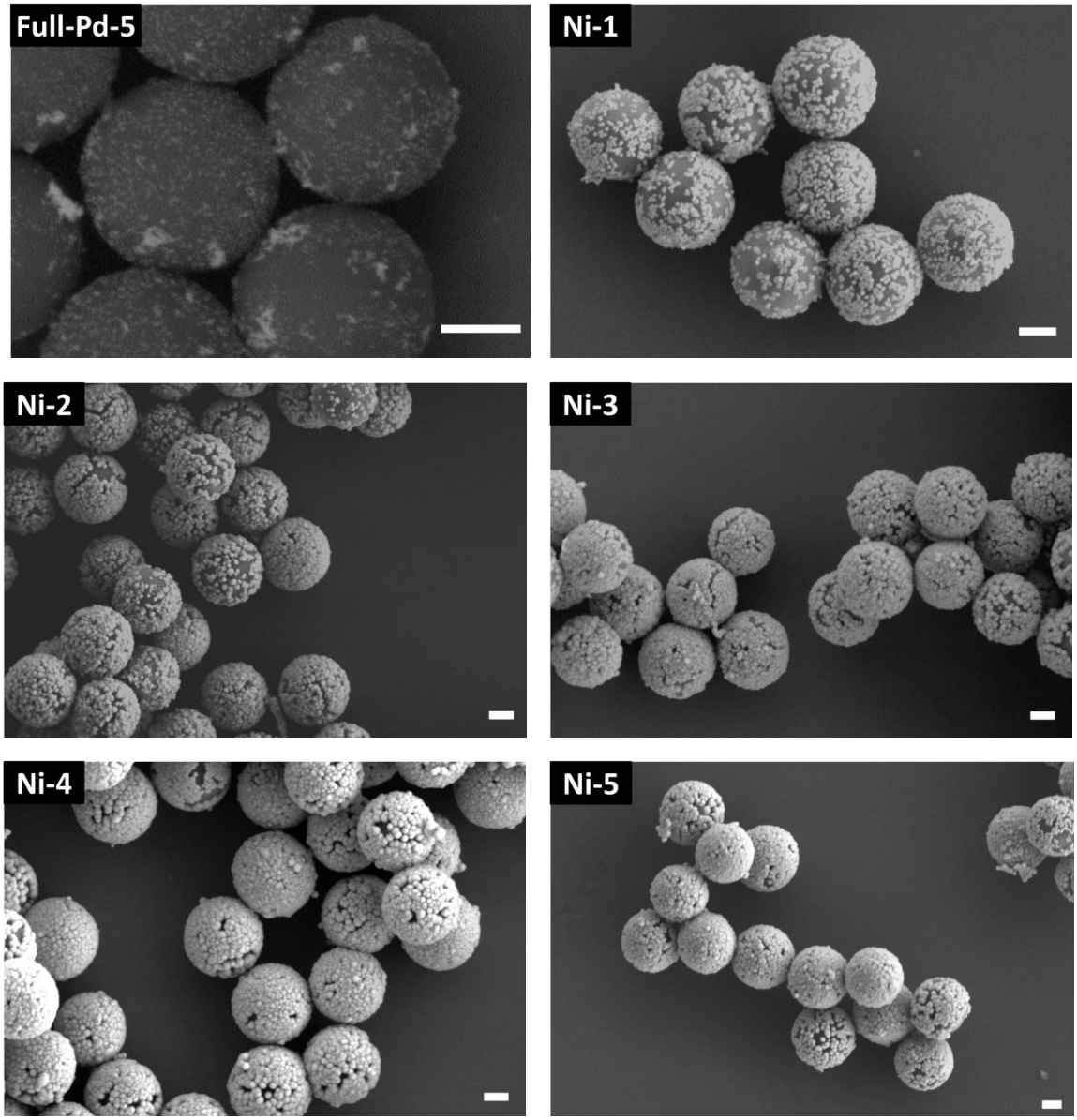


**FIGURE 4-25 SEM IMAGES OF APTES-FUNCTIONALIZED SILICA PARTICLES COATED WITH PD SEEDS (FULL-PD-5) AND MONITORING OF THE SHELL GROWTH WHEN THE THEORETICAL THICKNESS IS: NI-1) 6±2 NM (FULL-NI-1); NI-2) 12±2 NM (FULL-NI-2); NI-3) 16±1 NM (FULL-NI-3); NI-4) 23±1 NM (FULL-NI-4); NI-5), AND 33±1 NM (FULL-NI-5), SCALE BAR = 200 NM.**

In the case of sample Full-Ni-5, the Ni fullshells were additionally examined using FIB combined with SEM (See Figure 4-26 Ni-5-I and Ni-5-II), and an average layer thickness of 40±5 nm is obtained from the cross-section, which agrees well with the results from SEM. The images state that the nanoshells consist of Ni clusters that coalescence with adjacent ones.

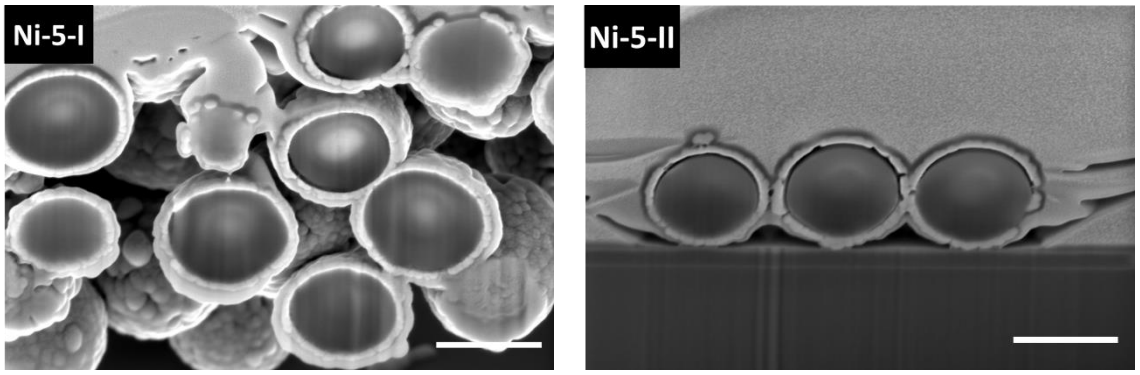


**FIGURE 4-26 SEM IMAGES OF THE CROSS-SECTION OF SILICA PARTICLES WITH NI FULLSHELLS WITH A THEORETICAL LAYER THICKNESS OF 33±0 NM (FULL-NI-5) OBTAINED USING FIB, SCALE BAR = 500 NM.**

In general, the Ni layer growth is characterized by the seeded-growth mechanism, where the Pd seeds serve as nucleation sites for the growth of Ni cluster. As mentioned in Chapter 2.3, the mechanism comprises of three simultaneous crystal-forming processes: nucleation, growth, and the coalescence of three-dimensional crystallites; followed by the formation of a linked network; and the formation of a continuous deposit, according to literature.[10a],[10b] The following Ni deposition model (see Figure 4-27) describes the observed layer growth after evaluating the SEM images from Figure 4-25. The deposition occurs at both small and large nucleation sites (A), whereby larger catalyst sites accelerate the metallization (B). The larger Ni particles grow laterally over smaller clusters (C) and create a continuous Ni film.

Similar observations were made by Brandow et al. when a silicon wafer was first modified with an organosilane film, then coated with Pd seeds followed by an electroless Ni deposition.[75c] Small nucleation sites are known to accelerate the mass transport caused by an additional non-linear diffusion of reactants. This results not only in an increase of plating reactants transported to the sites but also in an increased transport of dissolved oxygen and stabilizer if present, which are known to decelerate or even inhibit the electroless deposition.[163]

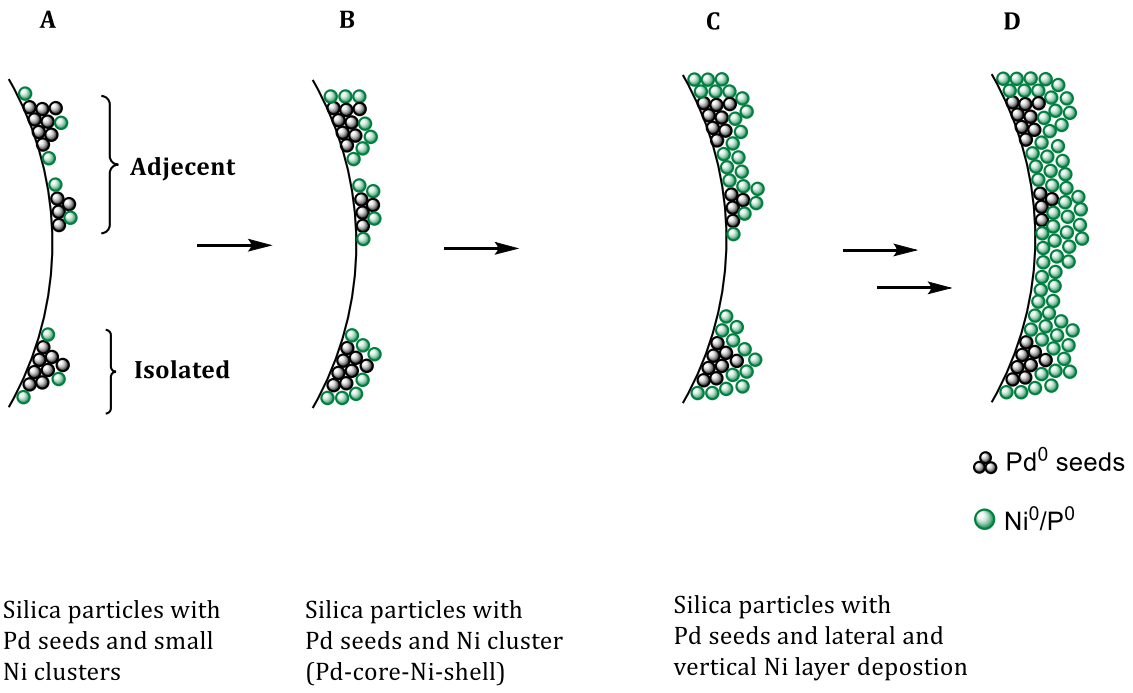


**FIGURE 4-27 SCHEMATIC ILLUSTRATION OF THE NI DEPOSITION ONTO PD SEEDS. WHEN PD SEEDS ARE IN CLOSE DISTANCE TO EACH OTHER, THE LATERAL GROWING NI CLUSTERS MERGE INTO NI LAYERS (B). IN THE CASE OF ISOLATED PD SEEDS WITH NO ADJACENT PD SEEDS, THE NI CLUSTERS GROW LATERALLY AND VERTICALLY CREATING LARGE AND BROAD NI CLUSTERS (C). IN THE PRESENCE OF SUFFICIENT NI SOURCE, EVEN DISTANT CLUSTERS CAN COALESCENCE INTO A NI LAYER (D).**

In the case of an isolated Pd cluster, an enhanced mass transport to the edges is also present caused by the non-linear diffusion in comparison to the bulk, which experiences only linear diffusion.[163b, 164] Once the Pd-core-Ni-shell composite is generated (B), the Ni cluster grows laterally (C). When the distance between two Ni clusters is too long, each cluster will grow in all dimensions generating larger and boarder clusters until they merge into a continuous and homogeneous layer (D) and no voids are present.[75c, 163a] Brandow et al. argued that a high nucleation density can promote the coalescence of adjacent clusters and generate a more continuous film.[75c] The findings during this present study confirme the correlation between the surface morphology of Ni deposition and the initial $Pd^0$ catalyst size distribution at the surface.[75c]

Once the Ni fullshell growth protocol was established, silica Janus particles with semishells were prepared. The experimental results from the colloidosome fabrication (Chapter 4.2) and from the Pd seeds coating (Chapter 4.3.1) suggest

that the colloid surface is covered approximately with 57—77% with Pd seeds or metal shells. Hence, a theoretical model of a 2/3 surface coverage was calculated, assuming a full conversion of all the metal source, for silica coated precursor particles (609±32 nm in diameter). The obtained results from ICP-OES are converted into a potential 2/3 Ni layer coverage. The shell thickness is directly measured from the cross-sections using FIB, and the data are provided in Table 4-18. Similar to the results for the synthesis of the full Ni nanoshell, no Ni nuclei were detected in the supernatant during the purification step or on the specimen during the investigation with SEM.

**TABLE 4-18 OVERVIEW OF ALL SHELL THICKNESS DATA OBTAINED FROM DIFFERENT CHARACTERIZATION METHODS FOR SILICA JANUS PARTICLES WITH DIFFERENT NI SEMISHELL THICKNESSES USING NI-EL 1**

| | Amounts used for ICP-OES | | Shell thickness [nm] calculated from | | |
|---|---|---|---|---|---|
| **Sample** | **$A_{Silica}$ $10^{18}$ [$nm^2$/L]** | **Ni content [mg/L]** | **Theoretical for 2/3-shell** | **ICP-OES for 2/3-shell** | **FIB** |
| JNP-Ni-1 | 0.6±0.1 | 95.4 | 37±2 | 25±8 | 37±1 |
| JNP-Ni-2 | 1.2±0.3 | 447.0 | 69±2 | 54±11 | 46±8 |
| JNP-Ni-3 | 1.0±0.2 | 403.5 | 80±2 | 60±14 | 62±16 |

The SEM image of JNP-Ni-1 (Figure 4-28 Ni-6) suggests the formation of two Ni shell types: (1) shells with a narrow distribution of small Ni clusters (20±3 nm) merged into a layer; and (2) shells consisting of slightly larger Ni clusters (35±8 nm) forming layers with occasional voids. When examining the SEM image from the precursor particles (Figure 4-28 JNP-Pd), the surface contains small Pd clusters in the size range of 10±3 nm that are mostly homogeneously distributed. Additionally, areas with no visible Pd seeds, as well as larger Pd clusters (>> 20nm in diameter) can be detected. This distribution of the Pd seeds can explain the observed Ni layer.

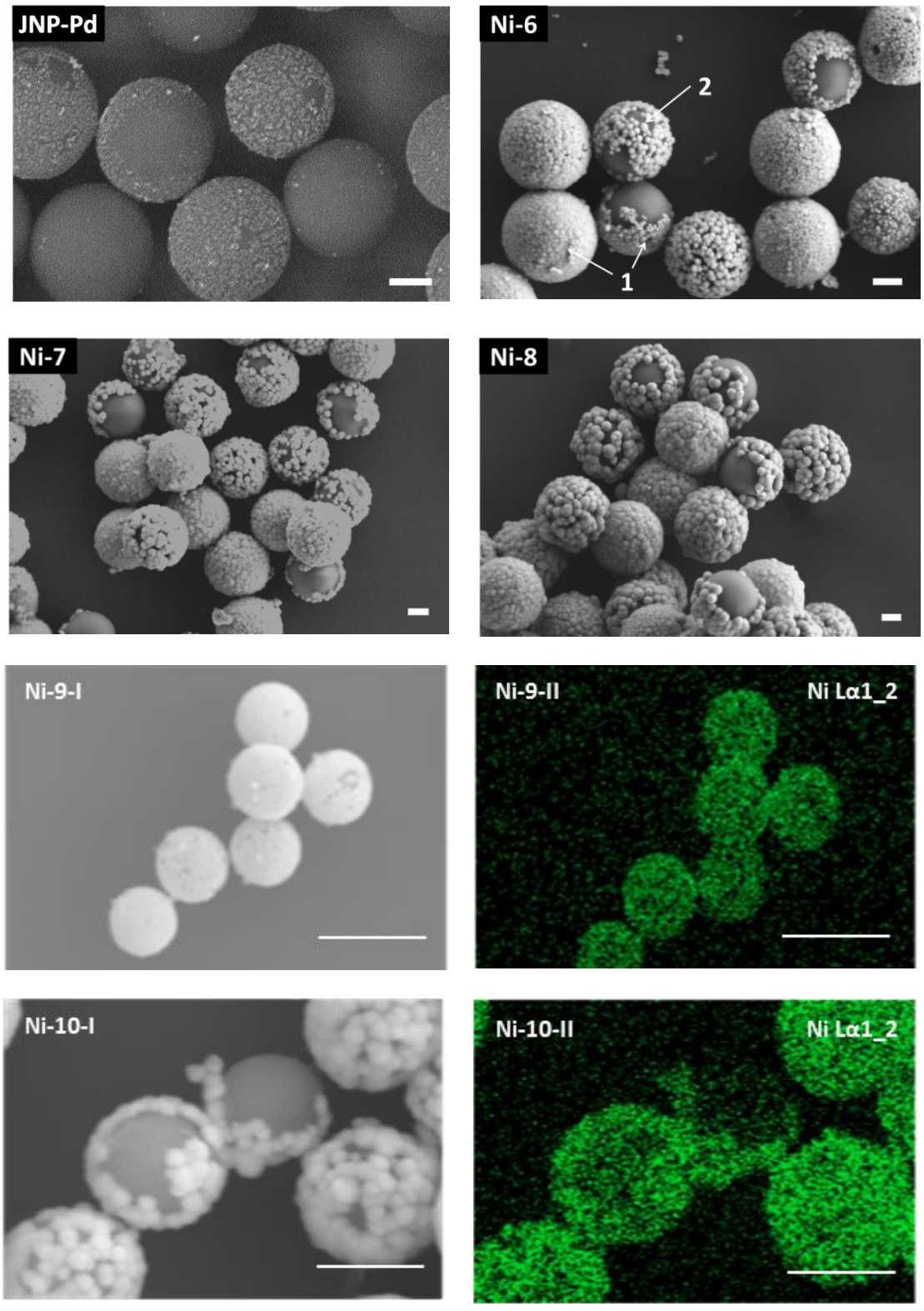


**FIGURE 4-28 SEM IMAGES OF JNP-PD) SILICA JANUS PARTICLES COATED WITH PD SEEDS AND THE CORRESPONDING JANUS PARTICLES WITH NI SEMISHELLS WITH A THEORETICAL THICKNESS OF: NI-6) 37±2 NM; NI-7) 69±2 NM; AND NI-8) 80±2 NM, SCALE BAR = 200 NM, NI-9-I) SILICA PARTICLES WITH NI FULLSHELLS (33±1 NM), SCALE BAR = 1 µM, AND NI-10-I) SILICA JANUS PARTICLES WITH NI SEMISHELLS (80±2 NM), AND THEIR CORRESPONDING EDX MAPPING IMAGES FOR NI MEASURED WITH 10 KV, SCALE BAR = 500 NM.**

The measured average Ni shell thickness, obtained from FIB, is 37±1 nm for JNP-Ni-1, and it corresponds to the theoretical thickness of (37±2 nm). However, the calculated thickness from the ICP-OES results is lower. In the case of JNP-Ni-2 and JNP-Ni-3, with theoretical 2/3-shell thicknesses of (69±2 and 80±2 nm, respectively), the layer thicknesses measured in FIB and using ICP-OES are ~20 nm thinner. The corresponding SEM images (Figure 4-28) show similar to JNP-Ni-1, small Ni clusters (34±7 nm in diameter) that merged into layers, as well as larger Ni clusters (62±15 nm in diameter) forming shells with occasional voids. The SEM images from the cross-section of the sample JNP-Ni-3 (Figure 4-29 Ni-8-I and Ni-8-II) show different shell thicknesses within one specimen, which explains the high error margins.

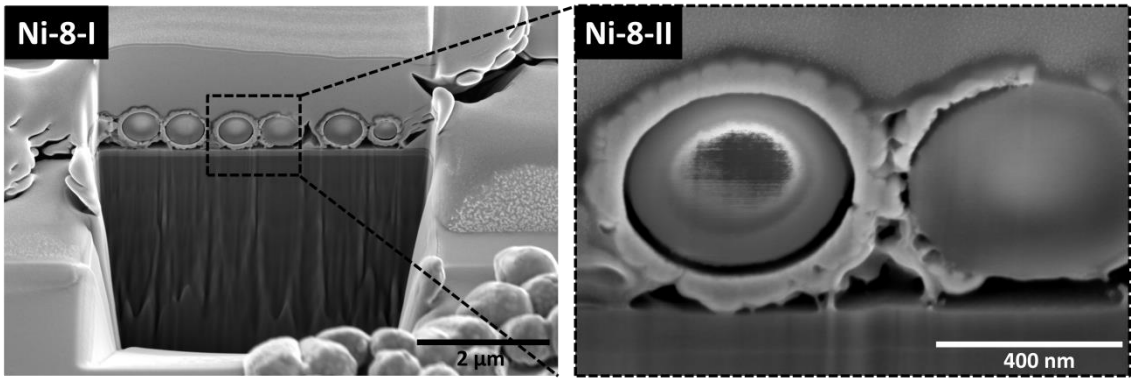


**FIGURE 4-29 SEM IMAGES OF THE CROSS-SECTION OF SILICA PARTICLES WITH COPPER SEMISHELLS WITH AN ESTIMATED LAYER THICKNESS OF 71±2 NM (JNP-NI-3) OBTAINED USING FIB. THE DARK SPOT INSIDE THE SILICA CORE IN THE IMAGE NI-8-II IS AN ARTIFACT GENERATED DURING THE PREPARATION OF THE IMAGE AND IS NOT PRESENT IN THE INITIAL IMAGE NI-8-I.**

The obtained experimental data for Janus semishells corresponds to the findings for full Ni nanoshells, and hence, the same shell growth model as described in Figure 4-27 can be applied. For the sake of completeness, the chemical composition was investigated using Energy Dispersive X-ray (EDX) spectroscopy at 10 kV. The so-called EXD mapping mode creates an image of the different emitted energies. The mapping image for Ni was generated for Ni fullshells (Full-Ni-4, Figure 4-28 Ni-9-II) and for silica particles with semishells (JNP-Ni-3, Figure 4-28 Ni-19-II). The image for the Ni contained a green crescent moon shape (particles labeled as “2”), where the Ni semishell appears in the SEM image (particles labeled as “1”).

After successfully plating and characterizing both precursor colloids with Ni-EL 1, the commercially available Nichem6200 was used. Colloids entirely coated with Pd seeds (547±36 in diameter), as well as partially coated silica Janus particles (609±32 nm in diameter) were plated with different amounts of Nichem6200 (see Table 4-19). For the silica particles with Ni fullshells (Full-Ni-6) the theoretical thickness (44±1 nm) is lower than the one measured by SEM (55±34 nm). Since the exact amount of Ni inside the solution was not tested, the discrepancy can result from the Ni content of the electrolyte. Alternatively, similar to the findings with Ni-EL 1, the higher value can result from the shrinking of the uncoated colloid by the electron beam.[162] In the case of silica particles with semishells (JNP-Ni-4) the theoretical layer thickness for a 2/3-shell coverage (74±2 nm) is in good agreement with the thickness measured by SEM (76±8 nm).

**TABLE 4-19 OVERVIEW OF THE SHELL THICKNESS DATA FOR SILICA PARTICLES WITH NI FULLSHELLS AND SEMI SHELLS (JANUS) WITH THE NICKEL ELECTROLYTE NICHEM6200**

| | Dispersion mixture | | Shell thickness [nm] calculated from | | |
|---|---|---|---|---|---|
| Sample | $A_{Silica}$ $10^{18}$ [$nm^2$/L] | Ni [g/L] | Theoretical for full shell | Theoretical for 2/3-shell | SEM |
| Full-Ni-6 | 2.2±0.7 | 1 | 44±1 | – | 55±34 |
| JNP-Ni-4 | 2.0±0.5 | 1 | – | 74±2 | 76±8 |

The SEM images of both samples (Figure 4-30 Ni-9 and Ni-10) resemble the corresponding images from the samples prepared with the Ni-EL 1 electrolyte regarding the layer deposition. The similar Ni film deposition can result from the similar Pd-seeds-coated precursor and from a similar electrolyte formulation. Since the sole purpose of testing a commercial electrolyte was to examine the transferability of the colloid plating to a different electrolyte, the SEM images serve as prove that the Pd-seeded precursor colloids are suitable to catalyze the electroless Ni deposition.

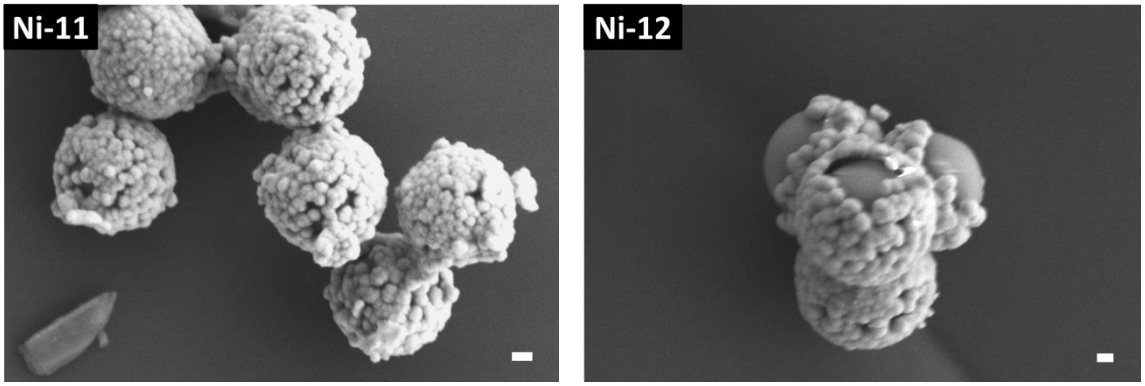


**FIGURE 4-30 SEM IMAGES OF NI-11) SILICA PARTICLES COATED WITH NI FULLSHELLS WITH A THEORETICAL THICKNESS OF 44±1 NM (FULL-NI-6) AND NI-12) SILICA JANUS PARTICLES NI SEMISHELLS WITH A THEORETICAL 2/3-COVERAGE THICKNESS OF 74±2 NM (JNP-NI-4), SCALE BAR = 100 NM.**

## Conclusion

A new method was described to prepare silica Janus particles with Ni semishells in large quantities (~60 %) in mg scale, what can be scaled-up. With Pd-seeds-activated silica particles were used as precursors to catalyze the Ni plating onto the activated areas. The Ni deposition was investigated on fully APTES-functionalized silica particles coated with Pd seeds by preparing homogenous nanoshells with thicknesses varying from 6—33 nm (see Figure 4-25). Once the protocol was established for the full Ni nanoshells, Janus particles with semishells were successfully prepared. For both precursor types, the shell thickness was tunable by varying the amount of Ni electrolyte. Several characterization methods were used to confirm the Ni content and the layer thickness, such as ICP-OES measurements, the investigation of the colloid size before and after plating in SEM, and for selected samples a cross-section with a FIB. The commercially plating bath (Nichem 6200) was applied for preparing full Ni nanoshells, as well as semishells. In both cases, the desired shells thicknesses were fabricated. That confirms that the precursor particles are suitable candidates for preparing shells from different Ni electrolytes.

### 4.3.4. JANUS PARTICLES COATED WITH COPPER SEMISHELLS

Silica Janus particles with copper (Cu) semishells were successfully synthesized for the first time during this present study, to our knowledge. Similar to the Ni semishell coatings (Chapter 4.3.3), silica particles coated with Pd seeds served as precursors to catalyze the electroless Cu deposition from two different electrolytes: a modified electrolyte described in the literature (Cu-EL 1);[10b] and a solution from Atotech called Printoganth PV (see Figure 4-31).

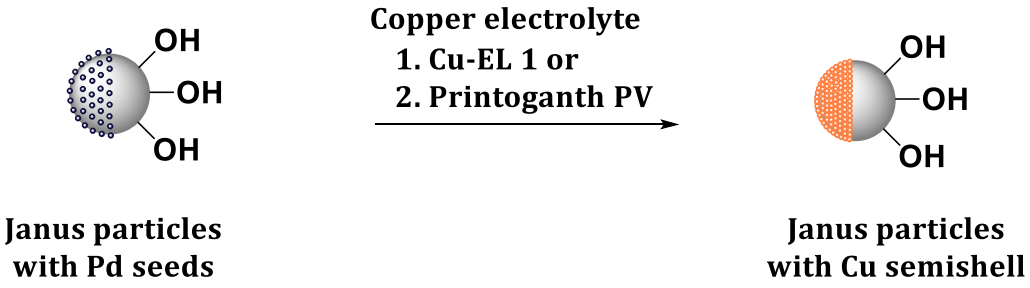


**FIGURE 4-31 SCHEMATIC OVERVIEW OF THE STRATEGY TO SYNTHESIZE SILICA PARTICLES WITH CU SEMISHELLS.**

As described for the electroless Cu plating in Chapter 2.3, a typical electroless Cu electrolyte comprises a Cu source, a reducing agent, complexing agents, and a stabilizer that prevents an excess of free $Cu^0$ seeds in the solution. Cu-EL 1 contained copper sulfate ($CuSO_4$, 0.01 M, 0.63 g/L Cu) as metal ion source. The reduction of $Cu^{2+} \rightarrow Cu^0$ was achieved with a reducing agent that has more negative redox potential than $Cu^{2+}/Cu$ (0.34 V (NHE)).[161] Formaldehyde (0.17 M) was a suitable candidate considering its redox potential of -1.11 V (NHE) in alkaline medium.[165] Sodium hydroxide (0.25 M) served as a pH regulator in the solution with pH ~13. Once the $CuSO_4 \cdot 5H_2O$ is dissolved in an alkaline solution, the insoluble $Cu(OH)_2$ is generated. To avoid precipitation and to prevent spontaneous metal reduction and deposition, a complexing agent (potassium sodium tartrate, 0.09 M) was added. Since copper(II) ions have the coordination number 4 and 6, depending on the coordination number and nature of ligands, either tetrahedral or square planar complexes are formed with four ligands, or octahedral complexes are formed with six ligands. To ensure the stability of the Cu electrolyte, stabilizers (2,2'-bipyridine, 0.03 mM and N,N'-diethyl thiourea, 1.51 µM) were introduced to suppress the formation of Cu(I) ions which can disproportionate to Cu(II) ions, as

well as to $Cu^0$ nuclei. These nuclei can catalyze the deposition of the Cu ions inside the solution. The stabilizer molecules shield the nuclei by adsorbing at their surface and hence hinder the adsorption of electroactive Cu species. In the case of the commercial electrolyte Printoganth PV, the technical datasheet only provided information about the Cu concentration (2.2±0.2 g/L).

In preliminary experiments, when the electrolyte (Cu-EL 1) containing all the ingredients was added to the precursor mixture, small $Cu^0$ nuclei were observed in the SEM, as well as silica colloids were detected without any Cu shells. Therefore, it was decided to introduce the reducing agent dropwise after the Cu-EL 1 was added to the precursor dispersion since it is well-known that once the reducing agent is introduced into the Cu electrolyte, $Cu^0$ nuclei start forming.[59]

The plating procedure was similar to the Ni deposition (Chapter 4.3.3). Depending on the desired shell thickness, different amounts of electrolyte were added to the dispersion mixture. Once the blue Cu electrolyte was introduced, the evolution of hydrogen gas started, and the color of the mixture changed from blue to metallic orange, caused by the creation of elementary $Cu^0$. The process continued until the Cu content in the bath was exhausted and the hydrogen evolution stopped (Equation (2-6)).

The growth of the Cu shell was investigated on fully APTES-functionalized silica particles coated with Pd seeds (568±36 nm in diameter, prepared according to Chapter 4.3.1) by varying the electrolyte concentration. In the case of sample Full-Cu-5, the reaction temperature inside the alkaline mixture was increased from 35 °C to 60°C, which dissolved the silica core inside the Cu shell during the deposition process. Since the silica was dissolved, the result from ICP-OES could not be used to calculate a shell thickness. In Table 4-20, all results for the step-by-step shell growth are summarized similarly to proceedings with the Ni data (Chapter 4.3.3). In general, the calculated theoretical shell thicknesses are confirmed by the experimental findings from the ICP-OES results for the samples Full-Cu-1 to Full-Cu-4.

**TABLE 4-20 OVERVIEW OF ALL REACTION PARAMETERS AND RESULTS FOR THE SYNTHESIS OF SILICA PARTICLES WITH DIFFERENT CU FULLSHELL THICKNESSES USING CU-EL 1 (0.63 G/L CU CONTENT)**

| | Amounts used for ICP-OES | | Shell thickness [nm] calculated from | | | |
|---|---|---|---|---|---|---|
| Sample | $A_{Silica}$ $10^{18}$ [$nm^2$/L] | Cu content [mg/L] | Theoretical | ICP-OES | SEM | FIB |
| Full-Cu-1 | 0.8±0.2 | 701±4 | 7±2 | 10±6 | 9±33 | — |
| Full-Cu-2 | 1.4±0.4 | 208±10 | 13±2 | 16±7 | 16±34 | — |
| Full-Cu-3 | 4.7±1.1 | 802±40 | 19±2 | 22±2 | 27±35 | — |
| Full-Cu-4 | 2.9±0.9 | 1090±54 | 35±1 | 38±3 | 39±34 | 42±7 |
| Full-Cu-5 | — | — | 35±1 | — | 48±33 | 43±10 |

The thicknesses calculated from the diameter differences in SEM is also in agreement with the corresponding theoretical shell thickness values. Only the thickness value obtained from SEM for Full-Cu-3 leads to a slightly higher value compared to the theoretical value but is still in the acceptable range. Consequently, it can be deduced that all the Cu inside the electrolyte was deposited onto the silica surface. The SEM image for Full-Cu-1 (Figure 4-32 Cu-1) shows that the silica surface is covered with single Cu clusters ranging from 13—35 nm in diameter, as well as some merged clusters, while sparing some areas, probably caused by heterogeneous Pd seeds coverage. In the presence of 0.21 g/L Cu during the plating, the corresponding image for Full-Cu-2 (Figure 4-32 Cu-2) shows colloids with closed and almost closed Cu layers. The SEM images for Full-Cu-3 and Full-Cu-4 (Figure 4-32 Cu-3 and Cu-4) resemble Full-Cu-2 regarding layer deposition.

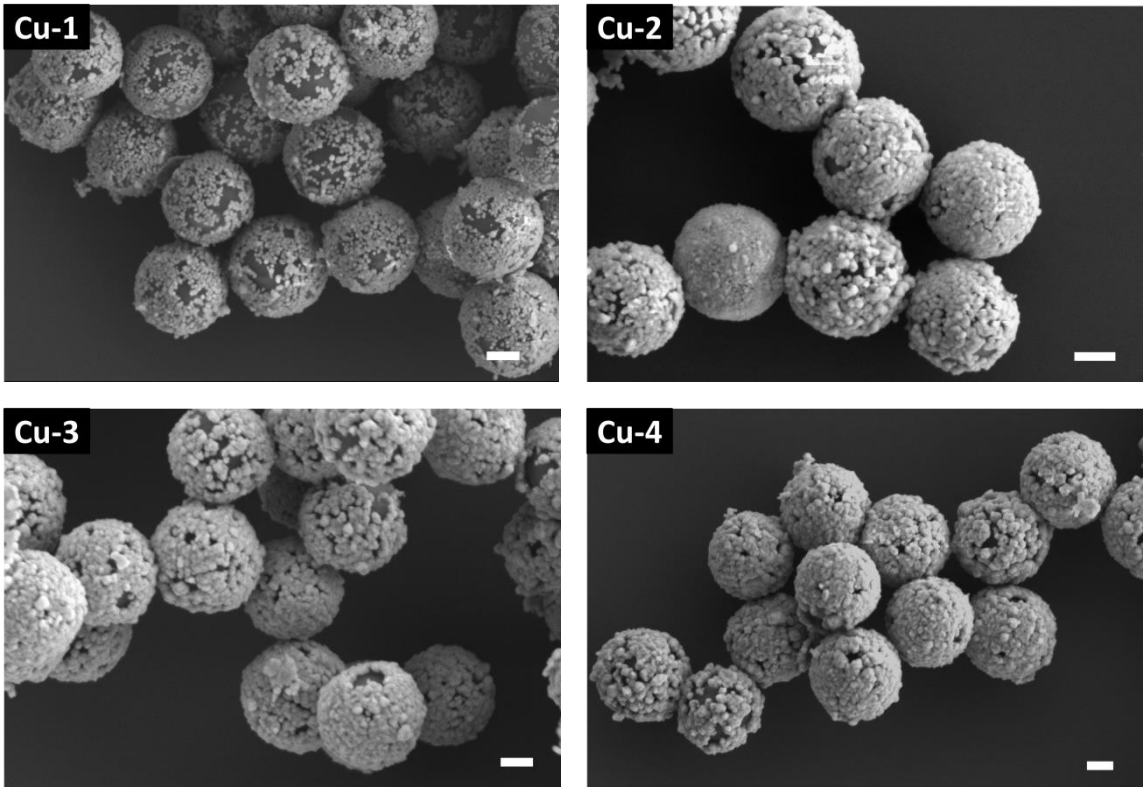


**FIGURE 4-32 SEM IMAGES OF THE MONITORING OF THE CU FULLSHELL GROWTH WHEN THE THEORETICAL SHELL THICKNESS WAS: CU-1) 7±2NM (FULL-CU-1), CU-2) 13±2 NM (FULL-CU-2), CU-3) 19±2NM (FULL-CU-3), AND CU-4) 37±1 NM (FULL-CU-4), SCALE BAR = 200 NM.**

The cross-section image of Full-Cu-4 (Figure 4-33 Cu-4-II) shows shell thicknesses between ~30 nm (particle labeled as "1") and ~50 nm (particle labeled as "2"), with small size deviation within one Cu shell. However, the overall mean of the measured shells (42±7 nm by SEM) is in good agreement with the other values.

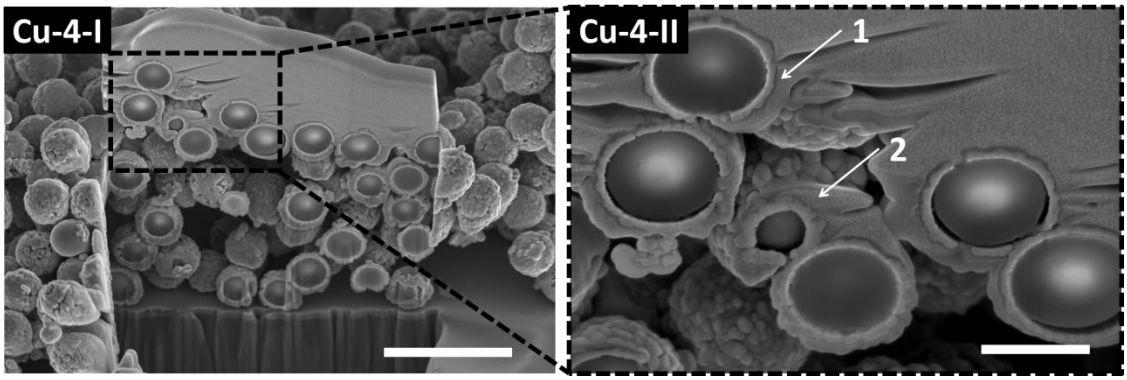


**FIGURE 4-33 SEM IMAGES OF THE CROSS-SECTION OF SILICA PARTICLES WITH CU FULLSHELLS WITH A THEORETICAL LAYER THICKNESS OF 37±1 NM (FULL-CU-4) OBTAINED USING FIB, CU-4-I) SCALE BAR = 2 μM AND CU-4-II) SCALE BAR = 500 NM.**

It can be summarized that the observed Cu layer deposition in SEM resembled the Ni layer deposition images (see Figure 4-25). A reason can be that the same precursor batch was utilized for both metal experiments and therefore, the same model as the illustrated for Ni in Figure 4-27 can be applied. Although the results of the different measurement methods for the shell thickness corresponds to the shell thickness assuming full conversion of the Cu precursor, sometimes small residues of Cu nuclei were detected in the supernatant after the centrifugation step but not on the specimen during the SEM investigations. Although the desired shell thicknesses were obtained, an increase in stabilizer concentration might reduce the presence of the Cu nuclei further.

When the reaction temperature was increased to 60°C at pH ~13 during the plating, the silica particles were completely dissolved, while leaving the Cu shell unharmed (Figure 1 16 Cu-5). The ICP-OES results confirmed that the Cu shell was empty since no silicon was detected. The SEM image of the cross-section (Figure 1 16 Cu-5-I) also shows the absence of the silica core. The measured thicknesses obtained from SEM (48±33 nm) and from the cross-section obtained using FIB (43±10 nm) are in good agreement with the theoretical value (37±1 nm).

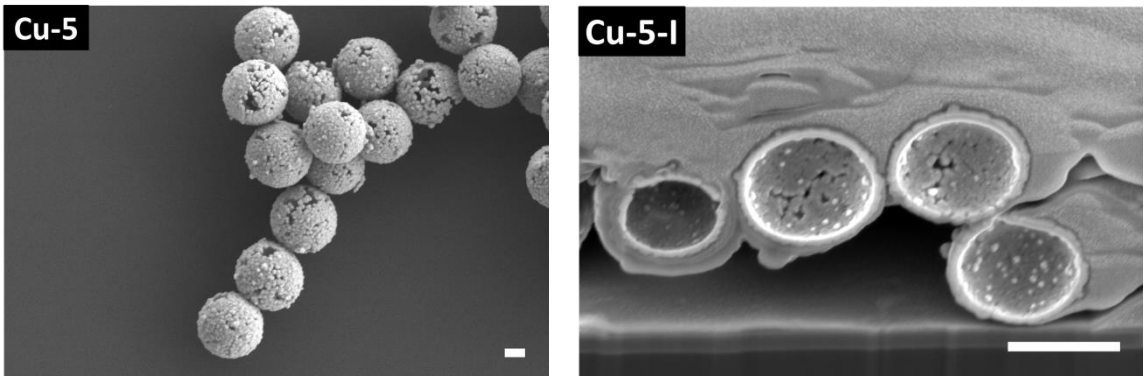


**FIGURE 4-34 SEM IMAGES OF CU-5) EMPTY CU FULLSHELLS WITH A THEORETICAL SHELL THICKNESS OF 37±1 NM (FULL-CU-5), SCALE BAR = 200 NM AND CU-5-I) CROSS-SECTIONS OF EMPTY COPPER FULLSHELLS WITH AN ESTIMATED SHELL THICKNESS OF 37±1 NM OBTAINED BY FIB, SCALE BAR =500 NM.**

Consequently, it can be deduced that all the Cu inside the electrolyte was deposited, while no Cu layer alteration was observed during the dissolution of silica. It can be suggested that the Cu deposition is faster ( ~5 nm/min at 35 °C and 30 nm/min at 60°C)[10b] than the silica dissolution at 60 °C. This method enables the creation of hollow Cu nanoshells in a one-pot manner and more important

without the usage of hazardous hydrofluoric (HF) etching. The Cu nanoshells can be applied in various fields because of their strong optical absorption at the near-infrared wavelength.[166]

After establishing a protocol for the Cu fullshells, silica Janus particles with semishell coatings were synthesized. Similar to the Ni semishells, coverage degrees of approximately 53—77% were suggested first; but for the sample JNP-Cu-1, a halfshell coverage is more in agreement with the SEM images (see Figure 4-35 Cu-6). When Pd-seeded precursor colloids (2.46±0.62 $10^{18}$ $nm^2/L$) reacted with the electrolyte Cu-EL 1 (0.18 g/L Cu), a theoretical thickness value of 22±4 nm was calculated (see Table 4-21). The result obtained by ICP-OES that was converted into a potential halfshell coverage (24±13) and the shell thickness measured directly from the cross-section using FIB (29±6 nm) are in good agreement with the theoretical value.

**TABLE 4-21 OVERVIEW OF ALL SHELL THICKNESS DATA FOR SILICA JANUS PARTICLES WITH CU HALFSHELLS USING CU-EL 1 (0.63 G/L CU)**

| | Dispersion mixture | | Shell thickness [nm] calculated from | | |
|---|---|---|---|---|---|
| Sample | $A_{Silica}$ $10^{18}$ [$nm^2/L$] | Cu [g/L] | Theoretical for halfshell | ICP-OES for halfshell | FIB |
| JNP-Cu-1 | 1.8±0.4 | 0.18 | 22±4 | 24±13 | 29±6 |

The SEM image of the cross-section (see Figure 4-35 Cu-6-I) shows Janus particles with uncoated areas (particle labeled as "1"), as well as semishells with thicknesses between ~20 nm (particle labeled as "2") and ~40 nm (particle labeled as "3"). Finally, the EDX mapping image for the Cu at 10 kV comprises green round shapes, where the Cu-coated full nanoshells appear in the SEM (Full-Cu-4, Figure 4-35 Cu-7-I); and contains a green crescent moon shape (particles labeled as "1"), where the Cu semishell appears in the SEM image (JNP-Cu-1, Figure 4-35 Cu-6-III).

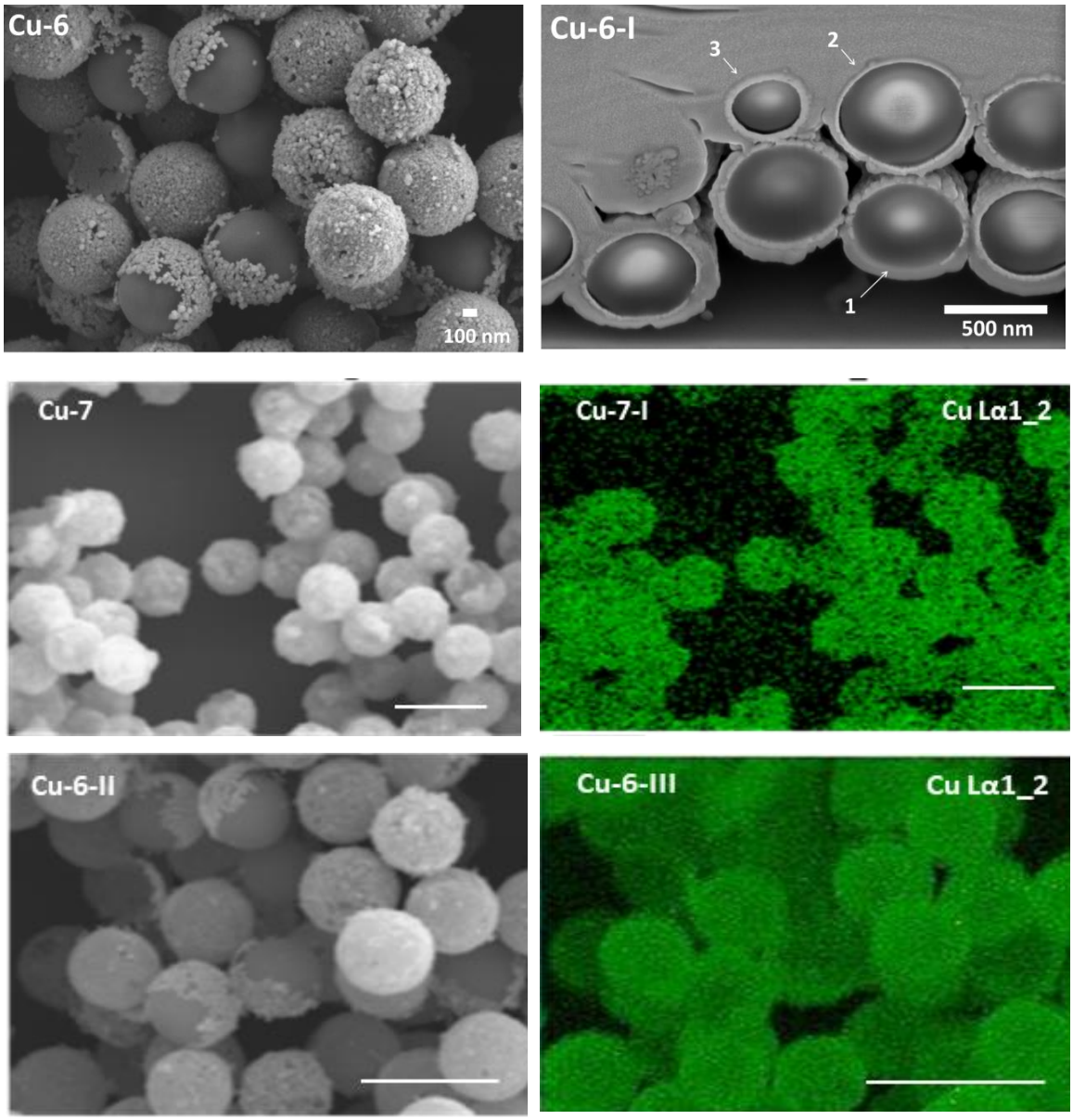


**FIGURE 4-35 SEM IMAGES OF CU-6) SILICA JANUS PARTICLES COATED WITH COPPER1/2-SEMISHELLS WITH A THEORETICAL THICKNESS OF 22±4 NM (JNP-CU-1), AND CU-6-I) THE CORRESPONDING CROSS-SECTION OBTAINED USING FIB AND CU-7) SILICA PARTICLES WITH CU FULLSHELLS (FULL-CU-4, 35±1 NM) AND CU-6-II) EQUAL TO CU-6 AND THEIR CORRESPONDING EDX MAPPING IMAGES FOR CU, MEASURED AT 10 KV, SCALE BAR= 1 µM.**

After successfully plating and characterizing both precursor colloids with the Cu-EL 1, the commercial solution Printoganth PV was used to test the reproducibility towards other Cu electrolytes. Janus particles coated with Pd seeds were plated with the electrolyte, and the results are summarized in Table 4-22. In both cases, the theoretical thickness was calculated assuming a halfshell coverage of the silica particles (46±3 nm).

TABLE 4-22 OVERVIEW OF SHELL THICKNESS DATA FOR SILICA JANUS PARTICLES WITH CU FULLSHELLS OBTAINED FROM THE ELECTROLYTE PRINTOGANTH PV (2.2 G/L CU)

| | Dispersion mixture | | Shell thickness [nm] calculated from | |
|---|---|---|---|---|
| Sample | $A_{Silica}$ $10^{18}$ [$nm^2$/L] | Cu [g/L] | Theoretical for halfshell | SEM |
| JNP-Cu-2 | 2.0±0.6 | 0.44 | 46±3 | 62±20 |
| JNP-Cu-3 | 2.0±0.6 | 0.44 | 46±3 | 49±21 |

The SEM image of JNP-Cu-2 (Figure 4-36 Cu-7) consists of particles with Cu layer thicknesses between 27—113 nm, with a mean value of 62±20 nm. Similar fluctuating layer thicknesses between 26—104 nm (mean = 49±21 nm by SEM) are observed for JNP-Cu-3 (see Figure 4-36 Cu-8). Both samples contain many non-coated particles and some small nuclei, which probably resulted from the reducing agent that was inside the electrolyte before the colloidal dispersion was added.

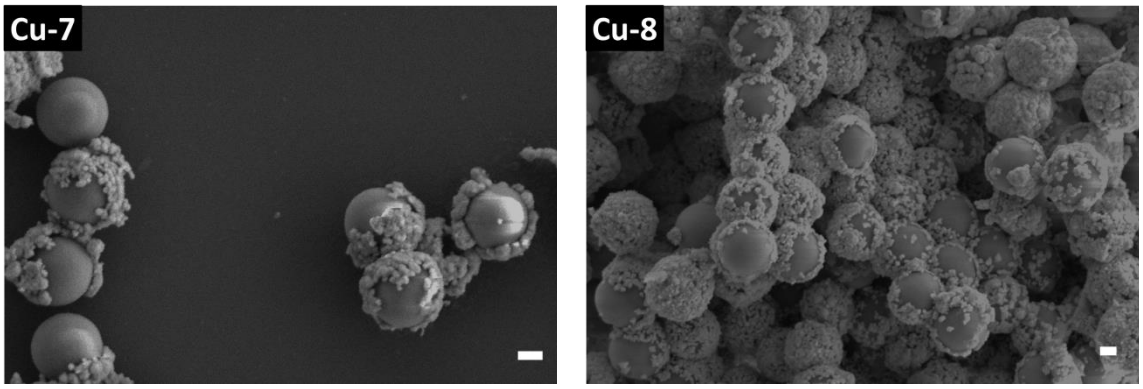


FIGURE 4-36 SEM IMAGES OF CU-7) SILICA JANUS PARTICLES COATED WITH CU SEMISELLS WITH A MEASURED THICKNESS OF 62±20 NM (JNP-CU-2) AND CU-8) SILICA JANUS PARTICLES COATED WITH CU SEMISELLS WITH A MEASURED THICKNESS OF 49±21 NM (JNP-CU-3), SCALE BAR = 200 NM.

Since the only purpose for plating with the second electrolyte was to investigate the applicability of the Pd-seeded precursor particles with different Cu electrolyte; it can be reasoned that the layer deposition is achieved but in an uncontrollable manner. Moreover, since the electrolyte contains six unknown ingredients; the reason for the heterogeneous deposition is not discussed further.

**Conclusion**

The experimental data for the Cu fullshell and semishell fabrication confirms the finding for the preparation of silica colloids with Ni nano-and semishells (Chapter 4.3.3). For the first time, colloids with Pd-activated surfaces are used to prepare silica particles with tunable Cu shell thicknesses using the electrolyte Cu-EL 1. The Cu layer morphology and the deposition process resemble those of the Ni samples. Since in both cases the same precursor batch is used, it can be reasoned that morphology depends of the catalyst distribution. Additionally, a one-step synthesis is introduced to create successfully hollow Cu nanoshells without HF etching. When the Cu electrolyte Printoganth PV was used, Cu semishells were prepared with heterogeneous layer thicknesses.

### 4.3.5. JANUS PARTICLES COATED WITH GOLD SEMISHELLS

Several procedures have been developed over the years to prepare silica particles with gold (Au) semishells. Here, silica particles coated with Pd seeds served as precursors to catalyze the electroless Au deposition and to create Au semishells (see Figure 4-37). The Au electrolytes (Au-EL 1) was prepared according to Graf et al.[68d] The purpose was to prove that these precursor colloids (prepared according to Chapter 4.3.1) are also suitable to generate Au semishells.

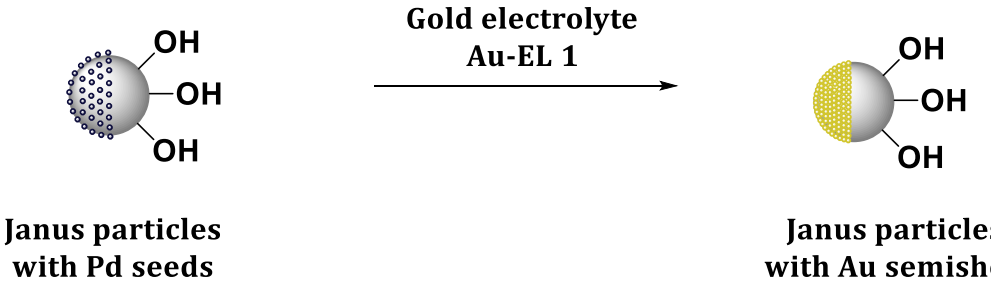


**FIGURE 4-37 SCHEMATIC OVERVIEW OF THE STRATEGY TO SYNTHESIZE SILICA PARTICLES WITH AU SEMISHELLS.**

Core-shell colloids with a dielectric core and noble metal shells (gold or silver) are attractive composites because of the versatile application fields (see Chapter 2.3.3). Especially when their symmetry is broken, the newly obtained properties expand the fields. Silica particles with gold (Au) semishells are usually prepared using the following procedures: 1) the evaporation of an Au film upon a close-packed monolayer of colloids;[49] 2) the toposelective coating of silica colloids with Au nanoparticles at the microdroplet interface;[104a] 3) the chemical synthesis of full Au fullshells followed by an anisotropic etching step of the accessible hemisphere;[49] or 4) the regio-selective growth of Au layers on with Au-seeds-coated Janus spheres.[52] In the latter process, Perro et al. coated partially APTES-functionalized silica colloids with Au nanoparticles to visualize the successful functionalization of the silica sphere with amino groups,[48] since protonated amino groups electrostatically interact with negatively charged Au nanoparticles.[51] These Au seeds served as nucleation sites for the deposition of Au ions from a solution to prepare full Au nanoshells, in the presence of a reducing agent.[68] Fernandéz et al. utilized silica particles partially covered with Au seeds and deposited an Au layer onto the activated spheres.[52]

During this present work, Pd seeds coated precursors are introduced for preparing silica particles with Au semishells instead of using Au-seeds-decorated colloids. The reasons are, as mentioned in Chapter 4.3.1, the lower production cost with Pd in comparison to Au (1 g Au ~38 €, 1 g Pd ~23 €, state 04/19/2017)[153] and the wide range of functional groups that interact with Pd ions.[152]

The Au electrolyte comprised a chloroauric acid solution ($HAuCl_4$, 0.44 mM, 86 mg/L Au) that was allowed to hydrolyze with potassium carbonate ($K_2CO_3$, 1.80 mM) to gold hydroxide ($[Au(OH)_4]^-$) over several days.[100] Hydroxylamine hydrochloride has a redox potential of $NH_2OH/N_2O$ -0.4 V (NHE)[167] and is thermodynamically capable of reducing $Au^{3+} \rightarrow Au^0$ ($Au^{3+}/Au$ +1.5 V (NHE)).[168] The mild reducing agent solution of $NH_2OH{\cdot}HCl$ (1.87 mM) was prepared separately. In contrary to the Ni electrolyte Ni-EL 1 (Chapter 4.3.3), the Au electrolyte did not contain any stabilizing agents to inhibit the formation of Au nuclei inside the solution.

Depending on the desired shell thickness, different amounts of $[Au(OH)_4]^-$ solution were added into the dispersion mixture containing full APTES-functionalized silica particles coated with Pd seeds (568±36 nm in diameter, prepared according to Chapter 4.3.1). An excess of the reducing agent was added drop-wise to the mixture to ensure the Au layer deposition on the colloid surface. The dispersion color changed slowly to purple followed by strong scattering caused by the creation of elemental $Au^0$ shells at the colloid surfaces. In Table 4-23, all results for the different samples and the corresponding theoretical shell thicknesses are summarized. For the samples Full-Au-1 to Full-Au-5, the theoretical shell thicknesses are in good agreement with the measured ones from the SEM images, respectively. The calculated thicknesses from the Au contents obtained from ICP-OES for sample Full-Au-3, 4, and 5 (20±1, 17±1, and 21±6 nm), are also in agreement with the theoretical value, respectively.

**TABLE 4-23 OVERVIEW OF THE SHELL THICKNESS DATA FOR THE SYNTHESIS OF SILICA PARTICLES WITH DIFFERENT AU FULLSHELLS USING AN AU ELECTROLYTE (0.086 G/L AU CONTENT)**

| | Amounts used for ICP-OES | | Shell thickness [nm] calculated from | | | |
|---|---|---|---|---|---|---|
| **Sample** | **$A_{Silica}$ $10^{17}$ [$nm^2$/L]** | **Au [mg/L]** | **Theoretical** | **ICP-OES** | **SEM** | **FIB** |
| Full-Au-1 | – | – | 12±2 | – | 10±33 | – |
| Full-Au-2 | – | – | 13±2 | – | 16±31 | – |
| Full-Au-3 | 8.5±2.6 | 346±17 | 16±2 | 20±1 | 22±28 | – |
| Full-Au-4 | 7.9±2.5 | 279±14 | 20±2 | 17±1 | 18±30 | – |
| Full-Au-5 | 1.6±0.5 | 70±4 | 23±2 | 21±6 | 18±33 | 14±5 |
| Full-Au-6 | – | – | – | 17±9 | 19±36 | 21±9 |

For preparing a thicker Au fullshell, traces of Full-Au-5 were reacted with additional electrolyte (+ 50.6 g/L Au, sample Full-Au-6) as a test experiment, what explains the absence of a theoretical thickness. Nevertheless, the results from ICP-OES and the diameter differences obtained in SEM are similar (17±9 and 19±36 nm), respectively. Although the results correspond to the calculated value in case of full conversion of all Au ions, the supernatant contained small Au nuclei, after the purification step in the centrifuge. The investigation of the SEM images for all the samples with different shell thicknesses (see Figure 4-38) demonstrates a similar seed-mediated deposition process as described for Ni (Chapter 4.3.3).

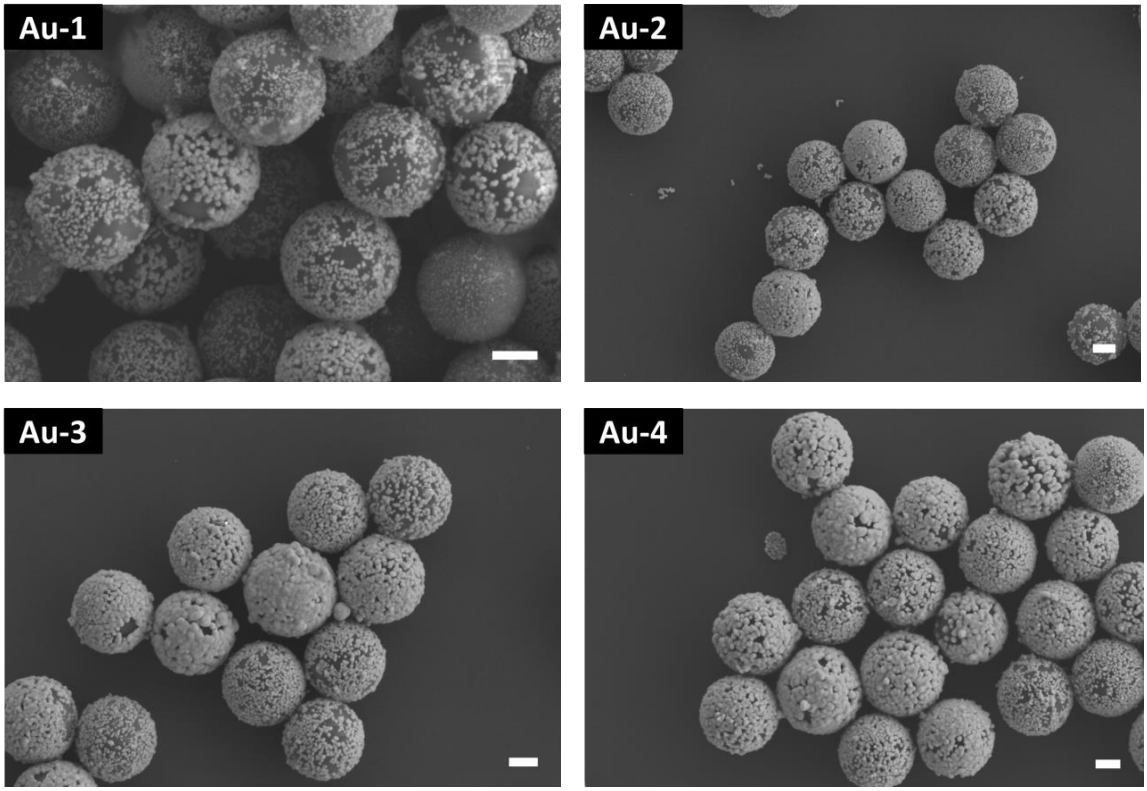


**FIGURE 4-38 SEM IMAGES OF THE MONITORING OF THE STEP-BY-STEP SHELL GROWTH OF AU FULLSHELLS WHEN THE THEORETICAL SHELL THICKNESS IS: AU-1) 12±2 NM (FULL-AU-1), AU-2) 16±2 NM (FULL-AU-3), AND AU-3) 24±2 NM (FULL-AU-5); AND WHEN THE CALCULATED NUMBER WAS THE DIAMETER DIFFERENCE IN SEM WAS AU-4) 19±1 NM (FULL-AU-6); SCALE BAR = 200 NM.**

The Pd seeds serve as nucleation site for the electron transfer from the reducing agent towards the $Au^{3+}$.[169] $NH_2OH$ is thermodynamically capable of reducing $Au^{3+}$, but the presence of Pd seeds accelerated the reaction towards the activated sphere. Nevertheless, Au nuclei were detected as side products since no stabilizer was present to prevent the formation of nuclei. The layer deposition morphology resembles the Ni layer deposition (Chapter 4.3.3), since the same precursor batch was used. It can be reasoned that the majority of the Au ions were deposited onto the activated silica colloids and the desired shell thickness can be tailored. Similar results have been reported regarding tunability of the final shell thickness, when Au seeds serve as nucleation sites.[68d, 100, 150, 170]

The Au fullshell thickness is also directly determined for the samples Full-Au-5 and 6 from the cross-section SEM images obtained using FIB (see Figure 4-39). In the image Au-3-I (Full-Au-5), layer thicknesses of ~9 nm (particle labeled as "1"), ~14 nm (particle labeled as "2"), as well as ~22 nm (particle labeled as "3") are

observed which results in an average number of 14±5 for sample Full-Au-5, which is lower than the theoretical thickness of 24±2 nm. The discrepancy in the thickness values might result from the low statistic (100 layer thickness points). When the colloids from sample Full-Au-5 were allowed to react with additional Au electrolyte, the obtained shell thicknesses in Figure 4-39 Au-4-I vary between small ~9 nm (particle labeled as "1"), medium ~20 nm (particle labeled as "2"), and large ~35 nm (particle labeled as "3"), with an average of 21±9 nm, which agrees with the calculated values from the ICP-measurement for Full-Au-5 and Full-Au-6.

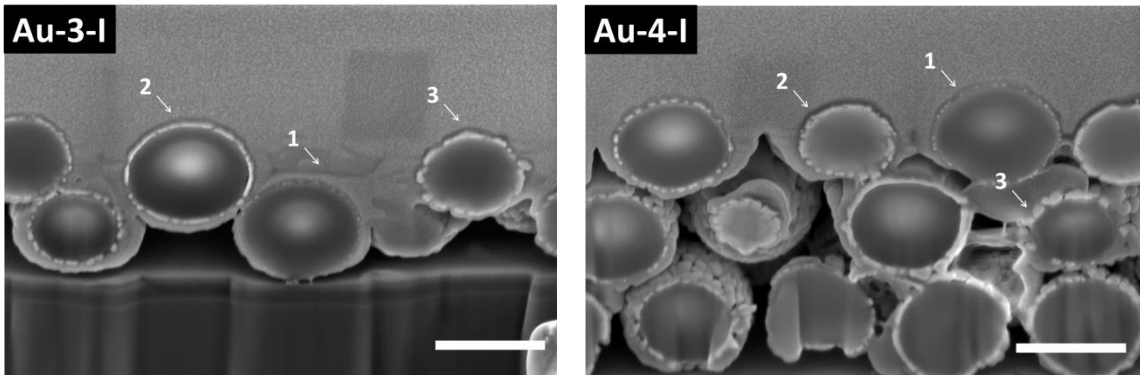


**FIGURE 4-39 SEM IMAGES OF THE CROSS-SECTION OF SILICA PARTICLES WITH AU FULLSHELLS WITH A DETERMINED LAYER THICKNESS OF 14±5 NM (FULL-AU-5) AND 21±9 NM (FULL-AU-6) OBTAINED USING FIB, SCALE BAR = 500 NM.**

It can be reasoned that the increase in the electrolyte concentration was not sufficient to alter the thickness in a significant manner. As mentioned previously for the Ni layer deposition (Chapter 4.3.3), a reason for the heterogeneous thickness is likely the inhomogeneous distribution of Pd seeds on the surface.

Similar layer depositions were also observed when Au-seeded precursor particles are utilized to deposit an Au layer from an electrolyte in the presence of reducing agents with different redox potential such as formaldehyde, hydroxylamine hydrochloride, or sodium borohydride.[68a, 68c] A direct correlation between the Au seed density and the final layer morphology was reported. Brinson et al. argued when using CO as a reducing agent; the final Au layer morphology was immune towards different variation in precursor batches or reagent preparation.[68b] During their research, a continuous layer without any voids was prepared in the presence of CO, albeit the same precursors resulted in Au layers with occasional

voids when formaldehyde was used as reducing agent. $CO/CO_2$ is a strong reducing agent for $Au^{3+} \rightarrow Au^0$ (redox potential of $CO/CO_2$ is -0.53 V (NHE)), and hence, fewer reagents are necessary for the layer deposition. It can be concluded that the layer morphology depends on the choice of the reducing agent, as well as on the Pd seeds distribution on the precursor surface.

In the next section silica Janus particles with Au semishells were synthesized and similar to the Ni semishell experiments (see Chapter 4.3.3), a 2/3 surface coverage was calculated for the precursor Janus particles. In Table 4-24 the corresponding data for sample JNP-Au-1 is presented. The theoretical shell thickness for 2/3-shells (27±2nm) is in good agreement with the result obtained from ICP-OES.

**TABLE 4-24 OVERVIEW ALL SHELL THICKNESS DATA FOR SILICA JANUS PARTICLES WITH AU SEMISHELLS USING AN AU ELECTROLYTE (0.086 G/L AU CONTENT)**

| | Dispersion mixture | | Shell thickness [nm] calculated from | | |
|---|---|---|---|---|---|
| Sample | $A_{Silica}$ $10^{17}$ [$nm^2$/L] | Au [g/L] | Theoretical For 2/3-shell | ICP-OES for 2/3-shell | FIB |
| JNP-Au-1 | 1.3±0.3 | 54.4 | 27±2 | 25±2 | 20±5 |

The corresponding images in Figure 4-40 show samples of a dense Au layer, as well as some with isolated Au clusters. Additionally, the EDX mapping image was generated for Au fullshells at 10 kV (Full-Au-6, Figure 4-40 Au-6-I) and for silica particles with Au semishells (JNP-Au-2, Figure 4-40 Au-7-I). The image for the Au contained a green crescent moon shape (particle labeled as “1”), where the Au semishell appears in the SEM image.

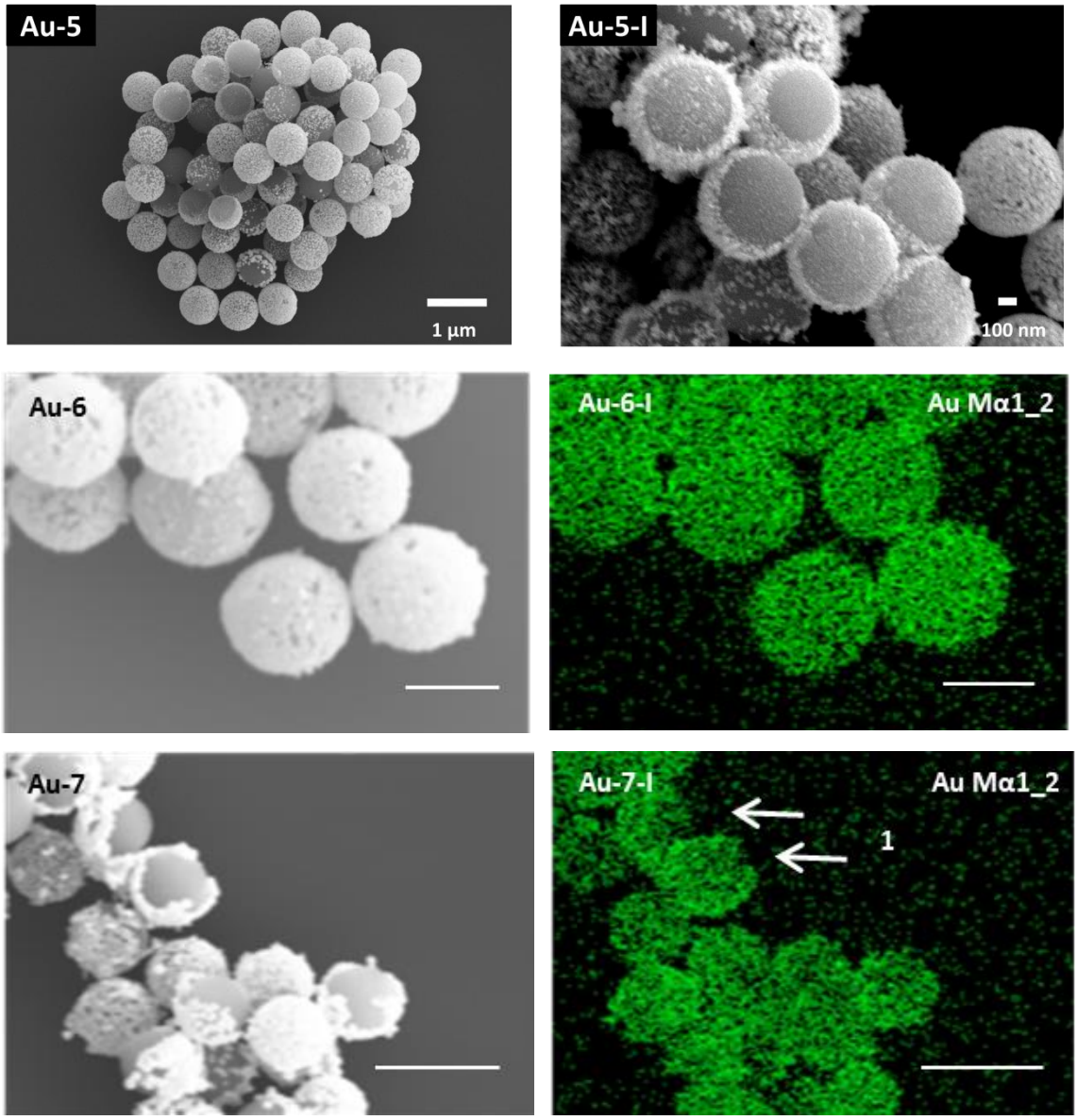


**FIGURE 4-40 SEM IMAGES OF SAMPLES AU-5 AND AU-5-I) TWO DIFFERENT REGIONS WITHIN THE SAME SPECIMEN OF JNP-AU-1WITH A THEORETICAL 2/3-SHELL THICKNESS OF 27±2 NM, AND AU-6) SILICA PARTICLES WITH FULL AU FULLHELLS (FULL-AU-6) AND AU-7) SILICA JANUS PARTICLES WITH AU SEMISHELLS (JNP-AU-2), AND THEIR CORRESPONDING MAPPING IMAGES FOR AU, MEASURED AT 10 KV (GREEN COLOR) OBTAINED FROM EDX SPECTROSCOPY, SCALE BAR TOP = 500 NM AND BOTTOM =1 µM.**

The actual shell thicknesses vary between 11—26 nm (mean = 20±5 nm by SEM), which is detected from the cross-section of the samples, and is in agreement with the thickness values obtained by the other characterization methods. In the images in Figure 4-41, closed Au shells, as well as individual Au clusters are observed. The SEM image of the cross-section resembles the findings of the Ni layer deposition in Chapter 4.3.3.

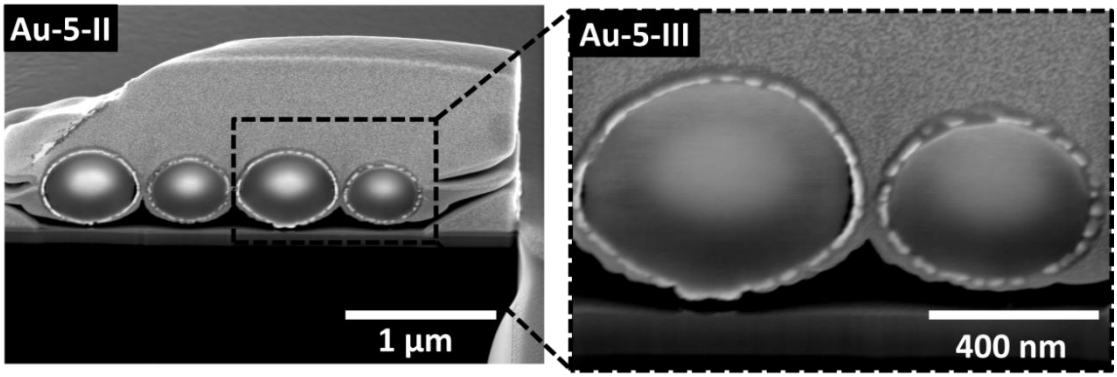


**FIGURE 4-41 SEM IMAGES OF THE CROSS-SECTION OF SILICA JANUS PARTICLES WITH AU SEMISHELL COATING (JNP-AU-1) OBTAINED BY FIB.**

## Conclusion

Au fullshells and semishells with tunable shell thickness were successfully prepared using Pd-seeded precursor particles and plating them with an Au electrolyte (Au-EL 1), similar to the experimental finding for silica colloids with Ni shells (Chapter 4.3.3). The Au layer morphology and deposition resembled those of the Ni samples and the Cu samples since in all three cases the same precursor batch was used.

### 4.3.6. JANUS PARTICLES COATED WITH SILVER SEMISHELLS

As mentioned previously for Au semishells (Chapter 4.3.5), nanocomposites of dielectric cores and noble metal shells such as silver (Ag) and Au have unique optical properties, and therefore, several approaches have been already introduced to prepare silica colloids with Ag semishells or patchy coverages.[104b, 104c] Since the purpose of this present study was to prepare potential adhesion promoter with versatile metal semishell coverages, the preparation of the silica colloids with Ag semishell was realized to test the feasibility for another metal. Here, silica particles activated with Pd seeds are used as precursor particles to catalyze the electroless Ag deposition onto the activated spheres using an electrolyte from literature (see Figure 4-42).[101]

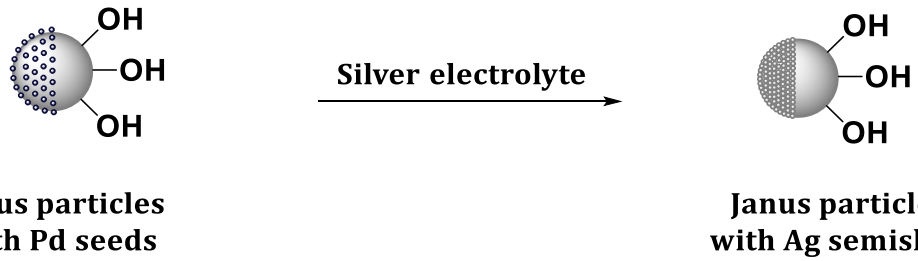


**FIGURE 4-42 SCHEMATIC OVERVIEW OF THE STRATEGY TO SYNTHESIZE SILICA PARTICLES WITH AG SEMISHELLS.**

The aspects of electroless Ag deposition are introduced in Chapter 2.3. The Ag electrolyte comprises $AgNO_3$ (0.005 M, 0.54 g/L Ag) as the metal source with a redox potential of $Ag^+/Ag$ +0.8 V (NHE).[168] Under acidic conditions, formaldehyde (12 %, 11.4 M) is a slow reducing agent (redox potential of +0.034 V (NHE)).[167] When the pH of the solution is increased ($NH_4OH$ solution, 3.7 %, 2.14 M), the redox potential is negative enough to accelerate the electron transfer (pH 11, -1.07 V (NHE)).[59, 167] The Ag ions are reduced in the presence of formaldehyde and base, even in the absence of a catalyst such as Pd or Au, which is known as the Tollens' reaction. Therefore, the sequence of compounds added to the mixture needs to be followed, as described in the following. In preliminary experiments, when the silica particle dispersion was added to the Ag bath after the addition of formaldehyde, no shell growth occurred on the silica particles. Instead, the formation of huge Ag

cluster was observed in SEM. When the correct sequence of the bath components was used, shell-like layers of Ag were deposited on the Pd-activated silica spheres.

Similar to the previous metal depositions (see Ni in Chapter 4.3.3), the preparation of the desired shell thickness was achieved by varying the Ag concentration in the plating solution. After the colloidal dispersion was added to the corresponding Ag solution, the pH of the mixture was changed to alkaline to increase the reduction abilities of formaldehyde. The reducing agent was slowly added to the mixture and the color changed immediately to gray caused by the creation of elemental $Ag^0$ shell on the silica surface. Some yellow nuances were observed given by the formation of small Ag nuclei. Ag nanoclusters tend to form large agglomerates because of the van der Waals or Coulomb's force, and therefore, an addition of a surfactant is essential to stabilize the created silica-core-Ag-shell colloids. In this present study, the ionic surfactant sodium dodecylbenzene sulfonate (SDBS) was used, since it shows the highest stabilizing effects in an aqueous dispersion of silver nanoparticles, according to literature.[171] The long hydrophobic chains adhere to the silver cluster surface[172], and the hydrophilic heads interact with the aqueous environment.[173] The surfactant concentration was kept below the critical micelle concentration ($8 \times 10^{-3}$ M). In the absence of surfactant, the dispersion precipitated completely, and even when the surfactant was added with a slight delay, some agglomerates were observed in SEM. Consequently, the reducing agents and the surfactant were added to the mixture simultaneously.

The shell growth was investigated by adding different electrolyte amounts (157.3—249.8 g/L Ag) to deposit Ag layers from ~19—42 nm thicknesses on silica particles entirely coated with Pd seeds (568±36 nm in diameter, prepared according to Chapter 4.3.1). In Table 4-25, all results for the theoretical thickness, as well as the experimentally obtained thickness are provided. Additionally, the actual Ag layer thickness was measured from the cross-section SEM image prepared from FIB for samples Full-Ag-5. The corresponding SEM images of the samples Full-Ag-1, 2, 4 and 5 are presented in Figure 4-43. Since the SEM images and the results for Full-Ag-3 and 4 resemble, only the image for Full-Ag-4 is presented.

TABLE 4-25 OVERVIEW OF THE SHELL THICKNESS DATA FOR THE SYNTHESIS OF SILICA PARTICLES WITH DIFFERENT AN AG FULLSHELL USING AG ELECTROLYTE (0.54 G/L AG CONTENT)

| | Dispersion mixture | | Shell thickness [nm] calculated from | | |
|---|---|---|---|---|---|
| Sample | $A_{Silica}$ $10^{18}$ [nm²/L] | Ag [mg/L] | Theoretical | SEM | FIB |
| Full-Ag-1 | 1.5±0.5 | 157.3 | 9±2 | 20±35 | – |
| Full-Ag-2 | 1.1±0.3 | 222.0 | 18±2 | 22±39 | – |
| Full-Ag-3 | 0.8±0.3 | 257.3 | 27±1 | 33±50 | – |
| Full-Ag-4 | 0.7±0.2 | 279.5 | 35±1 | 39±38 | – |
| Full-Ag-5 | 0.6±0.2 | 294.8 | 42±1 | 62±50 | 70±20 |

The corresponding SEM images of the samples Full-Ag-1, 2, 4 and 5 are presented in Figure 4-43. Since the SEM images and the results for Full-Ag-3 and 4 are highly similar, only the image for Full-Ag-4 is presented.

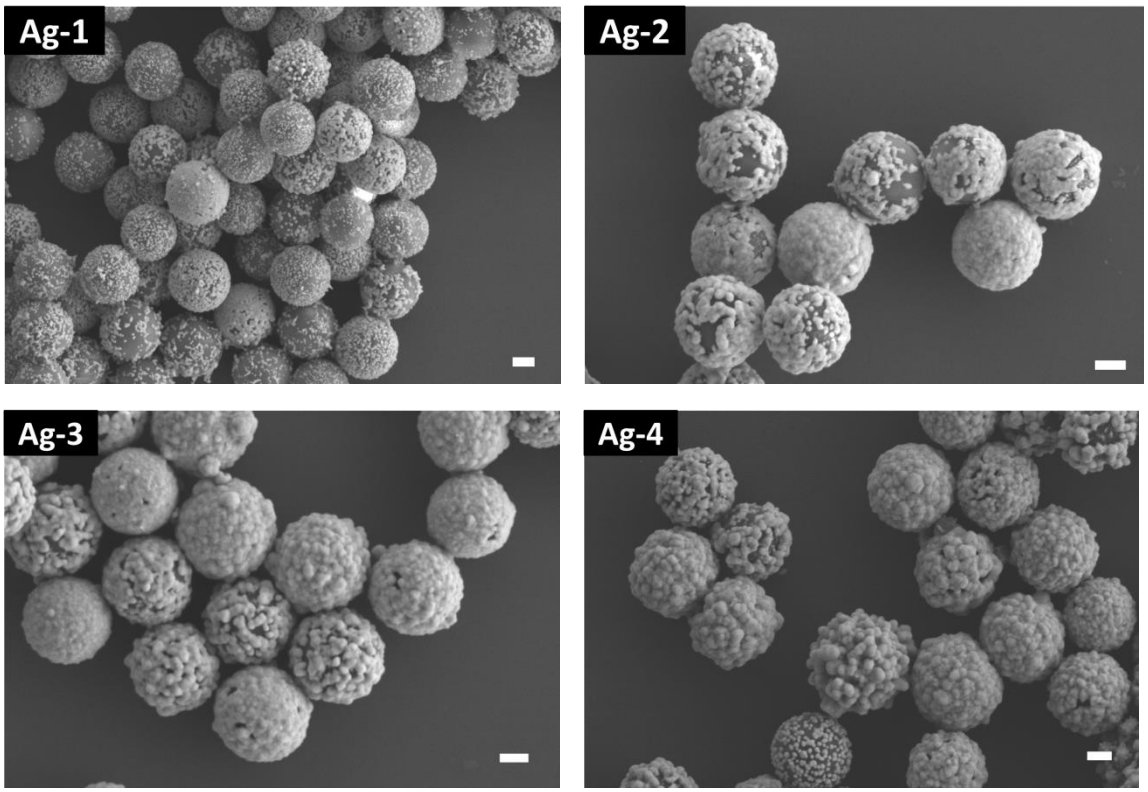


FIGURE 4-43 SEM IMAGES OF SILICA PARTICLES WITH AG FULLSHELLS WHEN THE THEORETICAL SHELL THICKNESS WAS AG-1) 9±2 (FULL-AG-1), AG-2) 18±2 (FULL-AG-3), AG-3) 35±1 (FULL-AG-4), AND AG-4) 42±1 (FULL-AG-5), SCALE BAR = 200 NM

In general, the measured shell thicknesses for Full-Ag-1 to Full-Ag-5 are higher than the theoretical values. The SEM image for Full-Ag-1 (Figure 4-43 Ag-1) shows silica colloids with single Ag clusters and some with continuous and smooth layers. The images of Full-Ag-2, 3, and 4 show mainly continuous layers with few voids. Although formaldehyde can reduce $Ag^+$ ions in alkaline solution, the Pd seeds served as nucleation sites for the electron transfer from the reducing agent towards metal ion, as described for the Ni deposition model in Chapter 4.3.3.

The SEM image of the cross-section of sample Full-Ag-5 contains Ag shell with smooth continuous layers with ~37 nm thickness (particle labeled as "1") and ~70 nm (particle labeled as "2"), and also shells comprising ~90 nm rough layers (particle labeled as "3") with an overall average of 70±20 nm thicknesses (see Figure 4-44).

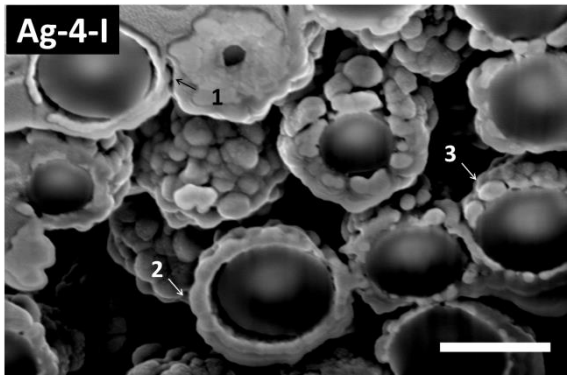


**FIGURE 4-44 SEM IMAGE OF THE CROSS-SECTION OF SILICA PARTICLES WITH AG FULLSHELLS (FULL-AG-5) OBTAINED BY FIB.**

Since the electroless Ag deposition is a fast process under these conditions, the higher thicknesses in SEM might result from the fact that some silica particles were not plated with an Ag shells and were removed during the purification step using centrifugation in conjunction with Ag nuclei. Maybe, a milder reducing agent could contribute to a more controllable deposition or the addition of stabilizing agents could prevent Ag nuclei formation, which is commonly used in industrial plating approaches,[10b] where a long lifetime of the electrolyte is favored.

In literature, the preparation of Ag nanoshells is achieved by using dielectric colloids (silica or polystyrene) with Ag seeds[174] or Au seeds[68c, 69, 175] as precursors. Thereby, the shell thicknesses can be tuned by varying the cycles of Ag depositions. In general, deposited Ag layers are rough which motivated Jackson et

al. to investigate the effects of different preparation methods on the surface morphology of silica-core-Ag-shell particles.[69] They claimed that when the base (ammonia) was introduced after the addition of formaldehyde to the dispersion mixture, the rapid increase in the pH resulted in a uniform deposition on the catalyst seeds rather than the nucleation of additional Ag colloids inside the solution. During this present study, ammonia was introduced before the reducing agent. The sequencing of the compounds might have resulted in fewer side products such as Ag nuclei and non-plated silica.

Subsequently, silica Janus particles partially coated with Pd seeds were introduced as precursor colloids (prepared according to Chapter 4.3.1). Different amounts of the Ag electrolyte were used for the deposition. During the plating process, ultrasonic agitation was not only used the provide well-dispersed precursor particles but also to ensure that the generated $[Ag(NH_3)_2]^+$ complex does not electrostatically adhere to the deprotonated silanol groups from the uncoated sphere. Moreover, ultrasound treatment prevents that the Ag complex reduces to a metal layer on the non-activated sphere, after the addition of a reducing agent. Experiments showed that the Ag layer deposition resulted in similar morphology when applying ultrasonic agitation (bath 35 kHz) or stirring at 300 rpm. The theoretical layer thickness for 2/3 coverage of particles and the shell thickness measured by SEM are summarized in Table 4-26. For sample JNP-Ag-1, shell thicknesses from 17—88 nm are detected by SEM and in case of sample JNP-Ag-2 the thicknesses varied between 26—61 nm.

**TABLE 4-26 OVERVIEW OF SHELL THICKNESS DATA FOR SILICA JANUS PARTICLES WITH AG SEMISHELL COATING USING AN AG ELECTROLYTE (0.54 G/L AG CONTENT)**

| | Dispersion mixture | | Shell thickness [nm] calculated from | |
|---|---|---|---|---|
| | $A_{Silica}$ $10^{18}$ [$nm^2$/L] | Ag [mg/L] | Theoretical for 2/3-shell | SEM |
| JNP-Ag-1 | 1.3±0.4 | 195.3 | 21±3 | 17—88 |
| JNP-Ag-2 | 0.8±0.2 | 257.3 | 43±3 | 26—61 |

In the corresponding SEM images in Figure 4-45, the different Ag layers/clusters are observed.

This heterogeneous distribution can be caused by heterogeneity of the Pd seed coverage of the precursor colloids, as well as uncontrollable Ag deposition from the unstable electrolyte itself. Similar to the other metal deposition results, the EDX mapping image were recorded for Ag fullshells at 10 kV (Full-Ag-5 Figure 4-45 Ag-7I) and for colloids with Ag semishells (JNP-Ag-2, Figure 4-45 Ag-8-I).

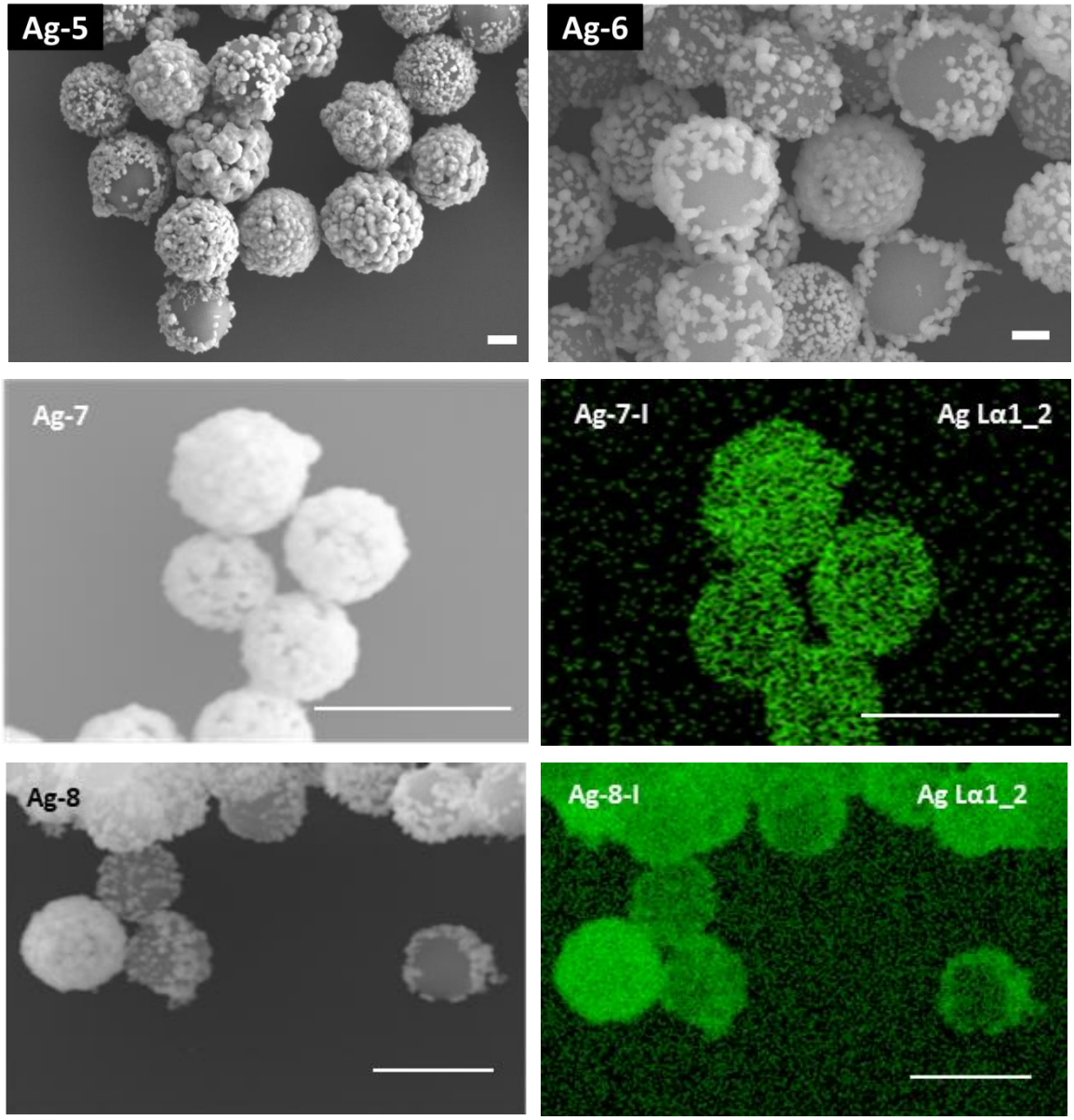


**FIGURE 4-45 SEM IMAGES OF SILICA JANUS PARTICLES WITH AG SEMISHELLS, WHEN THE THEORETICAL 2/3-SHELL THICKNESS WAS AG-5) 21±3 NM (JNP-AG-1) AND AG-6) 43±3 NM (JNP-AG-2), SCALE BAR =200 NM AND SEM IMAGES OF AG-7) SILICA PARTICLES WITH FULL AG FULLSHELLS (FULL-AG-5) AND AG-8) SILICA JANUS PARTICLES WITH AG SEMISHELLS (JNP-AG-2), AND THEIR CORRESPONDING MAPPING IMAGES FOR AG (GREEN COLOR) OBTAINED FROM EDX SPECTROSCOPY AT 10 KV, SCALE BAR=1 µM.**

The EDX image for the Ag shows the absence of Ag on the surface area of the particle that appears to be Ag-free in the SEM image (particle labeled as “1).

**Conclusion**

The precursor particles developed during this present research are also suitable to catalyze the metal deposition from an Ag electrolyte onto colloids. Since the Ag deposition was fast, the Ag layer morphology does not only depend on the catalyst distribution on the surface but also on the formation of Ag nuclei inside the solution. Ag fullshells and semishells with different thickness were prepared. Whereby, the tunability was not as precise as for the Ni samples in Chapter 4.3.3.

### 4.3.7. JANUS PARTICLES COATED WITH PALLADIUM SEMISHELLS

As mentioned previously, spherical silica Janus particles coated with Pd semishells have been up to now only prepared by the evaporation of a thin Pd film onto a monolayer of colloidal silica particles.[35] A disadvantage of the procedure is that only small amounts of particles can be metalized in one step and hence, are not suitable for industrial application. Here, we present the synthesis of silica Janus particles with Pd semishells, using Pd-seeds-activated silica spheres as precursor particles and a commercially available bath called PalladBond Pd, only to test feasibility towards another metal example (see Figure 4-46).

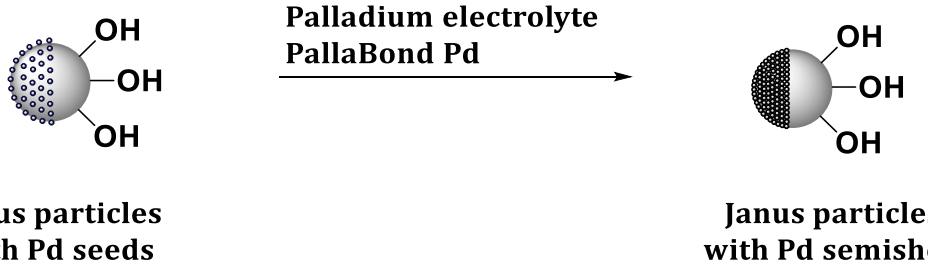


**FIGURE 4-46 SCHEMATIC OVERVIEW OF THE STRATEGY TO SYNTHESIZE SILICA PARTICLES WITH PD SEMISHELLS.**

The technical datasheet from the electrolyte PalladBond Pd provided only information about the Pd concentration (0.7±0.07 g/L) inside the solution. A common Pd bath comprises a Pd source, reducing agents, stabilizing agents, and complexing agents, similar to the Ni electrolyte (Chapter 4.3.3). Preliminary experiments demonstrated the necessity of an additional stabilizing agent for the Pd shell colloids because the dispersion precipitated after the color of the dispersion changed. Consequently, polyvinylpyrrolidone (PVP) was introduced as a stabilizing agent, once the dispersion started changing color from light gray to black, an indication of the formation of $Pd^0$. A ratio of 50 PVP molecules per silica particle resulted in a stable dispersion whereby other ratios of PVP were not tested. Full APTES-functionalized silica particles coated with Pd seeds (451±40 nm in diameter, Full-Pd-1) and Janus particles partially coated with Pd seeds (609±32 nm in diameter, JNP-Pd-1), prepared according to Chapter 4.3.1., reacted with PalladBond Pd. For the Janus particle a halfshell coverage was calculated. The

theoretical shell thicknesses, as well as the measured shell thicknesses in SEM, are presented in Table 4-27.

**TABLE 4-27 OVERVIEW OF SHELL THICKNESS DATA FOR SILICA PARTICLES WITH PD FULL FULLSHELLS AND JANUS PARTICLES WITH PD SEMISHELL COATINGS USING THE ELECTROLYTE PALLADOND PD**

| | Dispersion mixture | | Shell thickness [nm] calculated from | | |
|---|---|---|---|---|---|
| Sample | $A_{Silica}$ $10^{18}$ [nm²/L] | Pd [g/L] | Theoretical For full shell | Theoretical for halfshell | SEM |
| Full-Pd-1 | 1.1±0.5 | 0.47 | 31±1 | – | 43±45 |
| JNP-Pd-1 | 0.8±0.2 | 0.47 | – | 83±4 | 84±14 |

For Full-Pd-1, the estimated layer thickness (31±1 nm) is lower than the measured one from the diameter differences in SEM (43±45 nm). Aside from entirely metalized colloids, few non-plated particles are also observed in the SEM (see Figure 4-47 Pd-1), which means some particles were not plated and the others were plated with a thicker shell. In the case of the Janus particles coated with Pd semishells (JNP-Pd-1), the theoretical shell thickness of 83±4 nm for halfshell coverage is in agreement with the measured value from SEM 84±14 nm (see Figure 4-47 Pd-2). In both images, it can be noticed that the obtained Pd layer contains many adjacent single Pd clusters, which result in rough layers. Consequently, the same seeded growth process is assumed as for Ni (Chapter 4.3.3). Since the only purpose of preparing Pd fullshells and semishells was to confirm the feasibility towards other metal electrolytes, the SEM images are considered proof enough.

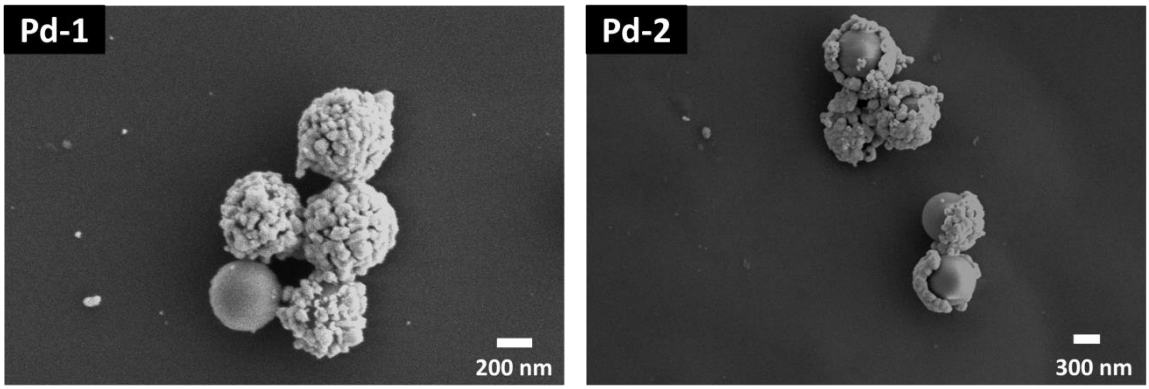


**FIGURE 4-47 SEM IMAGES OF PD-1) SILICA PARTICLES COATED WITH A FULL PD FULLSHELLS WITH A THEORETICAL SHELL THICKNESS OF 31±1 NM, AND PD-2) SILICA JANUS PARTICLES WITH PD SEMISHELLS WITH AN ESTIMATED SHELL THICKNESS OF 83±4 NM OF A ½-COVERAGE.**

### Conclusion

The precursor particles developed during this present research are suitable to catalyze the Pd deposition from a commercially available electrolyte Pallabond Pd onto Pd-activated silica colloids. The final shell thickness can be tailored for full Pd nanoshells, as well as for Pd semishells, similar to the experimental finding for silica colloids with Ni shells (Chapter 4.3.3). The Pd layer morphology varies slightly from the Ni deposition samples; a reason can be that the Pd shell samples were not prepared from the same precursor batch.

## 4.3.8. GENERAL SUMMARY OF THE METAL DEPOSITION

The same batch of precursor particles was utilized for the fabrication of all the silica-core-metal-nanoshell composites for Ni, Cu, Au, and Ag. The Pd samples were only made to confirm the feasibility towards another metal type. In general, the layer morphology is similar for Ni, Cu, and Au; and the desired shell thickness is easily tuned. Therefore, it can be reasoned that the morphology corresponds directly to the Pd seeds density and distribution on the silica surface, regardless of the deposited metal composition. In the case of the Ag deposition, the obtained layer thickness is constantly a little bit higher than the theoretically determined one, and side products such as non-plated colloids, as well as Ag nuclei are present. The presence of a stabilizer can reduce the formation of the metal nuclei inside the solution.

The results from the full metal nanoshells were used to prepare for the first time a facile route towards the synthesis of large amounts of silica Janus particles with tunable metal semishell coatings. The deposition of metal layers onto Pd-activated silica Janus precursors results in similar reproducible shell thickness as for the other metal nanoshells.

# 5. SUMMARY AND OUTLOOK

During this present work, challenges in the fabrication of asymmetric silica colloids with different semishell coatings were investigated, and a facile route was found towards the synthesis of large quantities of silica Janus particles with tunable shell thicknesses. As potential adhesion promoter between a dielectric surface and a metal, Janus particles were prepared where one side of the colloid can chemically interact with a polymer substrate, while the other side contains a metal that can directly activate the electroless deposition process. The results are summarized below:

In Chapter 4.1.1, monodisperse silica particles in sizes ranging from 60–1900 nm in diameter were successfully synthesized as starting materials by using different protocols from literature. For the micrometer-sized colloids, the additional electrolyte KCl was essential because the adsorption of cations with a large ionic radius reduces the surface potential and promotes coagulation at an early stage. These coagulated particles form the new nuclei, on which TEOS molecules hydrolyze and condense in the subsequent dosing step with a controlled dosing rate, causing the growth of larger colloids.

In Chapter 4.1.2, the silica particles, which were stored as a dry powder, were successfully deagglomerated in ethanol using different ultrasonic devices. The ultrasonic bath (35 kHz) redispersed particles with > 500 nm in diameter within 10 min so that the particles regained their initial hydrodynamic diameter and a PDI of ≤ 0.2, but the bath failed to disperse small particles (≤ 100 nm in diameter) into their original size with a PDI of ≤ 0.2 within 60 min. However, the application of an ultrasonic probe (sonotrode, 20 kHz) with lower frequency resulted in a regain of the initial hydrodynamic diameter and a PDI of ≤ 0.2 after 15 min. Consequently, all particles with a diameter > 500 nm were deagglomerated using bath type devices (35 kHz), and the ultrasonic probe was used for colloids ≤ 100 nm in diameter, for 10-15 min.

In the following Chapter 4.1.3, the influence of different reaction parameters such as temperature, time, and the presence of basic or acidic catalyst on the grafting of

a silica surface with a monolayer of 3-aminopropyltriethoxysilane (APTES) was investigated. Since the hydrolysis and condensation reaction in protic solvents is in a thermodynamic equilibrium, the monolayer grafting was achieved by an increase in reaction time, temperature, or the presence of a catalyst to enhance the surface functionalization. The environmental and industrial friendly way to synthesize silica particles with one monolayer of APTES molecules is accomplished by using an excess of APTES-molecules (5 equiv.), triethylamine (TEA) as base with a $mol_{APTES}/mol_{TEA}$ ratio of 1, 75 °C reaction temperature, and 1 h reaction time. Additionally, characterization methods to quantify the number of amino groups on the surface were discussed. The ninhydrin assay was a suitable derivatization method to quantify accessible amino groups on colloids of all sizes. The C/H/N elemental analysis confirmed the obtained values from the absorption data. The quantification method with salicylaldehyde was ruled out as a possible UV-Vis derivatization agent alternative; because the colloidal dispersion was unstable in chloroform and the solvent evaporated rapidly, which altered the results.

In Chapter 4.2, silica Janus particles were successfully synthesized with high mass yields, when the surfactants didodecyldimethylammonium bromide (DDAB, 50—60 % yield) or cetyltrimethylammonium bromide (CTAB, 60—70 % yield) were present during the preparation of the particle-wax colloidosomes. The surfactants interact with the colloid surface and increase the penetration into the wax, which resulted in an improved mass yield. Calculations were made using the radius of gyration as a parameter of the surface-bound surfactant molecule, to determine the area that the surfactant molecules occupy on the particle surface. It was possible to manufacture single colloidosomes with closed-packed monolayers of silica particles on the surface when the concentration ratio between surfactant and silanol groups of the colloids was kept < 5 % for DDAB (($mol_{DDAB}/mol_{OH}$) or ~6 % for CTAB ($mol_{CTAB}/mol_{OH}$). According to the radius of gyration calculation, at this point, the surfaces is entirely saturated with the surfactant molecules. A Langmuir-Freundlich isotherm fit was chosen to describe the experimental data. It is assumed that long alkyl chains of the surfactants are in continuous motion, and hence, an increase in surfactant loading reduces the ability for further molecules to bind to the silica surface. Instead, the additional molecules would interact with one another, form multilayer, and would not influence the mass yield. In the next step,

the silica colloids, embedded in wax, were grafted with a monolayer of APTES in the presence of TEA after reacting for 1 h at 0 °C to create a bonding site for the Pd in the subsequent step. Two characterization methods were successfully applied to compare the ratio of grafted and non-grafted surface area on the colloid, the so-called Janus balance. The APTES-functionalized spheres were coated with a metal layer and the corresponding semishells were observed in SEM. The results show that even small ratios of $mol_{DDAB}/mol_{OH}$ < 2 % or $mol_{CTAB}/mol_{OH}$ < 5 % increase the penetration of the silica into the wax and consequently result in a reduction of the metal surface coverage degree from 86±13 % to around 64±15 % for DDAB and to around 68±17 % for CTAB. The data demonstrates for both cases that the Janus balance cannot be adjusted with different surfactant ratios. As a second method, the amine density at the surface was converted into a UV-Vis detectable species with ninhydrin to quantify number of amino groups. The average amine coverage was 53±25 %, even when different $mol_{DDAB}/mol_{OH}$ ratios were applied. For different $mol_{CTAB}/mol_{OH}$ ratios, the amine coverage degree was 67±32 %. It can be reasoned that the calculated coverage degree for the amine density is an indirect method and highly depends on the reference. However, both methods indicate for each surfactant that the Janus balance on a particle cannot be predicted by varying the concentration of surfactant.

In Chapter 4.3.1, a method was successfully introduced to coat the APTES-functionalized spheres with Pd seeds as catalyst that support the electroless deposition of metals. The ICP-OES data demonstrates that a surface density of ~30 Pd atoms/$nm^2$ on the silica colloids is obtained, when the reaction mixture was stirred for 1 h at 70 °C. Janus particles yielded a surface density of ~20 Pd atoms/$nm^2$, which corresponds to a ~2/3 coverage of the silica colloid. This value confirms the findings in Chapter 4.2 regarding the metal layer coverage degree when different DDAB and CTAB amounts were used during the fabrication of the colloidosomes. Results also show that the distribution of Pd clusters varied within different batches, which might be caused by the state of the amino groups at the surface of Janus particles when $NH_2$ interacted with $CO_2$ from the environment; or the chain length of the Pd(II) oligomers influenced by the different hydrolysis state of the complex itself before the reduction step.

The same batch of Pd-seeded precursor particles was utilized for the fabrication of silica-core-metal-nanoshell composites for Ni, Cu, Au, Ag, and Pd using electrolytes reported in the literature, as well as commercially available ones. The layer morphology was similar for Ni, Cu, and Au; and the desired shell thicknesses were easily tuned by varying the amount of the electrolyte. The morphology corresponds directly to the Pd seeds density and their distribution on the silica surface, regardless of the deposited metal type. In the case of the Ag deposition, there was a discrepancy between the theoretical thickness, assuming the full conversion of all the metal ions inside the electrolyte, and the experimental thickness. Side products such as non-plated colloids and Ag nuclei were present, probably caused by the absence of a complexing agent or a stabilizer. To test the applicability of the precursor colloids towards a fifth metal electrolyte, Pd nanoshell samples were also prepared. The results from the metal fullshells were used to prepare silica Janus particles with different metal semishell coatings and tunable thicknesses. Different characterization methods were used to prove the shell thicknesses: the metal content from ICP-OES measurements and the calculated Si content were used to determine the shell thickness; the diameter size difference from the fully plated colloids versus the non-plated colloids resulted in the shell thickness; and for selected samples, a cross-section of the colloid was prepared using focused ion beam (FIB) to measure the actual shell thickness.

Based on the results of this present work, silica Janus particles with different types of metal semishell coating can be prepared, using the Pd-seeded precursor particles. The following steps will be to prepare a substrate with the desired functional group and modify the non-plated sphere with a functional group that can chemically bind to the surface. It is essential to prepare dispersions that are stable enough for industrial application and to find coating procedures that are suitable for the applications.

# 6. LIST OF FIGURES

# 7. LIST OF TABLES

# 8. LITERATURE


[1] W. Barthlott, C. Neinhuis, *Planta* **1997**, *202*, 1-8.
[2] T. Wagner, C. Neinhuis, W. Barthlott, *Acta Zool.* **1996**, *77*, 213-225.
[3] J. Sanders, *Acta Crystallogr. Sec. A* **1968**, *24*, 427-434.
[4] J. D. Moras, B. Strandberg, D. Suc, K. Wilson, *Science* **1996**, *271*, 933.
[5] C. F. Coombs Jr, *Printed circuits handbook*, McGraw-Hill, Inc., New York, **1987**.
[6] D. Schröer, R. Nichols, H. Meyer, *Electrochim. Acta* **1995**, *40*, 1487-1494.
[7] aJ. Ge, M. Turunen, J. Kivilahti, *Thin Solid Films* **2003**, *440*, 198-207; bJ. Ge, M. Turunen, J. Kivilahti, *J. Polym. Sci., Part B: Polym. Phys.* **2003**, *41*, 623-636.
[8] aS. Siau, A. Vervaet, E. Schacht, A. Van Calster, *J. Electrochem. Soc.* **2004**, *151*, C133-C141; bS. Siau, A. Vervaet, L. Van Vaeck, E. Schacht, U. Demeter, A. Van Calster, *J. Electrochem. Soc.* **2005**, *152*, C442-C455.
[9] H. Zumbahlen, *Basic linear design*, Analog Devices, Norwood, **2007**.
[10] aM. Paunovic, M. Schlesinger, *Fundamentals of electrochemical deposition, Vol. 45*, John Wiley & Sons, Hoboken, **2006**; bM. Schlesinger, M. Paunovic, *Modern electroplating, Vol. 55*, John Wiley & Sons, Hoboken, **2011**.
[11] aT. Thomas, L. Brandt, L. Stamp, H.-J. Schreier, Google Patents, **2012**; bT. Thomas, PhD thesis, Freie Universität Berlin (Berlin), **2016**.
[12] http://www.aerosil.com, (last visited 02/01/2018).
[13] http://nanopartikel.info/nanoinfo/materialien/siliziumdioxid/materialinfo-siliziumdioxid, (last visited 02/01/2018).
[14] Y. Hu, X. T. Zheng, J. S. Chen, M. Zhou, C. M. Li, X. W. D. Lou, *J. Mater. Chem.* **2011**, *21*, 8052-8056.
[15] W. Stöber, A. Fink, E. Bohn, *J. Colloid Interface Sci.* **1968**, *26*, 62-69.
[16] G. Bogush, M. Tracy, C. Zukoski Iv, *J. Non-Cryst. Solids* **1988**, *104*, 95-106.
[17] C. Brinker, *J. Non-Cryst. Solids* **1988**, *100*, 31-50.
[18] aJ. De Haan, H. Van Den Bogaert, J. Ponjee, L. Van De Ven, *J. Colloid Interface Sci.* **1986**, *110*, 591-600; bA. Van Blaaderen, A. Vrij, *J. Colloid Interface Sci.* **1993**, *156*, 1-18.
[19] aD. W. Schaefer, *MRS Bull.* **1988**, *13*, 22-27; bP. Meakin, *Phys. Rev. Lett.* **1983**, *51*, 1119.
[20] R. K. Iler, *Soil Science* **1955**, *80*, 86.
[21] V. K. LaMer, R. H. Dinegar, *J. Am. Chem. Soc.* **1950**, *72*, 4847-4854.
[22] W. Ostwald, *Z. Phys. Chem.* **1900**, *34*, 495-503.
[23] A. Van Blaaderen, J. Van Geest, A. Vrij, *J. Colloid Interface Sci.* **1992**, *154*, 481-501.
[24] R. D. Badley, W. T. Ford, F. J. McEnroe, R. A. Assink, *Langmuir* **1990**, *6*, 792-801.
[25] R. Jullien, M. Kolb, *J. Phys. A: Math. Gen.* **1984**, *17*, L639.
[26] L. Zhuravlev, *Colloids Surf. Physicochem. Eng. Aspects* **2000**, *173*, 1-38.
[27] C. Casagrande, M. Veyssie, *C. R. Acad. Sci.* **1988**, *306*, 1423-1425.
[28] P.-G. de Gennes, *Rev. Mod. Phys.* **1992**, *64*, 645.
[29] A. Walther, A. H. Müller, *Chem. Rev.* **2013**, *113*, 5194-5261.
[30] F. Obfusco, English Wikipedia, **2005**.

[31] C. Casagrande, P. Fabre, E. Raphael, M. Veyssie, *Europhys. Lett.* **1989**, *9*, 251-255.
[32] aV. N. Paunov, *Langmuir* **2003**, *19*, 7970-7976; bV. N. Paunov, O. J. Cayre, *Adv. Mater.* **2004**, *16*, 788-791.
[33] L. Hong, S. Jiang, S. Granick, *Langmuir* **2006**, *22*, 9495-9499.
[34] H. Takei, N. Shimizu, *Langmuir* **1997**, *13*, 1865-1868.
[35] J. C. Love, B. D. Gates, D. B. Wolfe, K. E. Paul, G. M. Whitesides, *Nano Lett.* **2002**, *2*, 891-894.
[36] O. Cayre, V. N. Paunov, O. D. Velev, *Chem. Commun.* **2003**, 2296-2297.
[37] O. Cayre, V. N. Paunov, O. D. Velev, *J. Mater. Chem.* **2003**, *13*, 2445-2450.
[38] K. Fujimoto, K. Nakahama, M. Shidara, H. Kawaguchi, *Langmuir* **1999**, *15*, 4630-4635.
[39] aL. Petit, E. Sellier, E. Duguet, S. Ravaine, C. Mingotaud, *J. Mater. Chem.* **2000**, *10*, 253-254; bL. Petit, J.-P. Manaud, C. Mingotaud, S. Ravaine, E. Duguet, *Mater. Lett.* **2001**, *51*, 478-484.
[40] A. Perro, S. Reculusa, S. Ravaine, E. Bourgeat-Lami, E. Duguet, *J. Mater. Chem.* **2005**, *15*, 3745-3760.
[41] S. E. Fosdick, K. N. Knust, K. Scida, R. M. Crooks, *Angew. Chem. Int. Ed.* **2013**, *52*, 10438-10456.
[42] C. Warakulwit, T. Nguyen, J. Majimel, M.-H. Delville, V. Lapeyre, P. Garrigue, V. Ravaine, J. Limtrakul, A. Kuhn, *Nano Lett.* **2008**, *8*, 500-504.
[43] G. Loget, D. Zigah, L. Bouffier, N. Sojic, A. Kuhn, *Acc. Chem. Res.* **2013**, *46*, 2513-2523.
[44] A. Dinsmore, M. F. Hsu, M. Nikolaides, M. Marquez, A. Bausch, D. Weitz, *Science* **2002**, *298*, 1006-1009.
[45] R. Aveyard, B. P. Binks, J. H. Clint, *Adv. Colloid Interface Sci.* **2003**, *100*, 503-546.
[46] C. Kaewsaneha, P. Tangboriboonrat, D. Polpanich, M. Eissa, A. Elaissari, *Colloids Surf. Physicochem. Eng. Aspects* **2013**, *439*, 35-42.
[47] S. Jiang, S. Granick, *Langmuir* **2008**, *24*, 2438-2445.
[48] A. Perro, F. Meunier, V. Schmitt, S. Ravaine, *Colloids Surf. Physicochem. Eng. Aspects* **2009**, *332*, 57-62.
[49] P. Van Dorpe, J. Ye, *ACS nano* **2011**, *5*, 6774-6778.
[50] aM. A. Correa-Duarte, V. Salgueiriño-Maceira, B. Rodríguez-González, L. M. Liz-Marzán, A. Kosiorek, W. Kandulski, M. Giersig, *Adv. Mater.* **2005**, *17*, 2014-2018; bJ. Yan, M. Bloom, S. C. Bae, E. Luijten, S. Granick, *Nature* **2012**, *491*, 578-581.
[51] S. L. Westcott, S. J. Oldenburg, T. R. Lee, N. J. Halas, *Langmuir* **1998**, *14*, 5396-5401.
[52] D. Rodríguez-Fernández, J. Pérez-Juste, I. Pastoriza-Santos, L. M. Liz-Marzán, *ChemistryOpen* **2012**, *1*, 90-95.
[53] aA. Brenner, G. E. Riddell, *J. Res. Nat. Bur. Stand* **1947**, *39*, 385-395; bA. Brenner, G. Riddell, *Nature* **1948**, *162*, 183-184.
[54] C. Wagner, W. Traud, *Z. Electrochem.* **1938**, *44*, 391.
[55] aM. Paunovic, *Plating* **1968**, *55*, 1161; bM. Saito, *Opt. Rev.* **1966**, *17*, 14.
[56] P. Bindra, J. Tweedie, *J. Electrochem. Soc.* **1983**, *130*, 1112-1114.
[57] P. Bindra, J. Roldan, *J. Appl. Electrochem.* **1987**, *17*, 1254-1266.
[58] J. Duffy, L. Pearson, M. Paunovic, *J. Electrochem. Soc.* **1983**, *130*, 876-880.

[59] G. O. Mallory, J. B. Hajdu, *Electroless plating: fundamentals and applications*, William Andrew, New York, **1990**.
[60] W. Franke, J. Mönch, *Liebigs Ann. Chem.* **1942**, *550*, 1-31.
[61] aG. Gutzeit, *Anti-Corros. Meth. Mater.* **1956**, *3*, 208-208; bG. Gutzeit, *Plat. Surf. Fin.* **1959**, *46*, 1158-1164.
[62] P. Hersch, *T. I. Met. Finish.* **1955**, *33*, 417-418.
[63] R. M. Lukes, *Plating* **1964**, *51*, 969-971.
[64] aG. Salvago, P. Cavallotti, *Plating* **1972**, *59*, 665-671; bJ. P. Rondin, H. Hintermann, *J. Electrochem. Soc.* **1970**, *117*, 160-167.
[65] G. Gawrilow, *Chemische (Stromlose) Vernicklung*, Leuze Verlag, Saulgau, **1974**.
[66] J. Sudagar, J. Lian, W. Sha, *J. Alloys Compd.* **2013**, *571*, 183-204.
[67] H. O. Ali, I. R. Christie, *Gold bulletin* **1984**, *17*, 118-127.
[68] aS. Oldenburg, R. Averitt, S. Westcott, N. Halas, *Chem. Phys. Lett.* **1998**, *288*, 243-247; bB. E. Brinson, J. B. Lassiter, C. S. Levin, R. Bardhan, N. Mirin, N. J. Halas, *Langmuir* **2008**, *24*, 14166-14171; cJ.-H. Kim, W. W. Bryan, T. Randall Lee, *Langmuir* **2008**, *24*, 11147-11152; dC. Graf, A. van Blaaderen, *Langmuir* **2002**, *18*, 524-534.
[69] J. Jackson, N. Halas, *J. Phys. Chem. B* **2001**, *105*, 2743-2746.
[70] R. Zsigmondy, *Z. Phys. Chem.* **1906**, *56*, 77-82.
[71] K.-S. Chou, C.-Y. Ren, *Mater. Chem. Phys.* **2000**, *64*, 241-246.
[72] L. G. Svendsen, T. Osaka, H. Sawai, *J. Electrochem. Soc.* **1983**, *130*, 2252-2255.
[73] W. J. Dressick, C. S. Dulcey, J. H. Georger, G. S. Calabrese, J. M. Calvert, *J. Electrochem. Soc.* **1994**, *141*, 210-220.
[74] N. B. Milić, Ž. D. Bugarčić, *Transition Met. Chem.* **1984**, *9*, 173-176.
[75] aS. L. Brandow, M. S. Chen, T. Wang, C. S. Dulcey, J. M. Calvert, J. F. Bohland, G. S. Calabrese, W. J. Dressick, *J. Electrochem. Soc.* **1997**, *144*, 3425-3434; bW. J. Dressick, L. M. Kondracki, M.-S. Chen, S. L. Brandow, E. Matijević, J. M. Calvert, *Colloids Surf. Physicochem. Eng. Aspects* **1996**, *108*, 101-111; cS. L. Brandow, W. J. Dressick, C. R. Marrian, G. M. Chow, J. M. Calvert, *J. Electrochem. Soc.* **1995**, *142*, 2233-2243.
[76] M. Lelental, *J. Electrochem. Soc.* **1973**, *120*, 1650-1654.
[77] L. M. Rossi, I. M. Nangoi, N. J. Costa, *Inorg. Chem.* **2009**, *48*, 4640-4642.
[78] B. J. Berne, R. Pecora, *Dynamic light scattering: with applications to chemistry, biology, and physics*, Courier Corporation, New York, **1976**.
[79] A. Wilkinson, A. McNaught, *IUPAC Compendium of Chemical Terminology*, Blackwell Scientific Publications, Oxford, **1997**.
[80] R. J. Hunter, *Zeta potential in colloid science: principles and applications, Vol. 2*, Academic press, London, **2013**.
[81] T. G. Waddell, D. E. Leyden, M. T. DeBello, *J. Am. Chem. Soc.* **1981**, *103*, 5303-5307.
[82] E. Soto-Cantu, R. Cueto, J. Koch, P. S. Russo, *Langmuir* **2012**, *28*, 5562-5569.
[83] D. McCaldin, *Chem. Rev.* **1960**, *60*, 39-51.
[84] H.-H. Perkampus, H.-C. Grinter, T. Threlfall, *UV-VIS Spectroscopy and its Applications*, Springer, Berlin, **1992**.
[85] *Elementar Analysensysteme GmbH, CHNOS Elementaranalysator Vario EL Cube Bedienungsanleitung* **2010**.
[86] M. Von Ardenne, *Z. Phys.* **1938**, *109*, 553-572.

[87] J. Goldstein, D. E. Newbury, P. Echlin, D. C. Joy, A. D. Romig Jr, C. E. Lyman, C. Fiori, E. Lifshin, *Scanning electron microscopy and X-ray microanalysis: a text for biologists, materials scientists, and geologists*, Springer Science & Business Media, New York, **2012**.
[88] L. Reimer, *Scanning electron microscopy: physics of image formation and microanalysis, Vol. 45*, Springer, Berlin, **2013**.
[89] L. A. Giannuzzi, *Introduction to focused ion beams: instrumentation, theory, techniques and practice*, Springer Science & Business Media, New York, **2006**.
[90] E. P. Bertin, *Principles and practice of X-ray spectrometric analysis*, Springer Science & Business Media, New York, **2012**.
[91] A. Montaser, D. Golightly, *Inductively coupled plasmas in analytical atomic spectrometry*, Wiley-Interscience, New York **1987**.
[92] X. Hou, R. S. Amais, B. T. Jones, G. L. Donati, *Inductively coupled plasma optical emission spectrometry*, Chichester, **2000**.
[93] aH. Santos, J. Capelo, *Talanta* **2007**, *73*, 795-802; bH. M. Santos, C. Lodeiro, J. L. Capelo-Martínez, *The power of ultrasound, Vol. 171*, WILEY-VCH Verlag GmbH & Co. KGaA, Weinheim, **2009**.
[94] J.-L. Capelo-Martínez, *Ultrasound in chemistry: analytical applications*, Wiley-VCH Verlag, Weinheim, **2008**.
[95] K. S. Suslick, D. A. Hammerton, R. E. Cline, *J. Am. Chem. Soc.* **1986**, *108*, 5641-5642.
[96] X. Lei, B. Yu, H.-L. Cong, C. Tian, Y.-Z. Wang, Q.-B. Wang, C.-K. Liu, *Integr. Ferroelectr.* **2014**, *154*, 142-146.
[97] R. Pashley, M. Karaman, *Applied colloid and surface chemistry*, John Wiley & Sons, West Sussex **2005**.
[98] A. Cobley, T. Mason, M. Alarjah, R. Ashayer, S. Mannan, *Ultrason. Sonochem.* **2011**, *18*, 37-41.
[99] N. Kanani, *Chemische Vernickelung, Nickel-Phosphor-Schichten, Herstellung–Eigenschaften–Anwendungen, 1. Auflage, Eugen G*, Leuze Verlag, Bad Saulgau, **2007**.
[100] D. G. Duff, A. Baiker, I. Gameson, P. P. Edwards, *Langmuir* **1993**, *9*, 2310-2317.
[101] A. Mayer, W. Grebner, R. Wannemacher, *J. Phys. Chem. B* **2000**, *104*, 7278-7285.
[102] T. Nisisako, T. Torii, T. Takahashi, Y. Takizawa, *Adv. Mater.* **2006**, *18*, 1152-1156.
[103] S. H. Kim, S. J. Jeon, W. C. Jeong, H. S. Park, S. M. Yang, *Adv. Mater.* **2008**, *20*, 4129-4134.
[104] aN. Hassan, A. Stocco, A. Abou-Hassan, *J. Phys. Chem. C* **2015**; bH. Bao, W. Peukert, R. K. Taylor, *Adv. Mater.* **2011**, *23*, 2644-2649; cR. N. Klupp Taylor, H. Bao, C. Tian, S. Vasylyev, W. Peukert, *Langmuir* **2010**, *26*, 13564-13571.
[105] G. Bogush, M. Tracy, C. Zukoski, *J. Non-Cryst. Solids* **1988**, *104*, 95-106.
[106] J. Zhang, P. Zhan, Z. Wang, W. Zhang, N. Ming, *J. Mater. Res.* **2003**, *18*, 649-653.
[107] L. Qi, J. Ma, H. Cheng, Z. Zhao, *Chem. Mater.* **1998**, *10*, 1623-1626.
[108] H. Nakabayashi, A. Yamada, M. Noba, Y. Kobayashi, M. Konno, D. Nagao, *Langmuir* **2010**, *26*, 7512-7515.
[109] D. Nagao, T. Satoh, M. Konno, *J. Colloid Interface Sci.* **2000**, *232*, 102-110.

[110] aM. Pohl, S. Hogekamp, N. Q. Hoffmann, H. P. Schuchmann, *Chem. Ing. Tech.* **2004**, *76*, 392-396; bS. Tang, J. Preece, C. McFarlane, Z. Zhang, *J. Colloid Interface Sci.* **2000**, *221*, 114-123; cF. Müller, W. Peukert, R. Polke, F. Stenger, *Int. J. Miner. Process.* **2004**, *74*, S31-S41; dG. Petzold, R. Rojas-Reyna, M. Mende, S. Schwarz, *J. Dispersion Sci. Technol.* **2009**, *30*, 1216-1222; eR. Mondragon, J. E. Julia, A. Barba, J. C. Jarque, *Powder Technol.* **2012**, *224*, 138-146; fS. Ramesh, Y. Koltypin, A. Gedanken, *J. Mater. Res.* **1997**, *12*, 3271-3277.
[111] Y. Liang, N. Hilal, P. Langston, V. Starov, *Adv. Colloid Interface Sci.* **2007**, *134*, 151-166.
[112] aK. A. Kusters, S. E. Pratsinis, S. G. Thoma, D. M. Smith, *Powder Technol.* **1994**, *80*, 253-263; bJ. S. Taurozzi, V. A. Hackley, M. R. Wiesner, *Nanotoxicology* **2011**, *5*, 711-729.
[113] T. J. Mason, D. Peters, *Practical sonochemistry: Power ultrasound uses and applications*, Woodhead Publishing, Cambridge, **2002**.
[114] T. J. Mason, *Philos. Trans. Royal Soc. A* **1999**, *357*, 355-369.
[115] aJ. M. Rosenholm, M. Lindén, *Chem. Mater.* **2007**, *19*, 5023-5034; bA. Simon, T. Cohen-Bouhacina, M. Porté, J. Aimé, C. Baquey, *J. Colloid Interface Sci.* **2002**, *251*, 278-283.
[116] aI. Rahman, M. Jafarzadeh, C. Sipaut, *Ceram. Int.* **2009**, *35*, 1883-1888; bS. L. Burkett, S. D. Sims, S. Mann, *Chem. Commun.* **1996**, 1367-1368; cS. Huh, J. W. Wiench, J.-C. Yoo, M. Pruski, V. S.-Y. Lin, *Chem. Mater.* **2003**, *15*, 4247-4256; dY. Naka, Y. Komori, H. Yoshitake, *Colloids Surf. Physicochem. Eng. Aspects* **2010**, *361*, 162-168.
[117] aH. Choi, I.-W. Chen, *J. Colloid Interface Sci.* **2003**, *258*, 435-437; bH.-S. Jung, D.-S. Moon, J.-K. Lee, *Journal of Nanomaterials* **2012**, *2012*, 48; cM. Pálmai, L. N. Nagy, J. Mihály, Z. Varga, G. Tárkányi, R. Mizsei, I. C. Szigyártó, T. Kiss, T. Kremmer, A. Bóta, *J. Colloid Interface Sci.* **2013**, *390*, 34-40.
[118] J. H. Moon, J. W. Shin, S. Y. Kim, J. W. Park, *Langmuir* **1996**, *12*, 4621-4624.
[119] M. Gimpel, K. Unger, *Chromatographia* **1982**, *16*, 117-125.
[120] L. Zhuravlev, *Langmuir* **1987**, *3*, 316-318.
[121] E. T. Vandenberg, L. Bertilsson, B. Liedberg, K. Uvdal, R. Erlandsson, H. Elwing, I. Lundström, *J. Colloid Interface Sci.* **1991**, *147*, 103-118.
[122] aK. N. Pham, D. Fullston, K. Sagoe-Crentsil, *Aust. J. Chem.* **2007**, *60*, 662-666; bM.-C. B. Salon, M. Bardet, M. N. Belgacem, *Silicon Chem.* **2008**, *3*, 335-350.
[123] aK. Vrancken, K. Possemiers, P. Van Der Voort, E. F. Vansant, *Colloids Surf. Physicochem. Eng. Aspects* **1995**, *98*, 235-241; bE. Vansant, P. V. D. Voort, K. Vrancken, K. Unger, *J. Chromatogr. A* **1996**, *738*, 313-313; cK. C. Vrancken, L. De Coster, P. Van Der Voort, P. J. Grobet, E. F. Vansant, *J. Colloid Interface Sci.* **1995**, *170*, 71-77.
[124] V. K. Sarin, S. B. Kent, J. P. Tam, R. B. Merrifield, *Anal. Biochem.* **1981**, *117*, 147-157.
[125] A. Samoc, *J. Appl. Phys.* **2003**, *94*, 6167-6174.
[126] A. Synytska, L. Isa, *ChemPlusChem* **2014**, *79*, 656-661.
[127] F. Boerio, L. Armogan, S. Cheng, *J. Colloid Interface Sci.* **1980**, *73*, 416-424.
[128] aA. C. Chang, S. S. Chuang, M. Gray, Y. Soong, *Energy & Fuels* **2003**, *17*, 468-473; bG. P. Knowles, J. V. Graham, S. W. Delaney, A. L. Chaffee, *Fuel Process. Technol.* **2005**, *86*, 1435-1448.

[129] Y. Niibori, M. Kunita, O. Tochiyama, T. Chida, *J. Nucl. Sci. Technol.* **2000**, *37*, 349-357.
[130] H. Engelhardt, P. Orth, *J. Liq. Chromatogr.* **1987**, *10*, 1999-2022.
[131] J. Kinkel, K. Unger, *J. Chromatogr. A* **1984**, *316*, 193-200.
[132] J. A. Howarter, J. P. Youngblood, *Langmuir* **2006**, *22*, 11142-11147.
[133] W. T. Grubb, *J. Am. Chem. Soc.* **1954**, *76*, 3408-3414.
[134] F. Osterholtz, E. Pohl, *J. Adhes. Sci. Technol.* **1992**, *6*, 127-149.
[135] S. Jiang, S. Granick, *J. Chem. Phys.* **2007**, *127*, 161102-161106.
[136] G. G. Warr, R. Sen, D. F. Evans, J. E. Trend, *J. Phys. Chem.* **1988**, *92*, 774-783.
[137] R. Atkin, V. Craig, E. Wanless, S. Biggs, *Adv. Colloid Interface Sci.* **2003**, *103*, 219-304.
[138] aI. Langmuir, *J. Am. Chem. Soc.* **1916**, *38*, 2221-2295; bI. Langmuir, *J. Am. Chem. Soc.* **1917**, *39*, 1848-1906.
[139] K. Vijayaraghavan, T. Padmesh, K. Palanivelu, M. Velan, *J. Hazard. Mater.* **2006**, *133*, 304-308.
[140] A. W. Adamson, A. P. Gast, *Physical chemistry of surfaces*, Wiley-Interscience, New York, **1967**.
[141] H. Yamakawa, *Modern theory of polymer solutions*, Harper & Row, New York, **1971**.
[142] K. Esumi, M. Matoba, Y. Yamanaka, *Langmuir* **1996**, *12*, 2130-2135.
[143] D. Chandler, *Nature* **2005**, *437*, 640-647.
[144] J. C. Schulz, G. G. Warr, P. D. Butler, W. Hamilton, *Phys. Rev. E* **2001**, *63*, 041604.
[145] J. Giermanska-Kahn, V. Laine, S. Arditty, V. Schmitt, F. Leal-Calderon, *Langmuir* **2005**, *21*, 4316-4323.
[146] aM. Bendayan, *Biotech. Histochem.* **2000**, *75*, 203-242; bR. Möller, A. Csáki, J. M. Köhler, W. Fritzsche, *Nucleic Acids Res.* **2000**, *28*, e91-e91.
[147] aY. Dirix, C. Bastiaansen, W. Caseri, P. Smith, *J. Mater. Sci.* **1999**, *34*, 3859-3866; bT. Sato, D. Hasko, H. Ahmed, *J. Vac. Sci. Technol., B* **1997**, *15*, 45-48.
[148] aE. Prodan, C. Radloff, N. J. Halas, P. Nordlander, *Science* **2003**, *302*, 419-422; bT. Pham, J. B. Jackson, N. J. Halas, T. R. Lee, *Langmuir* **2002**, *18*, 4915-4920.
[149] J.-H. Kim, H.-W. Chung, T. R. Lee, *Chem. Mater.* **2006**, *18*, 4115-4120.
[150] D. G. Duff, A. Baiker, P. P. Edwards, *Langmuir* **1993**, *9*, 2301-2309.
[151] J. C. R. Shipley*, Vol. U.S: Patent 3011920*, **1961**.
[152] aJ. Tsuji, *Palladium reagents and catalysts: new perspectives for the 21st century*, John Wiley & Sons, Hoboken, **2006**; bF. R. Hartley, P. L. Robinson, **1973**.
[153] http://www.gold.de/, (last visited 02/01/2018).
[154] aR. Cohen, K. West, *J. Electrochem. Soc.* **1973**, *120*, 502-508; bE. Matijević, A. Poskanzer, P. Zuman, **1975**.
[155] aG. S. Calabrese, J. M. Calvert, M.-S. Chen, W. J. Dressick, C. S. Dulcey, J. H. Georger Jr, J. F. Bohland Jr, Google Patents, **1996**; bH. Kind, A. M. Bittner, O. Cavalleri, K. Kern, T. Greber, *J. Phys. Chem. B* **1998**, *102*, 7582-7589.
[156] H. L. Rhodenizer*, Vol. U.S. Patent 4863758*, **1989**.
[157] J.-F. Boily, T. M. Seward, J. M. Charnock, *Geochim. Cosmochim. Acta* **2007**, *71*, 4834-4845.
[158] C. Bazzicalupi, A. Bencini, A. Bianchi, C. Giorgi, B. Valtancoli, *Coord. Chem. Rev.* **1999**, *184*, 243-270.

[159] S. Fedorenko, M. Jilkin, N. Nastapova, V. Yanilkin, O. Bochkova, V. Buriliov, I. Nizameev, G. Nasretdinova, M. Kadirov, A. Mustafina, *Colloids Surf. Physicochem. Eng. Aspects* **2015**, *486*, 185-191.
[160] C. Mortimer, *Rev. inorg. Chem.* **1984**, *6*, 233-257.
[161] P. Vanysek, *CRC handbook of chemistry and physics*, CRC Press, Illinois, **1998**.
[162] R. Egerton, P. Li, M. Malac, *Micron* **2004**, *35*, 399-409.
[163] aK. Lee, R. Thomas, A. Viehbeck, E. O'Sullivan, *J. Vac. Sci. Technol., B* **1993**, *11*, 2204-2209; bJ. W. Jacobs, J. M. Rikken, *J. Electrochem. Soc.* **1988**, *135*, 2822-2827.
[164] A. M. Van Der Putten, J. W. G. de Bakker, *J. Electrochem. Soc.* **1993**, *140*, 2229-2235.
[165] N. Kanani, *Electroplating: basic principles, processes and practice*, Elsevier, Oxford, **2004**.
[166] J. A. Creighton, D. G. Eadon, *J. Chem. Soc., Faraday Trans.* **1991**, *87*, 3881-3891.
[167] A. J. Bard, R. Parsons, J. Jordan, *Standard potentials in aqueous solution, Vol. 6*, CRC press, New York, **1985**.
[168] W. M. Haynes, *CRC handbook of chemistry and physics*, CRC press, Boca Raton, **2014**.
[169] aK. R. Brown, M. J. Natan, *Langmuir* **1998**, *14*, 726-728; bK. R. Brown, D. G. Walter, M. J. Natan, *Chem. Mater.* **2000**, *12*, 306-313.
[170] G. Stremsdoerfer, H. Perrot, J. Martin, P. Clechet, *J. Electrochem. Soc.* **1988**, *135*, 2881-2886.
[171] L. Kvitek, A. Panáček, J. Soukupova, M. Kolar, R. Vecerova, R. Prucek, M. Holecova, R. Zboril, *J. Phys. Chem. C* **2008**, *112*, 5825-5834.
[172] H. Gerischer, *American Association for the Advancement of Science*, Wiley-Interscience, New York, **1972**.
[173] A. Henglein, *J. Phys. Chem.* **1979**, *83*, 2209-2216.
[174] Z.-j. Jiang, C.-y. Liu, *J. Phys. Chem. B* **2003**, *107*, 12411-12415.
[175] K.-T. Yong, Y. Sahoo, M. T. Swihart, P. N. Prasad, *Colloids Surf. Physicochem. Eng. Aspects* **2006**, *290*, 89-105.

# APPENDIX I ABBREVIATIONS AND SYMBOLS

| | |
|---|---|
| AE | Auger electrons Absorbance |
| $A_{\tilde{\nu}}$ | Absorbance |
| BSE | Backscattered electrons |
| c | Concentration of absorbing species |
| CL | Cathodoluminescence |
| D | Diffusion coefficient |
| DLS | Dynamic Light Scattering |
| EA | Elemental analysis |
| EDX | Energy dispersive X-ray spectroscopy |
| $E_{eq}$ | Equilibrium potential |
| eless | Electroless deposition |
| $E_m$ | Mixed-potential |
| *f*(Ka): | Henry's function |
| FESEM | Field Emission Scanning Electron Microscope |
| FIB | Focused ion beam |
| i | Current density |
| ICP-OES | Inductively Coupled Plasma-Optical Emission Spectroscopy |
| i-E | Current-potential |
| $k_B$ | Boltzmann constant |
| L/S | Line width and spance |
| LMIS | Liquid metal ion source |
| $M^{z+}$ | Metal ions |
| n | Refractive index of the suspension |
| n(t) | Scattering intensity at time *t* |

| | |
|---|---|
| PCB | Printed circuit board |
| PDI | Polydispersions index |
| RF | Radio frequency |
| RLMCA | Reaction-limited monomer-cluster aggregation |
| rt | Room temperature |
| SCE | Saturated calomel electrode |
| SE | Secondary electrons |
| $S_N2$ | Nucleophilic substitution of the second order |
| TCD | Thermal conductive detector |
| US | Ultrasound |
| UV-Vis | Ultraviolet-Visible Spectroscopy |
| β | Intercept of the correlation function |
| Γ | Decay constant |
| ε | Molar absorptivity |
| $\varepsilon\tilde{\nu}$ | Molar decadic extinction coefficient |
| η | Viscosity of the solvent |
| Θ | Scattering angle in DLS |
| λ | Laser wavelength |
| π | Circle mathematical constant, 3.14 |
| τ | Delay time |
| Γ | Decay constant |
| β | Intercept of the correlation function |
| I(t) | Intensity at time t |

# APPENDIX II CALCULATIONS

## 1. Calculation of the number of amino groups from the absorption spectra

Below is an example calculation for a sample of APTES-functionalized silica particles with the following characteristics:

| | |
|---|---|
| $A_{475\text{-}750}$ | = 36.55 (from UV-vis absorption measurement) |
| Particle diameter | = 631 nm (from SEM measurement) |
| $m_{total}$ | = 0.28 g |

Part 1: Calculation of the number of APTES molecules

Using the calibration curve from Figure 3-2, the concentration of APTES in the solution is:

$$[\text{APTES}] = \frac{A_{475-750} + 2.7}{206.2} = \frac{36{,}55 + 2.7}{206.2} = 0.19$$

Dilution factors: the original solution was diluted by the factor 20. Thus, the original amount of APTES is:

$$[\text{APTES}]_{\text{original}} = \frac{0.19\ \text{mol}}{10^3\ \text{L}} \cdot \frac{50\ \text{L}}{10^3} = 9.52 \cdot 10^{-6}\ \text{mol}$$

Using the Avogadro's number, the number of APTES molecules is:

$$\text{Number of APTES molecules} = 9.52 \cdot 10^{-6}\ \text{mol} \cdot 6.022 \cdot 10^{23}\ \frac{1}{\text{mol}} = 5.74 \cdot 10^{18}$$

Part 2: Calculation of the total surface area of silica nanoparticles

When ONE nanoparticle is considered as a perfect sphere with a diameter of 631 nm and the density of silica ($\rho \sim 2.0\ \text{g/cm}^3$). The mass of this ONE nanoparticle can be approximated:

$$m_{\text{sphere}} = \frac{4}{3} \cdot \pi \cdot \rho \cdot r^3\ [r] = \text{cm}$$

$$m_{sphere} = \frac{4}{3} \cdot \pi \cdot 2.0 \frac{g}{cm^3} \cdot (31.55 \cdot 10^{-6} cm)^{3} = 2.63 \cdot 10^{-13}\ g$$

To get the number of nanoparticles, the total mass ($m_{total}$) is divided by the mass of a single nanoparticle:

$$\text{Number of particles} = \frac{m_{total}}{m_{sphere}} = \frac{0.28\ g}{2.63 \cdot 10^{-13}\ g} = 1.06 \cdot 10^{12}$$

The surface area of ONE nanoparticle considering again the nanoparticle as a perfect sphere is:

$$A_{sphere} = 4\pi r^2 = 4\pi \cdot (31.55 \cdot 10^{-6} cm)^2 = 1.25 \cdot 10^{-8}\ cm^2$$

Thus, the total surface area of the nanoparticles is:

$$A_{total} = \text{Number of particles} \cdot A_{sphere} = 1.06 \cdot 10^{12} \cdot 1.25 \cdot 10^{-8}\ cm^2$$
$$= 13317\ cm^2 = 1.33 \cdot 10^{18}\ nm^2$$

Part 3: Calculation of the amino functional group concentration

Thus, the total number of APTES molecules per $nm^2$ is:

$$\frac{\text{Number of APTES molecules}}{A_{total}} = \frac{5.74 \cdot 10^{18}}{1.33 \cdot 10^{18}\ nm^2} = 4.3\ \text{APTES molecules}/nm^2$$

## 2. Calculation of the area occupied by a DDAB molecule

Below is an example calculation for a sample of non-functionalized silica particles and the radius of gyration of a DDAB molecule with the following characteristics:

| | |
|---|---|
| Particle diameter | = 549 nm (from SEM measurement) |
| $m_{total}$ | = 0.3 g |
| Radius of gyration of DDAB | = 6.1 Å |
| Surface area occupied by 1 DDAB | =4.7 $nm^2$ |

As shown in the previous calculation the total surface area of all particles can be calculated when the total number of particle is multiplied by the surface area of 1 sphere($A_{sphere}$):

$$A_{total\ silica} = \text{Number of particles} \cdot A_{sphere} = 1.64 \cdot 10^{17}\ nm^2$$

Since the amount [mol] of the surfactant is known, the number of DDAB molecules is calculated using the Avogadro's number:

1 mL of DDAB (0.26 g/L) = $5.6 \cdot 10^{-8}$ mol DDAB

$$\text{Number of DDAB molecules} = 5.6 \cdot 10^{-8}\ \text{mol} \cdot 6.022 \cdot 10^{23}\ \frac{1}{\text{mol}} = 3.38 \cdot 10^{16}$$

Consequently, the area occupied by all DDAB molecules is calculated as:

$$A_{occupied\ by\ all\ DDAB} = \text{Number of DDAB molecules} \cdot A_{occupied\ by\ 1\ DDAB}$$
$$= 3.38 \cdot 10^{16} \cdot 4.7\ nm^2 = 1.59 \cdot 10^{17} nm^2$$

Thus, the ratio between the surface area occupied by all DDAB and the total surface area of all particles is calculated as:

$$\frac{A_{occupied\ by\ all\ DDAB}}{A_{total\ silica}} = \frac{1.59 \cdot 10^{17} nm^2}{1.64 \cdot 10^{17}\ nm^2} = 0.097 = 9.7\ \%$$

## 3. Calculation of the theoretical Ni shell thickness value

Below is an example calculation how the theoretical shell thickness value is obtained. The silica colloid has the following characteristics:

| | |
|---|---|
| Particle diameter | = 568 nm (from SEM measurement) |
| Particle radius | = $2.84 \cdot 10^{-5}$ cm |
| $m_{silica}$ | = 0.01 g |
| $A_{total}$ | = $5.28 \cdot 10^{16}$ $nm^2$ |
| $V_{total\ silica}$ | = 0.005 $cm^3$ |
| Number of all particles | =52110636146 |

When 2 mL out of a Ni electrolyte with a concentration of 5.87 g/L is used, the mass of the Ni ($m_{Ni}$) and the volume of Ni ($V_{Ni}$) is calculated, with a Ni density of ($\rho$ = 8.9 g/$cm^3$):

$$m_{Ni} = 2\ mL\ \cdot 5.87\ \frac{g}{L} =\ 0.0117\ g$$

$$V_{Ni} = \frac{0.0117\ g}{8.9\ \frac{g}{cm^3}} = 0.0013\ cm^3$$

Adding the mass of the Ni ($m_{Ni}$) and the volume of the Ni ($V_{Ni}$) to the total mass of the silica particles ($m_{total}$) and the total volume of silica particles ($V_{totoal}$ silica), respectively, the new total mass ($m_{new}$) and new total volume ($V_{new}$) are:

$$m_{new} =\ m_{Ni} + m_{total} = 0.0117\ g + 0.01\ g =\ 0.0217\ g$$

$$V_{new} =\ V_{Ni} + V_{total} = 0.0013\ cm^3 + 0.005\ cm^3 = 0.0063\ cm^3$$

The volume of One Ni coated perfect sphere can be calculated:

$$V_{one\ coated\ colloid} = \frac{V_{new}}{\text{Number of all particles}} = \frac{0.0063\ cm^3}{52110636146} = 1.21 \cdot 10^{-13} cm^3$$

Thus, the radius of the coated colloid $r_{coated\ colloid}$ can be calculated:

$$r_{one\ coated\ colloid} = \sqrt[3]{\frac{3 \cdot V_{one\ coated\ colloid}}{4 \cdot \pi}} = \sqrt[3]{\frac{3 \cdot 1.21 \cdot 10^{-13} cm^3}{4 \cdot \pi}} = 3.07 \cdot 10^{-5} cm$$

Consequently, the difference between the radius of the non-coated colloid and the radius of the coated colloid is the shell thickness:

$$\text{Shell thickness} = r_{one\ coated\ colloid} - r_{non-coated\ colloid}$$
$$= 3.07 \cdot 10^{-5} cm - 2.84 \cdot 10^{-5} cm = 2.30 \cdot 10^{-6} cm = 23\ nm$$

When it is assumed that all the Ni inside the electrolyte is converted, the theoretical shell thickness is 23 nm.

## 4. Calculation of the shell coverage degree

Below is an example calculation for the shell coverage degree of Janus particles from the SEM images. The Janus particles with the semishell coating is assumed as a perfect spherical cap and the silica core has the following characteristics:

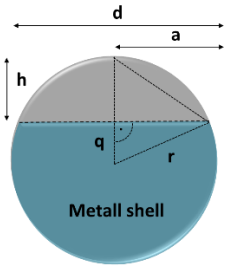


| | |
|---|---|
| Particle radius r | = 299 nm (SEM) |
| $A_{sphere}$ | = 1123446 nm² |
| Ring opening d = 2 ·a | = 396 nm² |

First, the Pythagorean theorem is used to calculate q:

$$q = \sqrt{r^2 - a^2} = \sqrt{(299\ nm)^2 - (198\ nm)^2} = 224\ nm$$

Followed by the calculation of the height h

$$h = \frac{a^2}{q} = \frac{(198\ nm)^2}{224\ nm} = 175\ nm$$

The curved surface area of the spherical cap is calculated, which represents non-coated area:

$$A_{\text{spherical cap}} = 2\pi rh = 2 \cdot \pi \cdot 299\ nm \cdot 175\ nm = 328732\ nm^2$$

Thus, the area of the coated sphere is calculated as:

$$A_{\text{coated sphere}} = A_{\text{sphere}} - A_{\text{spherical cap}} = 1123446\ nm^2 - 328732\ nm^2 = 794714\ nm^2$$

Consequently, the coverage degree can be calculated:

$$Coverage\ degree = \frac{A_{\text{coated sphere}}}{A_{\text{sphere}}} = \frac{794714\ nm^2}{1123446\ nm^2} = 0.71 = 71\ \%$$

Eidesstattliche Erklärung

Hiermit versichere ich, die vorstehende Dissertation in allen Teilen selbstständig und nur unter Zuhilfenahme der ausgewiesenen Quellen und Hilfsmittel erstellt zu haben. Ferner versichere ich, die Dissertation nicht bereits an einer anderen Hochschule oder in einem anderen Studiengang zur Erlangung eines akademischen Grades eingereicht zu haben.

Berlin, den 04. Januar 2018

Scheghajegh Kord Daroun Kalai